Geochemical fingerprints of paleoceanographic variability in the Subarctic Pacific over the last 500,000 years

Kassandra M. Costa

Submitted in partial fulfillment of the
requirements for the degree of
Doctor of Philosophy
in the Graduate School of Arts and Sciences

COLUMBIA UNIVERSITY

2018

Abstract

Geochemical fingerprints of paleoceanographic variability in the Subarctic Pacific over the last 500,000 years

Kassandra M. Costa

Marine sediments are a storehouse of the geochemical, biological, and physical changes in the ocean over thousands to millions of years. Intensive study of the Atlantic Ocean has well constrained the role of this basin in global climate change, but the vast Pacific Ocean, deeper and more corrosive to carbonate, has remained more elusive. This thesis leverages a new suite of sediment cores collected on the Juan de Fuca Ridge in the East Subarctic Pacific Ocean (~45˚N, 135˚W) to better understand how the paleoceanographic history of this region has evolved over the past 500kyr. In Chapter 1, I developed age models for multiple cores using benthic $\delta^{18}O$ and physical properties of sediment as stratigraphic markers. Despite the proximity of the cores (within $50km^2$), the sedimentation rates varied by an order of magnitude, likely reflecting remobilization of sediment caused by the high relief of the mid-ocean ridge bathymetry. In Chapter 2, I analyzed uranium series disequilibria in the sediment in order to investigate the processes generating the highly variable sedimentation rates. This chapter presents evidence that the particle flux settling through the water column (based on excess ^{230}Th) is relatively constant at six different sites, and the variability in sedimentation rates is largely driven by lateral sediment remobilization along the rough bathymetry of the ridge. Chapter 3, entitled "Trace element (Mn, Zn, Ni, V) and authigenic uranium (aU) geochemistry reveal sedimentary redox history on the Juan de Fuca Ridge, North Pacific Ocean", presented

high-resolution x-ray fluorescence records of metal diagenesis in response to changing oxygen conditions in the sediment. This study is the first to show strong evidence for low sedimentary oxygen conditions during interglacial periods in the North Pacific, which we suggest may be linked to hydrothermal sulfide deposition. In Chapter 4, I returned to uranium series disequilibria by utilizing $^{231}Pa/^{230}Th$ records from the Juan de Fuca Ridge to reconstruct productivity in the East Subarctic Pacific Ocean over the last 200kyr. Productivity across much of the Subarctic Pacific is low during glacial periods and high during interglacial periods, which is usually associated with changes in stratification. I investigated several different mechanisms for increasing stratification during glacial periods, and conclude that a combination of surface freshening, weak winds, and reduced subsurface nutrient concentrations likely created the stratification that led to low glacial productivity.

Finally, in Chapter 5, "Dust deposition in the East Subarctic Pacific on glacial-interglacial timescales", I reconstructed the patterns of dust fluxes in the East Subarctic Pacific Ocean over the last 500kyr to assess the climatic effects on the spatial distribution of dust in the North Pacific Ocean. I predict that migration of the westerlies would have caused a shift in dust provenance away from Asian dust and towards higher North American contributions during glacial periods. Although lithogenic endmembers are currently poorly constrained in this region, I present some evidence for variable provenance over time that may be consistent with the influence of the westerlies on dust fluxes in the East Subarctic.

Table of Contents

List of Figures and Tables

Chapter 1. Sedimentation, stratigraphy and physical properties of sediment on the Juan de Fuca Ridge

Acknowledgements

This dissertation exists today because of the support and encouragement from family, friends, and colleagues. Through all the ups and downs of graduate student life, I have made it out the other side because you reminded me to leave the lab once in a while… to drink coffee and eat oreos while working on the Friday crossword, to check out that turtle crossing the road, or to sit on the back patio with the bees. I thank my friends in geochemistry, for our nerdy (and delightful!) conversations about which element is the best, and I thank my friends outside of geochemistry, for reminding me that maybe, just maybe, there is more to life than thinking about geochemistry.

I am especially thankful for my family, my parents Raul and Isabel and my sisters Katherine and Kristine. My sisters have always made my life sound more interesting than I myself ever felt it was, and I appreciate their always believing in me. My parents are my closest allies who I can count on for anything. Literally anything. Their constant love and support is something that helps keep me going. I feel lucky, and grateful, that that they are always willing to help me through any tough situation, big or small, even when I'm at my most "difficult".

Besides human support, this thesis has benefited from generous behind-the-scenes science assistance from many researchers at LDEO. I especially thank Nicole Anest, the unflappable leader of the Core Repository, and Wei Huang, the patient Stable Isotope Lab Manager, both of whom have helped me in my pursuits of sampling, processing, and analyzing 1000s of sediment samples. I am exceedingly grateful to Marty Fleisher, the U-

Series Lab Manager, who really was my “Laboratory Advisor” and taught me everything I know about uranium series chemistry. Marty not only trained me to troubleshoot the ICP-MS when it died (which was often), donated hydrochloric acid when I ran out (less often), and gave me savillexes of Mix Pa (very, very often), but he also helped me to develop my chemical intuition and taught me how to teach others in the lab. I could never have run so many U-Th-Pa samples without Marty’s support. Last but not least, a special shout out to fellow graduate student Frankie Pavia, my U-Th-Pa lab cousin, who has talked me out of (and into?) many wacky ideas over the years.

I would like to acknowledge all the members of my committee, including Bob and Gisela who have toughed it out for 5 years, and Stephanie and Suzanne, who have joined us for the home stretch. Bob has been a tireless collaborator, who is almost always the first person to respond to any paper draft or slide presentation. Bob holds his research to a high standard, and I have become a better scientist because of it. Gisela has been the one to bring me down to Earth from my theoretical musings, to ask me to pin down what something *really* means and how it *actually* works. Gisela has taught me how to be critical of my own work and how to connect the details to the big picture. I am grateful to have collaborated with Suzanne since the VOICE cruise in 2014 on a (sometimes tumultuous) project, and I have great respect for her composure and fortitude, even in the midst of intransigence. I’d also like to thank Stephanie, a fellow constant flux proxy enthusiast, who I have enjoyed getting to know over the past five years. She has always put in the effort to stop by my posters at conferences, even on a Friday afternoon when the masses have deserted, and her consideration and support has really meant a lot to me, and helped me to have more confidence that maybe I can “make it” in the academic world.

Last, and most important of all, I could not say thanks enough to my advisor JERRY. Even though he refuses to dispense any actual “advice”, his socratic method and hands off mentoring style (though frustrating at times!) have helped me to develop into an independent and proactive scientist, able to reason through problems and draw my own conclusions, and to find a way to defend my ideas and decisions on my own. Jerry has always supported my endeavors, whether promising or ill-fated, and his belief in me helps me to believe in myself. I have tried to osmose as much of the affable and forgiving nature that fuels his “we’re not about blame” and “conservation of optimism” mentalities with the hope that someday I could be half the mentor and role model that Jerry is. I am immensely thankful to have had this opportunity to conduct my graduate research with Jerry, and I will never let him forget it!

To my parents

Raul and Isabel Costa

And all at once the whole earth, round, was beheld

Emerging from the deep blue

Fernando Pessoa

Chapter 1

Sedimentation, stratigraphy and physical properties of sediment on the Juan de Fuca Ridge

Note: A modified version of this chapter has been published in *Marine Geology*[1]

Abstract:

Sedimentation near mid-ocean ridges may differ from pelagic sedimentation due to the influence of the ridge's rough topography on sediment deposition and transport. This study explores whether the near-ridge environment responds to glacial-interglacial changes in climate and oceanography. New benthic $\delta^{18}O$, radiocarbon, multi-sensor track, and physical property (sedimentation rates, density, magnetic susceptibility) data for seven cores on the Juan de Fuca Ridge provide multiple records covering the past 700,000 years of oceanographic history of the Northeast Pacific Ocean. Systematic variations in sediment density and coarse fraction correspond to glacial-interglacial cycles identified in benthic $\delta^{18}O$, and these observations may provide a framework for mapping the $\delta^{18}O$ chronostratigraphy via sediment density to other locations on the Juan de Fuca Ridge and beyond. Sedimentation rates generally range from 0.5 to 3 cm/kyr, with background pelagic sedimentation rates close to 1 cm/kyr. Variability in sedimentation rates close to the ridge likely reflects remobilization of sediment caused by the high relief of the ridge bathymetry.

---

[1] *Authors:* K. M. Costa*[1,2], J. F. McManus[1,2], B. Boulahanis[1,2], S. Carbotte[1], G. Winckler[1,2], P. Huybers[3], C. Langmuir[3]. *Affiliations:* [1]Lamont-Doherty Earth Observatory of Columbia University, Palisades, NY 10964, USA. [2]Department of Earth and Environmental Sciences, Columbia University, New York, NY 10027, USA. [3]Department of Earth and Planetary Sciences, Harvard University, Cambridge, MA 02138, USA.

Sedimentation patterns primarily reflect divergence of sedimentation rates with distance from the ridge axis and glacial-interglacial variation in sedimentation that may reflect carbonate preservation cycles as well as preferential remobilization of fine material.

1.1. Introduction

Marine sediments are a storehouse of the geochemical, biological, and physical changes in the ocean over thousands to millions of years. Their archival utility is predicated on slowly settling sediment blanketing the submarine landscape to abyssal flatness, but rough topographic features like hills, seamounts, and ridges can distort flow fields and depositional dynamics of sediment on the seafloor (Dubois and Mitchell, 2012; Johnson and Johnson, 1970; Mitchell and Huthnance, 2013; Turnewitsch et al., 2013; von Stackelberg et al., 1979). Uneven topography can alternately deflect, accelerate, and decelerate bottom currents, generating a heterogeneous depositional environment over a wide range of spatial and temporal scales (Turnewitsch et al., 2013). Extensive two-dimensional topographic features, such as mid-ocean ridges and submarine canyons, exhibit prominent sediment mobilization and transport from bathymetric highs to lows, both by currents and by downslope gravitational flows. Acoustic profiling characterizes sediment distribution, thickness, and depositional processes in the modern near-ridge environments of the Mid-Atlantic Ridge and the East Pacific Rise (Ewing et al., 1964; Hauschild et al., 2003; Lister, 1976; Marks, 1981; Neil C. Mitchell et al., 1998; Ruddiman, 1972), but how these depositional environments respond to glacial-interglacial variability is poorly constrained. The unique geochemical and biological microcosm of a mid-ocean ridge motivates investigation into the integrity of the sediment medium to record the evolution of the ridge system over time.

Ridge-influenced sedimentary regimes can be recorded in the physical properties of sediments (Turnewitsch et al., 2013), such as accumulation rate, density, and magnetic susceptibility. These physical properties respond to changes in the porosity, the density and geochemical composition of the grains (e.g., calcium carbonate, terrigenous silicate, hydrothermal metals), and the grain size and shape (Breitzke, 2006). Variability in the flow field geometry translates into lower sediment accumulation rates and coarser grains under fast flows and higher sediment accumulation rates and finer grains in more quiescent areas. These spatial patterns compound with temporal variability, such as glacial-interglacial cycles in carbonate preservation (Farrell and Prell, 1989), which can affect both the density and grain size of the sediment medium. This paper presents sedimentation rates, density, and magnetic susceptibility for a suite of seven cores covering almost 700,000 years of sedimentation on the Juan de Fuca Ridge. We aim to determine the major modes of sedimentation in the near-ridge environment and explore how they may have varied with climatic and oceanographic changes associated with glacial-interglacial cycles.

1.2. Study Site & Oceanography

The Juan de Fuca Ridge (JdFR) is located in the Northeast Pacific Ocean about 500km off the coast of North America in the subpolar transition zone, where warm surface waters from the west wind drift diverge into the California Current, flowing south, and into the Alaskan Gyre, flowing north (Hickey, 1979). Bottom waters in the vicinity of the JdFR are composed of Pacific Deep Water (Macdonald et al., 2009) (Figure 1.1), which constitutes the oldest and most corrosive deepwater in the modern ocean (Key et al., 2002; Kroopnick, 1985). Because corrosivity of deep Pacific waters leads to poor carbonate preservation (e.g., Karlin et al., 1992), paleoceanographic investigations into this region have been limited by low sedimentation rates and difficulties generating age models via foraminiferal stable

isotope stratigraphy. Thus the relatively shallow sedimentary environment on the JdFR (<3000m), which rises above the corrosive bottom waters, may provide important information about ocean circulation and chemistry in this understudied region.

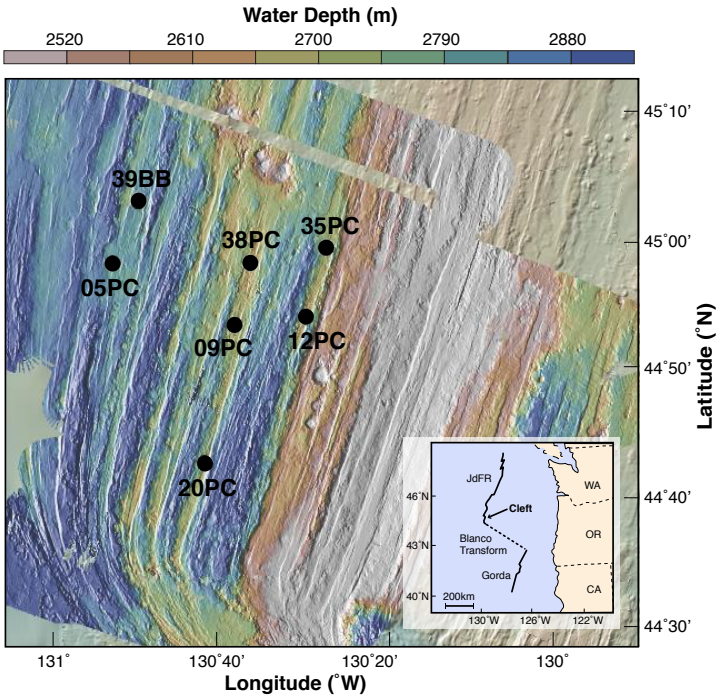

Figure 1.1. Map of the study region. (Left) Location of the Cleft Segment of the Juan de Fuca Ridge relative to the North American coast. (Right) Bathymetric map of the Cleft Segment generated by shipboard multibeam data. The ridge can be identified as the NE-SW trending bathymetric high (in white). AT26-19 core locations on the western flanks of the ridge are shown with black circles, and locations are provided in Table 1. All cores were recovered from the crests of abyssal hills in order to obtain sediments with adequate carbonate preservation to generate age models. Cores 12PC and 35PC are both located next to the scarp that defines the boundary of the poorly sedimented axial plateau.

The JdFR is an intermediate spreading ridge (56mm/yr) that is characterized by extensive hydrothermal activity and hot spot volcanism (Karsten and Delaney, 1989; Massoth et al., 1994; Normark et al., 1983; Wilson, 1993). The Cleft Segment of the JdFR is located at the southern end of the ridge system, bounded by the Vance Segment to the north and the Blanco Fracture Zone to the south. The Cleft segment is 55km long and contains a modest axial rift that is 50-150m deep and 2-4km wide (Baker et al., 1989; Carbotte et al., 2006). Hydrothermal activity occurs within the rift valley both as diffuse venting, along the southern 18km of the segment, and as discrete venting, via Pipe Organ,

Monolith, and Fountain vents at the north end of the segment (Massoth et al., 1994). Outside the rift valley is a thinly sedimented axial plateau with low relief abyssal hills that extends approximately 16km from the ridge axis and terminates in a 300m scarp before continuing into regularly spaced, ridge parallel crests and troughs further on the ridge flanks (Carbotte et al., 2008, 2006). Whereas the western flanks contain the preponderance of seamounts and hotspot activity (Davis and Karsten, 1986), the eastern flanks suffer from frequent turbidity current activity off the coast of North America (e.g., Goldfinger et al., 2012; Horn et al., 1971). Turbidity currents interrupt and sometimes erode hemipelagic sedimentation and interfere with sedimentological reconstructions of glacial-interglacial climate change, so that the spatial and temporal variability in sedimentation in this region is poorly constrained. To minimize the influence of turbidity currents, this study focuses on cores that were collected from the western flanks of the Cleft Segment on the SeaVOICE cruise (AT26-19) of the R/V Atlantis in September 2014 (Table 1).

Table 1.1 | AT26-19 cores included in this study.

Core	Lat (˚N)	Long (˚W)	Water Depth (m)	Core Length (cm)
05PC	44.97283	130.87850	2711	644.7
09PC	44.88717	130.63683	2678	765.9
12PC	44.89750	130.50433	2689	550.2
38PC	44.97053	130.60653	2655	736.1
20PC	44.70817	130.70383	2738	540.5
35PC	44.99118	130.45737	2731	642.4
39BB	45.04507	130.83318	2794	513.0

During the cruise, over 50m of sediment was collected on the JdFR flanks, in addition to basalt rock cores and high-resolution multi-beam sonar mapping. This paper focuses on the longest, stratigraphically intact records of six piston cores (05PC, 09PC, 12PC, 20PC, 35PC, 38PC) and one "Big Bertha" gravity core (39BB). Bathymetric highs were targeted for coring sites to maximize carbonate preservation, and so cores were recovered from a limited depth range (2655-2794 m) along the crests of ridge-parallel abyssal hills. This coring strategy resulted in both ridge-perpendicular transects as well as ridge-parallel transects along basement isochrons, based on geomagnetic reversals and spreading rates from the ridge crest (Wilson, 1993). Cores 05PC and 39BB are located on the oldest crust (~1.8 million years old), while cores 38PC, 09PC, and 20PC are located on intermediate age crust (1.0 million years old). Cores 35PC and 12PC are located on the youngest crust (700,000 years old), and core 12PC impacted basalt at its base.

1.3 Methods

1.3.1 $\delta^{18}O$ stratigraphy

Samples from four cores (05PC, 09PC, 12PC, and 38PC) were analyzed for $\delta^{18}O$ in order to establish baseline chronologies. Samples were freeze-dried, and then an aliquot was weighed into a 125mL Nalgene bottle, filled with approximately 100mL of tap water, and disaggregated on a tumble wheel for two hours. Samples were then sieved at 63□m, and a soft brush was used to gently break up clay clumps that did not sufficiently disintegrate during tumbling. The coarse sediment fraction remaining in the sieve was then dried and weighed, and the mass fraction of coarse material was calculated relative to the initial aliquot mass. *Uvigerina sp.* tests were picked from the coarse fraction and analyzed at Lamont Doherty Earth Observatory (LDEO) on a Thermo Delta V Plus equipped with a

Kiel IV individual acid bath device. Samples have been replicated at >20% frequency and standardized to NBS-19. All data are reported on the VPDB scale with precision ≤0.05‰. Samples from 35PC and 39BB were also sieved for coarse fraction, as described above.

1.3.2 Radiocarbon

Coretop radiocarbon dates for 05PC, 09PC, 12PC, and 38PC were analyzed on *Globigerinoides bulloides*. Samples were picked from the shallowest depth at which sufficient foraminifera tests were available for analysis, as shallow as 0 cm depth (38PC) and as deep as 16 cm depth (09PC). Analyses were performed at the National Ocean Sciences Accelerator Mass Spectrometry Facility at Woods Hole Oceanographic Institution. Radiocarbon ages were calibrated to calendar years using Calib 7.0 Marine13 (Reimer et al., 2013; Stuiver and Reimer, 1993) with a total reservoir correction of 800 years (ΔR = 400).

1.3.3 Multi-sensor track data

Bulk sediment physical properties were measured shipboard on a Geotek multi-sensor track (MST) system at 1cm resolution. Gamma ray attenuation is inversely dependent on the mass of sediment within a given volume (Gunn and Best, 1998), and it can be calibrated to density through discrete sample analyses. Volume controlled samples were taken from select cores by depressing standard paleomagnetic sample boxes (2x2x2cm) into the sediment, concentrated at the top of each core (5cm, 25cm, 50cm, and every 50cm thereafter) in order to constrain the density differences associated with high coretop porosity. Only those boxes that extracted the full 8cc volume were included in further analysis. Boxes were parafilmed and refrigerated to avoid evaporation during

transport back to LDEO, where they were weighed before and after freeze-drying to obtain the wet and dry sample masses. A salt correction was applied assuming S=35‰ and using the calculated mass of seawater lost. Wet and dry bulk densities could then be calculated using the known 8cc sample volume.

In addition to density, magnetic susceptibility (MS) was also analyzed on the Geotek multi-sensor track system. MS measures how easily a substance can be magnetized, and it is quantified as the magnetization induced by applying a magnetic field to a specific volume of material (Gunn and Best, 1998). The magnetic field is generated by a whole core loop sensor (diameter 14cm) that integrates over 12cm of the core. The MS of bulk sediment is a function of the concentration and type of magnetizable minerals within the induced magnetic field (Carmichael, 1982). The major mineral phases in marine sediment, such as quartz and calcite, are diamagnetic and exhibit no magnetism. Instead, the MS of bulk sediment reflects the concentration of trace minerals, such as clays (nontronite, montmorillonite, biotite) and Fe-rich phases (siderite, hematite, pyrite, magnetite), which exhibit magnetism within (and sometimes without) a magnetic field. Clays and Fe-rich phases characterize terrigenous sediment, and so MS is often a proxy for terrigenous sediment inputs (Bloemendal and deMenocal, 1989; deMenocal et al., 1991; Larrasoaña et al., 2008).

1.3.4 Age model generation

Age models were created by incorporating the temporal information in the coherent MST data with the benthic $\delta^{18}O$ records. Following standard practices, initial age models for 05PC, 09PC, 12PC, and 38PC were generated by graphic correlation (Prell et al., 1986) of the individual $\delta^{18}O$ records to the global benthic stack (Lisiecki and Raymo, 2005).

Tiepoints were limited to the midpoints of glacial terminations, where the $\delta^{18}O$ records have the highest signal to noise ratio. While greater numbers of tiepoints may create more precise age models when $\delta^{18}O$ are well-constrained, the high noise in the Juan de Fuca $d^{18}O$ records would have introduced significant temporal uncertainty if finer tiepoints were used. Thus we chose to only use the termination tiepoints for the initial alignment and to increase the precision of the age models during the secondary alignment (see below) using the much higher resolution MST records.

Radiocarbon-based ages were used to constrain the coretop ages, and ages were linearly interpolated between tiepoints. These initial age models were then applied to the dry bulk density and magnetic susceptibility records in order to loosely define the sequence of glacial-interglacial periods.

Secondary alignment of the age models was conducted to coordinate prominent features in the MST data: density peak in Marine Isotope Stage 2 (MIS2, 19-23ka, Mix et al., 2001), density transitions associated with Termination II (MIS6 to MIS5, 129.8ka, Martinson et al., 1987) and Termination V (MIS12 to MIS11, 424ka) and the magnetic susceptibility anomaly (272ka, as assigned by the $\delta^{18}O$ alignment). The coherent density records allowed the number of tiepoints ($n \geq 20$) to greatly exceed the number used for the initial oxygen isotope alignment. Core 09PC was designated the target age model because its $\delta^{18}O$ record had the highest signal to noise ratio and thus the most reliable age assignments. The magnetic susceptibility peak was collapsed onto a single timepoint, the apex of the peak, to accommodate a near-instantaneous depositional process. Other tiepoints associated with the $\delta^{18}O$ -record (e.g., for MIS8 to MIS7 boundary) were retained during the secondary alignment, and age models were linearly interpolated between tiepoints. Secondary alignment of cores adjusted the age models on average less than 10%,

with most of the changes around 250-300ka. Only these adjusted age models are presented throughout the paper.

After secondary alignment, the individual dry bulk density, $\delta^{18}O$, magnetic susceptibility, and coarse fraction records were averaged into regional stacks. Each record was interpolated onto a fine timestep (0.1kyr) to preserve the high-resolution detail present in the individual records, and then the values for 05PC, 09PC, 12PC, and 38PC were averaged at each timestep to create stacked regional records.

The generally well-constrained regional dry bulk density signal captured in the stacked record enables generation of stratigraphically derived age models for the remaining three cores (20PC, 35PC, 39BB) without independent $\delta^{18}O$ records. Instead age models were established by graphically correlating the individual dry bulk density records to the dry bulk density stack, using the same tiepoints as described above for the secondary alignment, and age models were linearly interpolated between tiepoints. A complementary alignment was also conducted using the magnetic susceptibility stack and individual magnetic susceptibility records, following the same procedure as used for dry bulk density. The magnetic susceptibility alignment and the dry bulk density alignment are nearly identical for all three cores. The stacking procedure was reiterated, now including all seven cores.

All seven age models are fairly robust for sediment younger than the magnetic susceptibility peak (272ka), but age assignments acquire greater uncertainty in older sediments. Over the last 272kyr, the dry bulk density records correspond in both trend and amplitude, with well-defined square function increases in dry bulk density during glacial periods, and three distinct glacial cycles occur after the magnetic susceptibility peak. In sediment older than the magnetic susceptibility peak, irregularities in the dry bulk density

records introduce greater subjectivity into the stratigraphic alignment of age models. The weak dry bulk density signal during MIS10 can make this glacial period difficult to align between MIS8 and MIS12 (e.g. 38PC), and the relatively flat magnetic susceptibility signal during this period provides no assistance. Some cores (12PC, 38PC) contain low density intervals within MIS12 but other cores (05PC) do not, complicating the alignment of the bottom age for those cores that end within MIS12 (09PC, 35PC). Core 12PC notably reaches only 605ka, nearly 100kyr younger than the estimated age of the underlying basement, yet basalt rock was impacted and recovered at the bottom of the core. While the two age estimates are not inconsistent, their apparent offset may provide insights into near-ridge processes, including the possibility of negligible sediment deposition on the youngest crust (Su et al., 2000), or emplacement of basalt within the sedimentary sequence, either by off-axis volcanism that produced more recent basalt at this location, or downslope movement of older rocks, perhaps along fault scarps. It should be noted that while the age models presented here represent our currently preferred interpretation of the alignment of benthic $\delta^{18}O$, dry bulk density, coarse fraction, and magnetic susceptibility, other interpretations remain possible, and may even become preferable in light of subsequent investigation into these cores.

1.4 Results

Oxygen isotope records for 05PC, 09PC, 12PC, and 38PC are presented in Figure 1.2. The $\delta^{18}O$ records largely correspond with the global benthic stack (Lisiecki and Raymo, 2005), with relatively enriched glacial periods ($\delta^{18}O \geq 4.5‰$) and relatively depleted interglacial periods ($\delta^{18}O \leq 4.0‰$), reflecting the dominant influence of global ice volume. The amplitude of these cycles is somewhat muted, which may be attributed in part to the

smoothing influence of bioturbation. However, isotope cycles from low sedimentation rate portions of, e.g., 09PC, show no further diminishing in the isotope range of glacial cycles (MIS9-10-11-12) despite the expectation for an enhanced bioturbation effect. One possible influence on the isotopic records may be the smaller glacial-interglacial temperature changes of approximately 2°C in the deep Pacific relative to those of ~4-5°C in the Atlantic (Chappell and Shackleton, 1986; Labeyrie et al., 1987; Schrag et al., 1996), which are heavily represented in the cores used for the global benthic stack (Lisiecki and Raymo, 2005). Regardless, the glacial-interglacial cycles are sufficiently identifiable for the purposes of constructing preliminary age models (see Supplementary Materials). Coretops for 12PC (~19.2ka) and 38PC (~16.6ka) only reach the last deglaciation, indicating no recovery of Holocene sediment at these sites. Slightly deeper samples from 05PC and 09PC date to the last deglaciation (~15.1ka and 13.7ka, respectively), which project to early Holocene ages at the respective coretops.

Table 1.2 | Radiocarbon ages.

Core	Depth (cm)	NOSAMS Accession #	14C Age (years)	±	Calendar Age (years)	±
05PC	8	OS-118739	15050	65	15399	208
09PC	16	OS-118740	13700	50	13447	227
12PC	1	OS-118741	18300	95	19185	317
38PC	0	OS-118613	16100	40	16625	131

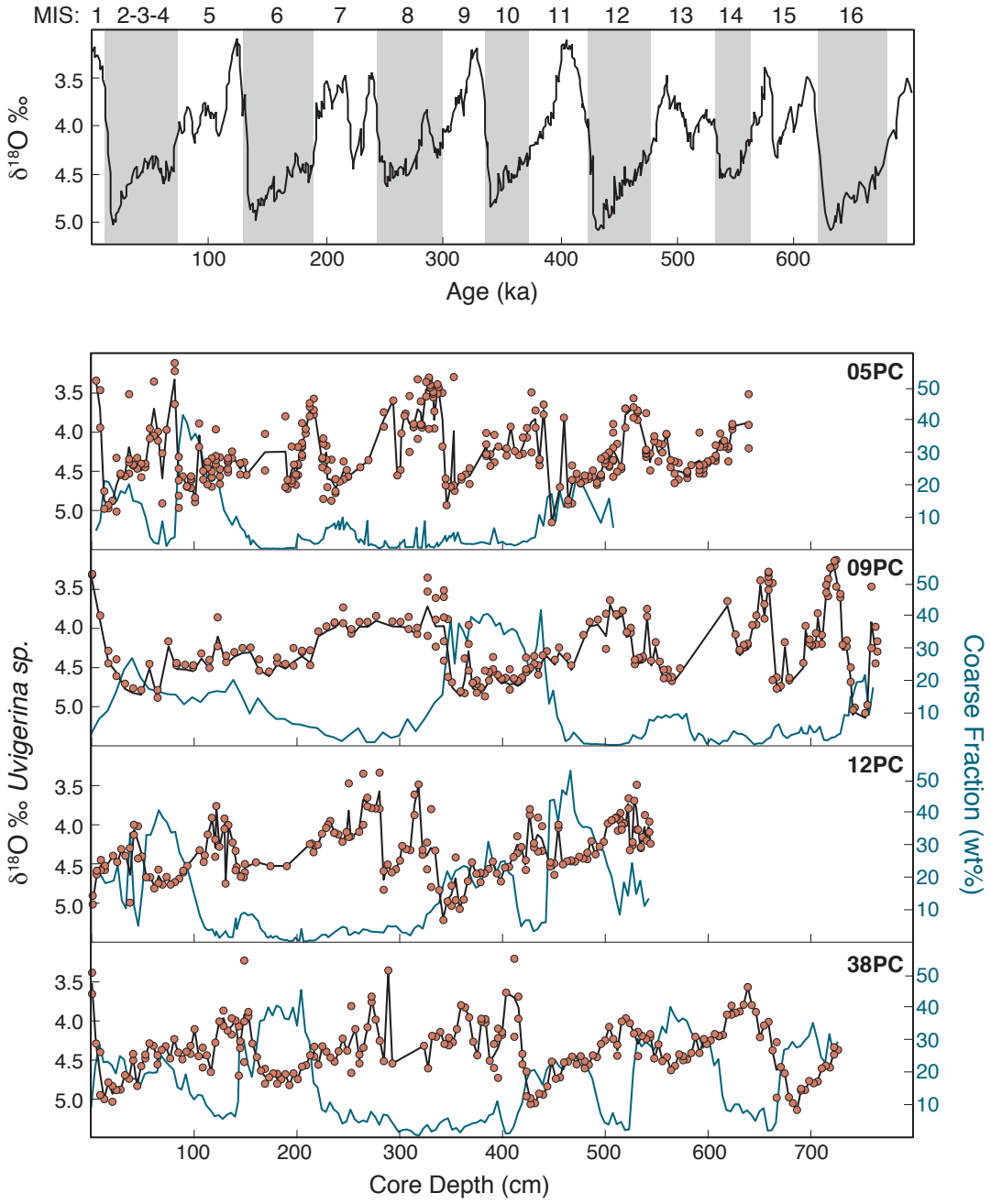

Figure 1.2. Oxygen isotope stratigraphies for 05PC, 09PC, 12PC, and 38PC. (Top) Target benthic δ18O stratigraphy based on the global stack (Lisiecki and Raymo, 2005). Marine Isotope Stages (MIS) are identified at the top. Glacial periods (even MIS) are highlighted in orange bands, after Martinson et al. (1987). (Bottom) Oxygen isotope data are reported on the VPDB scale with precision ≤0.05‰, and all replicates of individual samples are included (orange circles). Black lines pass through the average isotopic value for each sample. Intra-sample variability tends to be greater during interglacial than glacial periods, potentially reflecting bioturbation across abrupt isotopic changes. Coarse fraction is shown in blue and tends to increase during glacial periods, when carbonate preservation is enhanced.

Raw MST data for all seven cores are presented in Figure S1.1. The relationship between gamma attenuation and density appears consistent across multiple cores (Figure S1.2), and so one density calibration, using simple least squares and a linear fit, was applied to all cores. The calibrated records (Figure 1.3) indicate clearly defined cycles in dry bulk density (DBD) on the JdFR. The sediment appears to fluctuate between two steady states: high density periods with DBD ≈ 0.7 g/cm^3 and low density periods with DBD ≈ 0.4 g/cm^3, and the transitions between these periods appear relatively abrupt.

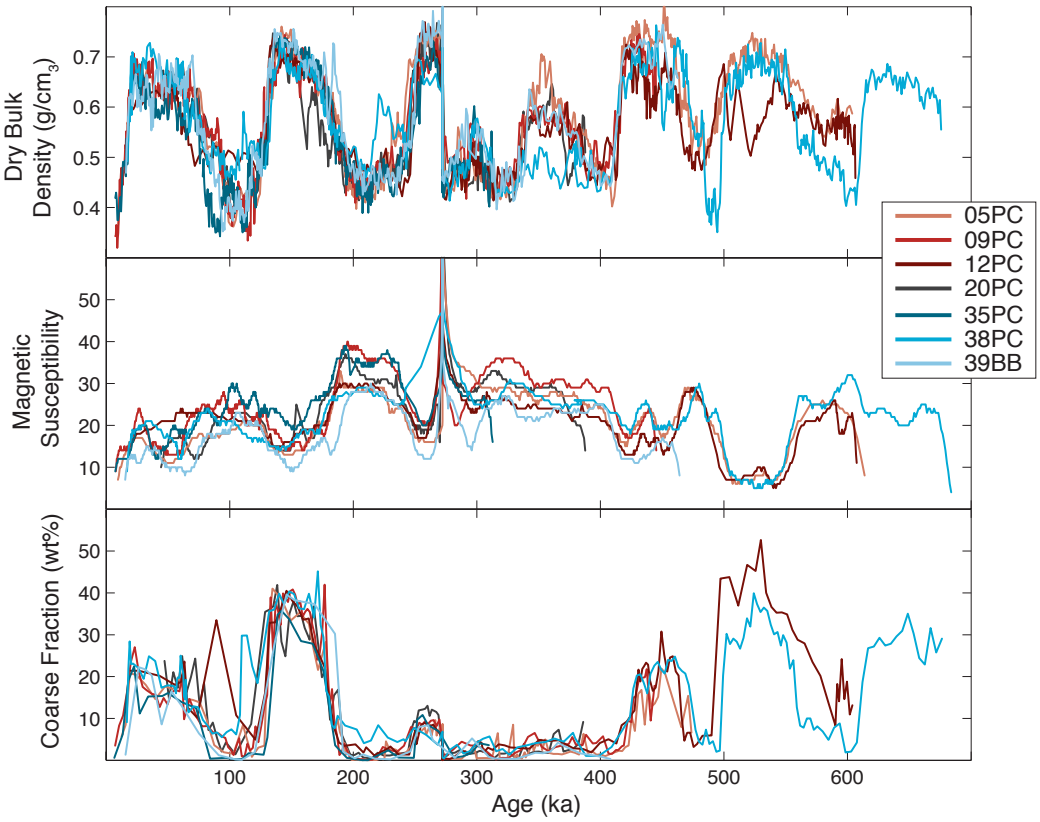

Figure 1.3. Density, magnetic susceptibility, and coarse fraction records from all seven cores. Color legend is the same in all three panels. Agreement between the cores is with the error of the calculation (±10%) for dry bulk density (see, e.g., Supplementary Figure 2). Low count rates for magnetic susceptibility would lead to large errors (±20%) that could account for the more variable inter-core comparison. Reproducibility of coarse fraction measurements (±10%) could also account for the general range of values, although spikes in coarse fraction, e.g. in 12PC ~90ka, likely reflect real features, in this case a bioturbation channel.

Unlike the DBD, the magnetic susceptibility (MS) records generally show low amplitude variability and have gradual transitions, which are likely derived from the smoothing effects of the MS measurement. The most prominent feature is a peak, approximately five times the amplitude of background levels, that occurs ~272ka before the last three DBD cycles. MS is otherwise low, showing a generally inverse relationship with DBD and ranging from 10-15 $*10^{-6}$ in high density periods to 30-40$*10^{-6}$ during low density periods (Figure 1.3).

The coarse fraction (mass percent > 63μm) positively correlates with density and tends to increase during high density periods, reaching a maximum of 52.7wt% in 12PC (Figure 1.3). Average coarse fractions during a high density period are comparable (30-40wt%) for 09PC, 12PC, 20PC, 35PC, 38PC, and 39BB, while 05PC often exhibits lower coarse fraction (20wt%). Low coarse fractions (<5wt%) are typical of low density periods, and near-zero coarse fractions characterize the sediment associated with the MS peak. Visual inspection of coarse material indicates that it is predominantly composed of planktonic foraminifera (*G. bulloides, N. pachyderma)* with occasional basalt, quartz, and mica chips.

1.5 Discussion

1.5.1 Physical properties

The consistent patterns of DBD, $\delta^{18}O$, magnetic susceptibility, and coarse fraction records from each cores permitted the extraction of a regional signal in the physical properties. The individual records were averaged into stacks (Figure 1.4), and the stacked records demonstrate the predictable effects of the climatic and oceanographic variability associated with glacial-interglacial cycles on the physical properties of sediments. Glacial

periods are characterized by high density, low magnetic susceptibility, and high coarse fraction, while interglacial periods are characterized by low density, high magnetic susceptibility, and low coarse fraction. Dry bulk density has previously been shown to correlate with carbonate content (Mayer, 1991, 1979), and changes in carbonate preservation could explain the temporal variability in physical properties. High carbonate preservation during glacial periods increases the sediment density and dilutes the MS, and the opposite occurs during interglacial periods. Partial dissolution weakens the integrity of the foraminifera tests and increases the degree of fragmentation (Berger, 1979), reducing the mass fraction of coarse material during interglacial periods. However, the glacial-interglacial cycles in carbonate preservation are inadequate to explain the anomalous peak in MS around 272ka. This peak corresponds with near-zero coarse fraction and relatively high density, equal to or slightly greater than the glacial average, and it indicates an extreme depositional event of 10s to 100s of centimeters of dense, fine and highly magnetizable material. The sediment is unique in the history of the JdFR, and it is bounded by a sharp base and bioturbation at the top. Deposition persists on the regional scale, not just on the flanks of the JdFR, but as far west as Cobb Square, where a similarly high MS event has been recorded in the same stratigraphic position (Karlin et al., 1992). The sedimentological characteristics and the severe and widespread nature of this event are an intriguing puzzle that certainly warrants further investigation, although it is beyond the scope of this paper.

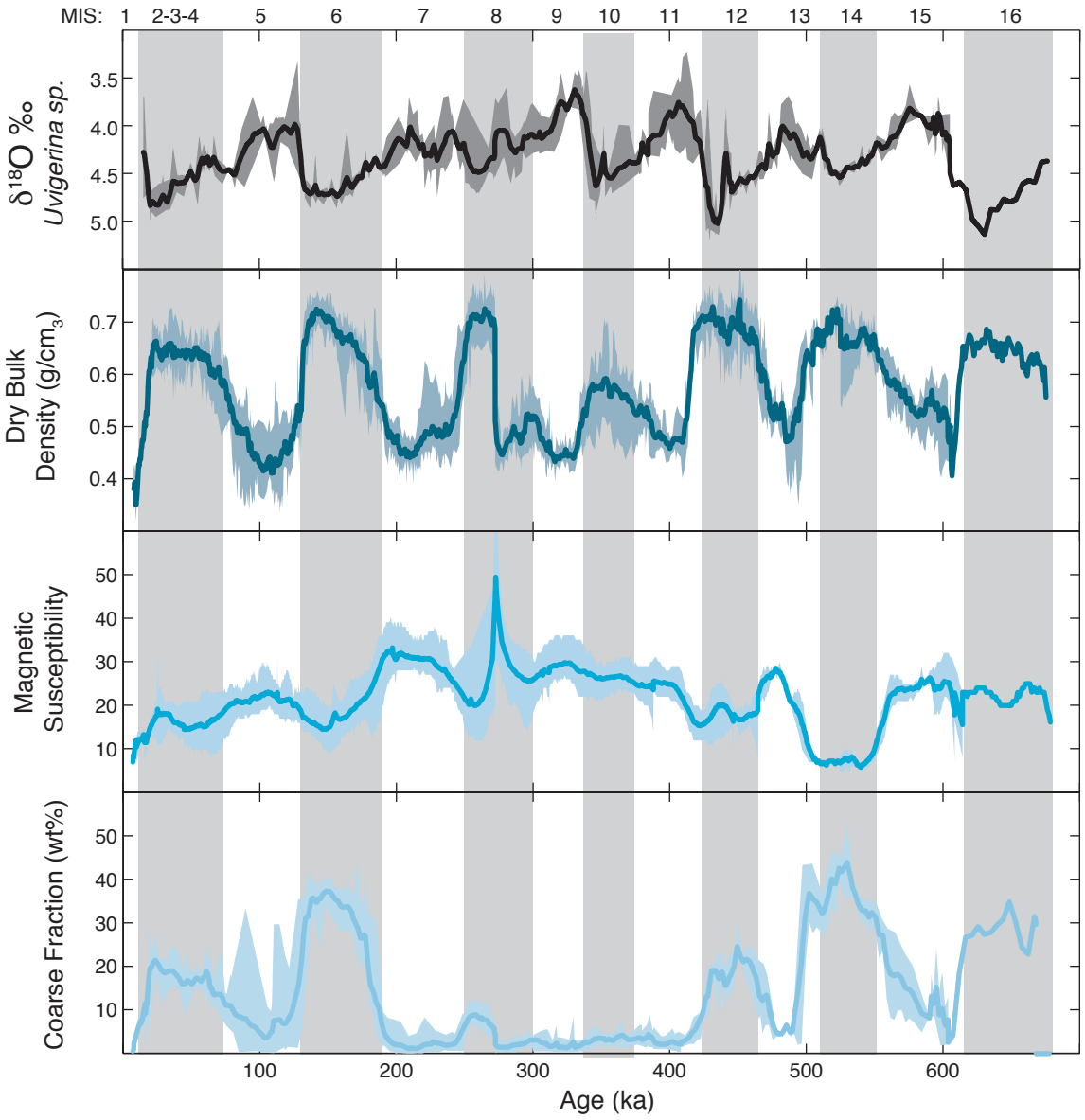

Figure 1.4. Stacked oxygen isotope, density, magnetic susceptibility, and coarse fraction records. Individual records from all seven cores were interpolated onto 0.1kyr timesteps and averaged at each timestep to generate the stacked records. Gray bars are as in Figure 1.2. Shaded envelopes show the full range of values averaged within each timestep.

1.5.2 Near-ridge sedimentation environment

Sedimentation rates are highly variable on the JdFR both spatially and temporally. Overall, sedimentation rates range between 0.25 to 3.18 cm/kyr (Figure 1.5), and this range is captured within single cores with variable sedimentation rates over time (35PC: 0.41cm/kyr in MIS9 vs 3.18cm/kyr in MIS5) and between cores during the same time slice (MIS5: 0.61cm/kyr at 05PC vs 3.18cm/kyr at 35PC). Comparable sedimentation variability has been observed in the near-ridge environment on the East Pacific Rise, Galapagos Spreading Center, and Southeast Indian Ridge (Mitchell, 1998, 1993), where sedimentation rates can vary by as much as 80%. All cores on the JdFR show relatively high sedimentation rates (1.3-1.8cm/kyr) during the MS peak at 272ka, but otherwise no consistent glacial-interglacial response is apparent in all cores. Some cores generally show higher sedimentation rates during glacial periods (05PC, 12PC, 20PC, 38PC) while others show higher sedimentation rates during interglacial periods (09PC, 35PC, 39BB).

Sediment accumulation in the near ridge environment is primarily controlled by three factors: vertical rain rate of pelagic sediment, degree of carbonate dissolution, and intensity of sediment redistribution along the seafloor (Hauschild et al., 2003). Because surface productivity is relatively stable at the regional scale (tens of kilometers), the pelagic rain rate is likely to be homogeneous across the seven cores on the JdFR. Bathymetry deepens with increasing distance from the ridge, and so carbonate dissolution may similarly increase as the core sites enter more corrosive bottom waters. Increased dissolution at deeper sites would reduce the sedimentation rates there, but the cores included in this study represent a relatively narrow depth range (2655-2794 m), so that changes in carbonate preservation are unlikely to explain much of the heterogeneity between cores. Alternatively, sediment redistribution on the seafloor can generate locally high and low sedimentation rates by gravitational slumping, resuspension, and transport in

bottom currents. Sediment redistribution is ubiquitous in the modern ocean (Francois et al., 2004), but mid-ocean ridges may present the most extreme example, in which deep pockets of sediment surround regions of nearly bare rock (e.g. Ewing et al., 1964). The spatially heterogeneous sedimentation on the JdFR evident from our cores suggests that sediment redistribution may be the dominant control on sedimentation rate in this region.

To assess the major modes of sedimentation, an empirical orthogonal function (EOF) analysis was conducted on the sedimentation rates for the time periods covered by all seven cores (MIS2-7). The sedimentation rates were normalized (z-scored) to place them all on the same amplitude scale before analyzing for the major modes and loading factors for each core. The analysis identified two major modes of deposition (Figure 1.6). The first mode explains 61.2% of the variance in sedimentation rates and comprises a divergence in sedimentation rates over time. It is particularly prominent at 09PC (positive correlation) and 12PC (negative correlation). The second mode explains 25.4% of the variance in sedimentation rates and consists of glacial-interglacial variation in sedimentation rates. It is particularly important at 38PC (negative correlation) and 05PC (positive correlation).

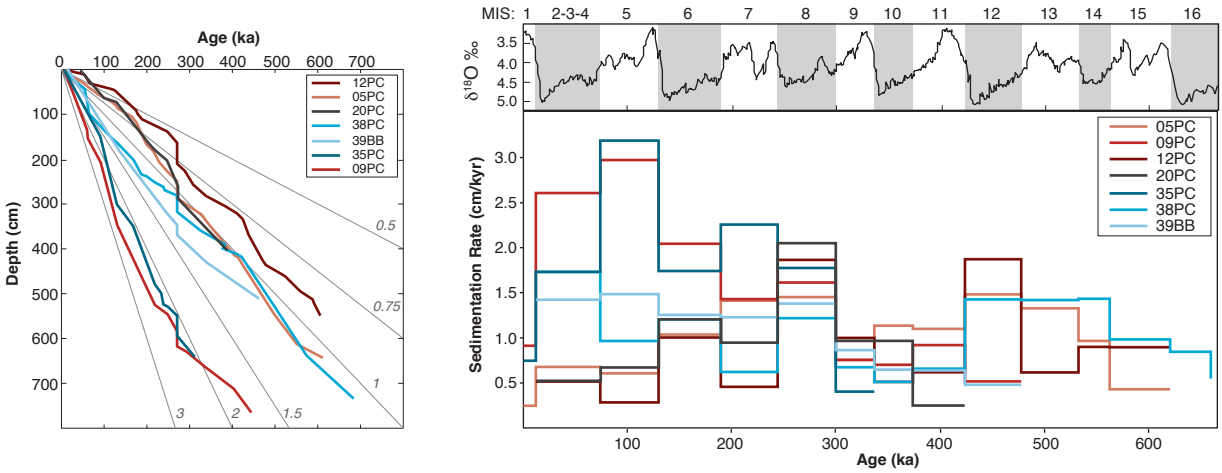

Figure 1.5. Temporal variability in sedimentation rates. *(Caption continued on next page)*

Figure 1.5. ***(Previous Page)*** **Temporal variability in sedimentation rates.** (Left) Age models for all seven cores. Gray reference lines indicate age vs depth for stable sedimenta- tion rates from 0.5 to 3 cm/kyr. Sedimentation rates for the JdFR cores generally fall within this range. 09PC and 35PC have the highest sedimentation rates, while 12PC has the lowest sedimentation rate. Abruptly high sedimentation rates ~272ka are associated with the MS peak. (Right, top panel) Global benthic δ18O stack (Lisiecki and Raymo, 2005). Marine Isotope Stages (MIS) are identified at the top, and glacial periods (even MIS) are highlighted in orange bands, as in Figures 2 and 4. (Right, bottom panel) Sedimentation rates over in glacial-interglacial timeslices. Several cores show glacial-interglacial cycling in sedimenta- tion rates, with 12PC showing higher sedimentation rates during glacial periods and 35PC showing higher sedimentation rates during interglacial periods.

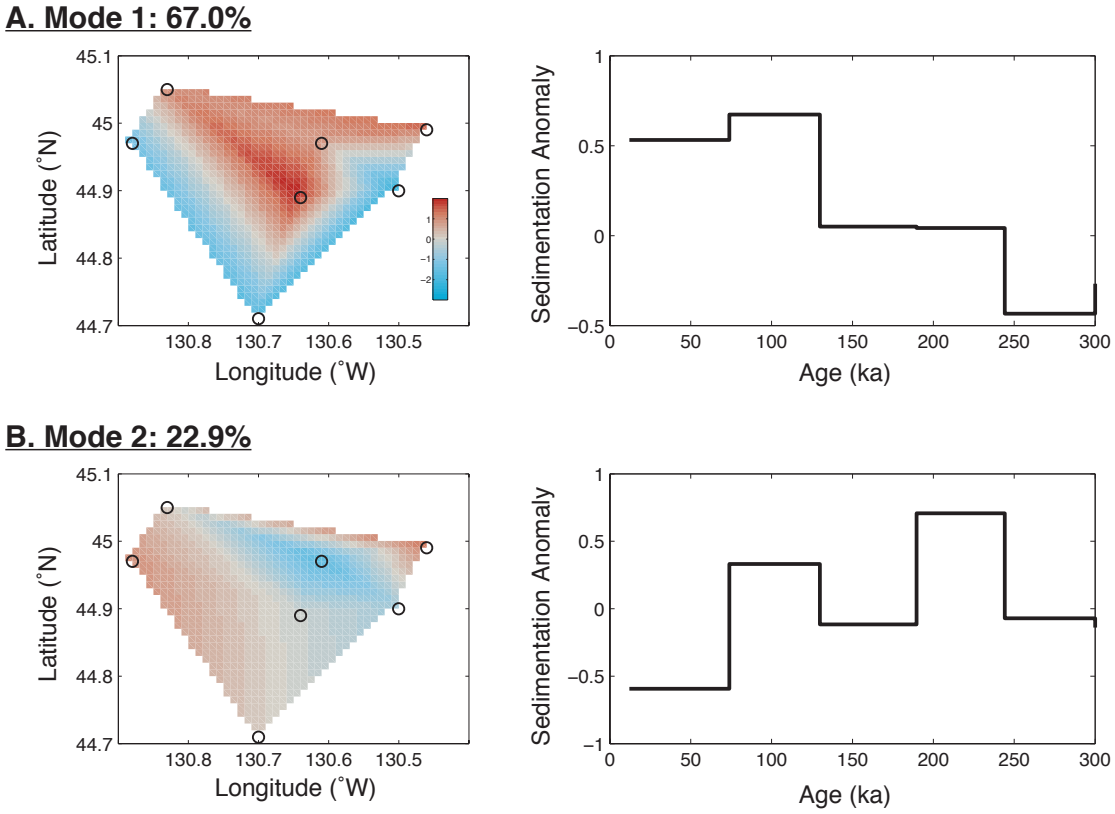

Figure 1.6. Empirical orthogonal function (EOF) analysis of the spatial variability in sedimentation rates. Left panels show the factor loading on each core interpolated across the region. Colorbar shown in the top panel for both modes, with red indicating a positive loading of the mode and blue indicating a negative loading of the mode. Right panels show the principal component that reflects the sedimentation anomaly over time. The first mode of sedimentation, divergence in sedimentation rates over time, accounts for 61.2% of the variance in sedimentation rates, and it is particularly important for cores 09PC and 12PC. The second mode of sedimentation, glacial-interglacial variation, accounts for 25.4% of the variance in sedimentation rates, and it is particularly important for core 38PC.

1.5.2.1 Mode 1 Sedimentation pattern: Divergence of sedimentation rates over time

Diverging sedimentation rates over time correspond with increasing distance from the ridge, with positive loadings indicating increasing sedimentation rates over time (09PC, 38PC, 35PC, 39BB) and negative loadings indicating decreasing sedimentation rates over time (12PC, 20PC, 05PC). Locally variable sedimentation in the near-ridge environment is expected because 1) the bathymetry of sparsely sedimented newly formed seafloor is rougher, 2) tidal dissipation increases near rough bathymetry, 3) bottom currents are faster and likely to interact with the elevated seafloor, 3) active tectonic faulting associated with the formation of abyssal hills may be ongoing, 4) micro-earthquakes may contribute to small scale sediment mobility, and 5) faults bounding abyssal hills are steeper having undergone less tectonic erosion. The biggest contributing factor for sediment redistribution in the study area is the steep relief of the JdFR (Mitchell, 1995; Neil C. Mitchell et al., 1998; Webb and Jordan, 2001), which is largely created as result of extensional faulting. Sediment redistribution from bathymetric highs to bathymetric lows occurs as localized downslope movements (Neil C Mitchell et al., 1998; Ruddiman, 1972; van Andel and Komar, 1969) that may be episodic, but often proceed as a gentle and semi-continuous flow or as abrupt and episodic slumps (Heezen and Rawson, 1977; Marks, 1981). Sediments develop cohesiveness that limits remobilization as they age, and thus sediment added through lateral remobilization, particularly by gentle gravity flows, is likely to be quasi-contemporaneous to surface-derived sediment. Such persistent small-scale lateral sedimentation is consistent with the dry bulk density and MS records of the study cores, which contain few sharp transitions diagnostic of slumps or other rapid shifts in sedimentation.

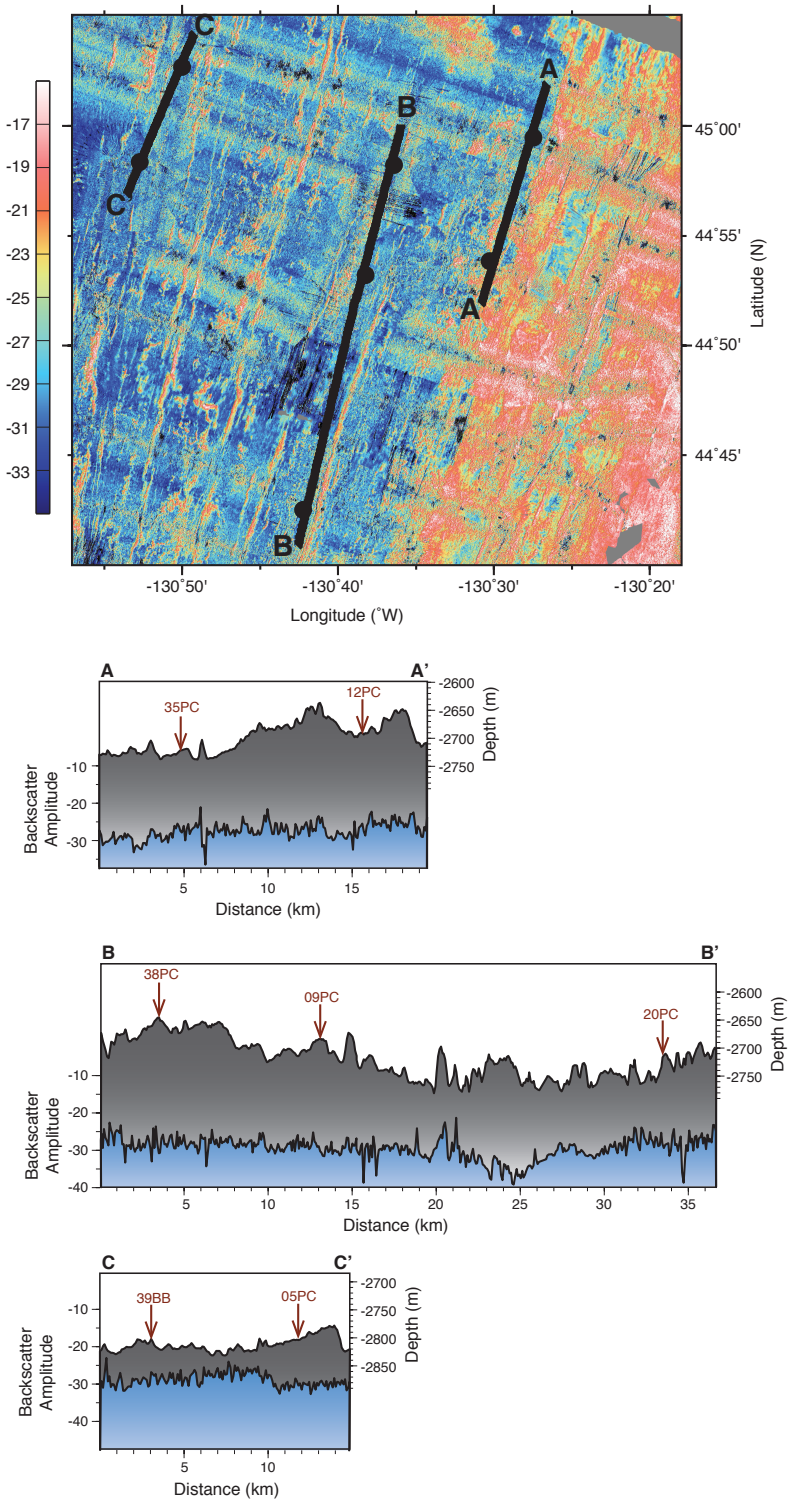

Figure 1.7. Backscatter amplitude map and profiles. (Top) Map of backscatter amplitudes across the JdFR region acquired with the shipboard EM122 multibeam sonar ranging from high backscatter amplitudes (orange) to low backscatter amplitudes (blue). Backscatter amplitude varies inversely with sediment thickness, so that the high backscatter on the axial plateau suggests a relatively thin sediment cover. Three north-south profiles passing through the core sites (black circles) are indicated with black lines. Ridge-perpendicular profiles are provided in Supplementary Figure 1.4. (Bottom) Three profiles of backscatter amplitude as defined in the map. Profiles correspond with crustal isochrons, so that A-A' is on ~700ka crust, B-B' is on 1Ma crust, and C-C' is on 1.8Ma. Bathymetry is on shown in gray, with depth indicated on the right y-axis. Backscatter amplitude is shown in blue, with amplitude indicated on the left y-axis.

The individual bathymetric setting for each study core suggests that local relief does play a role in controlling the sedimentation rates. Although all cores are located on or near the tops of abyssal hills, these features vary in relief along strike with local saddle points along their crest as well as longer wavelength deepening towards the ends of these hills (Figure 1.1 and 1.7). Core 12PC is located adjacent to a steep vertical scarp of nearly 200m (Figure 1.1, Figure S1.3c, Figure S1.4), and downslope transport away from the core site may explain the generally low sedimentation rates observed there. Core 35PC, on the other hand, with high average sedimentation rates, is situated in a relatively flat bathymetric low region near the end of this same abyssal hill that may readily accumulate sediment transported, for example, from the nearby axial plateau. Similarly, core 09PC, also located in a local broad bathymetric low, has high average sedimentation rates. Of the other cores, all with similar moderate average sedimentation rates, one is sited in a local bathymetric low (core 39BB) and three are located on local highs (05PC, 38PC, 20PC).

Although the interpretation of sediment cover in the 3.5 kHz subbottom profiler data acquired at the core sites (Figure S1.3) was complicated by side echoes associated with the rough seafloor topography and the short wavelength of variations in abyssal hill relief, simultaneous seismic backscatter amplitude mapping supports the inference of heterogeneous sediment deposition in the near ridge environment (Figure 1.7). Backscatter amplitude varies with fine-scale roughness of the seafloor, with gradually decreasing backscatter strength with distance from the ridge as the crust ages and accumulates sediment **(**Mitchell, 1993**).** In our study area, the high backscatter associated with the broad axial plateau at Cleft segment and lower backscatter of the older crust at our cores is overprinted by narrow linear zones of high backscatter, associated with large fault scarps, as well as more sinuous bands of higher backscatter, which mark the edges of volcanic flow fronts. Away from these zones of high backscatter/steeper topography, small regional

variations in backscatter amplitude above the sonar beam noise are consistent with the variability in sedimentation rates found in individual cores (Figure 1.7). For example, the low sediment rate core 12PC is located near an area of higher backscatter than at core 35PC, although both are sited in similar age crust. However, along the 1.8 Ma transect, core 05PC is located in a region of lower backscatter but has similar average sedimentation rates as 39BB. The lack of a correlation between acoustic backscatter and sedimentation patterns along the older transects likely reflects the limited sensitivity of these data to sediment thicknesses > 5-10 m given the acoustic penetration of the 12 kHz sonar used (e.g., Mitchell, 1993).

In addition to gravity flows and slumping from steep bathymetry, sediment redistribution along the seafloor due to bottom currents may also contribute to the sedimentation patterns. Sediment redistribution can occur anywhere bottom currents are strong enough to resuspend and laterally transport sediments in nepheloid layers on the seafloor (Francois et al., 2004). On mid-ocean ridges, these currents are predominantly tidal (Polzin, 1997; Thurnherr and Speer, 2003), which supply 40-50% of the kinetic energy (Thomson et al., 2003; Thurnherr et al., 2005) and generate enhanced diapycnal mixing over the rough topography (Polzin, 1997). Bathymetric features like seamounts and ridge parallel abyssal hills amplify tidal currents and create complex flow fields that can extend up to 10km from the feature (Turnewitsch et al., 2008, 2004). Transient currents as fast as 10cm/s due to tidal forcing have been documented on the nearby Endeavor Segment of the JdFR (Thomson et al., 2003). Such currents are capable of transporting fine particles, particularly phytodetritus and other biogenic material (Beaulieu, 2002), and especially in regions with high relief (Kienast et al., 2007; Lonsdale et al., 1972), although they are unlikely to entrain coarse particles, such as foraminifera and volcanic ash (Marcantonio et al., 2014).

Sediment on the JdFR is predominantly fine, averaging just 12% coarse, and fluctuating between 0-5% coarse (interglacial periods) to 30-40% coarse (glacial periods). In the near-ridge environment, this fine material can easily be remobilized by a wide range of influences, including tidal currents generated by the steep topography, near-ridge jets, shaking by micro-earthquakes, and bioturbation by macrofauna. This redistribution would result in low sedimentation rates at coarse lag deposits and high sedimentation rates at focused sediment deposition banks. Farther from the ridge, the subdued topography damps the tidal intensity, so that fine material is more likely to settle vertically to the seafloor, resulting in higher sedimentation rates. Thus the divergence in sedimentation rates over time likely reflects the migration of the core sites out of the variable current zone of the ridge crest into the more quiescent waters of the ridge flanks.

1.5.2.2 Mode 2 sedimentation pattern: Glacial-interglacial variation of sedimentation rate

A secondary glacial-interglacial cycle of sedimentation rates is weakly present at some of the core sites. Consistently variable sedimentation rates might be expected, given the cyclical calcium carbonate preservation in the Pacific Ocean that peaks during glacial intervals (Farrell and Prell, 1989). Accumulation rates in some of the study cores do vary in this way, yet others (5PC, 35PC) display the opposite pattern, suggesting an important additional influence of lateral redeposition. Because the stratigraphic indices of $\delta^{18}O$ and physical properties remain coherent, this sediment redistribution is likely to have occurred nearly syndepositonally and over relatively small spatial scales.

Sedimentary characteristics such as grain size and composition may have contributed to this cyclical redistribution. The sediment at all study sites is predominantly fine during interglacial periods because 1) poor carbonate preservation increases the degree

of fragmentation of large foraminiferal tests into fine pieces 2) reduced surface stratification in the North Pacific generally increases interglacial productivity in this region (Galbraith et al., 2008; Jaccard et al., 2005; Lam et al., 2013) thus increasing the fraction of fine phytodetritus 3) the lack of coarse particles reduces resistance to erosion (Mitchener and Torfs, 1996). These effects combine to form a more easily mobilized sediment substrate during interglacial periods, allowing sediment to pond by moving from local highs to nearby depressions in a process that would eventually contribute to the observed smoothing of the seafloor away from the ridge. Tidal currents (e.g., Lavelle and Cannon, 2001), ridge-associated jets (Lavelle, 2012), shaking from micro-earthquakes, and bioturbation by macrofauna could all contribute to resuspension that subsequently focuses sediment deposition into thick sediment ponds, resulting in high sedimentation rates for some sites (e.g., 05PC, 35PC) and low sedimentation rates in the sediment source regions.

Although it may be less likely, it is also possible that the relatively high sedimentation rates during interglacial periods could instead be related to increased erosion in the near-ridge environment during glacial periods. Lower sea level would result in a greater fraction of tidal dissipation over relatively rough bathymetry in the deep ocean rather than on the continental shelves (Egbert et al., 2004). This increase in tidal energy might increase winnowing of fine sediment during glacial periods, providing an alternative explanation for the coarser grain size during glacial intervals and relatively higher sedimentation rates in interglacial intervals observed at some study sites. Future investigation using ^{230}Th systematics and focusing factors may provide insights into the relative changes in focusing and winnowing on glacial-interglacial timescales.

1.6 Conclusions

This paper presented sedimentation rates, density, and magnetic susceptibility for a suite of seven cores covering almost 700,000 years of sedimentation on the Juan de Fuca Ridge. Age models were generated from benthic $\delta^{18}O$ and subsequently refined using dry bulk density stratigraphy, resulting in a shared chronostratigraphy within the North Pacific. Spatial and temporal sedimentation patterns were presented to investigate how near-ridge sedimentary environments may have varied with glacial-interglacial cycles. Sedimentation rates generally range from 1 to 3 cm/kyr, with background pelagic sedimentation rates close to 1cm/kyr, and they are spatially heterogeneous, likely reflecting sediment remobilization caused by the high relief and stronger bottom currents of the near ridge environment. The primary mode of sedimentation is diverging sedimentation rates with distance from the ridge, reflecting the pervasiveness of localized sediment redistribution. The secondary mode of sedimentation is glacial-interglacial variation in sedimentation rates, reflecting carbonate preservation cycles or the susceptibility of fine material to remobilization and lateral transport along the seafloor.

1.7 Data Archiving

All data are archived at the National Oceanic and Atmospheric Administration National Centers for Environmental Information (NCEI) database.

1.8 Supplementary Material

Figure S1.1. Raw multi-sensor track data. Gamma attenuation (blue) and magnetic susceptibility (gray) for all seven cores. Gamma attenuation shows distinct cycles over the length of each core. A prominent peak in magnetic susceptibility (MS ≥ 100 *10^{-6} SI), preceded by two cycles in gamma attenuation, is found in all cores.

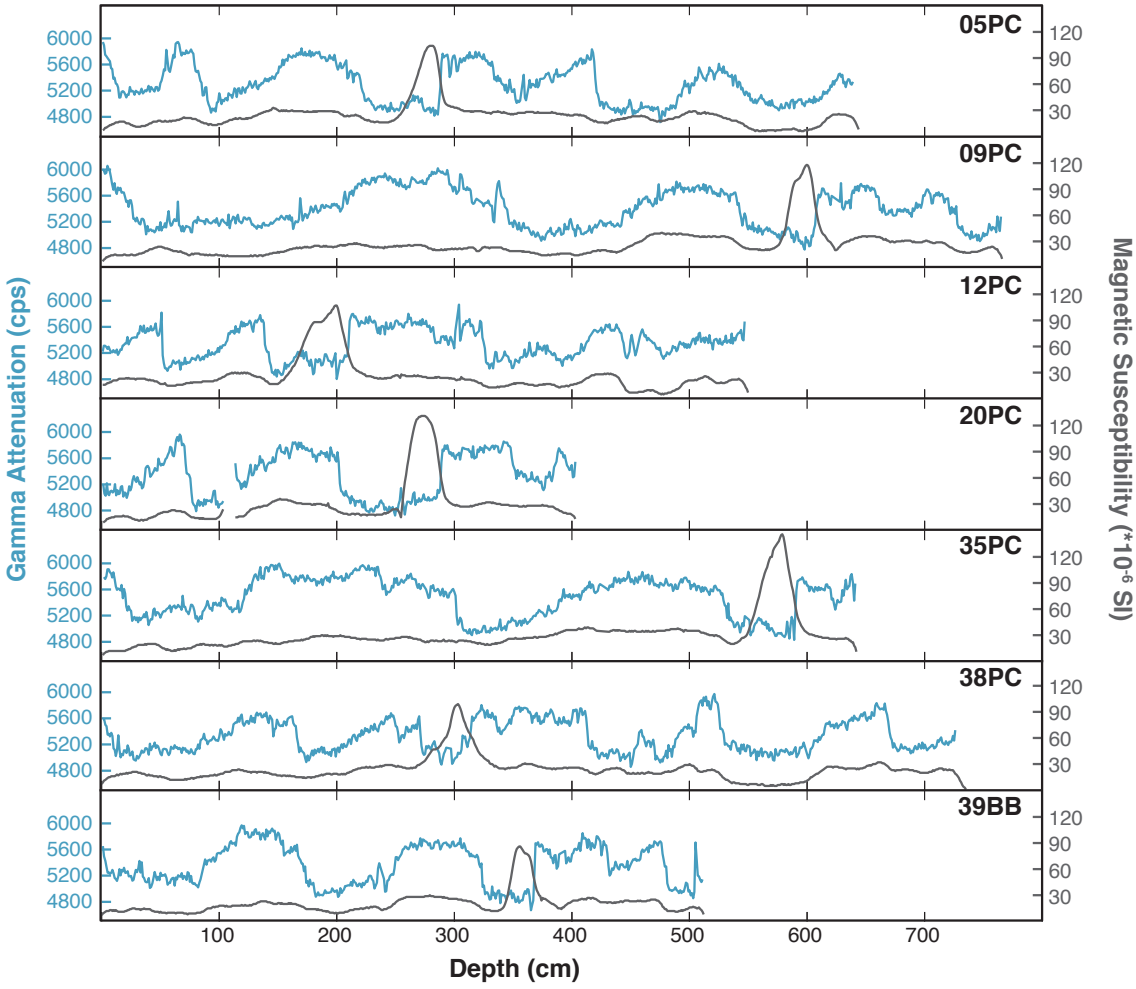

Figure S1.2. Calibration of raw gamma attenuation to porosity, wet bulk density, and dry bulk density. Discrete sampling was conducted on four cores: 05PC, 09PC, 12PC, and 35PC. Additional samples were taken from associated gravity cores 04BB (for 05PC) and 34GC (for 35PC) to better constrain low density coretop sediment. Consistent relationships between gamma counts and dry bulk density, wet bulk density, and porosity across these four sites suggest that a single regional calibration is appropriate. Errors on gamma counts are based on counting statistics, while errors on calculated densities and porosities are estimated at 10%, largely due to the assumption of constant volume. Dry bulk densities are salt-corrected.

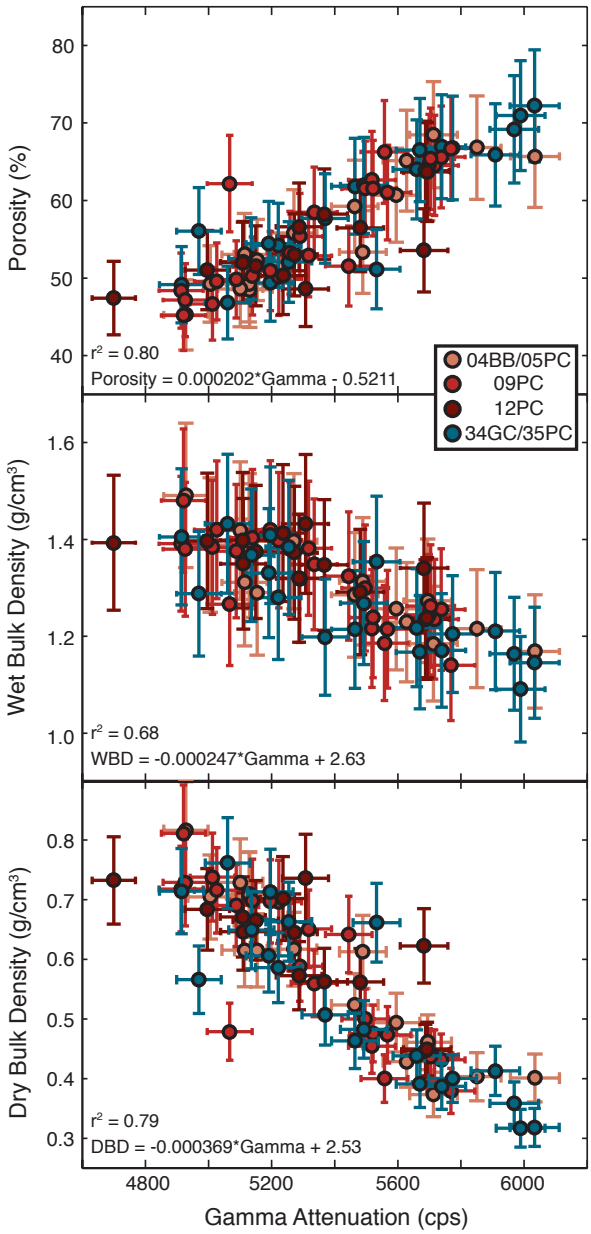

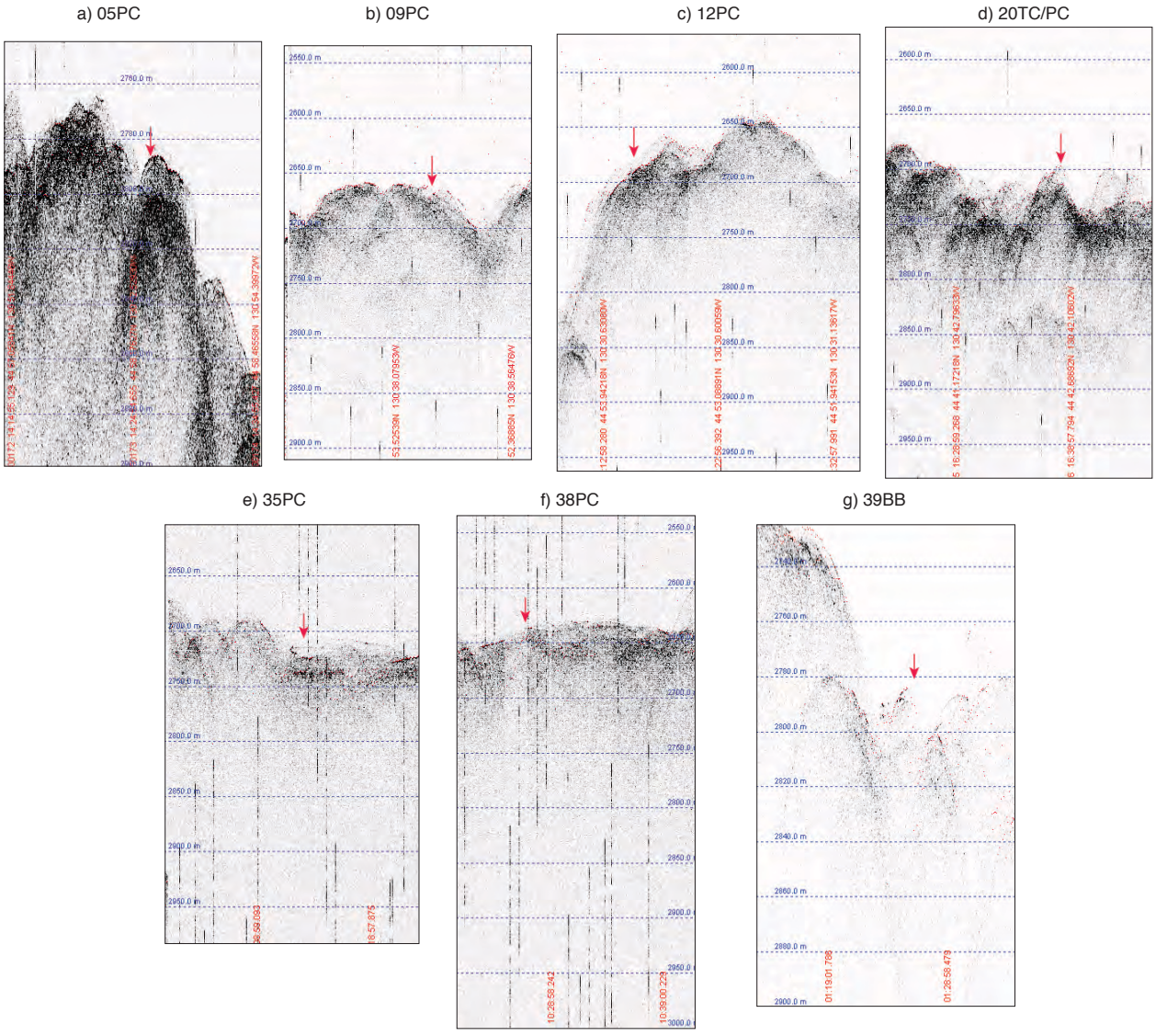

Figure S1.3. Seismic 3.5kHz records for the seven core sites. Sediment thickness profiles are difficult to interpret due to the abundance of side echoes off the rough topography. a) 05PC b) 09PC c) 12PC d) 20PC e) 35PC f) 38PC g) 39BB. Red arrows indicate core locations.

Figure S1.4. Backscatter amplitude map and profiles. (*Left*) Map of backscatter amplitudes across the JdFR region acquired with the shipboard EM122 multibeam. Backscatter amplitude varies inversely with sediment thickness, so that the high backscatter on the axial plateau suggests a relatively thin sediment cover. Core sites are indicated with black circles. Transects 1 and 2 are angled to go through the core sites. Transects 3 and 4 are true ridge-perpendicular profiles, but do not intersect the core sites *(Right*) Four profiles of backscatter amplitude as defined in the map. Bathymetry is on shown in gray, with depth indicated on the right y-axis. Backscatter amplitude is shown in blue, with amplitude indicated on the left y-axis. Red arrows indicate core locations. All transects are aligned with the ridge crest to the right.

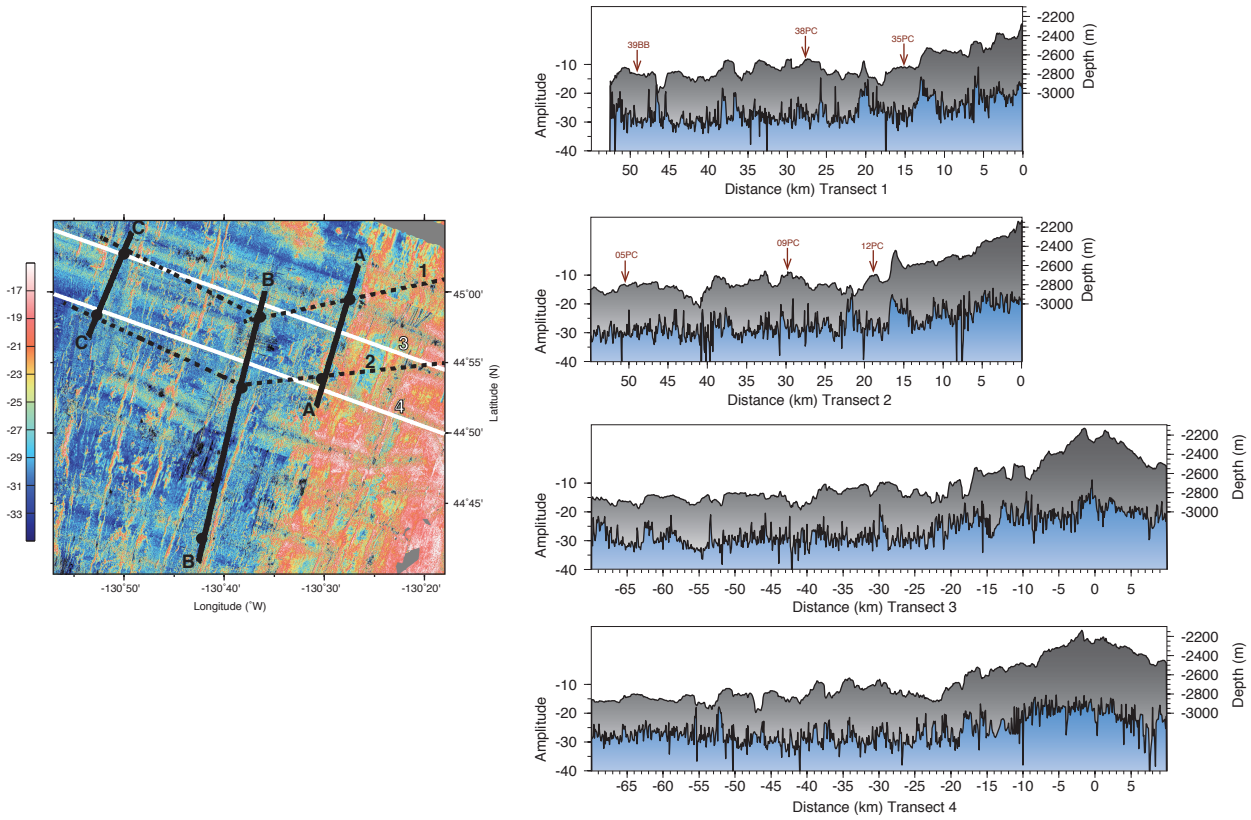

Chapter 2

Efficacy of ^{230}Th normalization in sediments from the Juan de Fuca Ridge, northeast Pacific Ocean

Note: A modified version of this chapter has been published in *Geochimica et Cosmochimica Acta*[2]

Abstract:

^{230}Th normalization is an indispensable method for reconstructing sedimentation rates and mass fluxes over time, but the validity of this approach has generated considerable debate in the paleoceanographic community. ^{230}Th systematics have been challenged with regards to grain size bias, sediment composition ($CaCO_3$), water column advection, and other processes. In this study, we investigate the consequences of these effects on ^{230}Th normalization from a suite of six cores on the Juan de Fuca Ridge. The proximity of these cores (<30km) suggests that they should receive the same particle rain rate of sediment, but the steep bathymetry of the ridge leads to substantial sediment redistribution and variable carbonate preservation, both of which may limit the usage of ^{230}Th in this region. Despite anticipated complications, ^{230}Th normalization effectively reconstructs nearly identical particle rain rates from all six cores, which are summarily unrelated to the total sedimentation rates as calculated from the age models. Instead the total sedimentation rates are controlled almost entirely by sediment focusing and winnowing, which are highly variable even over the short spatial scales investigated in this

[2] *Authors*: Kassandra Costa, Jerry McManus. *Affiliations*: Lamont-Doherty Earth Observatory of Columbia University, Palisades, NY 10964, USA. Department of Earth and Environmental Sciences, Columbia University, New York, NY 10027, USA.

study. Furthermore, no feedbacks on ^{230}Th systematics were detected as a consequence of sediment focusing, coarse fraction variability, or calcium carbonate content, supporting the robustness of the ^{230}Th normalization technique.

2.1. Introduction

Particle rain rate is one of the vital signs of the surface ocean. Changes in the abundance and composition of surface particles are fundamental to reconstructing productivity and carbon export over time. Gravimetric analyses of biological sedimentary components (opal, carbonate, organic carbon) integrate the production at the surface with dilution and preservation effects at the seafloor, and only by knowing the total particle rain rate can the mass fractions translate into absolute fluxes. Traditionally, particle rain rates are calculated using the age model tie points and the intervening sediment thickness to determine the average sedimentation rate over that time period (e.g., Broecker, 1971). But this method is confounded by the omnipresent sediment redistribution on the seafloor (Johnson and Johnson, 1970; Bacon, 1984; Francois et al., 2004), which appends a horizontal sediment flux onto the vertical particle rain. Age model based sedimentation rates can only reconstruct the total sediment delivery (vertical + horizontal), and significant sediment focusing in, e.g., drift deposits can lead to astonishingly high total sedimentation rates of 100cm/kyr or more (e.g., Keigwin and Schlegel, 2002). Using these age model-based total sedimentation rates as a stand-in for particle rain rates can lead to severe misinterpretations of the climatic and oceanographic history of a region (as discussed in Francois et al., 2004; Kienast et al., 2007). The need for reliable proxies for the particle rain rate has led to the development of age-model independent techniques using constant flux proxies, like ^{230}Th.

Constant flux proxies (^{230}Th, ^{3}He) have well-constrained source functions, and the flux of these nuclides to the sediment is known and constant. Therefore, their concentration in the sediment depends on the same dilution effects that influence surface productivity indicators like opal and organic carbon. These dilution effects are driven by changes in the particle rain rate, and normalizing to a constant flux proxy, especially ^{230}Th, has several clear advantages over the age model based reconstructions of sedimentation (Bacon, 1984; Suman and Bacon, 1989; Francois et al., 1990; Francois et al., 2004). First, ^{230}Th normalization allows point-by-point calculation of sedimentation rate regardless of and generally at much higher resolution than age model tiepoints. Second, ^{230}Th can distinguish between vertical and lateral sediment contributions because sediment focusing or winnowing would result in excess or deficient ^{230}Th compared to the known production rate. Finally since ^{230}Th specifically reconstructs particle rain rates, ^{230}Th-based sedimentation rates are more regionally homogeneous (Ruhlemann et al., 1996; Kienast et al., 2007; Anderson et al., 2008) than age model based sedimentation rates, which can show wide variations on scales as small as kilometers (Johnson and Johnson, 1970; Costa et al., 2016).

No proxy is perfect, and several shortcomings of the ^{230}Th technique have also been identified. Despite its short residence time in the water column (20-40 years) some diffusion and advection of ^{230}Th along concentration gradients leads to boundary scavenging and ^{230}Th fluxes elevated above the constant production rate (Anderson et al., 1983; Henderson et al., 1999; Lyle et al., 2005; Broecker, 2008; Singh et al., 2013). Similarly, ^{230}Th surpluses could occur as a result of preferential remobilization of fine sediments, which contain the majority of adsorbed ^{230}Th due to their high surface area (Suman and Bacon, 1989; Kretschmer et al., 2010; Lyle et al., 2014). Both water column transport and sediment focusing could decouple ^{230}Th from the particle rain rate, dissolving the foundation from which ^{230}Th is used as a constant flux proxy. The magnitude of these effects and the

implications for ^{230}Th normalization have led to considerable debate about its application for reconstructing sediment fluxes, particularly in carbonate rich sediments in the Equatorial Pacific (Lyle et al., 2005; Francois et al., 2007; Lyle et al., 2007; Broecker, 2008; Lyle et al., 2014; Marcantonio et al., 2014). Whether or not these challenges are regionally specific to the Equatorial Pacific or evident of a broader global pattern has yet to be established.

This paper investigates the utility of ^{230}Th normalization in sediments on the Juan de Fuca Ridge (JdFR), where rough topography generates substantial sediment focusing and winnowing (Costa et al., 2016). Age model based sedimentation rates range over an order of magnitude despite the expectation that the tightly gridded suite of cores (6 cores within 50 km) should receive nearly identical surface particle rain rates. Comparing the ^{230}Th-based sedimentation rates from these cores over the past 400-500,000 years will ascertain if the degree of sediment redistribution affects the ability of ^{230}Th to reconstruct particle rain rates. If sediment focusing has little to no effect on ^{230}Th systematics, then all six cores should yield the same ^{230}Th based sedimentation rate. If sediment redistribution decouples ^{230}Th from the particle rain rate, then the six cores will likely produce different ^{230}Th based sedimentation rates, which may instead scale with age model based total sedimentation rates, the fraction of fine sediment, or the carbonate content.

2.2. Materials & Methods

2.2.1. Core sites and stratigraphy

Samples were taken from six cores on the Juan de Fuca Ridge (Figure 2.1) collected on the SeaVOICE cruise (AT26-19) of the R/V Atlantis in September 2014. Cores were retrieved in two E-W transects in a semi-grid on the western flanks of the ridge, targeted on

ridge-parallel crests (2655-2794m) to maximize carbonate preservation (Costa et al., 2016). The average spacing between cores is about 20km. Utilizing a tight cluster of cores underlying one productivity regime eliminates the variability associated with crossing surface productivity gradients, which have characterized previous studies employing meridional transects (Lyle et al., 2005; Kienast et al., 2007; Mitchell and Huthnance, 2013; Marcantonio et al., 2014).

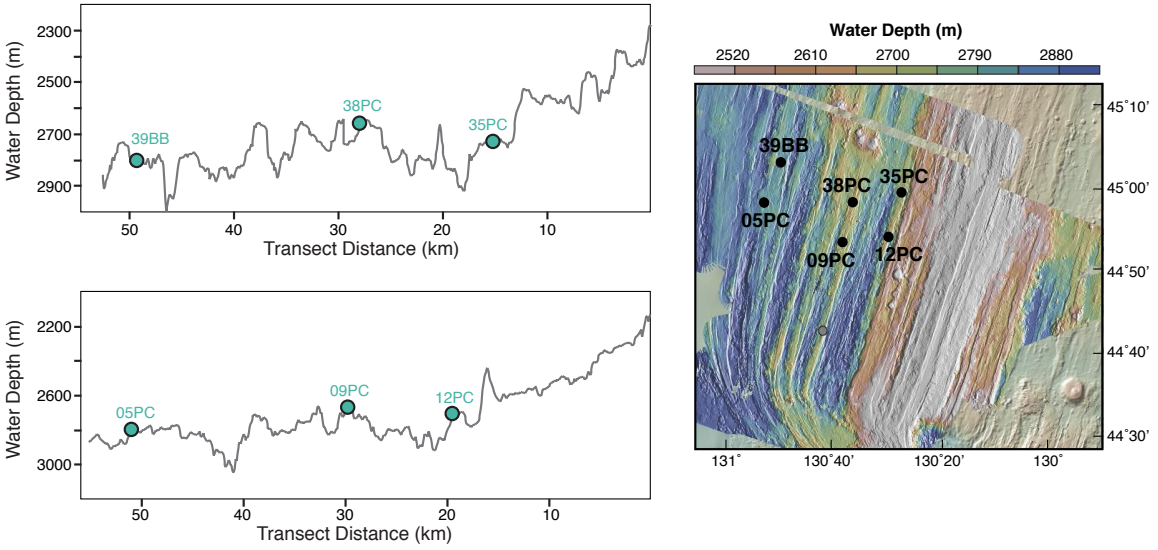

Figure 2.1. Core locations on the Juan de Fuca Ridge. (*Right)* Bathymetric map by shipboard multibeam data and showing the location of the Juan de Fuca cores relative to the ridge crest (in white). The cores were collected along two east-west transects. (*Left*) Bathymetric profiles from the ridge through the core locations at both the northern and southern transects. All cores were taken from relative bathymetric highs.

Age models for the JdFR cores are well-constrained based on radiocarbon dates, benthic $\delta\,^{18}O$, and stratigraphically tuned density cycles (Costa et al., 2016). Both density and coarse fraction >63 μ m (Costa et al., 2016) show distinct glacial-interglacial cycles,

with high-density, coarse sediment characterizing glacial deposition. Carbonate concentrations, measured by the standard coulometric method, are consistent with carbonate-rich glacial periods and carbonate-poor interglacial periods (Supplemental Figure S2.1).

2.2.2. U-Th isotopic analyses

Samples (n=1097) were analyzed for thorium (^{230}Th, ^{232}Th) and uranium (^{238}U, ^{235}U, ^{234}U) by isotope dilution inductively coupled plasma mass spectrometry (ICP-MS). In a randomized order, samples (100mg) were spiked with ^{229}Th and ^{236}U and processed with complete acid digestion and column chromatography (Fleisher and Anderson, 2003). Isotopes were measured on an Element 2 ICP-MS at Lamont-Doherty Earth Observatory (LDEO) of Columbia University. Discrete sediment aliquots (n=106) of an internal sediment standard (VOICE Internal MegaStandard, VIMS) were processed and analyzed for quality control, and these total replicates of VIMS indicate that the analytical procedure and measurement are externally reproducible within 6.2% on ^{238}U, 3.7% on ^{232}Th, and 4.9% on ^{230}Th (Figure 2.2). Excess initial ^{230}Th ($^{230}Th_{xs}^{0}$, hereafter ^{230}Th) was calculated by correcting for supported decay from lithogenic and authigenic uranium (Henderson and Anderson, 2003). Lithogenic uranium concentrations were determined using a detrital ^{238}U/^{232}Th of 0.48, the value which ^{238}U/^{232}Th reaches as the ^{232}Th concentration approaches its average lithogenic value (10.7ppm, Taylor and McLennan, 1995). Corrections for supported ^{230}Th become significant as the sediment ages: supported ^{230}Th remains constant while excess ^{230}Th decays away, increasing the supported to excess ^{230}Th ratio over time. By about 400ka, excess ^{230}Th composes less than 25% of the total ^{230}Th on the Juan de Fuca Ridge,

compared to 99% excess ^{230}Th in the core tops. The loss of excess ^{230}Th substantially increases the propagated errors, reported throughout as 2 σ .

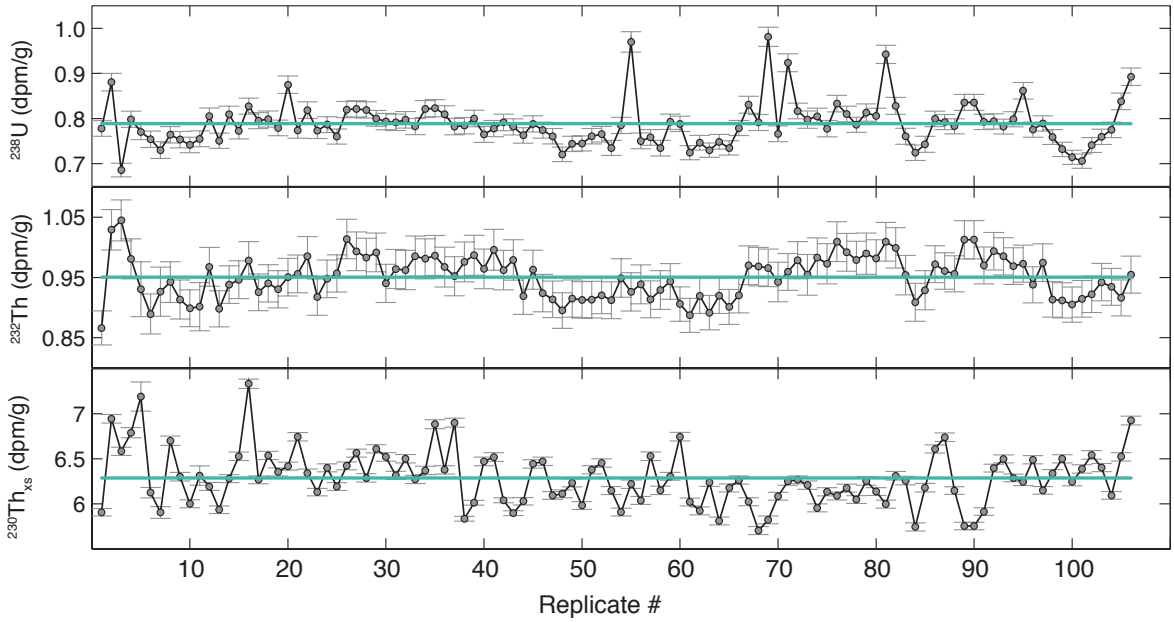

Figure 2.2. VIMS replicates. The Voice Internal MegaStandard (VIMS) was analyzed repeatedly (*n*=106) to assess reproducibility and to correct for inter-run offsets. Reproducibility is within 6% for all isotopes.

2.2.3. ^{230}Th normalization

^{230}Th is produced in the water column by the decay of ^{234}U. Uranium is highly soluble in seawater, with a fairly constant concentration (3.2ppb) that scales conservatively with salinity (Owens et al., 2011). The long residence time (400kyr) of uranium leads to a relatively uniform production of ^{230}Th (β_{230} = 2.555*10^{-5} dpm/cm^{3}kyr) across the global ocean. Unlike uranium, thorium is practically insoluble in seawater, and it is quickly removed by scavenging onto settling particles and burial in the underlying sediments, so that its decay is no longer supported by its parent nuclide. The residence time of ^{230}Th in

the ocean is so short (20-40 years; Nozaki et al., 1981) compared to its half-life (75,584 years; Cheng et al., 2013) that virtually all of the ^{230}Th produced by uranium decay in seawater is removed to sediments by scavenging.

The residence time of ^{230}Th is also much less than the time scale for lateral transport by mixing from regions of low scavenging intensity (low particle flux) to regions of high scavenging intensity. Consequently, in at least 70% of the ocean the flux of ^{230}Th carried to the seafloor by sinking particles is within ~30% of its production rate in the overlying water column (Henderson et al., 1999; Henderson and Anderson, 2003). Given a rate of supply that depends mainly on water depth, the concentration of excess ^{230}Th in the underlying sediment is a function of the particle flux (PF). Higher PF will dilute the excess ^{230}Th concentration in the sediment. Thus the PF can be calculated as follows:

Equation 1 $$PF = \beta * z / \text{excess } ^{230}Th_0$$

Where β*z is the integrated ^{230}Th production (P_{Th}) in the overlying water column, and excess $^{230}Th_0$ is the concentration of excess ^{230}Th in the sediment corrected for decay since deposition (Bacon, 1984; McManus et al., 1998; Henderson and Anderson, 2003; Francois et al., 2004). Corrections for fluctuations of sea level over time are negligible and within error of the Th measurements. From there, the sedimentation rates (cm/kyr) of particles, or particle rain rate (PRR), can be calculated by scaling the particle flux (g/cm^{2}kyr) by the dry bulk density (ρ , g/cm^3):

Equation 2 $$PRR = PF / \rho$$

Specifically, the PRR records the sedimentation of preserved particles, and it cannot reconstruct those particles that may have suffered dissolution in the water column or on the seafloor.

2.2.4. Calculating focusing factors (Ψ)

The degree of sediment focusing (Ψ) can be calculated by comparing the inventory of ^{230}Th in a dated sediment horizon with the inferred production of ^{230}Th in the overlying water column over the duration of the sediment deposition (Suman and Bacon, 1989):

Equation 3

$$\Psi = \frac{\rho \int_{z1}^{z2} {}^{230}Th_{xs}^{0} dz}{P_{Th}\,(\Delta t)} \approx \frac{\rho\, \overline{{}^{230}Th_{xs}^{0}}(\Delta z)}{P_{Th}\,(\Delta t)}$$

When Ψ = 1, the amount of ^{230}Th buried in the sediment is equivalent to the amount produced in the water column. When Ψ < 1, the amount of ^{230}Th buried is less than that produced, suggesting that ^{230}Th has been removed, for example by lateral transport or winnowing of a ^{230}Th-rich sedimentary phase. Conversely, Ψ > 1 indicates an excess of ^{230}Th over the amount produced in the water column, primarily due to ponding of ^{230}Th-containing sediment, although it could also reflect boundary scavenging or focusing of a ^{230}Th-enriched sedimentary phase.

Focusing factors can be quite sensitive to the temporal integration periods (Kienast et al., 2007), and age model uncertainties on the order of several thousand years can propagate into substantial errors on focusing factors calculated over short periods of time (Francois et al., 1990). Previous studies have targeted deglacial time scales (5-10kyr), but small age model adjustments can change focusing factor calculations on these timescales by as much as 100% (Loubere et al., 2004; Kienast et al., 2007). Therefore, this study only investigates full MIS focusing factors, which should be more robust against temporal uncertainties. Focusing factors were calculated by integrating ^{230}Th data from peak conditions of each MIS, covering durations ranging from 12.5-61.9 kyr and averaging 48.5kyr. Errors were propagated using the standard deviation of the ^{230}Th within the MIS

and assuming a 10% error on the age, a conservative estimate as errors >15kyr are unlikely given the stratigraphic constraints of the age model (Costa et al., 2016).

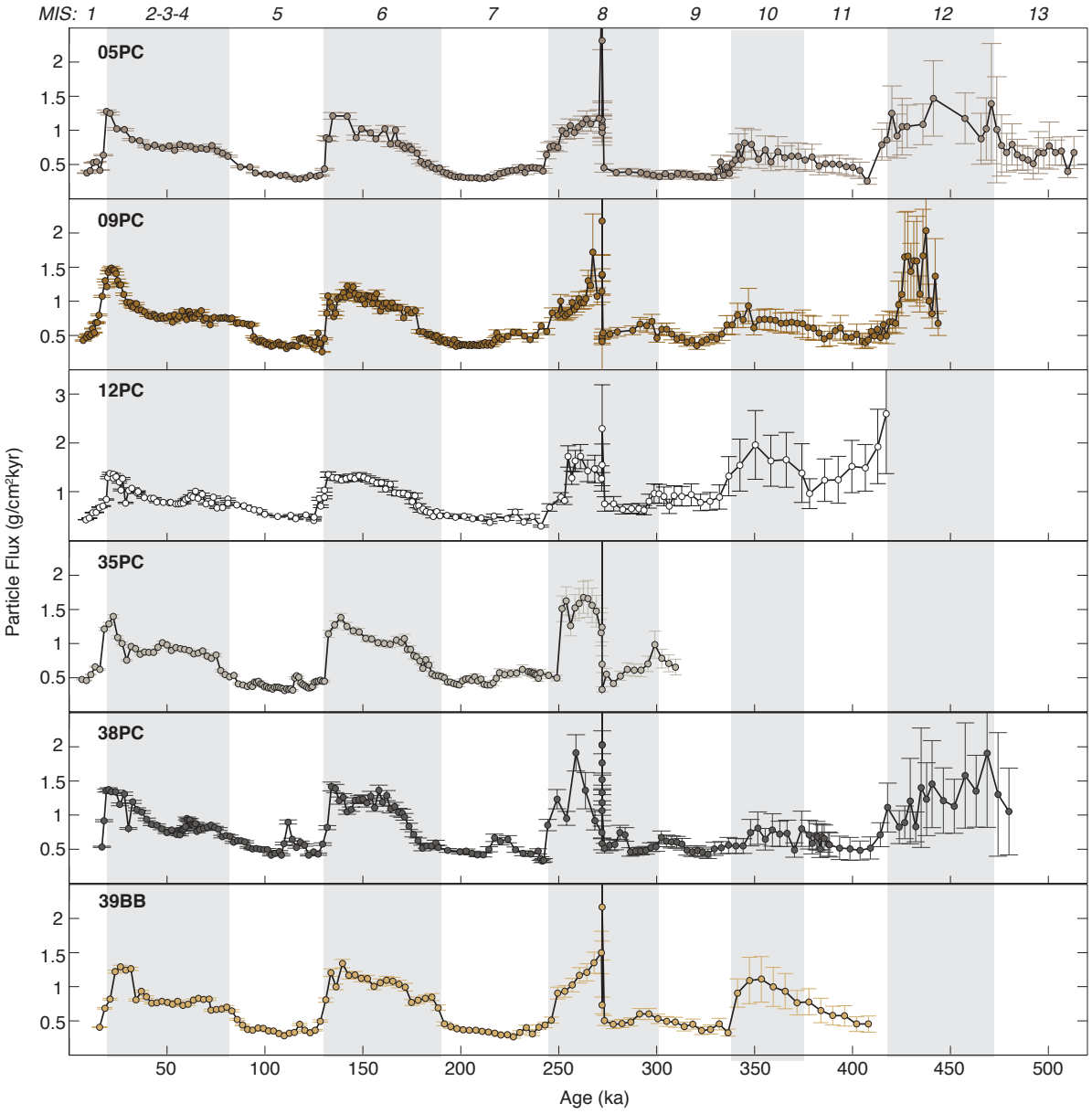

Figure 2.3. ^{230}Th-based particle fluxes. Particle fluxes are higher during glacial MIS (gray bars) than during interglacial MIS by about a factor of two. High particle fluxes at 272ka are associated with a magnetic susceptibility peak (Costa et. al., 2016). Error bars indicate 2 σ , which grows with the age of the sample.

2.3. Results

The particle fluxes show a coherent pattern of glacial maxima and interglacial minima across all six cores (Figure 2.3). Glacial periods average 0.98 g/cm^{2}kyr, which is nearly double the average flux during interglacial periods (0.53 g/cm^{2}kyr). The transitions between high and low flux regimes are particularly abrupt at the boundaries between glacial and interglacial periods (Termination I, ~17ka, and Termination II, ~130ka), while transitions associated with later glacial-interglacial boundaries are less consistent across the multiple core sites. Glacial onset tends to be gradual, with a relatively smooth increase into high glacial fluxes. In general, 12PC and 38PC tend to have the highest particle fluxes, while 05PC and 39BB have the lowest fluxes.

Because not all cores extend the full 500kyr, we recount the trends in particle flux backwards through time, from the young coretops (6 cores) to the end of the records (2 cores). All cores contain a deglacial particle flux maximum ~20ka that peaks at 1.5 g/cm^{2}kyr and lasts about 10kyr. Particle fluxes are fairly stable throughout MIS2-3-4 at 0.75-0.9 g/cm^{2}kyr before decreasing to interglacial values (0.29-0.53 g/cm^{2}kyr) at the MIS4-5 boundary. MIS5 is fairly stable, with one minor mass flux deviation (0.9 g/cm^{2}kyr) occurring at 112ka (MIS5.4-MIS5.3 transition) in 38PC. Several cores (05PC, 38PC, and 39BB) contain a deglacial particle flux maxima ~135ka, but it is not as prominent (~1.3 g/cm^{2}kyr) as the peak at Termination I. MIS6 is similar to MIS2-3-4 in terms of stability but with a slightly higher mean flux (0.88-1.33 g/cm^{2}kyr), and the transition between MIS6 and MIS7 is gradual. MIS7 is similar to MIS5 in terms of both stability and amplitude (0.29-0.47 g/cm^{2}kyr). MIS8 is more variable, with 12PC, 35PC, 38PC, and 39BB showing abrupt termination while 05PC and 09PC contain a gradual decrease in particle flux. Late MIS8 reaches consistent glacial particle fluxes (1.00-1.72 g/cm^{2}kyr) with MIS2 and MIS6, but they are preceded by a short pulse of high particle flux (up to 13 g/cm^{2}kyr) associated

with the prominent magnetic susceptibility peak at 272ka (Costa et al., 2016). Early MIS8 appears more similar to interglacial particle flux values, and the transition between MIS8-MIS9 is not readily apparent. Older glacial periods, particularly MIS10 but also MIS12, are not as homogeneous across all six cores. The particle flux maxima in MIS10 can be identified in 39BB and 12PC at glacial values (1.11-1.60 g/cm^{2}kyr), but in 05PC, 09PC, and 38PC the particle flux reaches only intermediate values of 0.55-0.81 g/cm^{2}kyr. MIS12 termination occurs later in 05PC than it does in 09PC, 12PC, and 38PC, potentially reflecting age model offsets. Particle fluxes during MIS12 tend to be higher (1.2-2.59 g/cm^{2}kyr) than observed in later glacial periods.

Most cores contain periods of winnowing and periods of focusing, with focusing factors ranging from 0.16 to 3.43 (Figure 2.4). Over the entire deposition period, the two cores (05PC and 39BB) farthest from the ridge are in near equilibrium with overlying water column (Ψ = 1.04-1.08), while 38PC and 12PC have net winnowing (Ψ = 0.48-0.73) and 35PC and 09PC have net focusing (Ψ = 1.42-1.73). Overall the region is net neutral, with Ψ = 1.08. While the other five cores fluctuate between the two modes, core 12PC experienced persistent winnowing (Ψ = 0.16-0.98), suggesting a relatively erosive environment as suspected from its lower than average total sedimentation rates (Costa et al., 2016). Near the coretops, 09PC and 35PC show particularly high focusing factors (Ψ = 2.91-3.43) corresponding to high total sedimentation rates (3.02-3.26 cm/kyr). There is no clear glacial-interglacial cycling in focusing factors, and instead they follow the disparate trends of total sedimentation rates.

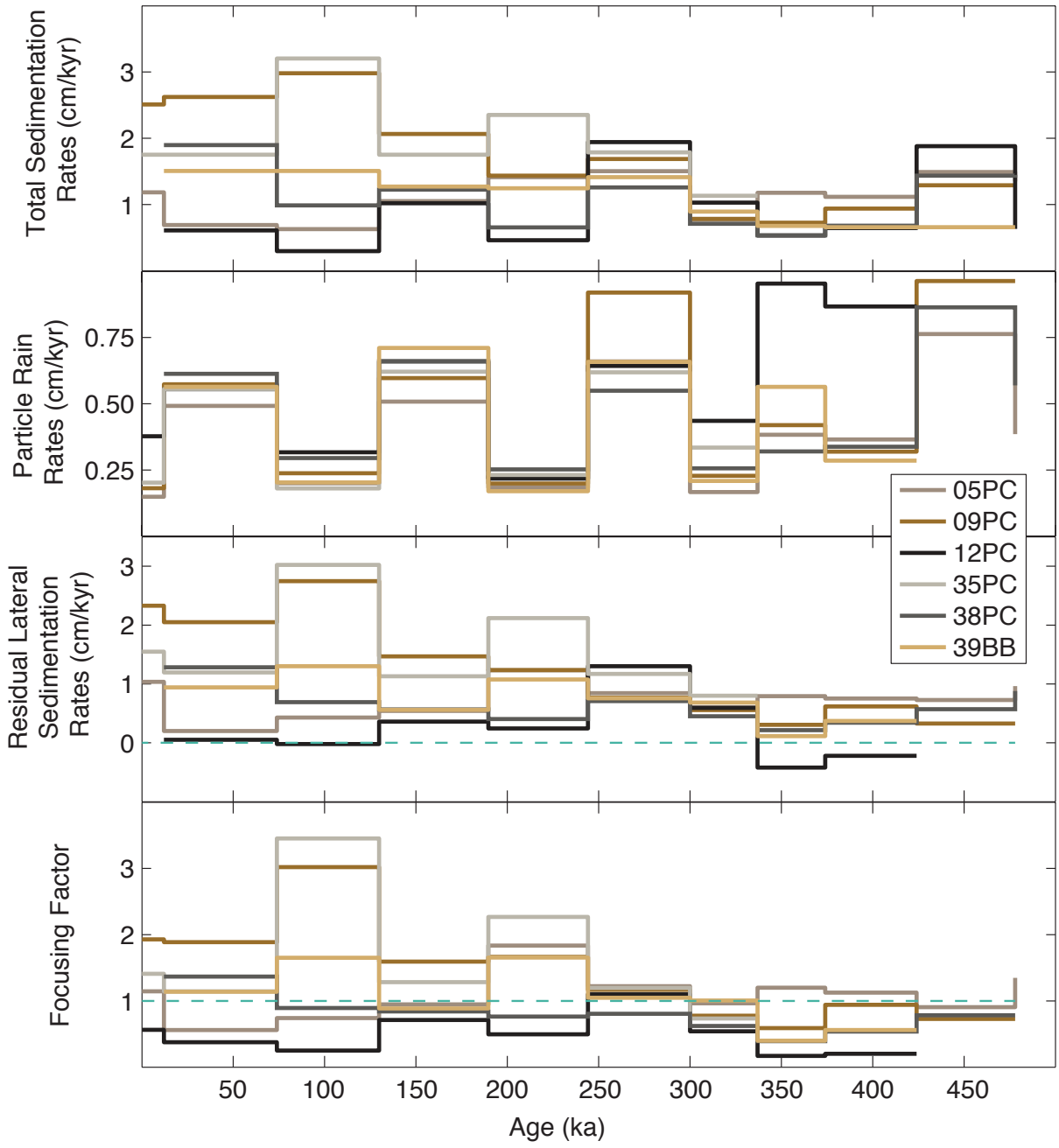

Figure 2.4. Comparison of total sedimentation rates, particle rain rates, residual lateral sedimentation rates, and focusing factors. Total sedimentation, lateral sedimentation, and focusing factors all resemble one another, with high variability in each MIS, especially during the last 250ka. Particle rain rates are always lower than total sedimentation rates, and they are the only parameter to show clear and consistent glacial-interglacial cycles.

2.4. Discussion

2.4.1. Particle fluxes and rain rates on the Juan de Fuca Ridge

The glacial-interglacial cycling of particle flux mirrors the observed cycles in density and carbonate (Supplemental Figure S2.1) that reflect carbonate preservation cycles in the Pacific Ocean (Farrell and Prell, 1989). Particle fluxes are high when density and $CaCO_3$ concentrations are also high. Independent of sediment focusing, the particle rain rates would scale with how much of the carbonate is preserved on the seafloor. If $CaCO_3$ is assumed to be zero during interglacial periods, then the interglacial particle flux (0.53 g/cm^2kyr) can be modeled as the noncarbonate flux, which appears relatively constant over time. Then the preservation of glacial carbonate rain would contribute 0.45 g/cm^2kyr of carbonate, accounting for the near doubling of particle flux. These rudimentary estimates would predict glacial $CaCO_3$ concentrations of nearly 50wt%, which would not be inconsistent with actual glacial values observed in these cores (50-70wt%). Therefore it would be reasonable to attribute the glacial-interglacial pattern of particle flux variations almost entirely to changes in preserved carbonate flux.

The large temporal fluctuations in particle flux easily overshadow the concurrent spatial variability between cores. Over the more recent 300kyr, particle flux varies between cores by $\leq 0.15 g/cm^2kyr$, or about 14-16% in glacial periods and 7-27% in interglacial periods (Figure 2.5). These intercore differences are exceptionally low, considering the nearly order of magnitude differences between the cores in total sedimentation rates (Costa et al., 2016). Intercore variability increases in MIS8 (31%) and continues to grow through MIS9, 10, and 11 due primarily to the divergence of 12PC from the other five cores. Excluding 12PC, the intercore variability would be about the same >300ka as it is <300ka. Fluxes at 12PC are at times more than double what is observed at the other cores.

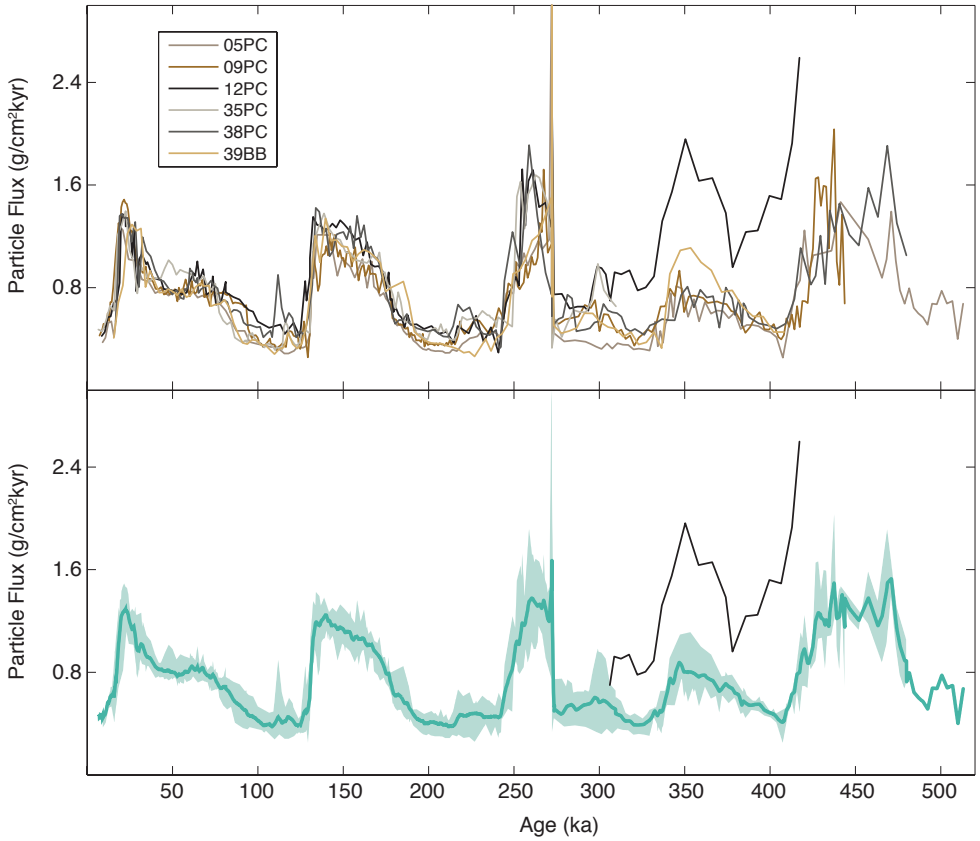

Figure 2.5. Compiled particle flux. When overlain together, it is apparent that particle fluxes from the six different cores are nearly identical for the last 300kyr. Older than 300ka, 12PC diverges to higher particle fluxes than the other cores. *Bottom*: Average particle flux, with shading that indicates the full range of values at each time step. Note the small variability envelope for the last 300ka. Older than 300ka, 12PC is shown as a black line and it is not included in the shaded envelope showing the range of values.

Elevated fluxes at 12PC may be related to distance from the ridge and the input of hydrothermal particles (Supplemental Figure S2.2). Particle fluxes are likely to be higher closer to the ridge, as heavy plume fallout, particularly basalt glass and sulfide grains, are limited to within several kilometers of the vent site (e.g., Clague et al., 2009). The bottom of 12PC contains abundant basalt glass that suggests hydrothermal and magmatic activity that corresponds with the high fluxes associated with the interval when the core was within 10km of the ridge. The decline in excess flux with increasing distance of the ridge would be

consistent with decreasing hydrothermal inputs as 12PC became more distal, until >10km when the additional particle flux reaches approximately zero, as observed in the other 5 cores. Alternatively, the high fluxes in 12PC may be a function of the extreme winnowing (Ψ = 0.158-0.205) taking place at that site at that time (Supplemental Figure 2). Winnowing may bias particle flux reconstructions by preferentially removing Th-rich fine material, thus reducing the Th inventory and inflating particle fluxes (Marcantonio et al., 2014). In this case, the high fluxes at 12PC may indicate a threshold effect in winnowing: the bias towards high fluxes is clearly apparent when Ψ = 0.158-0.205 (12PC, MIS10, 11) but appears negligible when Ψ = 0.243 (12PC, MIS5) or higher. At this time it is difficult to conclusively interpret the high fluxes in 12PC in favor of hydrothermal activity or winnowing, but future work on hydrothermal deposition (e.g., Fe, Mn fluxes) may prove decisive.

Particle rain rates can be obtained by scaling the particle flux by the dry bulk density (g/cm^3) (see Methods Section 2.2.3) (Figure 2.4). Because particle flux and dry bulk density are in phase, the scaling merely adjusts the amplitude of, or exaggerates the difference between, the glacial-interglacial cycles. Thus particle rain rates retain clear carbonate preservation cycles, with increased particle rain rates during glacial periods (0.55-1.06 cm/kyr) compared to interglacial periods (0.16-0.40 cm/kyr). Particle rain rates are comparable across all six cores, varying by as low as 4.8% during MIS2-3-4. Such consensus is not unexpected given the close proximity of the cores (<50km) and the relatively homogeneous surface productivity at this spatial scale (e.g., Kienast et al., 2007).

Particle rain rates are much more consistent than total sedimentation rates, which show considerable variability between the core sites, as much as 500% difference (MIS5: 0.61cm/kyr at 05PC vs 3.18cm/kyr at 35PC; Costa et al., 2016). There is little to no correlation between total sedimentation rates and particle rain rates (Figure 2.6), but

variability in total sedimentation rates seems to increase as the particle rain rate decreases. While particle rain rates of >1cm/kyr might co-occur with total sedimentation rates of 0.41-1.09 cm/kyr, particle rain rates of 0.4 cm/kyr could correspond with total sedimentation rates anywhere from 0.25-3.26 cm/kyr. The independent variability in total sedimentation rates and particle rain rates indicates that changes in the particle rain rate are not the dominant influence on total sedimentation on the JdFR. This discrepancy highlights the potential errors in interpretation that may be introduced when using age model based total sedimentation rates rather than particle rain rates based on constant flux proxies.

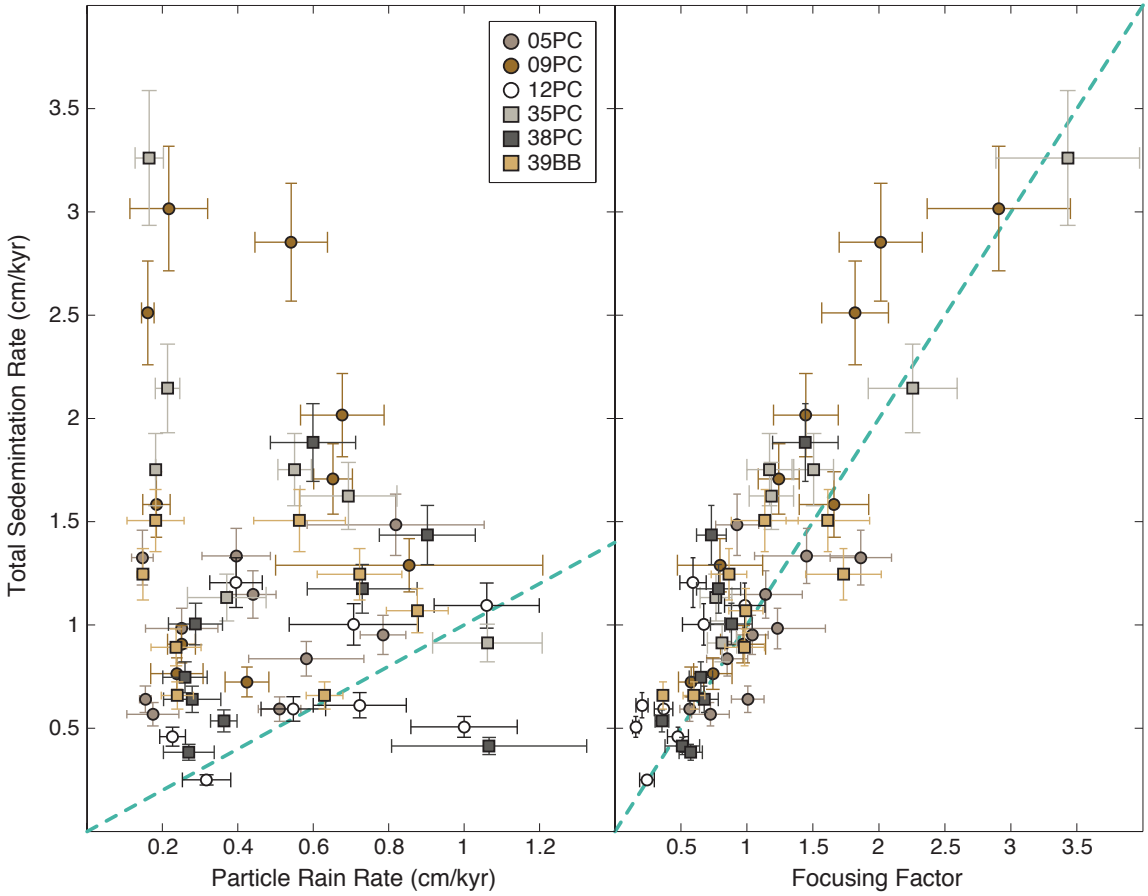

Figure 2.6. Scatter plots comparing total sedimentation rates, particle rain rates, and focusing factors. Total sedimentation rate shows little to no relationship with particle rain rate, whereas it has a strong positive, linear correlation with focusing factors (r^2=0.80). Dashed teal lines are 1:1 lines.

2.4.2. Focusing factors

Sedimentation rates are primarily controlled by two factors: the particle rain rate of pelagic sediment and the intensity of sediment redistribution along the seafloor (Hauschild et al., 2003). The lack of dependence of total sedimentation rates on particle rain rates suggests that sediment redistribution must be the dominant influence on the spatial variability in sediment deposition on the JdFR. Sediment redistribution can be parameterized using ^{230}Th systematics from two different perspectives: 1) residual lateral sedimentation and 2) focusing factors. Residual lateral sedimentation, as required by mass balance, can be calculated as the difference between total sedimentation rate and particle rain rate. Focusing factors are calculated based on the loss or gain of ^{230}Th above the production value (see Section 2.2.4), which is carried by ^{230}Th-laden sedimentary particles. Focusing factors and lateral sedimentation rates show the same pattern, so that both parameters are high when total sedimentation rates are high (Figure 2.4), and especially when particle rain rates are simultaneously low (e.g., MIS5 and MIS7). The nearly one to one relationship between focusing factors and total sedimentation rates reflects variability in sediment redistribution on small spatial scales (Figure 2.6), 10s of kilometers or less (Kienast et al., 2007). During MIS5, focusing at 35PC (Ψ = 3.43) and 12PC (Ψ = 0.24) is an order of magnitude different despite these sites being only 10.5km apart. This is in direct contrast to previous conclusions that sediment redistribution occurs on large spatial and temporal scales (Lyle et al., 2005). Sediment focusing is instead highly variable over small distances, and focusing, rather than particle flux, is the most important mechanism for total sedimentation on the JdFR and potentially in other topographically rugged regions.

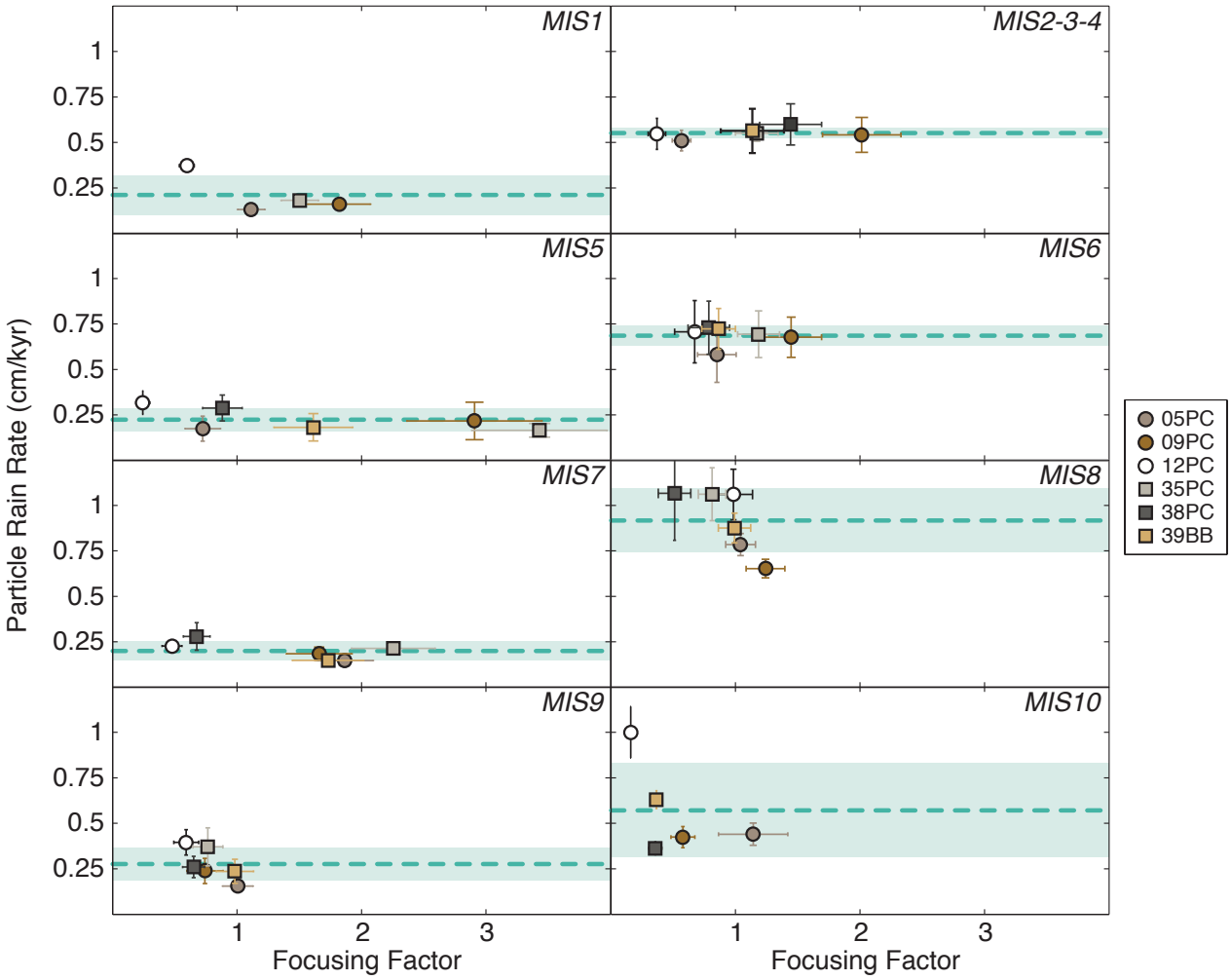

Figure 2.7. Particle rain rates and focusing factors during each MIS. Particle rain rates are nearly constant regardless of the focusing factors, indicating no biases in ^{230}Th normalization due to sediment redistribution. Dashed teal averages are the MIS averages, and shaded regions are the 1 σ range. Cores 38PC and 39BB do not extend into MIS1; their coretop ages are in late MIS2. Variability in MIS8 is largely due to high particle fluxes associated with the magnetic susceptibility peak at 272ka.

Even though focusing is highly variable and strongly controls total sedimentation, it does not interfere with the utility of ^{230}Th to reconstruct particle rain rate on the JdFR. It has long been recognized that ^{230}Th is concentrated in the fine fraction due to the high surface area to volume ratio (Suman and Bacon, 1989; Francois et al., 1990; Thomson et al.,

1993; Francois et al., 2004; McGee et al., 2010; Kretschmer et al., 2010). By extension, focusing (adding fine fraction) and winnowing (removing fine fraction) have been proposed to fractionate ^{230}Th and bias the particle rain rate reconstruction. Focused sites would contain excess ^{230}Th, thus underestimating the true particle rain rate, and winnowed sites would have a deficit of ^{230}Th, thus overestimating the particle rain rate (Marcantonio et al., 2014). But on the JdFR, with the possible exception of >300ka in 12PC (see Section 2.4.1), there is no dependence of the particle rain rate on the focusing factor (Figure 2.7). In MIS5, for example, the focusing factor has a wide range from 0.24 to 3.43, whereas the particle flux is narrowly constrained to 0.22±0.06 g/cm^{2}kyr. The variability between cores is nearly equivalent to the variability within a single core during the same time period (e.g., 0.22±0.10 g/cm^{2}kyr in 09PC during MIS5). This general lack of correlation between focusing factors and particle flux reconstruction demonstrates that decoupling of ^{230}Th from the sediment mass during sediment redistribution is negligible and does not interfere with the ^{230}Th systematics.

Sediment focusing is typically associated with fine fraction, so that more focused sites are expected to skew towards finer grain size distributions (e.g., lower coarse fractions) (Lyle et al., 2005; Kretschmer et al., 2010; Lyle et al., 2014; Marcantonio et al., 2014). On the JdFR, the two highest incidents of focusing (Ψ = ~3-3.5) coincide with low coarse fraction (<5%, Costa et al., 2016), but without those points any relationship between coarse fraction and focusing weakens (Figure 2.8). Sediment focusing (Ψ = 1.5) can result in sediment with 2%, 20%, or 35% coarse fraction, but sediment winnowing (Ψ = 0.75) could just as well generate those size distributions. Thus, while the fine fraction may be more susceptible to sediment redistribution, its preferential mobility along the seafloor does not significantly affect the ^{230}Th systematics.

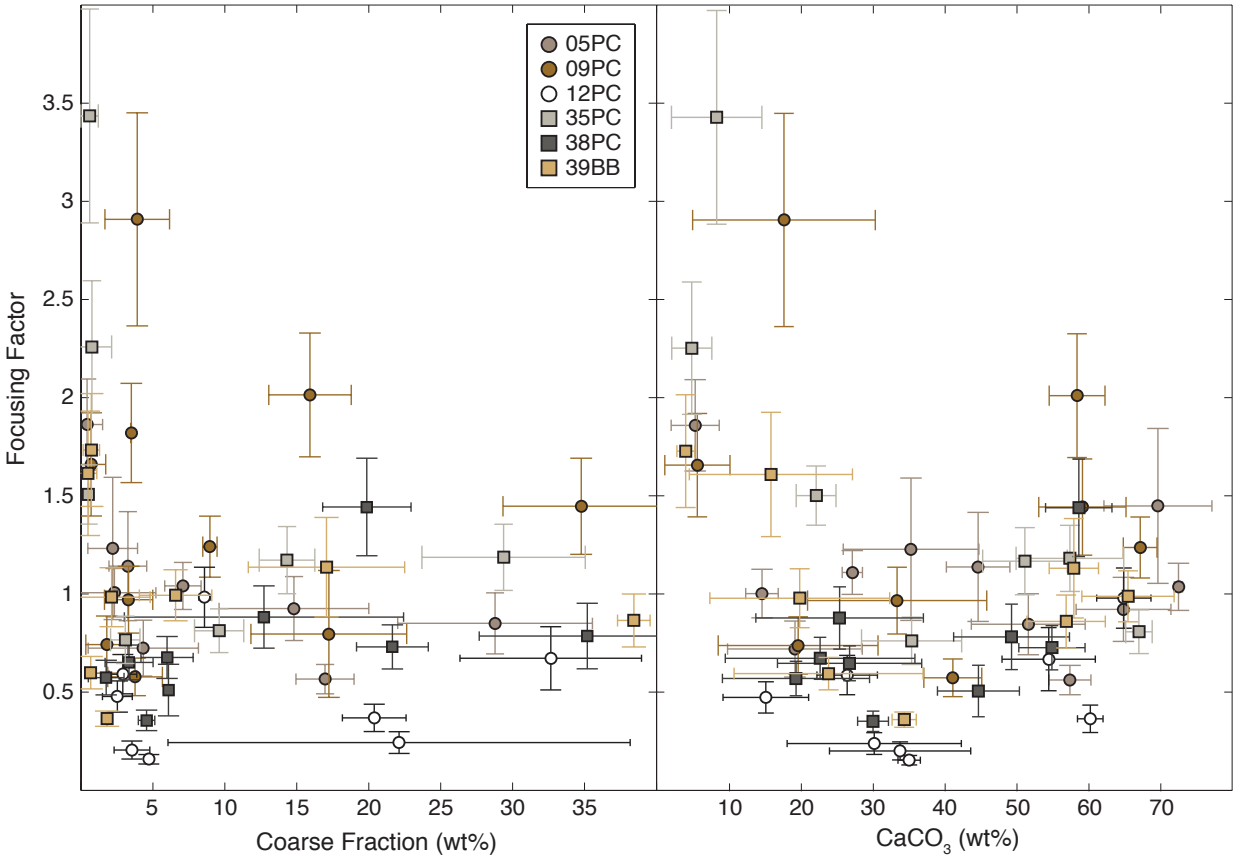

Figure 2.8. Focusing factors, coarse fraction, and carbonate content. Each datapoint represents are the MIS average, and the error bars are 1 σ . The highest focusing factors coincide with low coarse fraction and low calcium carbonate, but otherwise no strong relationship is observed between focusing factor and these two parameters. Carbonate concentrations may have a parabolic relationship with focusing factor, but the Juan de Fuca Ridge does not achieve high enough carbonate contents (>80wt%) to fully assess this observation.

The resilience of ^{230}Th to focusing may be derived from two different aspects of sediment redistribution. First, most pelagic sediment is relatively fine (<35% coarse), so that the size distributions between particle rain rate and lateral sedimentation may not be incongruous (McGee et al., 2010). For example, 50% winnowing (Ψ=0.5) of sediment that starts as 5 wt% coarse will only increase the coarse fraction to 8.3 wt%. Similarly, 50%

focusing (Ψ=1.5) of purely fine material to that 5 wt% coarse sediment would only decrease the coarse fraction to 3.7wt%. Such small changes in the coarse fraction are comparable to the variability in coarse fraction within a MIS period, and they suggest that the grain size distribution may not be particularly sensitive to the lateral flux of sediments. Second, the cohesion of fine particles may inhibit their resuspension from the seafloor and increase their effective particle size (McCave and Hall, 2006; McGee et al., 2010). Small ^{230}Th-rich particles (2 μ m, Kretschmer et al., 2010) are likely to aggregate into much larger particles (10 μ m) that would be significantly less mobile (McCave and Hall, 2006; McGee et al., 2010). This relatively small change in grain size appears to be effective in mitigating ^{230}Th fractionation even at relatively low current speeds, such as the zero-mean oscillatory currents (sporadically up to 10cm/s) observed on the JdFR (Thomson et al., 2003). Alternatively, the effects of grain size may only become relevant under extreme endmember conditions, such as the much higher coarse fractions (> 35wt%) that can be observed in the Equatorial Pacific.

Similarly, the influence of carbonate content on ^{230}Th systematics may only be important in extremely carbonate rich sediments (>80wt%), especially when much of this carbonate is in the coarse fraction (Marcantonio et al., 2014). The highest focusing factors on the JdFR are associated with low (but not the lowest) carbonate content, but otherwise there is little relationship between focusing and carbonate composition (Figure 2.8). Winnowing can result in a core with 20% $CaCO_3$ or 60% $CaCO_3$, just as well as focusing can do the same. This observation argues against a bias towards underestimating ^{230}Th in carbonate rich sediments, most likely due to the relatively uniform distribution of ^{230}Th on coarse and fine carbonate material in contrast to the fine skew in siliceous sediments (Kretschmer et al., 2010). Because there is no evident relationship between carbonate and

focusing, we can be confident in the continued utility of ^{230}Th normalization in carbonate-variable sediments.

2.5. Conclusions

On the Juan de Fuca Ridge, ^{230}Th normalization from six different cores produces a robust record of particle rain rate over the last 510kyr. Particle rain rates are high during glacial periods and low during interglacial periods, following the carbonate preservation cycles in the Pacific. Particle rain rates are always lower than age-model based total sedimentation rates, which are largely controlled by sediment focusing. Despite previous conjectures, no relationships have been found amongst focusing factors, grain size, and carbonate content that would suggest any disturbance in ^{230}Th systematics by sediment focusing and/or dissolution. Therefore, given the lack of correspondence between age-model versus ^{230}Th-normalized sedimentation rates, this study demonstrates the importance of using constant flux proxies when reconstructing particle rain rates.

Furthermore, this study provides the unique opportunity to determine the fate and transport of sediment on the seafloor in a relatively closed sedimentary system. Because the cores are so close together (<50km), the particle rain rate is both expected and demonstrated to be spatially homogeneous. In contrast, sediment redistribution is highly variable in the study area, with an order of magnitude range in focusing factors. Yet while some cores display net focusing (09PC, 35PC) and others display net winnowing (12PC, 38PC), the region as a whole is net neutral, with no large-scale import or export of sediment. This targeted demonstration exemplifies the processes that must, by necessity, apply to sedimentation on the sea floor globally. Thus the validation of ^{230}Th normalization on the Juan de Fuca Ridge presented here is likely to be an expression of its extensive efficacy in the world ocean.

2.6. Data Archiving

All data are archived at the National Oceanic and Atmospheric Administration National Centers for Environmental Information (NCEI) database.

2.7. Supplementary Material

Figure S2.1. Carbonate concentrations. Discrete carbonate measurements (teal circles) overlain on dry bulk density (Costa et al., 2016). Inset scatter plot shows the positive linear relationship between carbonate content and dry bulk density.

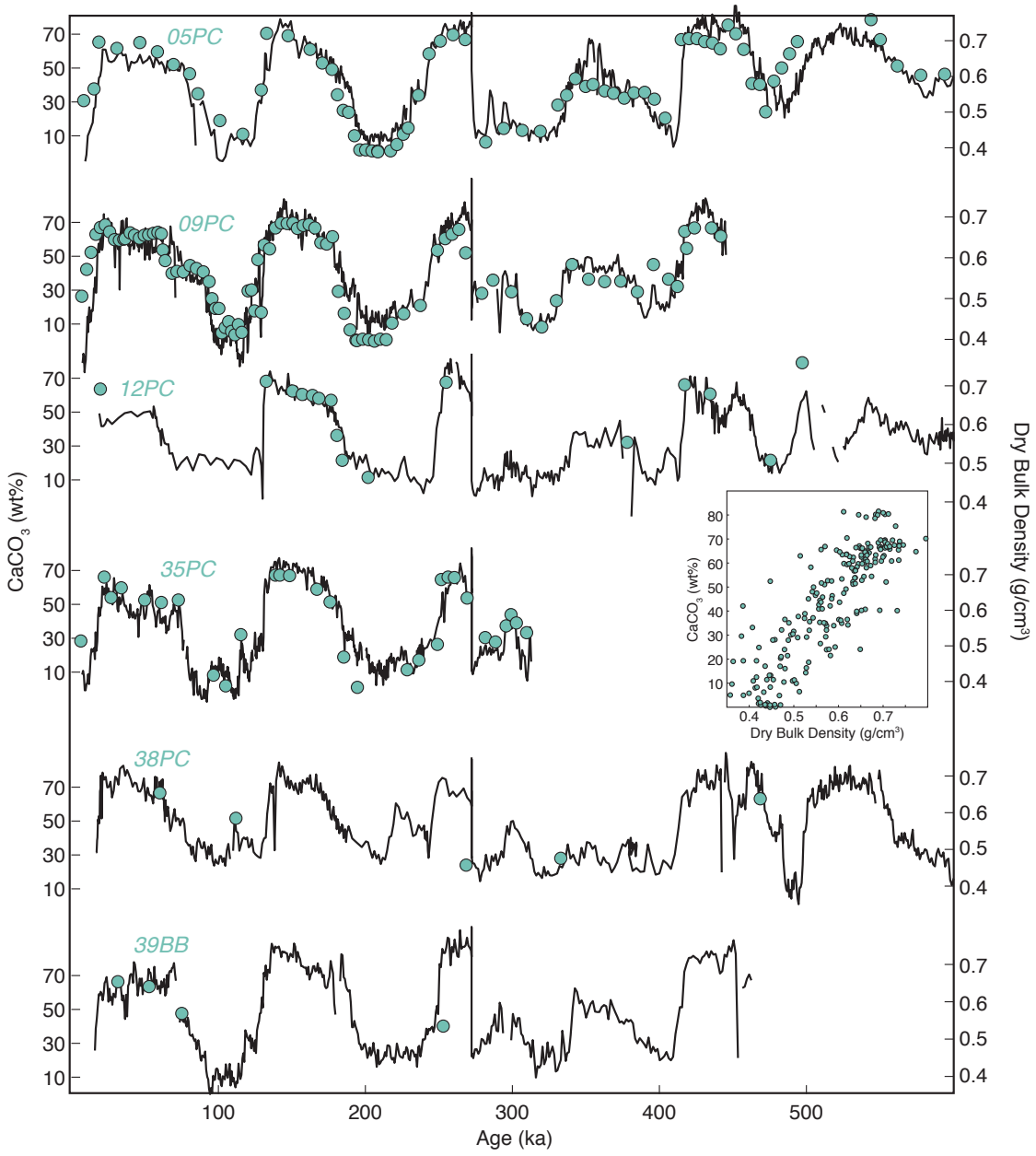

Figure S2.2. Deviations in particle flux from the average flux compilation. (*Top, Left)* Deviations (Δ Particle Flux) were calculated by subtracting the particle flux stack (Figure 2.5, *bottom*) from each individual particle flux record (Figure 2.5, *top*). Core 12PC shows clear positive deviation from the stack >300ka. All other cores vary about 0, indicating no net deviation from the average particle flux record. (*Bottom, Left)* As in the top, but plotted against distance from the ridge, calculated by backtracking the cores' positions using their modern locations and an average half spreading rate of 28 m/kyr. The high fluxes at 12PC occur within 10km of the ridge crest. (*Right*) MIS averages of flux deviations compared to focusing factors. The high fluxes at 12PC correspond with periods of extreme winnowing (low focusing factors).

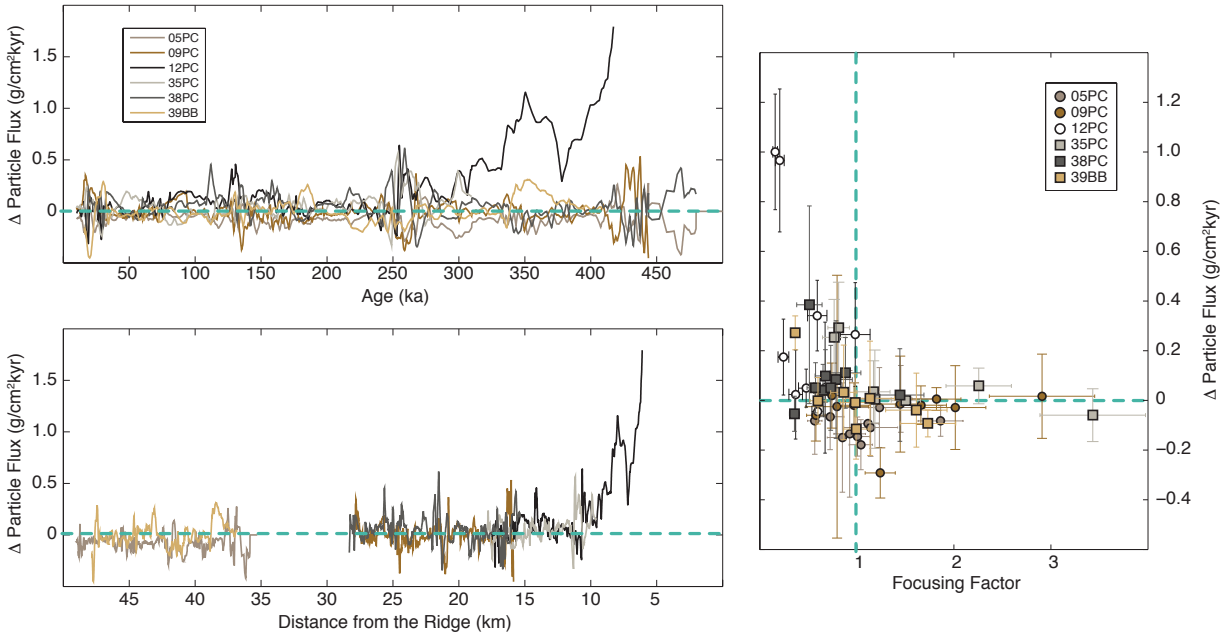

Chapter 3

Trace element (Mn, Zn, Ni, V) and authigenic uranium (aU) geochemistry reveal sedimentary redox history on the Juan de Fuca Ridge, North Pacific Ocean

Note: A modified version of this chapter has been published in *Geochimica et Cosmochimica Acta*[3]

Abstract:

Changes in meridional overturning circulation and water mass chemistry can be recorded by oxygen concentrations in the deep ocean. Because the deep Pacific is the largest ocean reservoir, its oxygen concentrations may be related to global climate change. In this study, oxygen conditions in the past are reconstructed by contrasting the sedimentary geochemistry of multiple redox-sensitive trace elements (Mn, Ni, Zn, V corrected for terrigenous and hydrothermal inputs) and authigenic U (aU) from six sediment cores on the Juan de Fuca Ridge from 2.7-2.8km depth. We find that Mn and Ni are indicators for oxygen-rich conditions, while Zn, V, and aU are indicators for oxygen-poor conditions. Relative Redox Potentials (RRPs) for each core are calculated by converting excess metal fluxes into binary presence/absence designations, weighting each element by the strength and direction of its redox indication, summing the five elements, and then averaging the data in 5kyr bins. Metal depositional histories from all six cores demonstrate low oxygen

---

[3] *Authors*: Kassandra M. Costa[a,b], Robert F. Anderson[a,b], Jerry F. McManus[a,b], Gisela Winckler[a,b], Jennifer L. Middleton[a], Charles H. Langmuir[c] *Affiliations*: [a]Lamont-Doherty Earth Observatory of Columbia University, Palisades, NY 10964, USA. [b]Department of Earth and Environmental Sciences, Columbia University, New York, NY 10027, USA. [c]Department of Earth and Planetary Sciences, Harvard University, Cambridge, MA 02138, USA.

conditions during interglacial periods, particularly during 100-120ka (MIS5) but also 200-250ka (MIS7), and high oxygen conditions during glacial periods (MIS2-4 and MIS6). This redox pattern does not appear to be driven by organic matter flux to the sediment, as reconstructed by three different paleo-productivity proxies (organic carbon, opal, and excess barium). Instead higher oxygen concentrations on the Juan de Fuca Ridge may be a result of better ventilation during glacial periods, possibly due to enhanced North Pacific Intermediate Water formation. Alternatively, sedimentary redox conditions on the Juan de Fuca Ridge may be locally controlled by the deposition of hydrothermal sulfides from nearby vent fields.

3.1. Introduction

Oxygen concentrations in the deep ocean are an important indicator of global climate conditions. While today oxygen persists in deepwaters due to the continuous irrigation of more recently ventilated water, changes in circulation geometry in the past could have displaced this supply pipeline. Reduced ventilation limits the starting oxygen concentrations, but biological processes are largely responsible for the magnitude of subsequent oxygen depletion as the water mass transits at depth. The coupling of carbon and oxygen in respiration may therefore cause oxygen depletion coincident with greater carbon storage. Reconstructions of paleo-redox conditions in the deep waters of the Pacific can help determine the water mass structure and chemistry that allowed the ocean to take up so much CO_2 during past glacial periods (Broecker, 1982; Sigman and Boyle, 2000).

Paleo-oxygen concentrations can be straightforward to interpret under the right conditions, such as when the onset of anoxic conditions suffocates benthic organisms and allows the development and preservation of fine sedimentary laminations (Crusius et al., 2004; Davies et al., 2011). But where low sedimentation rates limit the record of

laminations, oxygen concentrations in the past can be reconstructed by contrasting the sedimentary geochemistry of multiple redox-sensitive trace elements (Elderfield, 1985). Various combinations of V, Mo, U, Re, Cd, Mn, Cu, and Fe have been employed to reconstruct redox conditions across the global ocean, including the Cariaco Basin (Yarincik et al., 2000), the California Margin (McManus et al., 2005; Shimmield and Price, 1986), and the eastern margin of North America (Morford et al., 2009), amongst many others. Beyond the coastal margins, sedimentary environments near mid-ocean ridges have proven advantageous to paleo-redox studies of deepwaters because hydrothermal activity increases redox-sensitive trace element concentrations that offer stronger indications of past changes in sedimentary redox conditions than can be extracted from sediments elsewhere (Mills et al., 2010; Schaller et al., 2000).

In this study, we use sedimentary concentrations of trace metals (Mn, Ni, Zn, V) and authigenic U (aU) to reconstruct redox conditions over the past 250kyr on the Juan de Fuca Ridge. The antiphased chemistry of aU and Mn anchor calculations of relative redox potential (RRP), which records the relative changes in sedimentary redox conditions based on the presence or absence of aU, Mn, Ni, Zn, and V. Because sedimentary redox records integrate changes in bottom water oxygen with the local flux of reductants (electron donors), the variability in organic matter and hydrothermal sulfide deposition must be considered before variability in RRP can be interpreted as changes in ventilation. We present new records of organic carbon, excess barium, and opal fluxes to constrain the variability in paleoproductivity and burial of organic matter in this region. We also compare the RRP with previously published records of hydrothermal activity along the ridge to investigate whether sulfide deposition may be influencing the redox history of North Pacific sediments.

3.2. Methods

3.2.1 Core sites and stratigraphy

Samples were taken from six cores on the Juan de Fuca Ridge (Figure 3.1) collected on the SeaVOICE cruise (AT26-19) of the R/V Atlantis in September 2014. Cores were retrieved in two E-W transects in a semi-grid on the western flanks of the ridge and targeted on ridge-parallel crests (2655-2794m) to maximize carbonate preservation (Costa et al., 2016). The average spacing between cores is about 20km. Age models for the JdFR cores are well-constrained based on radiocarbon dates, benthic $\delta^{18}O$, and stratigraphically tuned density cycles (Costa et al., 2016). Dry bulk density and coarse fraction >63 μ m (Costa et al., 2016), as well as bulk particle flux (Costa and McManus, 2017) all show distinct glacial-interglacial cycles, with high-density, coarse sediment characterizing glacial deposition.

3.2.2 Uranium analyses

Samples (n=1097) were analyzed for uranium (^{238}U, ^{235}U, ^{234}U) by isotope dilution inductively coupled plasma mass spectrometry (ICP-MS) following the procedure described by Costa and McManus (2017). Samples (100mg) were randomized and spiked with ^{236}U and ^{229}Th before processing with complete acid digestion and column chromatography (Fleisher and Anderson, 2003). Isotopes were measured on an Element 2 ICP-MS at Lamont-Doherty Earth Observatory (LDEO) of Columbia University. Discrete sediment aliquots (n=106) of an internal sediment standard (VOICE Internal MegaStandard, VIMS) were processed and analyzed for quality control. The VIMS replicates indicate that the analytical procedure and measurement are externally reproducible within 6.2% on ^{238}U and

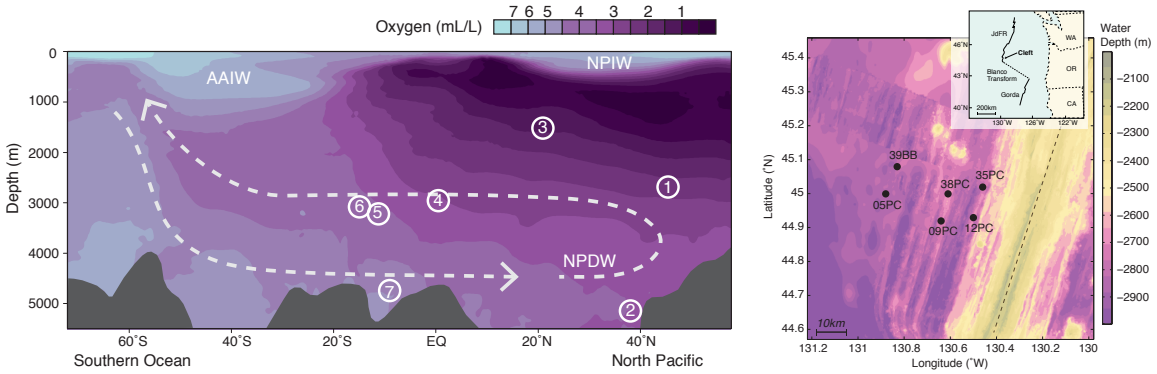

Figure 3.1. (*Left*) Longitudinal section of oxygen concentrations from a 500km swath along 140˚W (Garcia et al., 2014). Dashed arrows show general Pacific meridional overturning circulation. Water masses are labeled as NPDW (North Pacific Deep Water), AAIW (Antarctic Intermediate Water), and NPIW (North Pacific Intermediate Water). Core locations referred to in this study have been zonally projected onto the oxygen section (white circles). 1. AT26-19 set of 6 cores (this study) 2. SO202-1-39-3 (Korff et al., 2016) 3. 72DK-9 (Mangini et al., 1990) 4. ML1208-17PC (Jacobel et al., 2017) 5. Y-71-7-53P (Lund et al., 2016; Schaller et al., 2000) 6. GS7202-35 (Mills et al., 2010) 7. VA13-2 (Mangini et al., 1990). (*Right*) Bathymetric map of the Cleft Segment, with inset showing the geographic position of the Juan de Fuca Ridge in the Northeast Pacific Ocean. The ridge can be identified as the NE-SW trending bathymetric high (in yellow), and the axis is identified with a dashed line. AT26-19 core locations on the western flanks of the ridge are shown with black dots (Costa et al., 2017c).

3.7% on ^{232}Th (Costa and McManus, 2017). The lithogenic fraction of uranium was calculated using a detrital ^{238}U/^{232}Th activity ratio of 0.48 (Costa and McManus, 2017), the value which ^{238}U/^{232}Th reaches as the ^{232}Th concentration approaches the average lithogenic value (10.7ppm, Taylor and McLennan, 1995) and similar to other lithogenic ^{238}U/^{232}Th values from elsewhere in the North Pacific: 0.5±0.1 (Serno et al., 2015) and 0.53 (Taguchi and Narita, 1995). Subtracting the lithogenic uranium from the total uranium concentration determines the concentration of authigenic uranium (aU). aU fluxes are

calculated using age model based mass accumulation rates (MAR) derived from the dry bulk density and linear sedimentation rates (Costa et al., 2016). MAR include both the particle rain rate through the water column as well as the lateral particle contributions due to sediment focusing (or winnowing). The total sedimentation rates influence sedimentary aU precipitation because they control the diffusion depth of dissolved U(VI) from overlying bottom waters through pore waters to the redox boundary where reduction to U(IV) occurs (Anderson, 1982; Anderson et al., 1989b; Barnes and Cochran, 1990; Klinkhammer and Palmer, 1991). The in situ precipitation of sedimentary aU means that the total (age model-based) MAR is the appropriate parameter to use when evaluating the diffusive flux of U into the sediments. Constant flux proxies, like ^{230}Th, specifically reconstruct the particle rain through the water column and thus are not relevant to formation of authigenic metals within the sediment.

3.2.3 Trace element concentrations

Intensities (count rates) of V, Ni, Zn, Fe, Mn, Ba, and Ti were measured with an x-ray fluorescence (XRF) core scanner (ITRAX, Cox Ltd., Sweden) at Lamont-Doherty Earth Observatory of Columbia University (LDEO). Split core surfaces were smoothed and covered with ChemPlex Proline transmission film to minimize desiccation during analysis. XRF was performed at 2mm resolution, using an integration time of 2s and a molybdenum x-ray source set to 30 kV and 45 mA. XRF intensities were calibrated using discrete measurements analyzed by flux fusion as previously described in Costa et. al., 2017c. Samples from 05PC, 09PC, and 12PC were selected to cover the full range of XRF intensities observed in each core, and elemental concentrations were analyzed by flux fusion following the procedure of Murray et al. (2000). Dried, homogenized samples (100±5mg) were combined with lithium metaborate flux (400±10mg) in graphite crucibles

and fused at 1050˚C for 8-10 minutes. The graphite crucibles were removed from the furnace and agitated to ensure aggregation of the fused material. After reheating to 1050˚C, the fused bead was dissolved in 10% HNO_3, agitated for approximately 10 minutes, and then filtered and diluted for analysis. Samples were analyzed on an Agilent 720 Inductively Coupled Plasma Optical Emission Spectrometer (ICP-OES) at LDEO, and ICP-OES intensity data were calibrated to concentrations with fluxed standard reference materials (JLS-1, JDO-1, SCO-1, AGV-2, JB1-a, W-2a, BCR, BHVO-2, Supplementary Figure 3.1). Empirical calibrations of the XRF data were generated by least squares linear regression of the XRF intensities and discrete elemental data. The XRF records were smoothed at 1cm scale and interpolated onto the depths of the discrete samples. Overall the ICP data provide robust calibrations for the high-resolution XRF records (Figure 3.2). As no inter-core discrepancies were apparent, the same calibration was applied to all six cores. Calibrations for Mn (r^2=0.87), Fe (r^2=0.92), and Ti (r^2=0.86) were previously published (Costa et al., 2017c).

Total metal concentrations (V, Ni, Zn, Mn, Fe) in pelagic sediment may be governed by several different processes, including variations in hydrothermal activity and lithogenic inputs in addition to redox conditions. It is therefore necessary to quantitatively account for the lithogenic and hydrothermal variability of each metal before interpreting the redox signals. Ti is almost entirely derived from the lithogenic fraction (Murray et al., 1993), in contrast to Al, which can be enriched in hydrothermal fluids (Elderfield et al., 1993; Lunel et al., 1990; Resing et al., 2015; Von Damm et al., 1985). Multiplying Ti by the average ratio of upper continental crust (e.g., Fe/Ti of 11.7wt%/wt%, Taylor and McLennan, 1995) constrains the lithogenic metal contributions. Additional discussion of lithogenic endmembers is provided in Costa et al. (2017c). Despite the potential hydrothermal effects

on Al, Al/Ti ratios vary by only ~2% throughout the interval of interest,which would be consistent with relatively stable lithogenic endmembers.

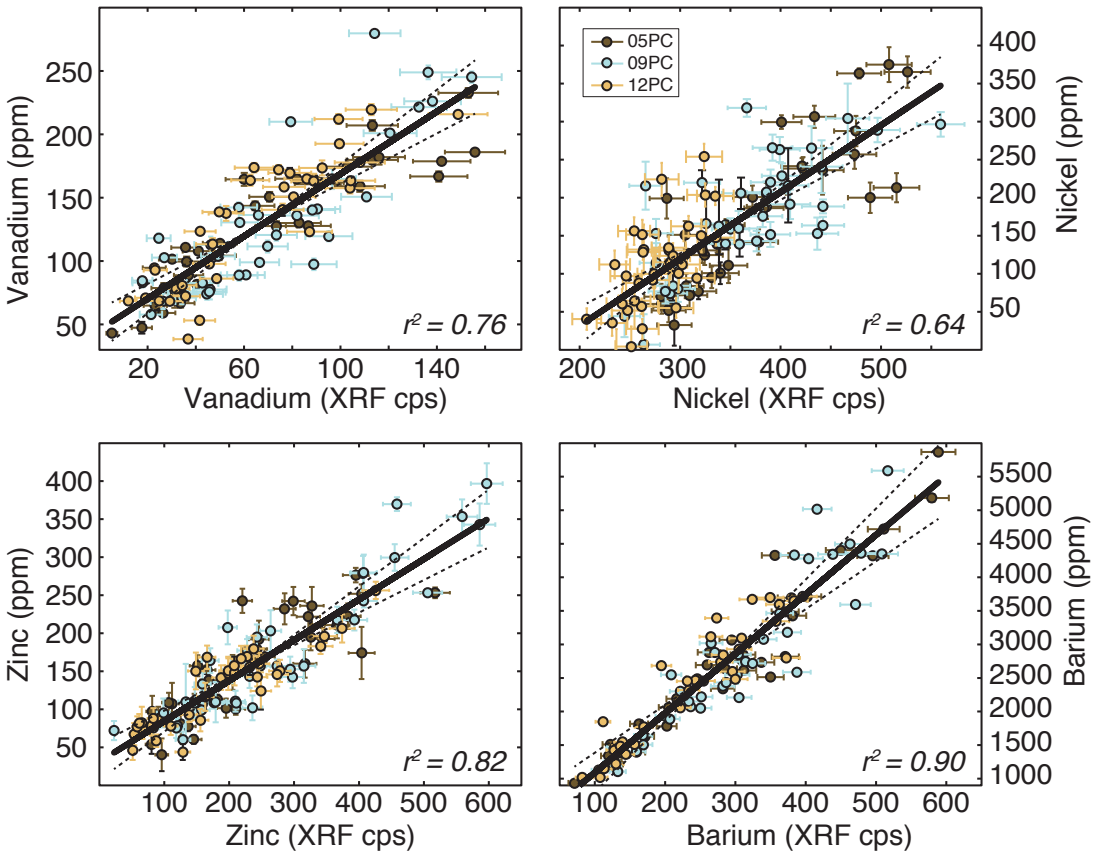

Figure 3.2. Calibration of XRF scan data from counts per second (cps) to mass concentration (ppm) was determined by analyzing discrete sediment samples by flux fusion and ICP-OES. Pearson's correlation coefficients (r^2) are indicated for each element, all at $p<0.001$. Agreement amongst the three cores (05PC, 09PC, and 12PC) analyzed by discrete analysis justifies the use of a single calibration curve for all six cores analyzed by XRF (05PC, 09PC, 12PC, 35PC, 38PC, 39BB). Error bars are 2 σ , not shown when smaller than symbols. Calibrations for Mn ($r^2 = 0.87$), Fe ($r^2 = 0.92$), and Ti ($r^2 = 0.86$) have been previously published (Costa et al., 2017c).

Once the lithogenic metal concentration is subtracted from the total metal concentration, the residual metal concentration varies both in terms of hydrothermal activity and diagenesis. Because iron is the major component of hydrothermal particulates

(Edmonds and German, 2004; Feely et al., 1994, 1987), scaling the non-lithogenic Fe record by average metal/Fe ratios within the hydrothermal plume will approximate the variability in hydrothermal metal inputs over time. Hydrothermal ratios (75th percentile) for Mn/Fe (0.0174 wt%/wt%), V/Fe (28.2 ppm/wt%), and Zn/Fe (32.7 ppm/wt%) were measured in hydrothermal particulates from the Cleft Segment at the Juan de Fuca Ridge (Feely et al., 1994). Ni/Fe ratios were not reported. Because hydrothermal V/Fe and Zn/Fe are relatively similar in value, we assume that hydrothermal Ni/Fe will behave comparably and assign it a value of 30 ppm/wt%. This assumption is not unreasonable given that the hydrothermal correction is insensitive to variability in the metal/Fe ratios within the range of 10-50ppm/wt% (Supplementary Figure 3.2).

Subtracting the hydrothermal metal component from the non-lithogenic metal component leaves the residual excess metal (M_{xs}) interpreted here as the redistributed metal content in response to changing redox conditions within the sediment. As in aU fluxes, excess metal fluxes are calculated using age-model based mass accumulation rates derived from the dry bulk density and linear sedimentation rates (Costa et al., 2016)

In summary

$$M_{xs}\ flux = \left(M_{total} - Ti * \left(\frac{M}{Ti}\right)_{Lith} - Fe_H \left(\frac{M}{Fe}\right)_{Hydrothermal} \right) * \rho * LSR$$

where M is V, Ni, Mn, or Zn, ρ is the dry bulk density, and LSR is the linear sedimentation rate.

Although plume particulate metal/Fe is likely to be variable through time, possibly skewed towards sporadically high ratios (Feely et al., 1994), there is currently no independent method of constraining this variability in the composition of hydrothermal particulates. Assuming a constant metal/Fe ratio, then, the main effect of employing

different metal/Fe ratios is to adjust the absolute value of the excess metal fluxes. Higher hydrothermal metal/Fe ratios push the excess metal fluxes closer to zero, while lower hydrothermal metal/Fe ratios increase the excess metal fluxes. Within a conservative range of metal/Fe ratios (10-50 ppm/wt%), however, the excess metal fluxes record nearly identical temporal patterns (Supplementary Figure 3.2). Since our redox interpretation is based on a binary presence/absence calculation (see Section 3.4.3), from relative peaks above and below the mean value, it is not dependent on the absolute value of the excess metal fluxes. Therefore, we do not expect variable metal/Fe ratios to introduce major artifacts in the redox interpretations presented in this paper.

3.2.4 Paleo-productivity proxies

Biogenic opal was measured by alkaline extraction (Mortlock and Froelich, 1989) at LDEO. Samples were acidified with dilute hydrochloric acid and then oxidized with stabilized hydrogen peroxide. The residual sediment was then extracted in 2N sodium carbonate for five hours at 80˚C. A silico-molybdate photoindicator was added to the leachates, and absorbance intensities at 812μm were analyzed on a spectrophotometer. Total replicates (n=6) of VIMS indicate that the analytical procedure and measurement are reproducible within ±6.7%.

Organic carbon concentrations were analyzed by combustion on an Element Analyzer at LDEO. Samples were acidified with dilute hydrochloric acid and then rinsed with deionized water till neutral pH was achieved. The residual non-carbonate fraction was freeze-dried and loaded in tin capsules. Because this analytical procedure has a poor yield (50% or less), the absolute organic carbon values may not be accurate and should not be employed in, e.g., direct comparisons with other published organic carbon records.

Fortunately, reproducibility within ±6% on total replicates (n=5) of VIMS allows confidence in the temporal trends and relative variability, as the data are interpreted in this study.

Barium concentrations were measured by XRF and ICP-OES as detailed in Section 3.2.3. Excess barium (Ba_{xs}) was calculated by subtracting the lithogenic barium inputs using the Ti record and a lithogenic Ba/Ti ratio of 1833 ppm/wt% (Taylor and McLennan, 1995). Because these productivity proxies are delivered to the sediment in a vertical particle rain from the surface ocean, organic carbon, opal, and Ba_{xs} fluxes were calculated using ^{230}Th-normalized particle fluxes (Costa and McManus, 2017).

3.3. Results

3.3.1 Authigenic uranium

Authigenic uranium (aU) is generally low (<1ppm) on the Juan de Fuca Ridge over the past 500kyr (Figure 3.3). This relatively constant background level is interrupted by peaks in aU that can reach as high as 5.3ppm (Figure 3.3A). Notably, high aU concentrations only occur in the two highest sedimentation rate cores, 09PC and 35PC (Costa et al., 2016) (Figure 3.3B), whereas the other four cores (05PC, 12PC, 38PC, 39BB) record nearly constant (low) aU concentrations over the past 500kyr. The highest aU concentrations in 35PC and 09PC occur during Marine Isotope Stage 5 (MIS5, 74-130ka), but the two cores record different amplitudes and durations of the aU peak. In core 09PC, aU rises above background levels at 122ka, peaks at 114ka at 5.3ppm, declines to a brief plateau at 109ka at 2.8ppm, and then returns to background aU levels (0.1ppm) by ~90ka. Thus, the high aU depositional period appears to last ~32kyr in 09PC. In core 35PC, aU rises above background levels at 121ka, peaks at 111ka at 4.3ppm, where it remains until 88.8ka when it starts gradually declining to background levels by 61ka. Therefore, although the increase in aU concentrations in 35PC occurred at nearly the same time as in 09PC, the

high aU depositional period lasted ~50ka, nearly twice as long and burying twice as much aU. Core 35PC also records peaks of aU of about ~2ppm in the older interglacial period 199-237ka (MIS7), which is not found in the other 5 cores. The earliest peak in aU in this core occurred during 272-306ka (MIS8), and it is capped by the major turbidite event at 272ka.

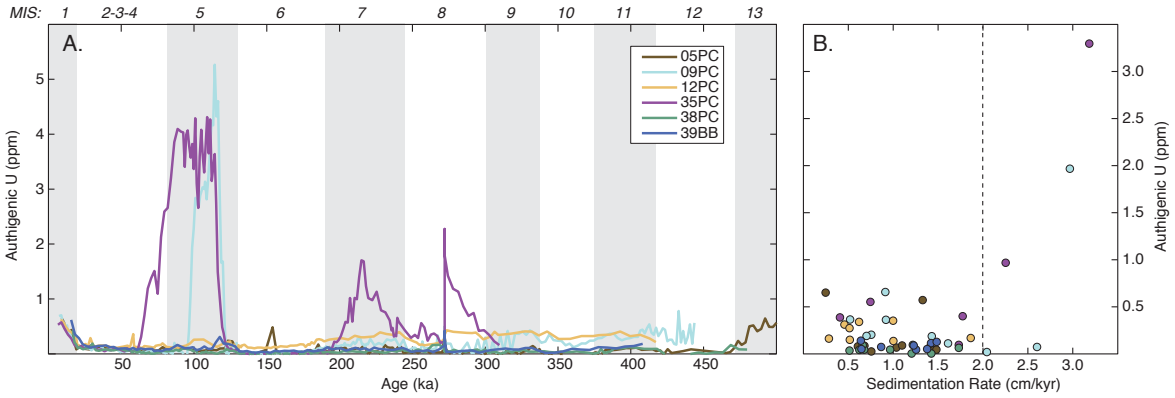

Figure 3.3. Authigenic uranium (aU) records from the Juan de Fuca Ridge. A) Peaks in aU occur during the last interglacial period in cores 09PC and 35PC, while the other cores show relatively constant and low aU burial over the entire 500kyr period. B) aU concentrations vs. sedimentation rates, averaged over marine isotope stages (MIS; interglacial periods highlighted with gray bars). High aU concentrations are only preserved in the sedimentary record when sedimentation rates are greater than 2cm/kyr (dashed line).

3.3.2 Trace Metals

3.3.2.1 Manganese

The redox-mobile fraction of manganese (Mn_{xs}) represents, on average, 74% of total manganese concentrations in the sediment. Mn_{xs} fluxes average 1.5-3.3 mg/cm^{2}kyr in all cores except 09PC, where average Mn_{xs} fluxes are higher (5.0 mg/cm^{2}kyr) and peak fluxes can reach as high as 35.7 mg/cm^{2}kyr (Figure 3.4). In general, Mn_{xs} fluxes are lower during interglacial periods than during glacial periods, and this cycling has the greatest range in the highest accumulation rate cores (09PC and 35PC). For example, in 09PC, Mn_{xs} fluxes average 1.9 mg/cm^{2}kyr in MIS5 (100-120ka) and 11.2 mg/cm^{2}kyr in MIS2-4 (20-60ka), a nearly tenfold increase in Mn_{xs} flux. Glacial-interglacial variability is damped in the oldest part of the core (>300ka).

3.3.2.2 Nickel

The redox-mobile fraction of nickel (Ni_{xs}) represents, on average, 57% of total nickel concentrations in the sediment. Ni_{xs} fluxes average 24-118 μg/cm^{2}kyr in all cores (Figure 3.4). Peak fluxes reach as high as 625 μg/cm^{2}kyr, and high frequency variability is particularly prominent in the high sedimentation rate cores (09PC, 35PC). Low sedimentation rate cores, notably 12PC and 38PC, record relatively constant Ni_{xs} deposition (e.g., -11 to 78 μg/cm^{2}kyr in 12PC) compared to higher sedimentation rate cores (e.g., 7.7 to 625 μg/cm^{2}kyr in 09PC). The Ni_{xs} and Mn_{xs} fluxes appear to be correlated over the last glacial cycle, with the highest correlation (r^2=0.67) of any two redox-sensitive elements (Figure 3.5). From 150-250ka, this relationship seems to reverse, with higher Mn_{xs} fluxes in MIS6 (150-200ka) and MIS8 (250-300ka), and higher Ni_{xs} fluxes in MIS7 (200-250ka).

Figure 3.4. Excess trace element fluxes over the past 500ka. Fluxes are calculated using age-model based mass accumulation rates. Mn_{xs} and Ni_{xs} fluxes are generally higher during glacial periods (MIS2-4 and MIS6) while Zn_{xs}, V_{xs}, and aU fluxes are higher during interglacial periods (MIS5 and MIS7). This variability is consistent with higher sediment oxygen concentrations during glacial periods and lower oxygen concentrations during interglacial periods. The presence of negative deposition rates, particularly in the oldest part of the record (>400ka), may indicate 1) net loss of element from the sediment, presumably through diffusion to the water column, or 2) much lower metal/Fe ratios are present during that interval. Gray bars highlight interglacial periods, as identified by odd marine isotope stages (MIS).

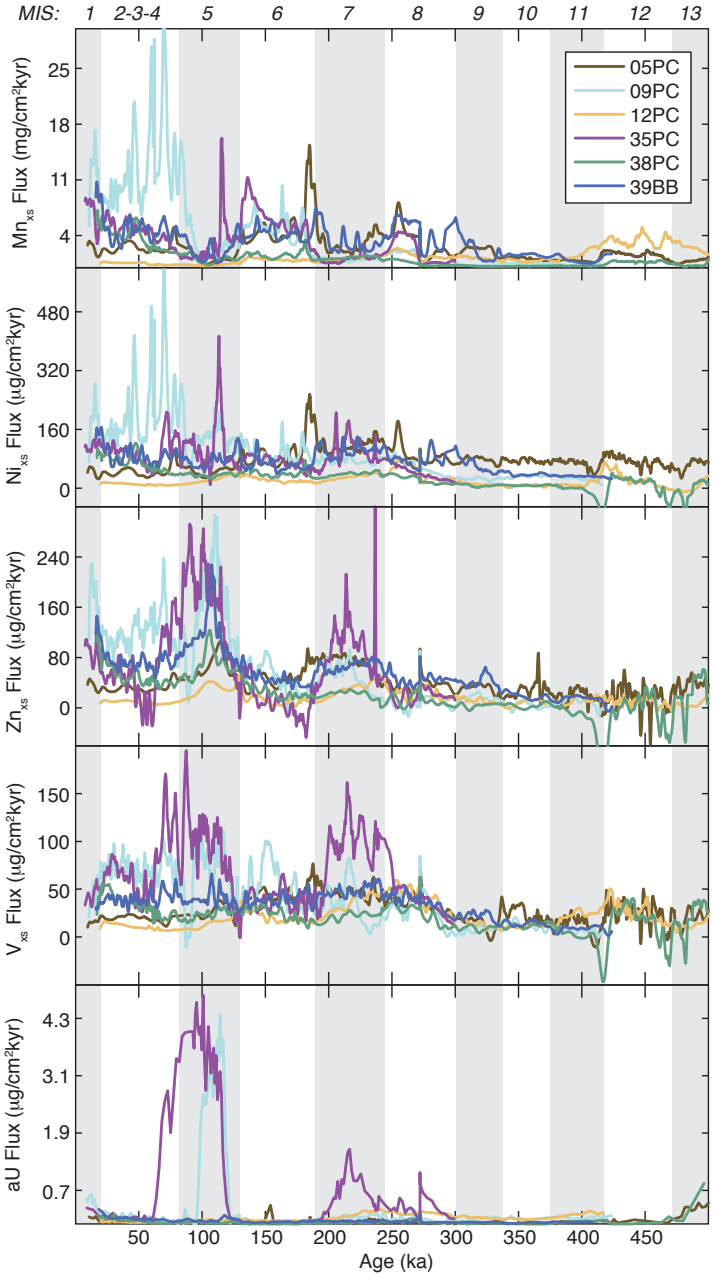

3.3.2.3 Zinc

The redox-mobile fraction of zinc (Zn_{xs}) represents, on average, 32% of total zinc concentrations in the sediment. Zn_{xs} fluxes average 20-83 μg/cm^{2}kyr in all cores (Figure 3.4), with variability scaling with sedimentation rate as observed in Ni_{xs} fluxes. Peak fluxes reach as high as 354 μg/cm^{2}kyr in 35PC, the core that also demonstrates the greatest dynamic range. Zn_{xs} fluxes are better correlated with aU fluxes (r^2=0.47) and Ni_{xs} fluxes (r^2=0.47) than with Mn_{xs} fluxes (r^2=0.17) (Figure 3.5). High Zn_{xs} fluxes (greater than 120 μg/cm^{2}kyr) occur during the last interglacial periods (MIS5), with several cores recording a peak at 110ka. The duration of this high flux period scales with that of the aU fluxes, lasting the longest in 35PC (~50kyr) and in 09PC (~30kyr), with the other cores only recording a brief event. Zn_{xs} fluxes are also elevated in MIS7 in 35PC, peaking at 200 μg/cm^{2}kyr at 214ka, coincident with the high aU fluxes preserved in that core.

3.3.2.4 Vanadium

The redox-mobile fraction of vanadium (V_{xs}) represents, on average, 32% of total vanadium concentrations in the sediment. V_{xs} fluxes average 22-70 μg/cm^{2}kyr in all cores (Figure 3.4), and the overall lower fluxes lead to more similar depositional records from the high and low sedimentation rate cores. Peak fluxes reach as high as 195 μg/cm^{2}kyr in 35PC, the core that also demonstrates the greatest dynamic range. V_{xs} fluxes are better correlated with aU fluxes (r^2=0.34), Zn_{xs} fluxes (r^2=0.56), and Ni_{xs} fluxes (r^2=0.41) than with Mn_{xs} fluxes (r^2=0.15) (Figure 3.5). High V_{xs} fluxes (greater than 80 μg/cm^{2}kyr) occurred during oxygen poor interglacial periods (MIS5, MIS7) and low V_{xs} fluxes (below 60 μg/cm^{2}kyr) occurred during oxygen rich glacial periods (MIS2-4, MIS6). High fluxes of V_{xs} during

interglacial periods record a more square waveform than either aU or Zn_{xs}, which tend to peak in the middle of the oxygen poor interval.

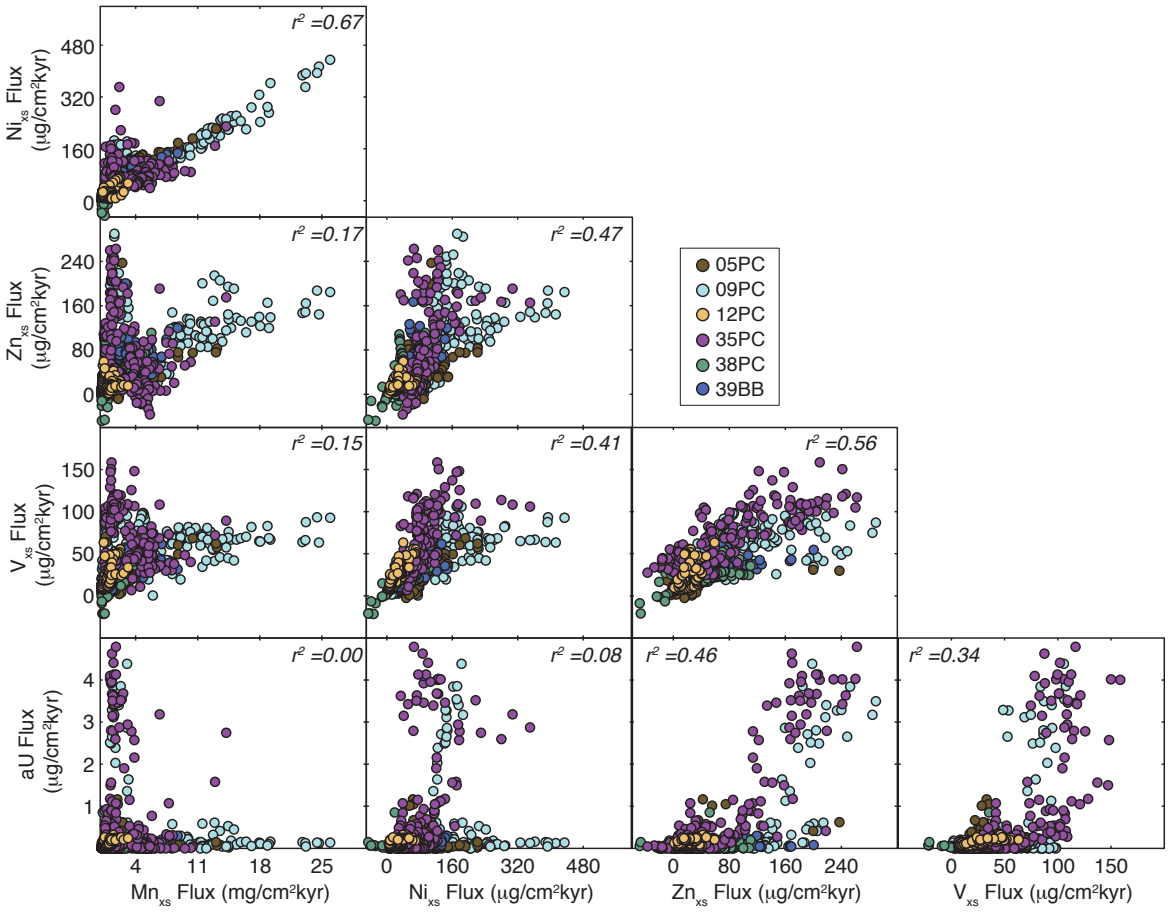

Figure 3.5. Scatter plots showing relationships between Mn_{xs}, Ni_{xs}, Zn_{xs}, V_{xs}, and aU fluxes on the Juan de Fuca Ridge. Mn_{xs} and Ni_{xs} fluxes have the highest correlation (r^2=0.67), while Mn_{xs} and aU fluxes have no correlation at all (r^2=0.00). Zn_{xs} and V_{xs} fluxes are better correlated with aU fluxes than with Mn_{xs} fluxes. All correlations are at $p < 0.001$.

3.3.3 Productivity

3.3.3.1 Organic Carbon

Organic carbon fluxes range from 2.2 to 8.9 mg/cm^{2}kyr, but substantial scatter within the data suggests that a composite record may be more representative of the regional variability (Figure 3.6). The data from the four cores examined were averaged (mean) within 5kyr bins to create one regional record (black line, Figure 3.6). Organic carbon fluxes are relatively low (less than 4 mg/cm^{2}kyr) before 180ka, but low resolution in this interval may alias higher frequency variability. From 180ka onwards, the composite record demonstrates ~25kyr cycles between relatively low organic carbon fluxes (4.3 mg/cm^{2}kyr) and relatively higher organic carbon fluxes (5.9 mg/cm^{2}kyr). The organic carbon flux peaks occur at 10, 35, 75, 100, 125, and 160ka. Maximum organic carbon fluxes (greater than 8 mg/cm^{2}kyr) occur just following the two glacial terminations, at 127ka and 9.5ka.

3.3.3.2 Opal

Fluxes of opal (biogenic silica), unlike organic carbon, are relatively consistent amongst the six different cores and show little to no temporal variability older than 50ka (Figure 3.6). Individual data hover between 5-15 mg/cm^{2}kyr throughout the greater portion of the record, with the compiled data (binned as in the organic carbon fluxes) averaging around 10-11mg/cm^{2}kyr. The amplitude of orbital scale variability is quite muted, but some of the features in the opal flux record do align with those of the organic carbon record. During the early last interglacial (120-130ka), several high opal flux values coincide with the slightly elevated organic carbon fluxes at that time. Opal fluxes increase from 110ka (8.6 mg/cm^{2}kyr) to local maxima at 80ka and 65ka (12.5-12.6 mg/cm^{2}kyr) before reaching a minimum at 50ka (7.9 mg/cm^{2}kyr). After 50ka, there is an upward trend in opal fluxes that

reaches a maximum (23.7mg/cm^{2}kyr) in the early Holocene ~8.9ka, approximately the top of the record. Overall, there appears to be a nearly exponential decay in opal flux from the most recent period (0-20ka, 22mg/cm^{2}kyr) to the oldest part of the record (200-250ka, 5.3mg/cm^{2}kyr).

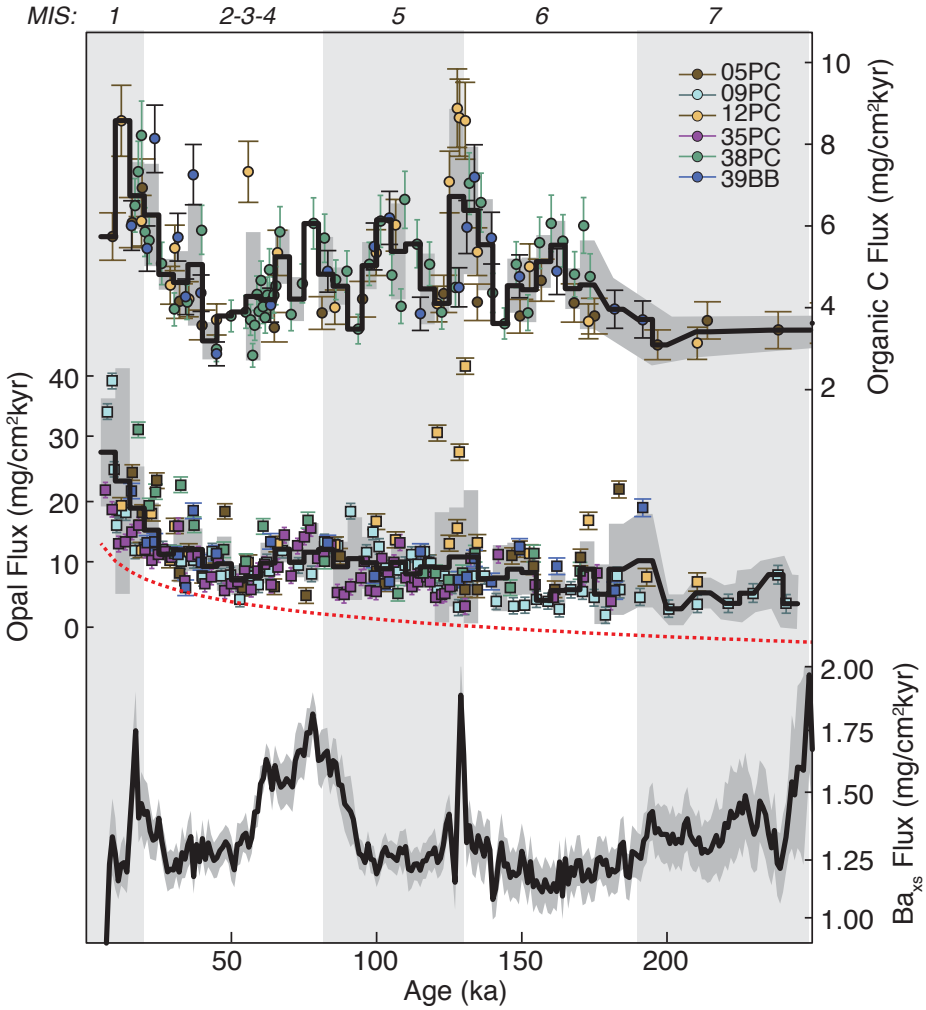

Figure 3.6. Comparison of paleo-productivity records from the Juan de Fuca Ridge: organic carbon fluxes, opal fluxes, and Ba_{xs} fluxes. Gray bars highlight interglacial periods, as identified by odd marine isotope stages (MIS). One opal datapoint greater than 40 mg/cm^{2}kyr is not shown (63 mg/cm^{2}kyr at 12.4ka).

3.3.3.3 Excess Barium

Excess barium (Ba_{xs}) fluxes show a much more consistent pattern amongst the six different cores, which have been averaged (mean) in 1kyr bins to produce a single regional Ba_{xs} stack (Figure 3.6). Background fluxes of Ba_{xs} are between 1.1 and 1.3 mg/cm^{2}kyr, and this relatively constant baseline is punctured by only four prominent high flux features. Three are productivity spikes at 249ka, 130ka and 17ka that occur during late deglaciation or early interglacial periods. The fourth feature is a broad productivity maximum that rises at 93ka, peaks at 78ka (1.8 mg/cm^{2}kyr), and returns to background levels by 56ka. This peak may be related to the much lower amplitude features in the organic carbon flux and opal flux records 65-80ka.

3.4. Discussion

3.4.1. Precipitation and preservation of authigenic uranium

In oxygen-rich seawater, hexavalent uranium forms a highly soluble carbonate species $[UO_2(CO_3)_3]^{4-}$ (Langmuir, 1978) that imparts conservative behavior such that dissolved uranium concentrations scale with salinity in the water column (Owens et al., 2011). Within oxygenated porewaters, dissolved uranium maintains relatively high concentrations, but if the oxygen pool within the sediment pile becomes depleted, e.g. by benthic respiration, soluble U(VI) reduces to insoluble U(IV) and precipitates as solid UO_2 (Anderson, 1982; Anderson et al., 1989a; Morford and Emerson, 1999). This uranium reduction requires exceptionally low oxygen concentrations, equivalent to those required for iron reduction, Fe(III) to Fe(II) (Barnes and Cochran, 1990; Crusius et al., 1996; Zheng et al., 2002a), or the even lower oxygen conditions of sulfate reduction, S(VI) to S(-II) (Klinkhammer and Palmer, 1991). Dissimilatory iron-reducing microorganisms such as *Clostridium sp., Desulfovibrio sp.,* and *Shewanella sp.* likely facilitate the formation of

reduced uranium precipitates by utilizing dissolved uranium as an electron acceptor to fuel their chemolithotropic growth (Francis et al., 1994; Ganesh et al., 1997; Lovley et al., 1991; Sani et al., 2004). Although abiotic surface-catalyzation of uranium reduction is also possible (Kochenov et al., 1977; Liger et al., 1999; Nakashima et al., 1984), the low temperature sedimentary conditions are suboptimal for kinetically relevant inorganic uranium reduction compared to biologically mediated uranium reduction (Anderson et al., 1989a, 1989b; Cochran et al., 1986; Lovley et al., 1991; Tribovillard et al., 2006). Once uranium reduction commences, a steep uranium concentration gradient forms in the porewater along which additional soluble U(VI) will diffuse from the water column to support continued precipitation of authigenic U (aU) in the low oxygen zone (Anderson, 1982; Anderson et al., 1989b; Barnes and Cochran, 1990; Klinkhammer and Palmer, 1991). This diffusion-dependent, but otherwise unlimited, uranium source can thus create sedimentary aU peaks substantially enriched over U concentrations typically found in biogenic or lithogenic phases.

The disparate records of aU concentration from the six different cores (Figure 3.3) most likely reflect the secondary effects of diagenesis on the preservation of aU in the sediment (Figure 3.7). While the reduction of U occurs slowly without biological mediation, the kinetics of aU oxidation from U(IV) back to soluble U(VI) appear to be quite fast (Anderson et al., 1989a; Cochran et al., 1986), creating the phenomenon known as "burndown" (Jung et al., 1997; Mangini et al., 2001). If oxygen returns after some transient hypoxic period of aU deposition, that oxygen will diffuse into the sediment, oxidize uranium, and mobilize it into porewaters (McManus et al., 2005). Redissolution of U into porewaters reverses the concentration gradient with the overlying bottom waters so that U diffuses upwards and escapes into the water column (Mangini et al., 2001; Zheng et al., 2002b). Fluxes of U out of recently oxidized sediments have been observed in seasonally

anoxic basins that experience cyclic aU deposition and reoxygenation (Anderson et al., 1989b; Cochran et al., 1986; Klinkhammer and Palmer, 1991; McManus et al., 2005; Zheng et al., 2002b). The loss of aU back to porewater may compromise sedimentary records of aU as a complete history of redox conditions (Mangini et al., 2001; McManus et al., 2005). If the aU is completely remobilized, its sedimentary record is eliminated entirely. For example, it is possible that aU precipitated in cores 05PC, 12PC, 38PC, and 39BB during MIS5, but subsequent reoxygenation of those sites obliterated the aU from their sedimentary records. Partial remobilization of aU may leave an aU record that does not extend as far in the sediment pile, as in 09PC relative to 35PC, and migration of U-rich porewater deeper in the sediment column can cause the precipitation of a secondary aU peak where the porewaters re-encounter reducing conditions (Mangini et al., 2001). This secondary peak may then stratigraphically pre-date the actual onset of reducing conditions (Jacobel et al., 2017; Mills et al., 2010). These combined diagenetic effects suggest that relict aU peaks found in sedimentary records may be skewed towards lower amplitude, shorter duration, and earlier timing than the reducing conditions existed (Morford et al., 2009).

The extent to which burndown will alter the sedimentary aU record depends on both the organic carbon content (Mangini et al., 2001) and the sedimentation rate (Elderfield, 1985). Respiration of organic carbon in sediment consumes pore water oxygen and thus inhibits its availability to remobilize aU. Because higher organic carbon contents contribute to maintaining low oxygen conditions in the sediment, more intense burndown of aU will occur in sediments with low organic carbon fluxes (Jung et al., 1997; Mangini et al., 2001). The Juan de Fuca cores, however, are all proximal to one another (<30km), and so variability in organic carbon delivery to the sediment is unlikely to explain the different degrees of burndown experienced amongst the six cores. Instead, they are subject to rates of

burndown that are most likely determined by their highly variable sedimentation rates (Costa et al., 2016).

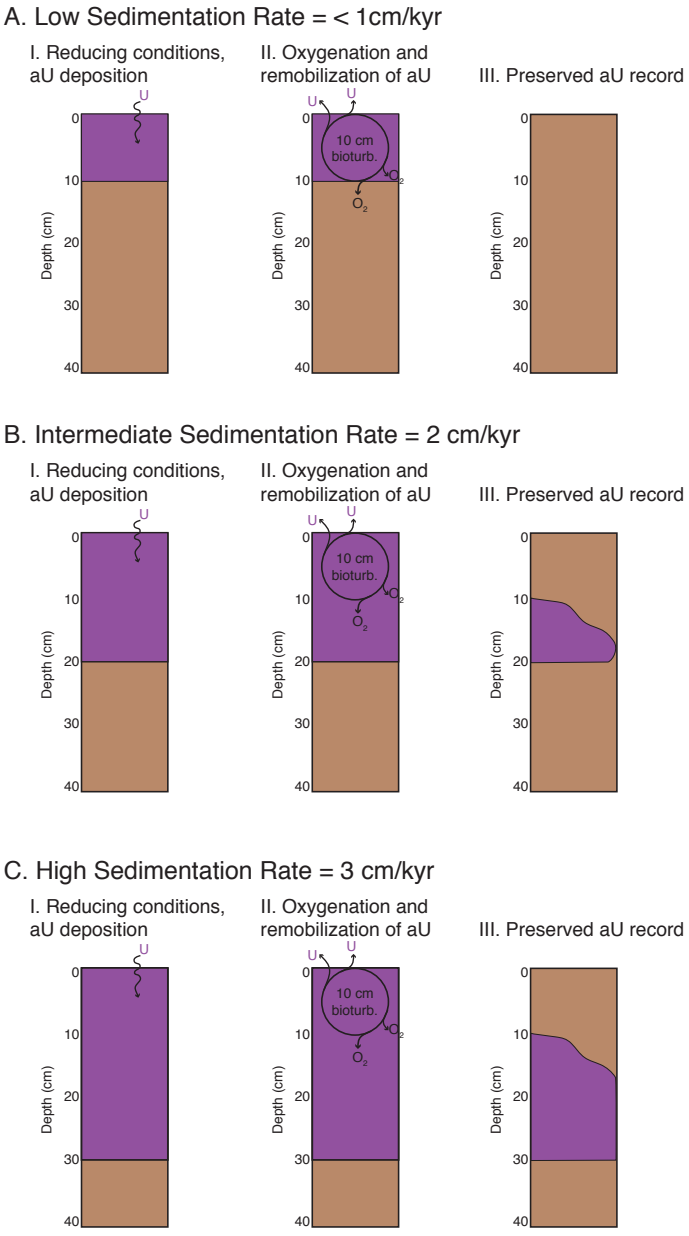

Figure 3.7. Effect of burndown on aU preservation in sediments with varying sedimentation rates. I. All cores experience 10kyr of reducing conditions under which aU precipitates in the sediment. II. When oxygen subsequently returns to the sediment, bioturbation assists oxygen penetration down to 10cm depth. In the presence of oxygen, aU remobilizes and diffuses out of the sediment. III. The preserved aU record depends on the sedimentation rate of the core. When sedimentation rates are low (A), no aU record may survive the re-oxygenation of the sediment pile. When sedimentation rates are higher (B and C), some aU is preserved in the sediment, but the record does not extend the full 10kyr duration of the reducing conditions.

Low-sedimentation-rate sites are susceptible to complete redissolution of aU because their sedimentary aU pile will be relatively thin (Figure 3.7A). After 10kyr of reducing conditions, a sediment core with 1cm/kyr sedimentation rate will only contain 10cm of sediment with elevated aU. When bottom waters reoxygenate, bioturbation may pump the oxygen-rich water through the mixed layer (10cm, in this example) and facilitate aU oxidation and diffusion out of the sediment (McManus et al., 2005; Morford et al., 2009; Shimmield and Price, 1986; Zheng et al., 2002b). When sedimentation rates are higher (Figure 3.7B and Figure 3.7C), some of the aU is buried deep enough to be protected from oxygen exposure, but the duration of the preserved aU record is still shorter (5kyr or 6.7kyr) than the actual reducing conditions persisted (10kyr). Previous studies have suggested that authigenic U preservation is compromised at sedimentation rates less than 2cm/kyr (Mangini et al., 2001), and indeed, substantial aU burial on the JdFR only seems to occur when sedimentation rates are higher than 2cm/kyr (Figure 3.3B). The proximity of the six cores suggests that any change in redox conditions should be coincidentally observed in all six cores, but only the two cores with high sedimentation rates (≥3cm/kyr) retain an aU signal during, e.g., MIS5. The older interglacial aU peak (MIS7) is only observed in 35PC, which maintains a sedimentation rate >2cm/kyr in these intervals while even 09PC does not have high enough sedimentation rates to retain aU. The anomalous glacial peak (MIS8), also in 35PC, may be an artifact of the turbidite at 272ka, which deposited 10s of centimeters of sediment nearly instantaneously and thus cut off the porewater exchange with the overlying water column. Overall, it is likely that all six cores experienced high aU deposition during interglacial periods, but subsequent reoxygenation combined with intense bioturbation (10-15cm, Costa et al., 2017b) removed the aU records from the slow-accumulating cores (05PC, 12PC, 38PC, 39BB). Thus, while the presence of aU is a good

indicator for low-oxygen conditions, the absence of aU does not necessarily equate with persistent high-oxygen conditions.

3.4.2 Other trace metal (Mn, Ni, Zn, V) evidence for redox changes over time

While aU can provide an excellent redox history, sedimentation rates across much of the ocean, and particularly in the Pacific, fall below the 2cm/kyr threshold for diagenetic resilience. In these regions, other redox-sensitive metals can be combined with aU to constrain the variability in sedimentary oxygen concentrations over time. We investigate the utility of Mn, Zn, Ni, and V, all of which can be analyzed by high-resolution core-scanning XRF, as candidates for fast, accessible, and low-cost redox indicators in the near ridge sedimentary environment. Detailed trace metal behavior in sediments has been previously reviewed (e.g., Morford and Emerson, 1999; Schaller et al., 2000; Tribovillard et al., 2006; Morford et al., 2009; Mills et al., 2010), so only a synopsis of the relevant elements is included here.

3.4.2.1 Manganese

Mn is a major component of hydrothermal discharge, and most hydrothermal manganese in a plume is present in the dissolved form: >75% near the vent and ~50% in the plume on the EPR (Fitzsimmons et al., 2017) and generally >50% on the JdFR (Feely et al., 1994; Seyfried et al., 2003; Zheng et al., 2017). Oxidation of Mn occurs slowly via microbial catalyzation (Cowen et al., 1986; Dick et al., 2009; Tebo et al., 2004), and hydrothermal Mn is generally deposited to the underlying sediments as oxy-hydroxide particles rather than as sulfides (Von Damm et al., 1998, 1985). Under changing redox conditions, sedimentary Mn responds in stark contrast to U. Mn solubility increases when it is reduced from Mn(IV) to Mn(II) (Froelich et al., 1979), so that it will mobilize out of

sediment at the same time that aU is precipitating (Burdige and Gieskes, 1983; Lynn and Bonatti, 1965). Mn(II) does not substantially complex with organic matter or sulfides (Huerta-Diaz and Morse, 1992; Middelburg et al., 1987; Tribovillard et al., 2006) and only marginally reacts with carbonate (Boyle, 1983; Pedersen and Price, 1982). Sediments under reducing, noneuxinic conditions easily become depleted in Mn as it freely diffuses upward and escapes to the water column (e.g., Scholz et al., 2013; Shimmield and Price, 1986). Alternatively, when the oxygen pool within the sediment pile is high, particulate Mn oxy-hydroxides will be retained with the sediment while aU is mobilizing out of the sediment. Thus, redox driven diagenesis should result in anti-correlated Mn and aU profiles in sedimentary records, and coupling of these two redox indicators is a strategy often employed in pelagic sediment in which aU records are suspected to be influenced by preservation artifacts (e.g., Mangini et al., 2001; Morford et al., 2009).

The contrasting behavior of Mn and aU is apparent on the Juan de Fuca Ridge (Figure 3.4). Where aU concentrations are high (last interglacial, MIS5), Mn_{xs} fluxes are at their lowest (less than 4 mg/cm^{2}kyr). Where aU concentrations are low (glacial periods, MIS2-4 and MIS6), Mn_{xs} fluxes are high, greater than 5 mg/cm^{2}kyr and spiking at as much as 25 mg/cm^{2}kyr. These trends in aU and Mn_{xs} fluxes are demonstrated by the extreme division (anti-correlation) between aU and Mn_{xs} fluxes (Figure 3.5). Lower than average burial of hydrothermal Mn during interglacial periods suggests irreversible loss of Mn through diffusion back to the water column under reducing conditions. Excess burial during glacial periods may indicate precipitation of dissolved Mn out of seawater, possible due to the greater reservoir of dissolved hydrothermal Mn than other dissolved hydrothermal metals (Butterfield et al., 1997; Massoth et al., 1994). We therefore interpret high Mn_{xs} fluxes as strong evidence for oxidizing conditions.

3.4.2.2 Nickel

In the typical pelagic sediments of the abyssal ocean, sedimentary Ni concentrations are generally low (20ppm in upper continental crust, Taylor and McClennan, 1995) and often not reported (or perhaps, not analyzed). Ni is not particularly soluble, and it is primarily sourced from deposition of lithogenic material, with additional contributions from organic matter in regions like continental margins with high organic fluxes (Calvert and Pedersen, 1993; Westerlund et al., 1986). In the near-ridge environment, sedimentary Ni concentrations are elevated due to scavenging of Ni from seawater by Fe oxyhydroxides (Dunk and Mills, 2006; Ford et al., 1999) and/or Mn oxyhydroxides (Kuhn et al., 2000; Metz et al., 1988). Increasing particulate Ni concentrations with increasing distance from the source vent are consistent with a hydrogenous rather than hydrothermal source of Ni (Dymond, 1981; Metz et al., 1988). This affiliation with hydrothermal particles increases the sedimentary inventory of Ni, which can subsequently be redistributed as a result of changing redox conditions.

Ni only has one prevalent oxidation state, Ni(II), and so its behavior in response to changing redox conditions is not geochemically inherent. Empirical evidence suggests that Ni remobilization may be largely controlled by co-precipitation and adsorption processes associated with the redox cycling of Mn (Dunk and Mills, 2006; Elderfield, 1985; Muñoz et al., 2012; Tribovillard et al., 2006). This affiliation between Ni and Mn is also observed on the Juan de Fuca Ridge (Figures 3.4 and 3.5): high Ni_{xs} fluxes occur simultaneously with high Mn_{xs} fluxes during the last two glacial periods (MIS2-4, MIS6), and low Ni_{xs} fluxes (below 100 $\mu g/cm^2kyr$) coincide with low Mn_{xs} fluxes (and high aU) during the last interglacial (MIS5). This correspondence suggests that Ni is predominantly associated with Mn oxides (as on the East Pacific Rise, Dunk and Mills, 2006), and that when Mn

remobilizes in the sediment under reducing conditions, so does Ni (Feely et al., 1994; Santos-Echeandia et al., 2009; Shaw et al., 1990). The correlation between Ni and Mn appears weaker in older periods, particularly in MIS7 where low Mn_{xs} fluxes seem to coincide with slightly elevated Ni_{xs} fluxes and elevated aU fluxes. This behavior may indicate that complexation with organic matter (Calvert and Pedersen, 1993; Elderfield, 1981; Olson et al., 2017; Westerlund et al., 1986) or incorporation into relatively insoluble sulfides (Dyrssen and Kremling, 1990; Huerta-Diaz and Morse, 1992) may influence the redox distribution of Ni independently of Mn. However, the dominant redox mobilization of Ni appears to be in affiliation with Mn, and so we cautiously interpret high Ni_{xs} fluxes as evidence for oxidizing conditions.

3.4.2.3 Zinc

Unlike Mn or Ni, the primary source of Zn in the near ridge environment is hydrothermal sulfides, which precipitate in the buoyant plume shortly after being emitted from the vent (Edmonds and German, 2004; Feely et al., 1994; Findlay et al., 2015; German et al., 1991). Close to the vent, 80-90% of the emitted Zn is precipitated (German et al., 2002), primarily into sphalerite rather than pyrite or chalcopyrite (Findlay et al., 2015), but Fe may dope the sphalerite or circumprecipitate as an iron sulfide around the existing zinc sulfides (Findlay et al., 2015; Koski et al., 1994; Scott, 1983). The remaining 10-20% of emitted hydrothermal Zn may be scavenged by iron oxyhydroxides (German et al., 2002, 1991; Trocine and Trefry, 1988), stabilized as a dissolved species by chloro-complexation (Seewald and Seyfried, 1990; Trefry et al., 1994; Von Damm and Bischoff, 1987), or complexed with organic matter (Little et al., 2015). Dissolved Zn has been observed over 4000km away from its hydrothermal origin (Roshan et al., 2016), but particulate Zn/Fe

ratios in the plume decrease as the plume ages, likely due to Zn redissolving or settling out faster than Fe (Feely et al., 1994; Roshan et al., 2016; Trocine and Trefry, 1988).

Once deposited in the sediment, Zn is likely to be most mobile under oxidizing conditions that are corrosive to hydrothermal sulfides. Like Ni, Zn only has one oxidation state, Zn(II), and its redox sensitivity is largely controlled by its chemical environment. When sulfides are oxidized to sulfates, Zn will be released to porewaters where it can migrate out of the sediment, thus creating low Zn concentrations under high oxygen conditions. This result is similar to that observed in aU, and indeed Zn_{xs} fluxes show the same basic patterns as aU fluxes (r^2=0.47, Figures 3.4 and 3.5). High Zn_{xs} fluxes (greater than 120 μg/cm^{2}kyr) occur during the last interglacial periods (MIS5), with several cores recording a peak at 110ka coincident with the aU peak. At the same time, there appears to be a component of the Zn_{xs} fluxes that is correlated with Mn_{xs} fluxes, despite the poor overall correlation (r^2=0.17). This Mn-driven redox behavior is particularly evident in 09PC in the last 60kyr, during which Zn_{xs} fluxes remain relatively high (>80 μg/cm^{2}kyr) despite aU fluxes returning to background levels. This behavior may reflect limited diffusion of dissolved Zn in porewaters, such that the mobilized Zn during high oxygen periods may not have been able to escape the sediment pile at high accumulation rate sites (like 09PC). Alternatively, if sphalerite is only a small proportion of the total sulfide population, then Zn_{xs} fluxes may be influenced by sulfide capture (Huerta-Diaz and Morse, 1992), in which mobile Zn within porewaters can be pyritized by free sulfide ions released from other sulfide species. Overall the correlation between aU and Zn_{xs} fluxes suggests a primary sensitivity to reducing conditions, and so we tentatively interpret high Zn_{xs} fluxes as evidence for reducing conditions.

3.4.2.4 Vanadium

V, like Ni, is a hydrogenous metal that is scavenged from the water column by hydrothermal particulates, primarily iron oxyhydroxides (Morford and Emerson, 1999; Rudnicki and Elderfield, 1993; Schaller et al., 2000; Trocine and Trefry, 1988). Because seawater V concentrations are relatively low, sedimentary V concentrations due to scavenging tend to have low signal to noise ratios that can be difficult to identify and interpret. In the near ridge environment, high fluxes of hydrothermal iron may supply sufficient V that subsequent redox redistribution within the sedimentary pile can be distinguished. V becomes less soluble when it is reduced from V(V) to V(IV) (Calvert and Pedersen, 1993; Morford and Emerson, 1999), at which point it behaves like U (also IV in its reduced state), so that high sedimentary V_{xs} fluxes would be associated with low oxygen conditions. Furthermore, the redox threshold of V reduction is thought to be lower than that of Fe or Mn but higher than that of U (Morford and Emerson, 1999; Shaw et al., 1990), making it, theoretically, a sensitive indicator for the timing of redox transitions from aU precipitation to Mn retention. Indeed, on the Juan de Fuca Ridge, V_{xs} fluxes show the same basic patterns as Zn_{xs} and aU fluxes, with high V_{xs} fluxes during MIS5 and MIS7 coincident with peaks in aU (Figure 3.4).

However, sedimentary V is often confounded by other processes that can affect both its delivery to the sediment and its response to changes in redox conditions. These complications are evident in the component of V_{xs} fluxes, mostly in 09PC, that is correlated with Mn_{xs} fluxes (Figure 3.5). This component may reflect a susceptibility of V to Mn precipitation and dissolution cycles (Mills et al., 2010), such that V burial may actually be better preserved in oxic sediments than in anoxic sediments (Dunk and Mills, 2006). Furthermore, the efficiency of V scavenging from seawater is inversely dependent on phosphate concentrations (Edmonds and German, 2004; Feely et al., 1994), with which V

competes for adsorption sites on iron oxyhydroxide particles (Dunk and Mills, 2006). Because phosphate is more readily scavenged than vanadate, higher phosphate concentrations may result in lower particulate V/Fe within hydrothermal plumes (Edmonds and German, 2004; Feely et al., 1994). A consequence of this exchange is that sedimentary V_{xs} fluxes may be recording changes in deep water nutrient concentrations rather than sediment redox variability. These factors all complicate the straightforward interpretation of V as a redox proxy, but its relationship with aU suggests that there is a redox signal also playing a role in V_{xs} fluxes. We therefore tentatively include V_{xs} fluxes in our redox reconstructions, with high V_{xs} fluxes as possible evidence for reducing conditions.

3.4.3 Relative Redox Potential (RRP) over the past 250ka

Because redox reactions proceed too slowly to achieve thermodynamic equilibrium (Balzer, 1982; Lindberg and Runnells, 1984; Postma, 1993), it is nearly impossible to reconstruct a precise paleo-redox history in absolute oxygen concentrations. Instead, we combine the information from multiple redox-sensitive elements (Mn, Ni, Zn, V, aU) to create a probabilistic relative redox potential (RRP) on an arbitrary scale. This conservative approach, outlined below, accommodates the many uncertainties associated with paleo-redox reconstructions. For example, the mineralogy and complexation of each element, which can affect the desired redox state and the kinetics of reaction, are poorly constrained, and mineralogical analyses on existing sediment may not be able to diagnose initial compositions or the formation of diagenetic ghost phases (like pyrite) that may have subsequently redissolved (Yarincik et al., 2000). We focus this calculation on the last 250ka, for which aU variability is present. As previously mentioned (Section 3.4.1), the absence of aU (i.e., older than 250ka) may be a diagenetic artifact and should not be interpreted as reflecting continuous high oxygen conditions.

Relative Redox Potentials (RRPs) for each core were calculated by converting Mn_{xs}, Ni_{xs}, V_{xs}, Zn_{xs} and aU fluxes into binary presence/absence designations, weighting each element by the strength and direction of its redox indication, summing the five elements, and then averaging the data in 5kyr bins. Binary fluxes were assigned as follows: 0 for any flux below the mean for that element in that core, and 1 for any flux above that mean. To create an arbitrary scale in which positive values are more oxidizing and negative values are more reducing, the following weights were employed: Mn = 2 (strong evidence for high oxygen conditions), Ni = 1 (weak evidence for high oxygen conditions), Zn = -1 (weak evidence for low oxygen conditions), V = -1 (weak evidence for low oxygen conditions) and aU = -2 (strong evidence for low oxygen conditions). The goal is to weight the elemental evidence of which we are more confident in a redox interpretation (aU and Mn) over those that are more tentative (Zn, V, Ni). When summed within each core, the elements create a quantized RRP with possible values limited to integers between -4 and 3 (Figure 3.8A). The six cores were then averaged (mean) within each 5kyr bin to generate a single (unquantized) regional RRP (Figure 3.8B). The RRP results are not sensitive to the inclusion of any one specific element (Supplementary Figure 3.3), and they are robust even in the low sedimentation rate cores with poor preservation of aU (Supplementary Figure 3.4). The results are further corroborated by RRPs calculated with metal/Mn ratios (Supplementary Figure 3.5) or metal concentrations on a carbonate free basis (Supplementary Figures 3.6 and 3.7).

This analysis demonstrates that the metal depositional histories from all six cores are all consistent with low sedimentary oxygen conditions during interglacial periods, particularly during 100-120ka (MIS5) but also 200-250ka (MIS7). The records do not extend sufficiently into the Holocene to be conclusive. Sedimentary oxygen levels are relatively high during the last glacial period as well during MIS6. In fact, sedimentary oxygen levels

may peak during peak glacial conditions, ~135-140ka and 20-25ka. This finding of higher oxygen conditions during glacial periods contrasts with previous studies that have found evidence for lower oxygen concentrations during glacial periods in the Pacific (Jacobel et al., 2017; Korff et al., 2016; Mills et al., 2010). However, there are three different processes that can account for low sedimentary oxygen concentrations: 1) bottom water oxygen 2) organic matter deposition and 3) sulfide deposition. In the next section, we will explore the evidence for and against each of these as drivers of the redox history of the sediment on the JdFR.

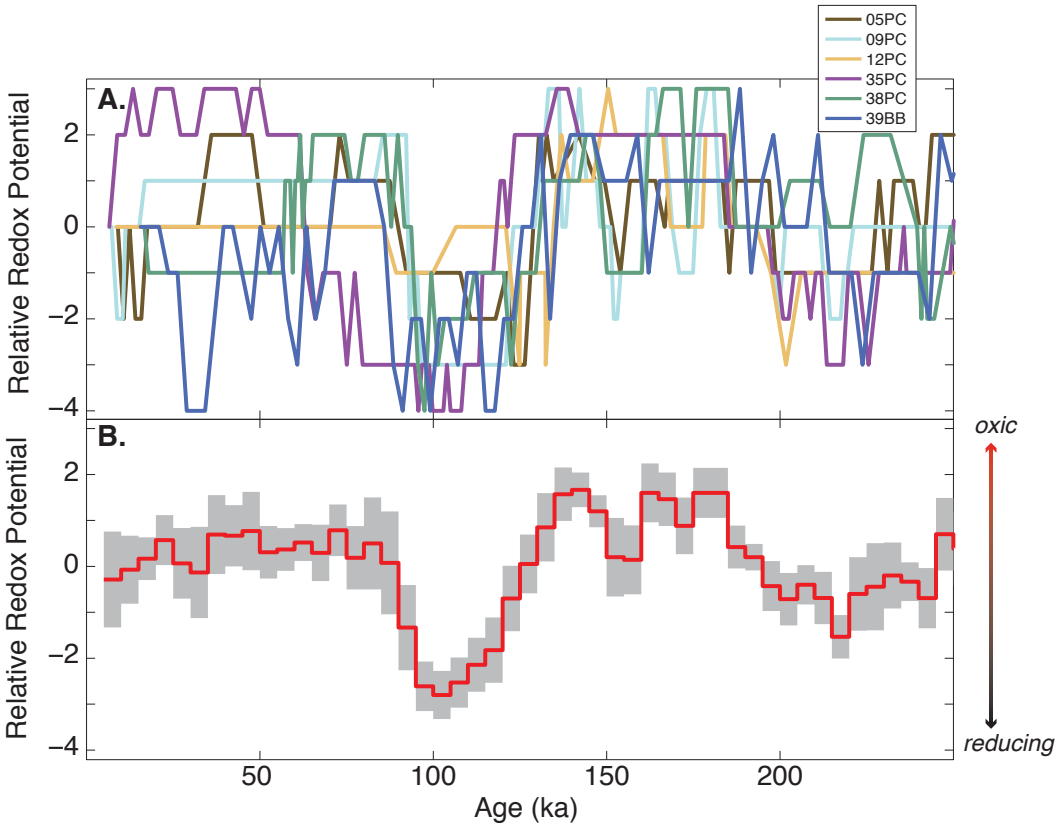

Figure 3.8. Relative redox potentials (RRPs) for individual cores (A.) and the regional mean (B.) on the Juan de Fuca Ridge. RRPs are calculated by summing presence/absence records of each excess metal flux weighted by its relative redox indication (Mn=2, Ni=1, Zn=-1, V=-1, and U=-2). Individual records were calculated on a point-by-point basis by interpolating the excess metal fluxes onto the depths of the aU measurements. Individual records (A.) were averaged (mean) within 5kyr bins to generate the regional mean signal in B. Each 5kyr bin is constrained by 11 datapoints, on average, and up to 45 datapoints. Positive values indicate more oxygen rich conditions.

3.4.4 Mechanisms for changing sediment oxygen concentrations over time

3.4.4.1 Bottom water oxygen concentrations

In modern Pacific overturning circulation, the northernmost extent of North Pacific Deep Water (NPDW) blankets the Juan de Fuca Ridge before it retroflects and travels southward at depths of 2.5-3.5km (e.g., Schmitz, Jr., 1995; Macdonald et al., 2009). Last ventilated in the Southern Ocean, this old and corrosive water mass has low oxygen concentrations due to the cumulative effect of respiration along its flowpath (Figure 3.1) (Key et al., 2002; Kroopnick, 1985). Multiple lines of evidence, including sedimentological laminations, foraminiferal assemblages, magnetite dissolution, manganese nodule growth, trace metal deposition, and $\delta^{15}N$ diagenesis, have demonstrated that oxygen concentrations in Pacific deep waters (>2km) were lower during the last glacial period (Figure 3.8) (e.g., Bradtmiller et al., 2010; Galbraith et al., 2007; Galbraith and Jaccard, 2015; Jaccard and Galbraith, 2012; Jacobel et al., 2017; Korff et al., 2016; Mangini et al., 1990; Mills et al., 2010; Sigman and Boyle, 2000, and references there in). Glacial oxygen-depletion in deep waters was likely a consequence of increased stratification in the Southern Ocean (Anderson et al., 2009; Burke and Robinson, 2012; Francois et al., 1997; Sigman and Boyle, 2000) as well as increased storage of respired carbon at depth (Anderson et al., 2014; Bradtmiller et al., 2010; Jaccard et al., 2016, 2009; Jacobel et al., 2017; Martinez-Garcia et al., 2014; Matsumoto et al., 2002). Therefore, any oxygen record capturing changes in NPDW would be expected to show lower oxygen concentrations during glacial periods.

The same would not necessarily be true for overlying intermediate waters (1-2km). During the last glacial period, the upper ocean generally experienced better ventilation and higher oxygen concentrations than it does in interglacial periods (e.g., Duplessy et al., 1988; Jaccard and Galbraith, 2012; Poggemann et al., 2017; Sigman and Boyle, 2000; Stott et al.,

2000). In the North Pacific, this water mass would be North Pacific Intermediate Water (NPIW), formed today in the Okhotsk Sea through cabbeling of the saline Kuroshio and the cold Oyashio current (You, 2003), an extrapolation of dense Okhotsk Sea Mode Water formed in the winter as a result of brine rejection (Talley, 1993). NPIW can easily be identified as a salinity minimum in the North Pacific (Keigwin, 1998), and this relatively low density (σ = 26.8) and steep halocline is what prevents true deep water formation and restricts NPIW to the upper water column (Emile-Geay et al., 2003; Warren, 1983). Oxygen concentrations in NPIW start out high near the formation zone but they are expended almost entirely en route to the California Margin (Bray, 1988). High intermediate water oxygen concentrations recorded on the California Margin during the last glacial period (Keigwin and Jones, 1990; Kennett and Ingram, 1995; Nameroff et al., 2004; Stott et al., 2000) are therefore a good indication that the NPIW, overall, was better ventilated.

Higher oxygen concentrations in NPIW could be generated if its glacial formation was more vigorous and/or more voluminous, both of which would aid oxygen retention as far to the east as the California Margin. Stronger NPIW formation has been modeled as a consequence of weakened AMOC (Max et al., 2017; Menviel et al., 2017; Okazaki et al., 2010), particularly during the last glacial termination. For example, during Heinrich Stadial 1 (17.5ka), a near shutdown of AMOC (McManus et al., 2004) may have caused a pulse of NPIW formation that could account for transient ventilation peaks at that time (Mikolajewicz et al., 1997; Okazaki et al., 2010; Rae et al., 2014). Expectations for the production of NPIW during the glacial period itself would be much smaller, however, since the glacial-interglacial difference in AMOC vigor is relatively small compared to the changes during deglaciations (Böhm et al., 2015; Gherardi et al., 2009; McManus et al., 2004). Alternatively, enhanced NPIW formation during the glacial period might be a result

of closure of the Bering Strait and new sources of NPIW formation in the Bering Sea (Horikawa et al., 2010; Knudson and Ravelo, 2015; Max et al., 2017).

Regardless of the mechanism driving NPIW formation, proxy evidence for the glacial expansion of a younger, better ventilated, lower nutrient water mass at intermediate water depths has been found not just near California but also elsewhere in the North Pacific. Glacial oxygenation is fairly well documented above 1.5km (Jaccard and Galbraith, 2012), but the influence of NPIW below 2km is still debated. Some proxy records propose that NPIW could not have penetrated below 2km (Herguera et al., 2010; Keigwin, 1998; Matsumoto et al., 2002; Stott et al., 2000), while others have interpreted glacial NPIW signatures at 2.4km depth (Gorbarenko, 1996), 2.6km depth (Duplessy et al., 1988), and even 3.6km during the deglaciation (Rae et al., 2014). Models have suggested that NPIW export may peak at 1.4km (Menviel et al., 2017) but during deglaciation it may reach 2km (Menviel et al., 2017) or 2.7km (Okazaki et al., 2010). Similar patterns of manganese nodule growth at 1.55km and 4.83km water depth (Mangini et al., 1990) indicate similar changes in oxygen concentrations throughout the water column, and they suggest that any NPIW influence is limited to just the upper 1.5km. As yet there is little proxy evidence or model simulations to support glacial NPIW reaching depths of 2.6-2.8km, the depths of the Juan de Fuca Ridge cores, although data from this region are altogether sparse (Jaccard and Galbraith, 2012, see their Figure 2). Glacial ventilation by NPIW would be consistent with increased oxygen concentrations reconstructed on the Juan de Fuca ridge in this study, but future work generating transects of ventilation from 2 to 3km depth would be required to provide better constraints on the lower depth-limit of NPIW influence in the glacial North Pacific.

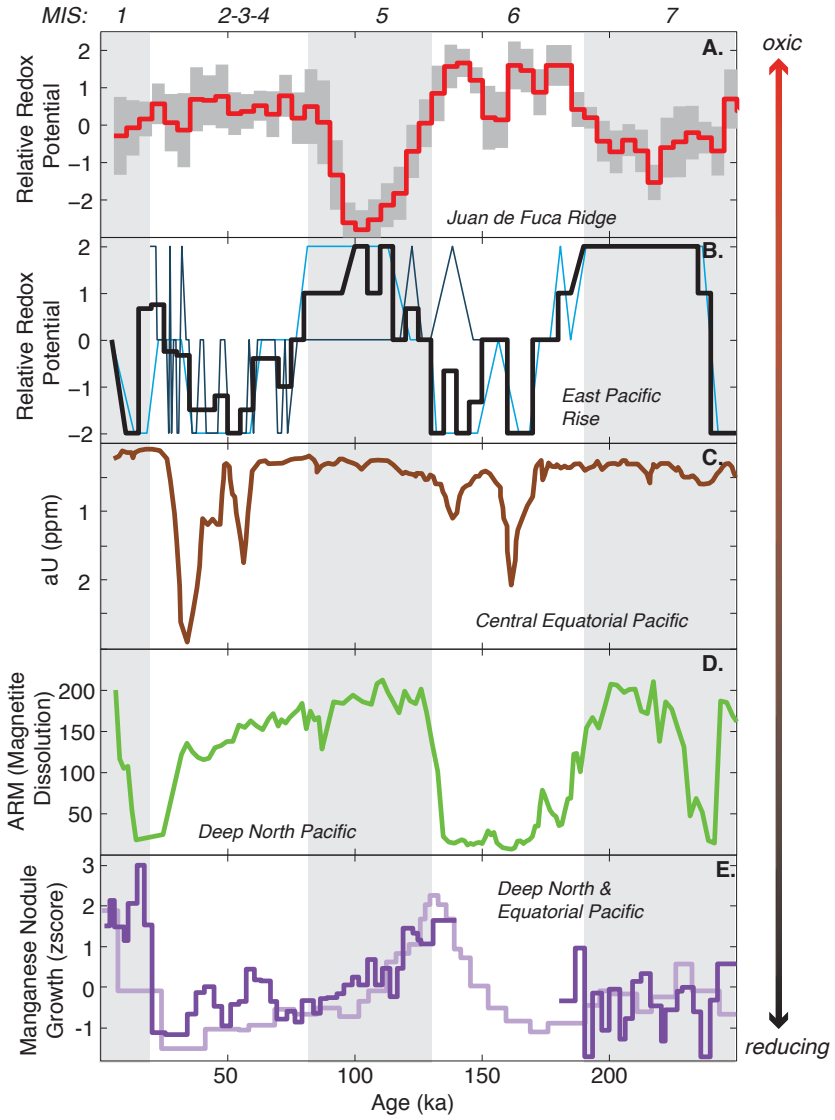

Figure 3.9. Comparison of paleo-redox variability on the Juan de Fuca Ridge with other published redox records covering the last 250kyr in the Pacific. All records are oriented such that up indicates more oxygen rich conditions. A. RRP for the Juan de Fuca Ridge, as in Figure 8. B. RRP for the East Pacific Rise, calculated using aU, Mn_{xs}, and V_{xs} fluxes from GS7202-35 (light blue) (Mills et al., 2010) and Y-71-7-53P (dark blue) (Lund et al., 2016; Schaller et al., 2000) as described in Section 3.4.4.1. Thick black line is the regional mean RRP of the two cores averaged (mean) within 5kyr bins. C. aU from Central Equatorial Pacific, ML1208-17PC (Jacobel et al., 2017). Metal concentrations in this carbonate-rich sediment core are too low to calculate RRPs. D. Anhysteretic remanent magnetization (ARM) from deep core SO202-1-39-3 (Korff et al., 2016). Low ARM indicates magnetite dissolution as a result of reducing conditions. E. Manganese nodule growth rates from 1550m (light purple) and 4830m (dark purple) (Mangini et al., 1990), normalized (zscore) to display on the same y-axis. Nodule growth depends on the flux of MnO_2, and so higher growth rates indicate periods of higher oxygen concentrations in the water column. Discontinuation of nodule growth 160-190ka at the deeper site indicates particularly low oxygen concentrations compared to the shallower site during MIS6.

3.4.4.2 Organic matter delivery to the sediment

Organic matter is one of the strongest reducing agents available in the ocean. The aerobic respiration of organic matter can rapidly consume oxygen levels to the point of generating suboxic conditions and aU precipitation within the surface sediments (Anderson, 1982). Remineralization below high productivity regions can create oxygen deficient zones in the underlying water column (Key et al., 2002), and high fluxes of organic matter to the sediment can drive oxygen deficiency down into the sedimentary record. The extensive productivity peak during the Bolling-Allerod (~15ka) in the North Pacific (Kohfeld and Chase, 2011) created locally hypoxic conditions observed in aU peaks (Lam et al., 2013), benthic foraminiferal assemblages (Praetorius et al., 2015), and sediment laminations (Davies et al., 2011). Besides this deglacial productivity peak, much of the North Pacific is characterized by lower productivity during glacial than during interglacial periods (e.g., Jaccard et al., 2005; Galbraith et al., 2007; Kohfeld and Chase, 2011; Costa et al., 2017). Biological growth during glacial periods may have been inhibited by both light limitation and prevention of upward mixing of deep nutrients due to enhanced surface stratification (Brunelle et al., 2010, 2007; Kienast et al., 2004; Ren et al., 2015; Sigman et al., 2004). If productivity was low during glacial periods and high during interglacial periods on the Juan de Fuca Ridge, then the cycles in organic fluxes to the sediment could generate the observed variability in RRP.

However, the three productivity proxies measured in this study each reconstructs a different productivity history, none of which would be consistent with the calculated RRP (Figure 3.6). To attribute the reducing conditions in MIS5 to organic carbon fluxes, a particularly high flux of organic carbon throughout the interglacial period would be expected. Instead, the organic carbon, opal, and Ba_{xs} fluxes record only transient features that suggest high productivity peaks during late deglaciation and early interglacial

conditions. Other features in the productivity records, like the ~25kyr cycles in organic carbon fluxes or the broad peak ~75ka in Ba_{xs} fluxes, do not translate into similar features in the RRP. Overall, there appears to be very little evidence to definitively link the RRP to variability in organic matter.

Admittedly, this conclusion is dependent on taking the paleo-productivity proxies at face value, while the disagreement between them may instead indicate that they are imperfect records. The generally corrosive bottom waters combined with hydrothermal alteration of water column and sediment properties may create an environment simultaneously but variably harmful to the preservation of organic matter, opal, and Ba_{xs}. The nearly exponential decay in opal flux from the most recent period (0-20ka, 22mg/cm^{2}kyr) to the oldest part of the record (200-250ka, 5.3mg/cm^{2}kyr) suggests that opal, rather than being more robust than organic carbon to diagenesis, is in fact much more susceptible to post-depositional redissolution. Barite ($BaSO_4$) may be sensitive to changes in oxygen concentrations, in that intensive sulfate-reducing conditions, with substantial depletion of dissolved sulfate in pore waters, would reduce the preservation of Ba_{xs} and its utility as a productivity proxy (Torres et al., 1996; van Os et al., 1991). Within these limitations, however, there does not appear to be any conclusive evidence indicating that fluxes of organic matter have had a large influence on redox conditions. Future work using paleo-productivity proxies that are less susceptible to preservation issues, like Pa/Th, may help to provide more robust support for this conclusion.

3.4.4.3 Sulfide deposition due to hydrothermal activity

Instead of organic matter, another source of electron donors near mid-ocean ridges may be hydrothermal sulfides (Mills et al., 2010). Sediments near hydrothermal vents often contain concentrated aU deposits (>10ppm) (Mills et al., 1993, 1994; Mills and Dunk, 2010;

Schaller et al., 2000; Shimmield and Price, 1988) that have been ascribed to 1) deposition and subsequent oxidation of hydrothermal sulfides and/or 2) scavenging of U from seawater by settling hydrothermal particles. Elevated U/Fe ratios (~4 ppm/wt%) have been observed in suspended particles up to 200m from the hydrothermal vents on the EPR (German et al., 2002) but they rapidly decline to negligible U enrichment (U/Fe ≤ 0.02ppm/wt%) by 1.2km from the ridge (Edmonds and German, 2004; German et al., 1991). Thus scavenging of U from seawater is not likely to be an important U delivery mechanism to sediment on the ridge flanks, and elevated U concentrations in sedimentary records (Metz et al., 1988; Mills et al., 1994; Sani et al., 2004; Shimmield and Price, 1988) must be generated by some in-situ process. Oxidation of sulfide minerals to soluble sulfates may be coupled to uranium reduction, in which U(VI) acts as the electron acceptor (Klinkhammer and Palmer, 1991; Langmuir, 1978; Wersin et al., 1994). Alternatively, oxidation of sulfide minerals may rapidly consume existing oxygen such that the benthic microbial assemblage shifts towards anaerobic microbes, including those that reduce uranium (see Section 3.4.1), so that sulfide oxidation and uranium reduction occur in rapid succession rather than coincidentally. The possible coupling between U and sulfide would produce a causal relationship between increased hydrothermal activity and more reducing conditions in the sediment.

Extensive study of hydrothermal deposits on the East Pacific Rise supports the hypothesis that the supply of hydrothermal sulfides is a major control on redox conditions in the sediment (Dunk and Mills, 2006; Mills et al., 2010; Mills and Dunk, 2010). If this is also the case on the Juan de Fuca Ridge, then interglacial reducing conditions may be a result of relatively higher hydrothermal activity at that time. Reconstructions based on hydrothermal Fe fluxes indicate high overall hydrothermal deposition during the last interglacial period, with two elevated peaks at 83ka and 129ka (Costa et al., 2017c). This pattern is broadly consistent with the RRP showing lower sedimentary oxygen

concentrations during the last interglacial period (Figure 3.8). Although the RRP does not capture the millennial scale peaks in hydrothermal activity, this may be an artifact of the RRP compilation that smooths the records over 5kyr bins. Alternatively, sulfides supplied intermittently by hydrothermal solutions may drive reducing conditions in the sediments over much longer sustained periods, especially when bioturbation rates are high. The influence of sulfides on the RRP is further corroborated by high Zn_{xs} fluxes during the last interglacial period, since the main carrier phase of Zn is indeed sulfides (Section 3.4.4.3). Redox reactions proceed slowly, so a small fraction of sulfides may oxidize and trigger aU precipitation while a large fraction of sulfides (e.g., Zn-sulfides) remain unreacted. If sulfide deposition is indeed an important influence on redox conditions, then it may imply that metal depositional environments are the most reducing at the same time that metal inputs from hydrothermal activity are the highest. This conjunction could have the potential effect of moderating metal burial such that hydrothermal deposition reconstructed from redox-sensitive metals may be underestimated.

5. Conclusions

Sedimentary concentrations of trace metals (Mn, Ni, Zn, V) and authigenic U (aU) were used to reconstruct redox conditions over the past 250ka on the Juan de Fuca Ridge. Mn and Ni are indicators for high sedimentary oxygen concentrations, while Zn, V, and aU are indicators for low sedimentary oxygen concentrations. In contrast to previous studies from across the North Pacific at other depths and locations, sediment redox conditions were relatively oxygen rich on the Juan de Fuca Ridge during glacial periods compared to interglacial periods. We do not find strong evidence to attribute the low sediment oxygen conditions to an enhanced local organic carbon flux to the sediments during interglacial periods, although each of the three paleo-productivity proxies may be compromised by poor

preservation. Alternatively, higher oxygen concentrations on the Juan de Fuca Ridge may result from better ventilation during glacial periods, possibly due to enhanced North Pacific Intermediate Water (NPIW) formation, although there is as yet little evidence that NPIW can penetrate so deep in the water column. Finally, increased delivery and oxidation of hydrothermal sulfides from the nearby ridge may have created locally low sedimentary oxygen conditions during interglacial periods as a result of enhanced hydrothermal activity. If sulfides are indeed the dominant influence on the sediment redox reconstruction on the Juan de Fuca Ridge, then changes in sedimentary oxygen concentrations will be independent of any changes that may be occurring in bottom water oxygen concentrations.

3.6. Data Archiving

All data are archived at the National Oceanic and Atmospheric Administration National Centers for Environmental Information (NCEI) database.

3.7. Supplementary Material

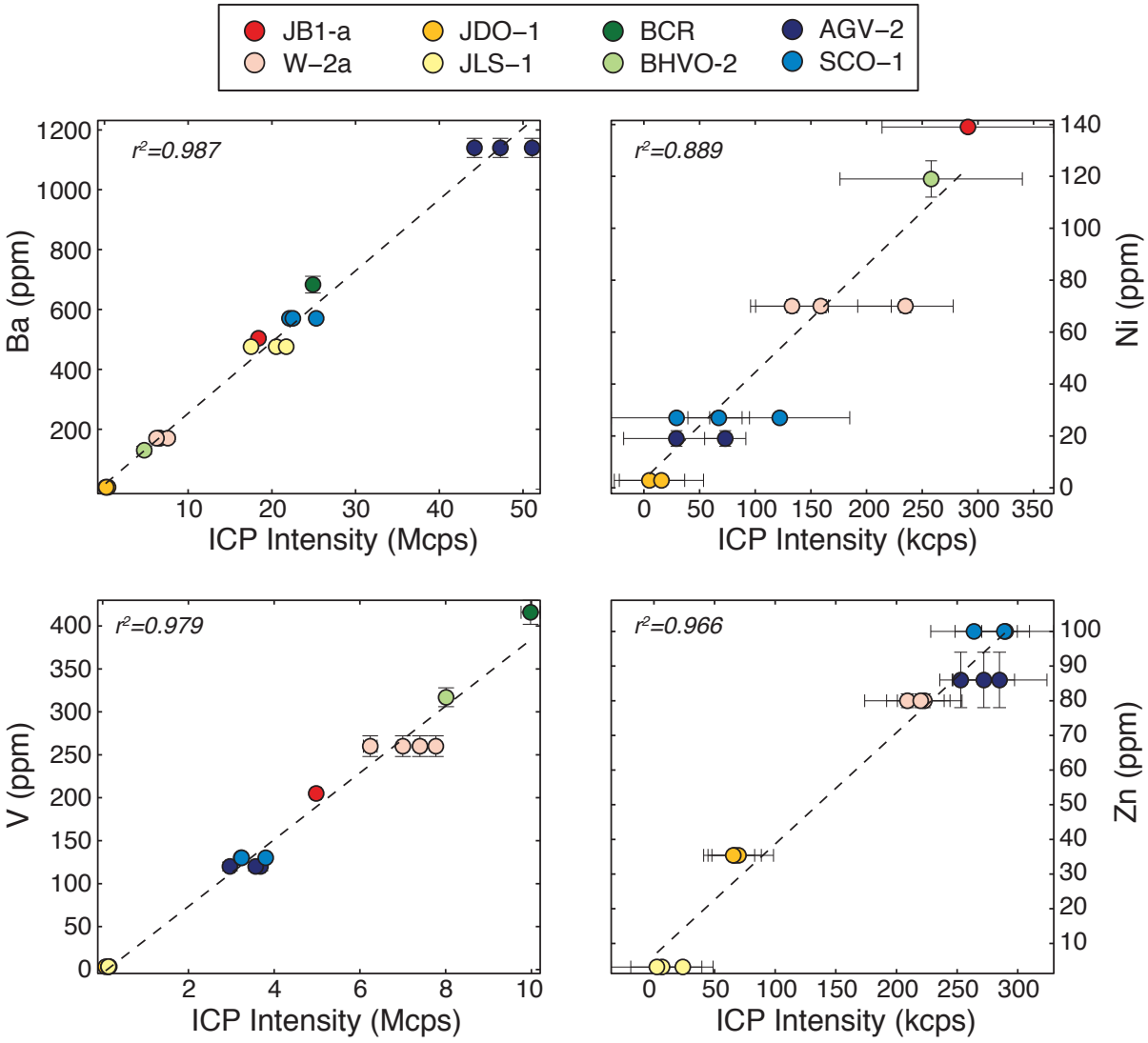

Figure S3.1. Calibration of ICP-OES data with fluxed standard reference materials. Standard reference materials (AGV-2, W-2a, SCO-1, JLS-1, JDO-1, JB1-a, BHVO-2, BCR) were analyzed to convert ICP-OES intensity measurements (million counts per second, or Mcps) to concentrations (wt% or ppm). ICP intensities and elemental concentrations are all highly correlated ($r^2 \geq 0.99$, $p < 0.001$). Because the sedimentary composition of the JdFR samples was so variable in carbonate and metal content, no single standard reference material could provide a perfect matrix match. Instead, standard reference materials were chosen to best approximate the range of sediment compositions found on the Juan de Fuca Ridge (Costa et al., 2017, 2016): carbonate-rich (JLS-1, JDO-1), clay-rich and/or average continental crust (SCO-1, AGV-2), and metal-rich and/or basalt (BHVO-2, JB1-a, BCR, W-2a).

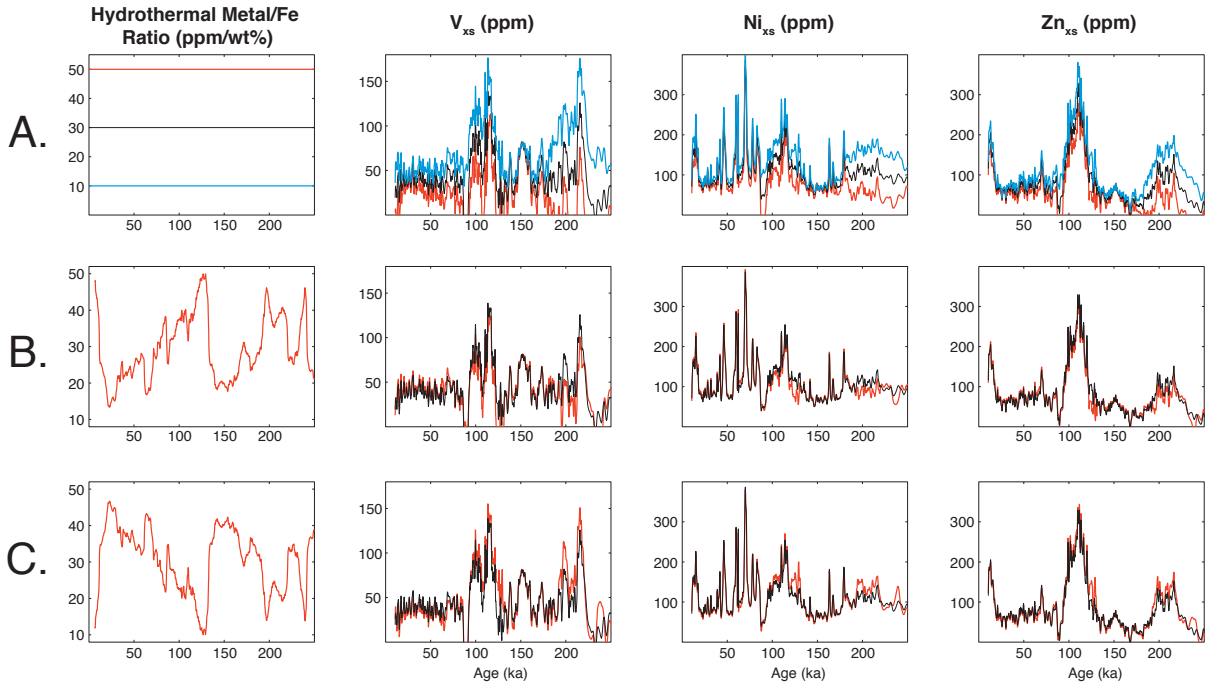

Figure S3.2. Effect of changing the hydrothermal metal to iron ratio on excess metal concentrations. Hydrothermal metal/Fe ratios employed in this paper are shown as black lines: Ni/Fe (30 ppm/wt%), V/Fe (28.2 ppm/wt%), and Zn/Fe (32.7 ppm/wt%). Alternative metal/Fe are shown in blue and red. A) Constant but lower hydrothermal endmembers would slightly increase the excess metal concentrations, but would not substantially alter the temporal variability. The effect of varying the hydrothermal endmember is most prominent in vanadium, due to its lower non-lithogenic concentration relative to nickel or zinc. In all three elements, the specific hydrothermal endmember appears most important in the record older than 175ka, where the spread between endmembers seems to widen. B) Hydrothermal endmember that varies with climate such that higher metal/Fe ratios occur during interglacial periods. The difference between this variable endmember (red) and a constant endmember of 30ppm/wt% (black) is minimal. C) Hydrothermal endmember that varies with climate such that higher metal/Fe ratios occur during glacial periods. Again, the difference between this variable endmember (red) and a constant endmember of 30ppm/wt% (black) is minimal.

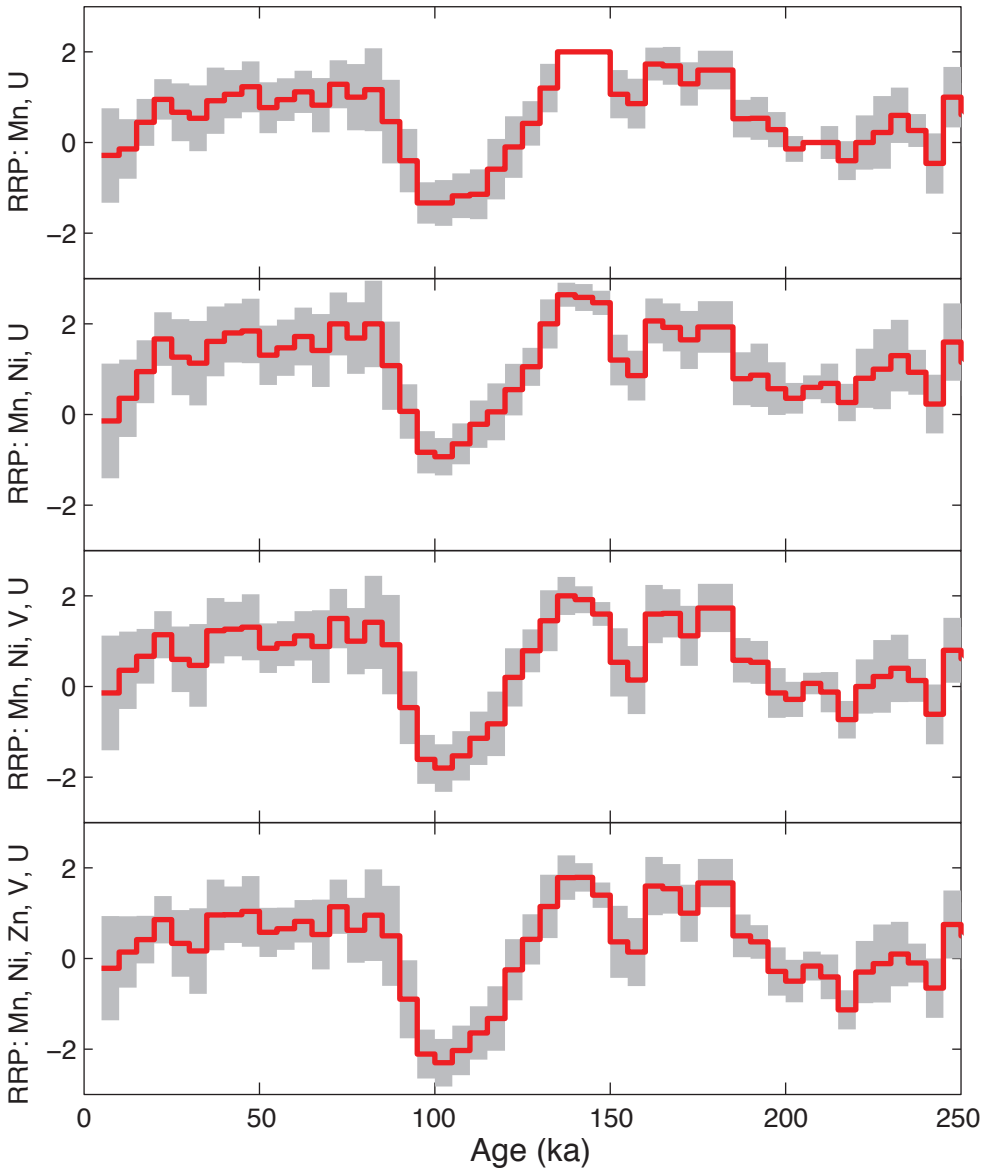

Figure S3.3. Relative redox potentials (RRPs) as in Figure 3.8, but using different combinations of elements. The top panel only includes Mn and U, and then each subsequent panel adds in one extra element in the order Ni, V, and Zn. The key result of low oxygen conditions during the last interglacial period is not sensitive to the inclusion of Ni, V, or Zn.

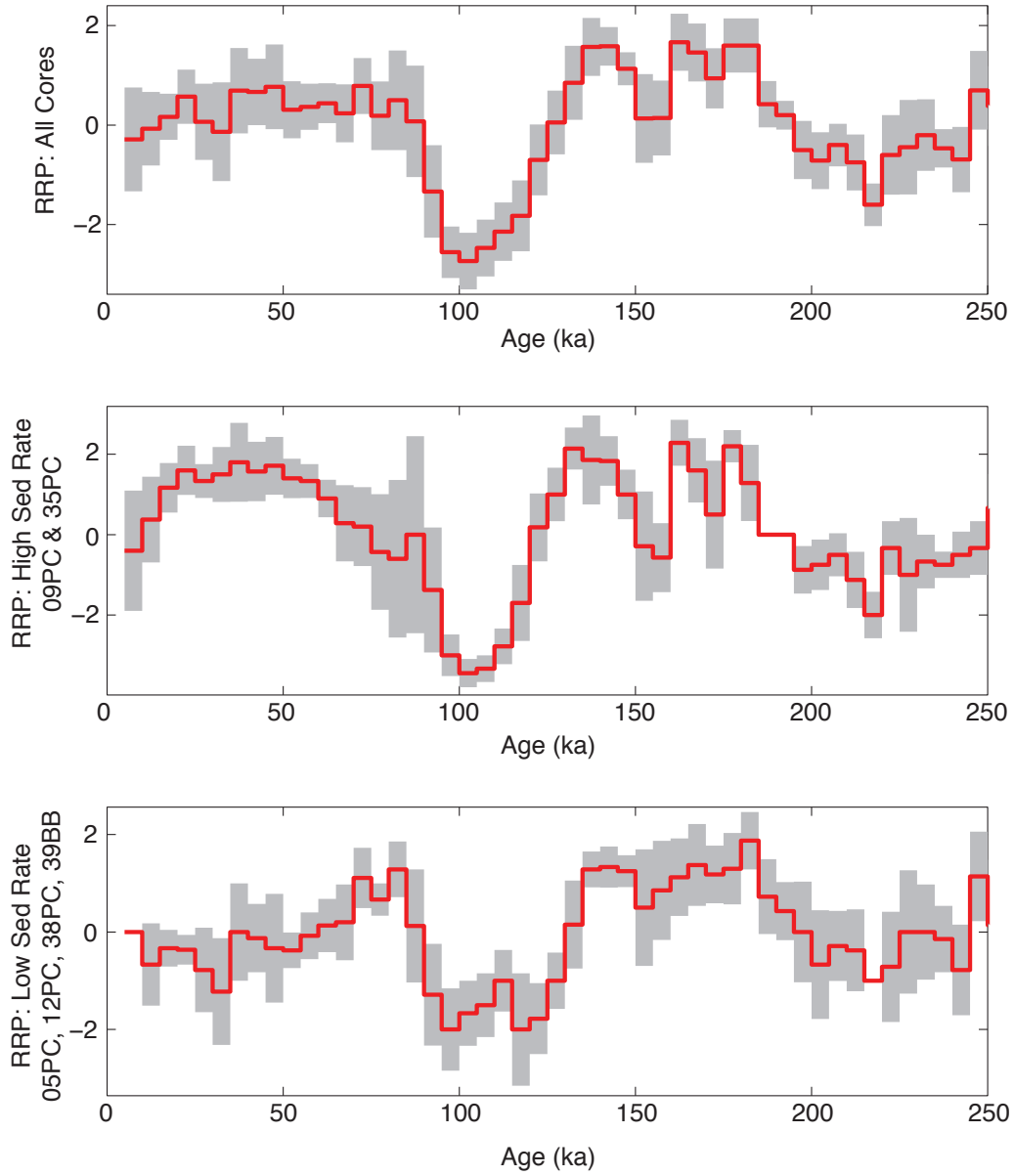

Figure S3.4. Relative redox potentials (RRPs) as in Figure 3.8, but separated by average accumulation rate of each core. High accumulation rate cores (09PC and 35PC) preserve large peaks in authigenic U (see Figure 3.3). Low accumulation rate cores (05PC, 12PC, 38PC, and 39BB) do not preserve any significant variability in authigenic U. Thus the RRPs of the low accumulation rate cores are driven primarily by the metal records. While they do not capture the full amplitude of the event as recorded in the higher accumulation rate cores, the key result of low oxygen conditions during the last interglacial period is not sensitive to the preservation of authigenic U.

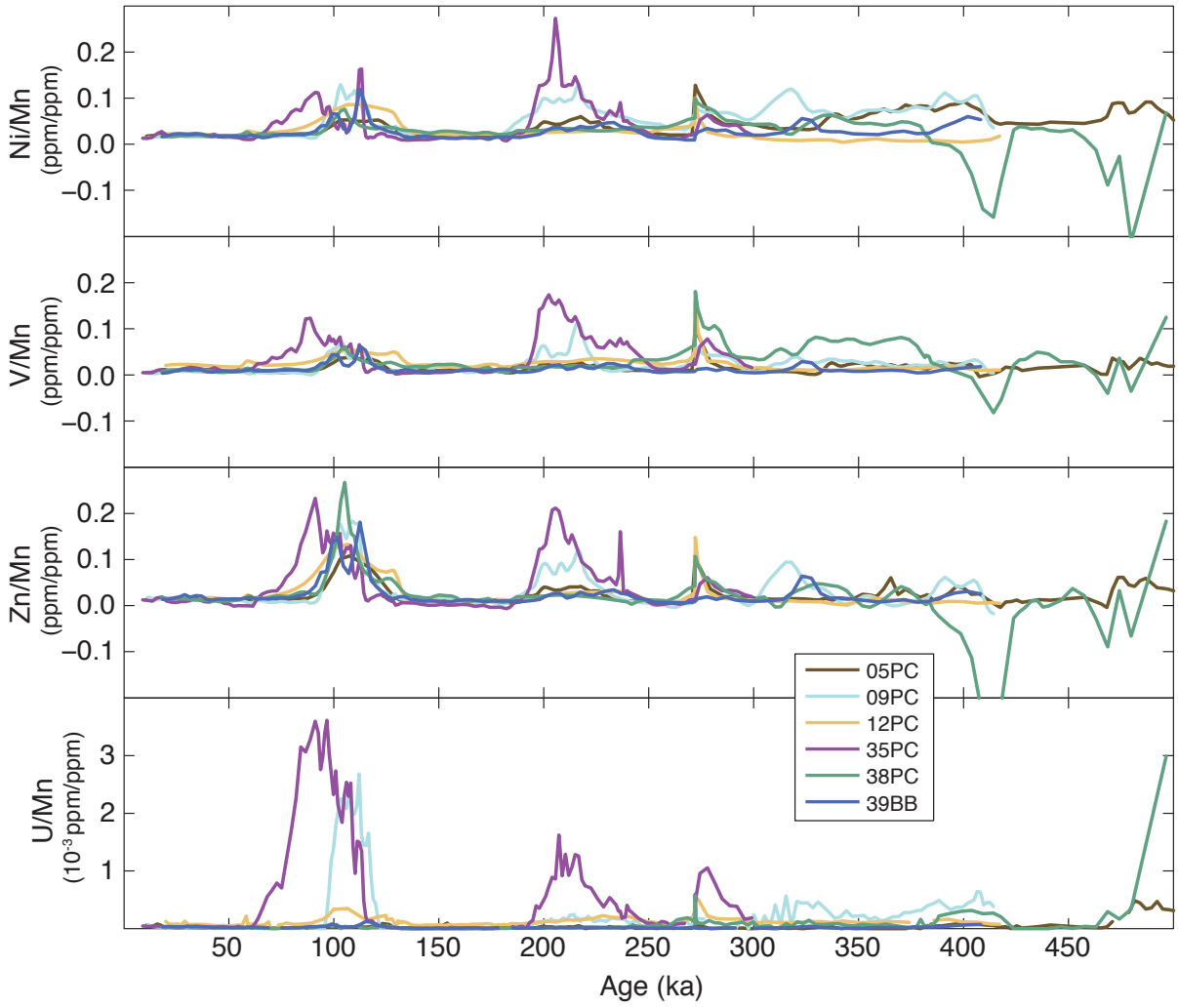

Figure S3.5. Metal to manganese ratios, in which higher values indicate lower oxygen conditions. All metal/Mn ratios support the key result of low oxygen conditions during the last interglacial period.

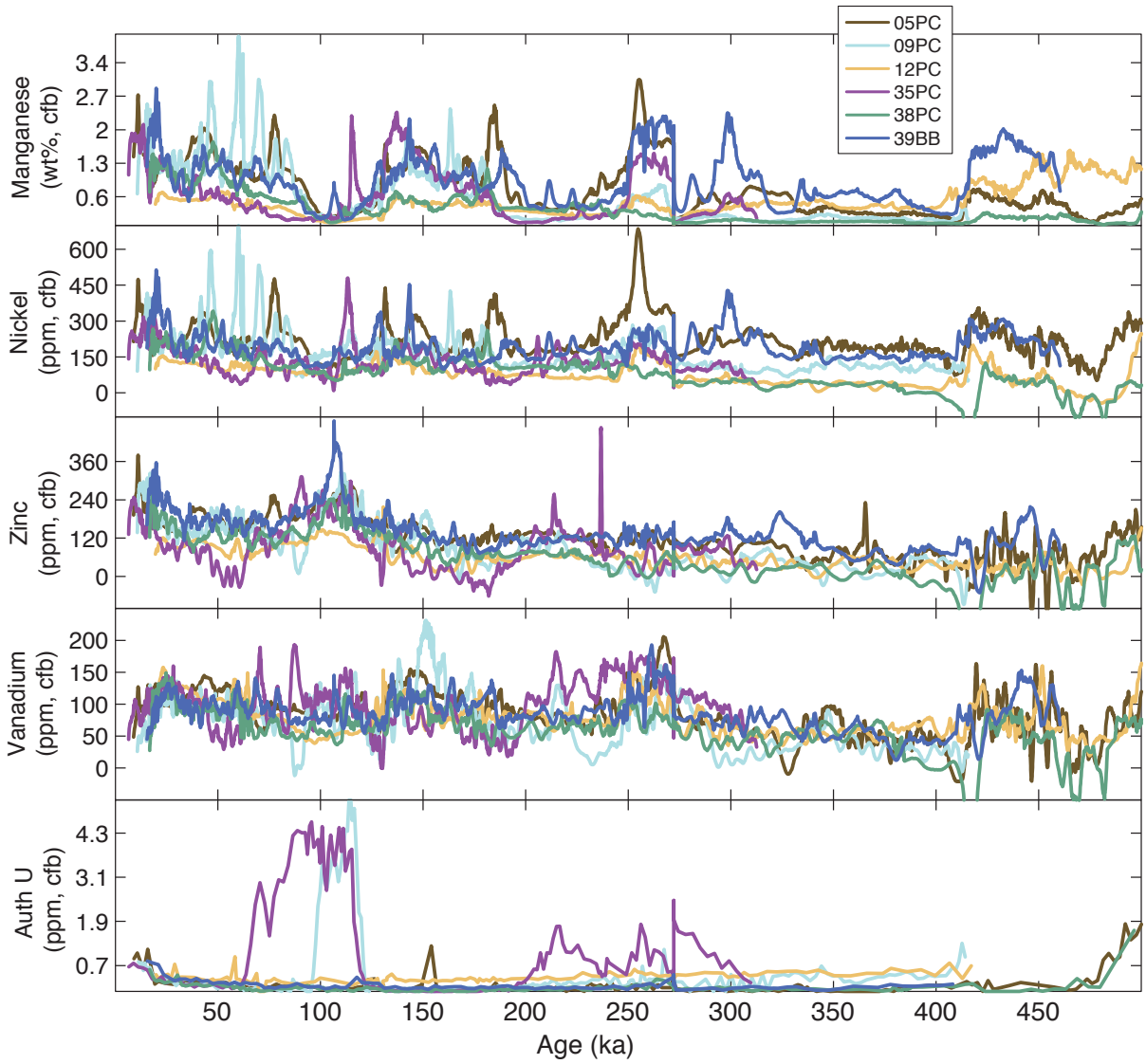

Figure S3.6. Excess elemental concentrations presented on a carbonate free basis. The redox-driven cycles in manganese and uranium are easily identifiable, while the variability in nickel, zinc, and vanadium suffers from much higher background levels.

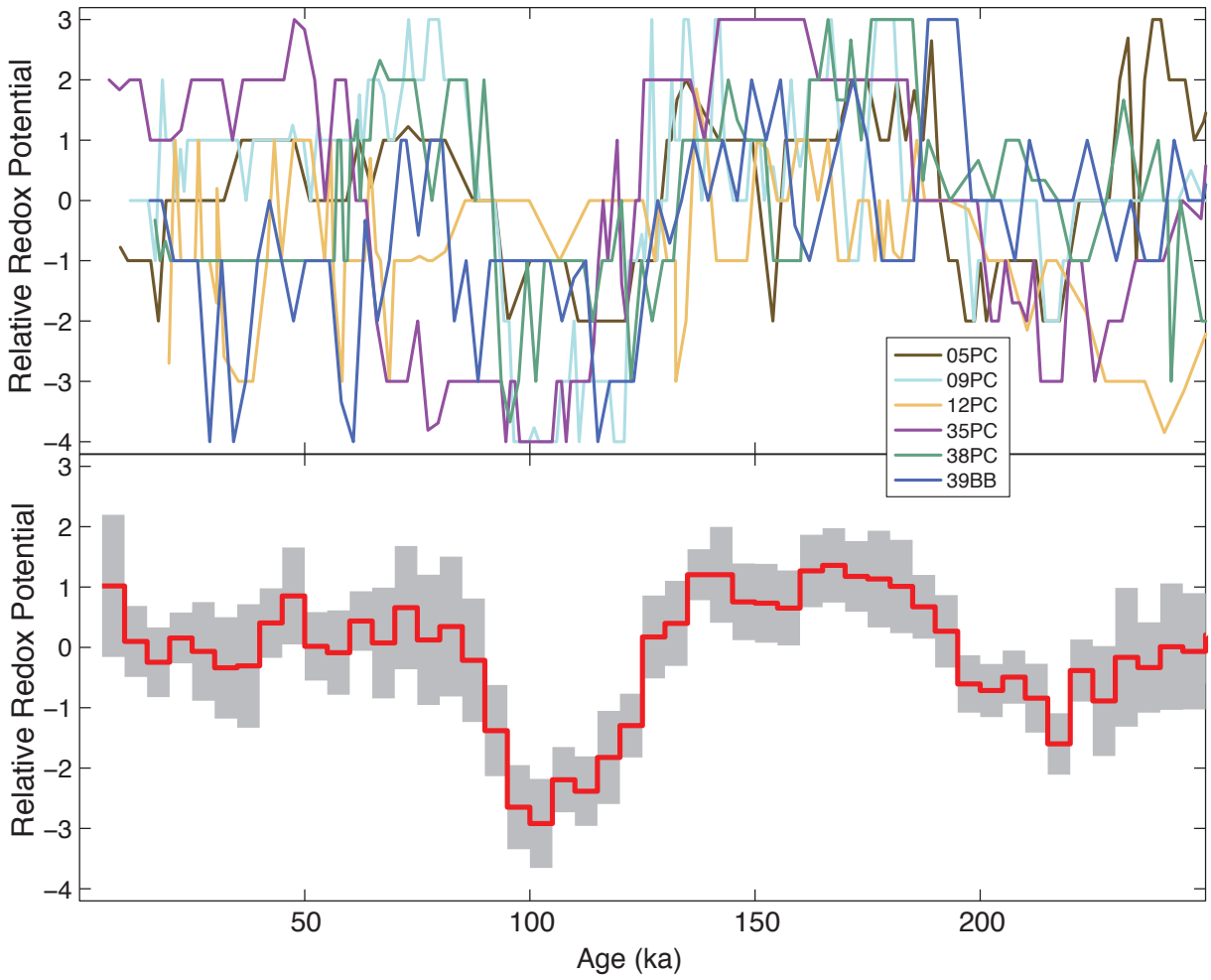

Figure S3.7. RRP calculated as in Section 3.4.3, but using excess elemental concentrations on a carbonate free basis rather than mass accumulation rate based fluxes. This method of reconstruction also supports the key result of low oxygen conditions during the last interglacial period.

Chapter 4

Paleo-productivity and stratification across the Subarctic Pacific over glacial-interglacial cycles

Note: A modified version of this chapter has been submitted for publication in *Paleoceanography and Paleoclimatology*

Abstract:

In the Subarctic Pacific, variability in productivity on glacial-interglacial timescales is often attributed to changes in stratification and nutrient delivery to the surface, but the mechanisms driving this relationship are poorly constrained. Records extending beyond the last glacial maximum from both the open ocean and the marginal seas are required to investigate the timing and magnitude of different influential processes through the full glacial cycle. In this study we generated $^{231}Pa/^{230}Th$ over 210,000 years in order to capture two full glacial cycles of paleo-productivity on the Juan de Fuca Ridge in the East Subarctic Pacific. The sedimentary $^{231}Pa/^{230}Th$ ratios are always equal to or greater than the seawater production ratio (0.093), consistent with enhanced biological scavenging in this region. The temporal pattern of $^{231}Pa/^{230}Th$ burial is remarkably coherent with changes in climate, with high values (0.20) during peak interglacial periods descending to low values (0.10) during peak glacial conditions, consistent with other long productivity records from this region. Nevertheless, a mechanism based on surface temperature changes alone is insufficient to create stratification due to the dominant role of the halocline in determining the vertical density profile of the upper ocean in this region. We investigate the possible contributions of sea ice formation, Bering Strait closure, wind strength, upwelling, and subsurface nutrient concentrations as possible mechanisms by which stratification emerged. Both sea

ice formation and Bering Strait closure would contribute to freshening of surface waters during glacial periods, which would strengthen the pycnocline and enhance stratification. In addition, winds in this region were likely weaker during glacial periods due to the southward shift of the westerlies, reducing the mixing depths and increasing the wind stress curl over the Subarctic. Increased wind stress curl would enhance Ekman divergence, but those upwelling waters may have had lower nutrient concentrations. Thus surface freshening, weak winds, and subsurface nutrient concentrations may all have contributed to lower productivity during glacial periods in the Subarctic Pacific.

4.1. Introduction

Productivity in the Subarctic Pacific is sensitive to light and nutrient limitation controlled by the physical processes of stratification, winter mixing, and sea ice formation. At the onset of Northern Hemisphere glaciation, the development of a steep halocline created a permanent shift towards greater stratification and lower baseline productivity [*Haug et al.*, 1999]. During the last deglaciation, abrupt and transient climate events stimulated productivity peaks at the Bolling-Allerod [*Gorbarenko et al.*, 2004; *Cook et al.*, 2005; *Gebhardt et al.*, 2008; *Hendy and Cosma*, 2008; *Davies et al.*, 2011; *Kohfeld and Chase*, 2011; *Addison et al.*, 2012; *Lam et al.*, 2013; *Ren et al.*, 2015], for a variety of proposed mechanisms related to, for example, meltwater pulses, iron fertilization, subsurface nutrient concentrations, and vertical mixing. Yet neither million-year nor millennial mechanisms are directly analogous to those of glacial-interglacial variability in productivity, which arises from a gradual transition to a semi-permanent glacial state that lasts for tens of thousands of years. Glacial-interglacial changes in productivity are often attributed to greater stratification and reduced nutrient delivery to surface waters during glacial periods [*Narita et al.*, 2002; *Kienast et al.*, 2004; *Sigman et al.*, 2004; *Jaccard et al.*,

2005; *Brunelle et al.*, 2007, 2010; *Galbraith et al.*, 2008; *Knudson and Ravelo*, 2015a], but the mechanism(s) by which these stable conditions develop and persist on orbital timescales remain elusive.

In this study, we generate new records of productivity ($^{231}Pa/^{230}Th$, opal flux, and excess silica flux) from the East Subarctic Pacific (approximately 45˚N, 230˚E, 2700m) over the last two glacial cycles. Disagreement between various productivity proxies is not uncommon and may lead to widely diverging interpretations of paleo-productivity trends (e.g., in the Equatorial Pacific, [*Anderson and Winckler*, 2005; *Costa et al.*, 2017a], and in the Subarctic [*Serno et al.*, 2014; *Costa et al.*, 2018]). Because $^{231}Pa/^{230}Th$ is the productivity proxy least susceptible to preservation biases, it may provide the most reliable reconstruction of paleoproductivity while allowing the qualitative assessment of the impact of preservation and diagenesis on other proxies, particularly opal, in the Subarctic Pacific. Compiling this new record with other long productivity records from across the region, including the Okhotsk Sea [*Sato et al.*, 2002; *Gorbarenko et al.*, 2004; *Brunelle et al.*, 2010], Bering Sea [*Brunelle et al.*, 2007; *Riethdorf et al.*, 2013a; *Knudson and Ravelo*, 2015a], West Subarctic [*Shigemitsu et al.*, 2007; *Jaccard et al.*, 2009; *Brunelle et al.*, 2010], and East Subarctic [*McDonald et al.*, 1999; *Kienast*, 2003], allows for the distinction of both spatial and temporal patterns that may help to identify or eliminate possible mechanisms for increased stratification during glacial periods [*Kienast et al.*, 2004]. We consider the roles of temperature change, sea ice formation, Bering Strait closure, wind strength, upwelling rates, and subsurface nutrient concentrations as potential processes contributing to variability in stratification and productivity over glacial-interglacial periods.

4.2. Theoretical Framework and Analytical Methodology

4.2.1. Scavenging of ^{230}Th and ^{231}Pa in the water column

^{230}Th is produced in the water column by ^{234}U decay (β = 0.02556 dpm/m^{3}yr, at salinity of 35), and it is rapidly removed from the water column by adsorption onto settling particles, in a process referred to as scavenging. Uranium decay to ^{230}Th is spatially constant due to the high solubility and long residence time (400kyr) of uranium, which results in a fairly constant uranium concentration (3.2ppb) that scales conservatively with salinity [*Owens et al.*, 2011]. The uncertainty introduced by using a constant production rate is small (<5%), both spatially, because salinity varies little in the deep ocean where most ^{230}Th is produced, and temporally, because glacial-interglacial changes in salinity are offset by changes in sea level. Therefore, the ^{230}Th flux to the sediment is primarily dependent on the water column depth over which the sediment integrates [*Henderson and Anderson*, 2003], and its sedimentary concentrations are inversely proportional to the flux of sediment with which the ^{230}Th is diluted [*Francois et al.*, 2004]. The residence time of ^{230}Th in the ocean is so short (20-40 years; Nozaki et al., 1981) compared to its half-life (75,584 years; Cheng et al., 2013) that virtually all of the ^{230}Th produced by uranium decay in seawater is removed to sediments by scavenging in the water column. The residence time of ^{230}Th is also much less than the time scale for lateral transport by mixing from regions of low scavenging intensity (low particle flux) to regions of high scavenging intensity. Consequently, most ^{230}Th is buried in sediment underlying the very same water column in which it was produced [*Henderson et al.*, 1999; *Henderson and Anderson*, 2003].

^{231}Pa, like ^{230}Th, is produced by uranium (^{235}U) decay (β = 0.00245 dpm/m^{3}yr, at salinity of 35) in the water column and scavenged by particles settling to the seafloor, but unlike ^{230}Th, ^{231}Pa has a residence time long enough to advect and diffuse away from the

water column in which it was produced. Scavenging of ^{231}Pa from the water column is much less effective, and it can be dependent on both the particle flux [*Anderson et al.*, 1983, 1990; *Bacon*, 1988; *Hayes et al.*, 2013] and the particle composition [*Chase et al.*, 2002, 2003; *Geibert and Usbeck*, 2004; *Kretschmer et al.*, 2011]. In regions with low particle flux, more ^{231}Pa will escape local scavenging, and particles will likely acquire a ^{231}Pa/^{230}Th much lower than that of production in the water column ($\beta_{231Pa}/\beta_{230Th} = 0.093$; activity ratio, at salinity of 35). In regions of high particle flux, in situ and allochthonous ^{231}Pa will be more efficiently scavenged so that particles acquire high ^{231}Pa/^{230}Th, potentially greater than production. Similarly, opal has a particular affinity for ^{231}Pa, so that opal rich sediments will tend to have relatively high ^{231}Pa concentrations and thus ^{231}Pa/^{230}Th greater than production (^{231}Pa/^{230}Th > 0.093). The lateral mobility of ^{231}Pa relative to ^{230}Th generates sedimentary ^{231}Pa/^{230}Th unequal to the production ratio over much of the ocean [*Hayes et al.*, 2014], with the high ^{231}Pa/^{230}Th concentrated in a limited zone along continental margins (Figure 4.1). These high ^{231}Pa/^{230}Th are generated at continental boundaries because terrigenous inputs, coastal upwelling, and high productivity combine to generate high particle and opal fluxes, and so the major removal process of ^{231}Pa in these settings is known as "boundary scavenging" [*Anderson et al.*, 1983, 1990; *Bacon*, 1988; *Hayes et al.*, 2013].

4.2.2. Materials and methods

Sediment cores were collected from the Juan de Fuca Ridge (JdFR) on the SeaVOICE cruise (AT26-19) of the R/V Atlantis in September 2014 (Table 4.1). The cores are closely clustered (within 50km) and from similar depth range (2655-2794m), such that they can be combined as if multiple iterations of the same paleo-record (e.g. Costa and

McManus, 2017). Age models for the JdFR piston cores are well-constrained based on radiocarbon dates, benthic $\delta^{18}O$, and stratigraphically tuned density cycles [*Costa et al.*, 2016b]. Additionally, two multicores (06MC, 10MC) corresponding to piston cores (09PC, 12TC/PC respectively) are added to cover the Holocene. Age models for these multicores are primarily based on benthic $\delta^{18}O$ due to bioturbative effects on coretop radiocarbon dates [*Costa et al.*, 2017b]. Sedimentation rates over the past 500kyrs generally range from 1 to 3 cm/kyr, with background pelagic sedimentation rates close to 1cm/kyr, and they are spatially heterogeneous, likely reflecting sediment remobilization caused by the high relief and stronger bottom currents of the near-ridge environment [*Costa et al.*, 2016b].

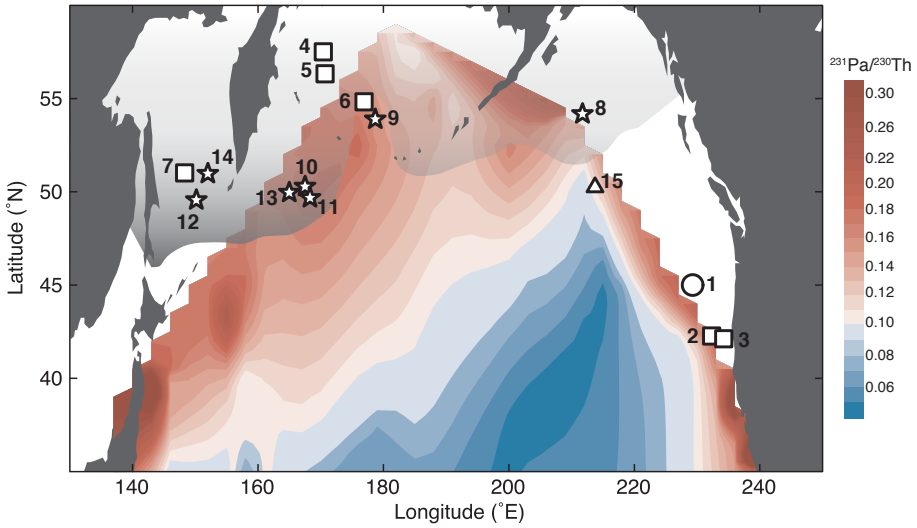

Figure 4.1. Distribution of coretop $^{231}Pa/^{230}Th$ in the North Pacific. Compiled by Hayes et al., 2014]. $^{231}Pa/^{230}Th$ follows modern productivity patterns, with low values (below production, 0.093 activity ratio) characterizing the gyre and high values (above production) characterizing the continental margins. The white circle (1) identifies the location of the Juan de Fuca Ridge. Squares indicate long productivity records based on organic carbon: (2) W8709-8 and (3) W8709-13 [Kienast, 2003], (4) SO201-2-85 and (5) SO201-2-77 [Riethdorf et al., 2013a], (6) U1342 [Knudson and Ravelo, 2015a], and (7) PC936 [Gorbarenko et al., 2004]. Stars indicate long productivity records based on excess barium: (8) ODP887 [McDonald et al., 1999], (9) JPC17 [Brunelle et al., 2007], (10) ODP882 [Jaccard et al., 2009], (11) RNDP-PC13 and (12) GGC27 [Brunelle et al., 2010], (13) MR98-05-3PC [Shigemitsu et al., 2007], and (14) X98-01PC [Sato et al., 2002]. See Table 4.1 for site locations. Ocean Station PAPA (15) is shown as a triangle. Gray shaded area indicates the maximum seasonal sea ice extent during the LGM, based on reconstructions from diatom assemblages, ice rafted debris, and IP_{25} [Matul, 2017; Méheust et al., 2018].

Table 4.1. Core locations used in this study.

Region	Core	Lat °N	Long °E	Water Depth (m)	Sed Rate (cm/kyr)	Proxy	Reference
East Subarctic	AT26-19-05PC	44.973	229.122	2711	0.93	Pa/Th	*this study*
East Subarctic	AT26-19-09PC/06MC	44.887	229.363	2678	1.95	Pa/Th	*this study*
East Subarctic	AT26-19-12PC-TC/10MC	44.898	229.496	2689	0.63	Pa/Th	*this study*
East Subarctic	AT26-19-35PC	44.991	229.543	2731	1.85	Pa/Th	*this study*
East Subarctic	AT26-19-38PC	44.971	229.393	2655	1.11	Pa/Th	*this study*
East Subarctic	AT26-19-39BB	45.045	229.167	2794	1.18	Pa/Th	*this study*
East Subarctic	W8709A-8	42.270	232.320	3111	9.49	Organic C	[*Kienast*, 2003]
East Subarctic	W8709A-13	42.120	234.250	2712	14.11	Organic C	[*Kienast*, 2003]
West Subarctic	ODP882	50.330	167.500	3244	6.03	Biogenic Ba	[*Jaccard et al.*, 2009]
East Subarctic	ODP887	54.220	211.730	3647	7.08	Biogenic Ba	[*McDonald et al.*, 1999]
West Subarctic	RNDP-PC-13	49.720	168.300	2393	4.33	Biogenic Ba	[*Brunelle et al.*, 2010]
Okhotsk Sea	GGC27	49.601	150.180	995	2.52	Biogenic Ba	[*Brunelle et al.*, 2010]
Bering Sea	JPC17	53.933	178.699	2209	12.90	Biogenic Ba	[*Brunelle et al.*, 2007]
Bering Sea	U1342	54.828	176.917	818	3.65	Organic C	[*Knudson and Ravelo*, 2015a]
Okhotsk Sea	PC936	51.015	148.313	1305	5.35	Organic C	[*Gorbarenko et al.*, 2004]
West Subarctic	MR98-05-3PC	50.000	164.983	5507	3.59	Biogenic Ba	[*Shigemitsu et al.*, 2007]
Okhotsk Sea	X98-01PC	51.015	152.008	1100	8.11	Biogenic Ba	[*Sato et al.*, 2002]
Bering Sea	SO201-2-85	57.505	170.413	975	10.67	Organic C	[*Riethdorf et al.*, 2013a]
Bering Sea	SO201-2-77	56.330	170.699	2133	9.49	Organic C	[*Riethdorf et al.*, 2013a]

4.2.2.1. Uranium series chemistry

A total of 520 samples from six cores were analyzed for thorium (^{230}Th, ^{232}Th), uranium (^{238}U, ^{235}U, ^{234}U), and protactinium (^{231}Pa) by isotope dilution using inductively coupled plasma mass spectrometry (ICP-MS). Data for ^{230}Th have been previously published by Costa and McManus (2017), and ^{231}Pa data were analyzed by a similar methodology. Samples (100mg) were spiked with ^{233}Pa and processed with complete acid digestion and column chromatography [*Fleisher and Anderson*, 2003]. Isotopes were measured on an Element 2 ICP-MS at the Lamont-Doherty Earth Observatory of Columbia University. Discrete sediment aliquots (n=40) of the VOICE Internal Mega-Standard (VIMS) (Costa and McManus, 2017) were processed and analyzed for quality control, and these total replicates of VIMS indicate that the analytical procedure and measurement are externally reproducible within 8.7% on ^{231}Pa. Excess initial ^{231}Pa ($^{231}Pa_{xs}^{0}$) concentrations were calculated by correcting for supported decay from lithogenic and authigenic uranium [*Henderson and Anderson*, 2003]. Throughout this text, ^{231}Pa/^{230}Th will refer specifically to the excess initial isotope ratio, corrected for radioactive decay since deposition.

4.2.2.2. Opal and excess silica fluxes

Biogenic opal was measured by alkaline extraction [*Mortlock and Froelich*, 1989] at LDEO and has been previously published [*Costa et al.*, 2018]. Total replicates (n=6) of VIMS indicate that the analytical procedure and measurement are reproducible within ±6.7%.

Total silica and titanium concentrations were analyzed by flux fusion following the procedure of Murray et al. (2000). Dried, homogenized samples (100±5mg) were combined with lithium metaborate flux (400±10mg) in graphite crucibles and fused at 1050˚C for 8-10 minutes. The graphite crucibles were removed from the furnace and agitated to ensure

aggregation of the fused material. After reheating to 1050˚C, the fused bead was dissolved in 10% HNO_3, agitated for approximately 10 minutes, and then filtered and diluted for analysis. Samples were analyzed on an Agilent 720 Inductively Coupled Plasma Optical Emission Spectrometer (ICP-OES) at LDEO, and ICP-OES intensity data were calibrated to concentrations with fluxed standard reference materials (JLS-1, JDO-1, SCO-1, AGV-2, JB1-a, W-2a, BCR, BHVO-2). Total replicates (n=10) of VIMS indicate that the analytical procedure and measurement are reproducible within ±2.8% for Si and ±1.8% for Ti.

Total silica concentrations comprise both terrigenous silica and biogenic (or excess) silica. To isolate the excess silica (Si_{xs}) fraction, the terrigenous silica is estimated using titanium concentrations and a constant lithogenic Si/Ti ratio. Bulk continental crust has a Si/Ti of 49.6 wt%/wt% [*Taylor and McLennan*, 1995], but the slightly lower value of 47 wt%/wt% was used here to eliminate negative results. In summary:

$$[Si_{xs}] = [Si_{total}] - [Ti] * \left(\frac{Si}{Ti}\right)_{Lith}$$

4.2.2.3. Data compilation

This study focuses on paleoproductivity changes on glacial-interglacial timescales, and thus it requires long productivity proxy records that extend beyond the last glacial maximum (Table 4.1). The criteria for inclusion in this study were 1) at least the last 60kyr of continuous data coverage, 2) sufficient data available to correct for dilution by major sedimentary components, and 3) location in the Subarctic Pacific above 40˚N. Age models used in this study have not been changed from their originally published values.

Ideally, productivity proxies would be normalized to a constant flux proxy (CFP), like ^{230}Th or ^{3}He, which can be used to calculate the absolute flux of a sedimentary component over time [*Francois et al.*, 2004]. Unfortunately many productivity proxy records

are published without CFP normalization, and they are instead presented as age-model based mass accumulation rates or simply as concentrations. Compared to CFP derived fluxes, age-model based mass accumulation rates are notoriously inaccurate [*Francois et al.*, 2004; *Kienast et al.*, 2007; *Winckler et al.*, 2016; *Costa and McManus*, 2017], due to omnipresent lateral sediment redistribution on the seafloor. Because using these mass accumulation rates can cause misleading interpretations (e.g., [*Murray et al.*, 2012] compared to [*Winckler et al.*, 2016]), we do not employ them for any of the proxy records in this study.

Instead we use proxy concentration data that have been corrected for dilution by variability in major sedimentary components, specifically calcium carbonate and opal. Calcium carbonate preservation in the Pacific varies on glacial-interglacial timescales such that calcium carbonate burial is higher during glacial periods than interglacial periods [e.g., *Farrell and Prell*, 1989]. An increase in the relative concentration (wt%) of, e.g., organic carbon may be due to increased productivity, but it could just as easily result from a decreased concentration of calcium carbonate. The dilution correction is calculated by determining the proxy concentration on a calcium carbonate (and opal) free basis as follows:

$$[Proxy]_{cfb} = [Proxy] * \left(\frac{100}{100 - [CaCO_3] - [Opal]}\right)$$

Corrections were made for both calcium carbonate and opal where available, with the largest effects due to calcium carbonate in the Subarctic Ocean and opal in the Okhotsk and Bering Seas.

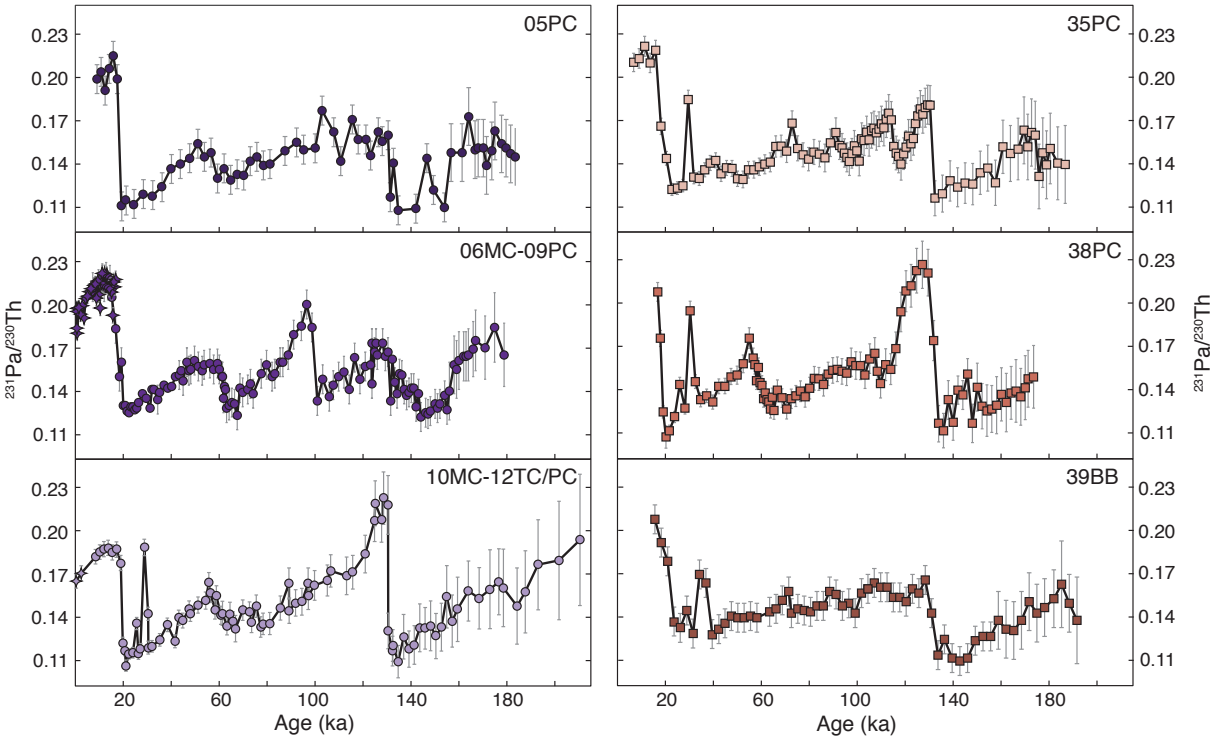

Figure 4.2. Individual $^{231}Pa/^{230}Th$ from the Juan de Fuca Ridge. All datapoints are greater than or equal to the production ratio in the overlying water column (0.093), indicating that this region is characterized by boundary scavenging. Error bars show 2 σ . For 09PC and 12PC, stars indicate data from multicores 06MC and 10MC, respectively. Sedimentary $^{231}Pa/^{230}Th$ ratios track climate, with high burial ratios during interglacial periods and low burial ratios during glacial periods. Peak in 09PC at ~100ka is distinct from the later peak at ~125ka observed in other cores and cannot be attributed to age model error (Supplemental Figure S4.1).

4.3. Results

$^{231}Pa/^{230}Th$ from the six cores on the Juan de Fuca Ridge show similar glacial-interglacial trends (Figure 4.2). The ratios are generally high during interglacial periods and low during glacial periods, with a temporal evolution that mimics the sawtooth pattern of a climate record (e.g., benthic $\delta^{18}O$, Lisiecki and Raymo, 2005). Throughout the last 200kyr, $^{231}Pa/^{230}Th$ sedimentary ratios have always been equal to or greater than the production ratio (0.093), which means that this region not only buries the ^{231}Pa and ^{230}Th produced in the overlying water column but it also buries extra ^{231}Pa delivered from elsewhere in the ocean. Burial of extra ^{231}Pa is greatest during the Holocene, in which $^{231}Pa/^{230}Th$ values range from 0.172 (in 05PC) to 0.211 (in 35PC). Similarly high ratios (0.209-0.227) during the last interglacial period (MIS5) are only achieved in two cores (38PC and 12PC). In the other four cores, $^{231}Pa/^{230}Th$ values in MIS5 can only be classified as high when juxtaposed with the particularly low values in MIS6 (0.093-0.134). The near-production sedimentary ratios in MIS6 characterize the later glacial periods MIS2 and MIS4 as well, suggesting that the burial of extra ^{231}Pa on the Juan de Fuca Ridge is a phenomenon of warm interglacial intervals.

In addition to the glacial-interglacial variability in sedimentary $^{231}Pa/^{230}Th$, four of the six cores (12PC, 35PC, 38PC, 39BB) capture a high $^{231}Pa/^{230}Th$ event (0.164-0.195) around 30ka. Peculiarly this feature does not appear in the core with the highest sedimentation rate in this interval (09PC, see Table 4.1), but its existence in the majority of the other cores as well as its constraint, at times, with more than one datapoint (e.g., 12PC), suggests that it may be a real feature of the data. A peak in sedimentary $^{231}Pa/^{230}Th$ at 30ka may conform with earlier peaks at 55ka, 71ka, 96ka, and 113ka to create a quasi-precessional cycle. While the peak in 09PC at 96.5ka approaches the interglacial values

observed at ~125ka (MIS5e) in 38PC and 12PC, this feature cannot be attributed to age model offsets. The age model is well constrained at glacial-interglacial transitions [*Costa et al.*, 2016b], and the oxygen isotopes and physical properties of 09PC firmly position the high $^{231}Pa/^{230}Th$ peak in late MIS5 (Supplemental Figure S4.1). Thus this peak at 96.5ka in 09PC represents an additional ^{231}Pa burial event that is distinct from those older peaks at ~125ka.

Because the glacial-interglacial trends captured in the six records are so similar, they can easily be combined into a single $^{231}Pa/^{230}Th$ stacked record (Figure 4.3A and B). The $^{231}Pa/^{230}Th$ stack averages all the datapoints within 2-kyr bins to generate a regional average record, and errors are calculated as the standard error of the datapoints within each bin. The stacked record (Figure 4.3B) is characterized by high interglacial values in MIS5 (0.183-0.190) and MIS1 (0.203-0.211) and low glacial values in MIS6 (0.123-0.136) and MIS2 (0.125-0.127). Higher frequency variability is retained with peaks in $^{231}Pa/^{230}Th$ at 29ka, 55ka, and 73ka, and step changes from higher to lower $^{231}Pa/^{230}Th$ at 158ka and 87ka, but the peaks in $^{231}Pa/^{230}Th$ at 96ka and 113ka captured by individual cores are lost in the regional compilation. Overall, the major feature of the long JdFR $^{231}Pa/^{230}Th$ record is its remarkable consistency with climate (Figure 4.3C), as seen in the regional benthic oxygen isotope stack from the JdFR [*Costa et al.*, 2016b].

4.4. Discussion

4.4.1 $^{231}Pa/^{230}Th$ as a productivity proxy in the Subarctic Pacific

Sedimentary $^{231}Pa/^{230}Th$ in the modern Pacific Ocean is largely driven by opal scavenging [*Hayes et al.*, 2014], suggesting that $^{231}Pa/^{230}Th$ should be an effective indicator for changes in productivity in the past. Comparisons of $^{231}Pa/^{230}Th$ and other paleo-

productivity proxies (e.g., opal fluxes) in the Pacific often yield highly positive correlations [*Bradtmiller et al.*, 2006; *Costa et al.*, 2016a], but the relationship is stronger in some

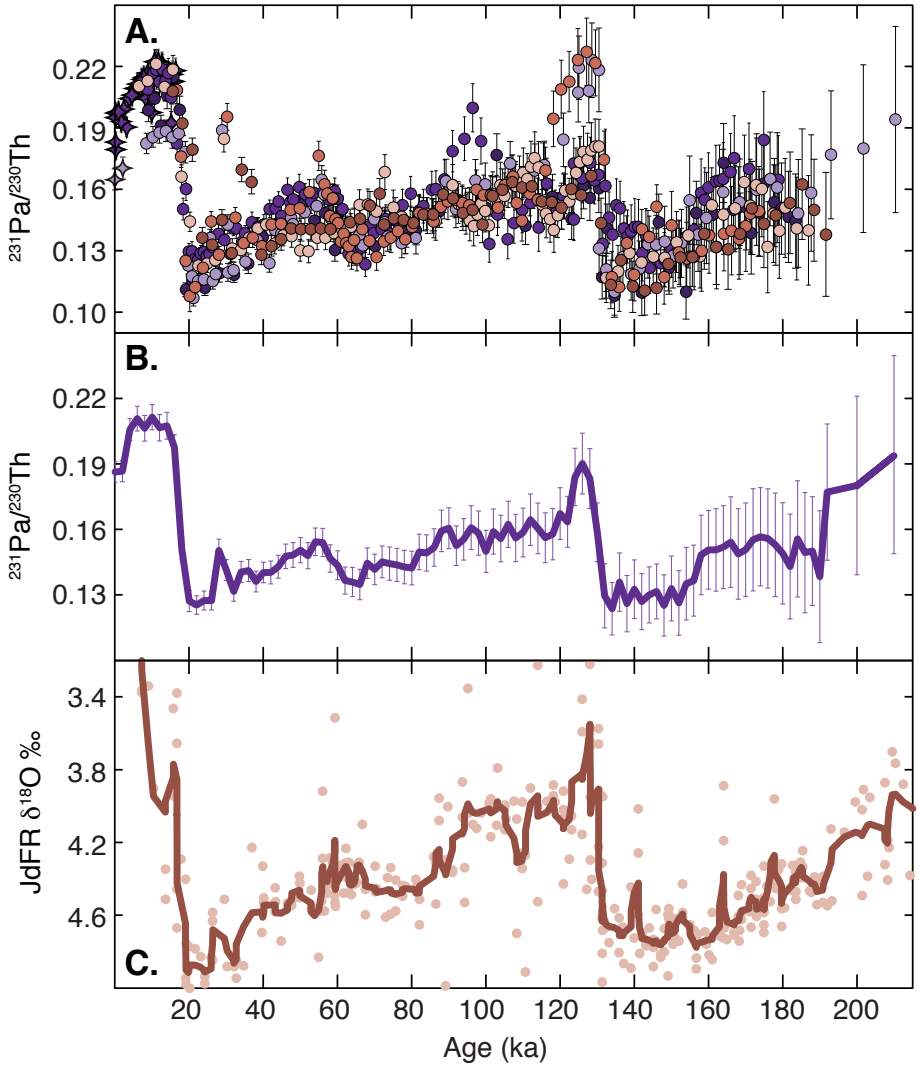

Figure 4.3. Compiled ^{231}Pa/^{230}Th records for the past 210ka. A. Individual datapoints from the Juan de Fuca Ridge overlain in the same panel, using the color scheme in Figure 4.2 to identify each of the study cores, Error bars show 2 σ . B. Stacked ^{231}Pa/^{230}Th record from the Juan de Fuca Ridge. Datapoints from all six sites were averaged in 2kyr bins, and error bars represent 2 standard error. Burial ratios are always higher than the production rate (0.093). C. Juan de Fuca Ridge benthic d^{18}O record [*Costa et al.*, 2016b], to which stacked ^{231}Pa/^{230}Th record is quite similar.

regions than in others [*Pichat et al.*, 2004; *Dubois et al.*, 2010; *Lam et al.*, 2013]. Some degree of inter-proxy disagreement is not uncommon when reconstructing productivity [e.g., see discussions in *Anderson and Winckler*, 2005; *Kohfeld and Chase*, 2011; *Serno et al.*, 2014], and for $^{231}Pa/^{230}Th$ it arises because 1) $^{231}Pa/^{230}Th$ may be integrating different kinds of productivity (e.g., diatomaceous vs. coccolithophorid) and 2) organic components are susceptible to post-depositional changes in preservation and diagenesis. Opal scavenges $^{231}Pa/^{230}Th$ due to both the particle-flux effect and the particle-composition effect, and therefore opal and $^{231}Pa/^{230}Th$ should be highly correlated in regions where surface productivity is dominated specifically by diatoms and other siliceous biota. Where non-siliceous biota constitute an important component of the surface ecology, high productivity may increase scavenging due to the particle flux effect alone, thus elevating sedimentary $^{231}Pa/^{230}Th$ independent of opal. The disparate trends in organic carbon, excess barium, and opal fluxes from these sites on the JdFR [*Costa et al.*, 2018] suggest that productivity in this region may be diverse, and so the relationship between sedimentary $^{231}Pa/^{230}Th$ and productivity is likely to be nonlinear.

Preservation and diagenesis can have an even greater confounding effect on paleo-productivity reconstruction, because the specific environmental parameters controlling preservation are unique to each proxy [*Anderson and Winckler*, 2005; *Kohfeld and Chase*, 2011]. For example, organic carbon is sensitive to oxygen concentrations in bottom and pore waters [e.g., *Ganeshram et al.*, 1999; *Hedges et al.*, 1999; *Arndt et al.*, 2013], but its preservation is additionally affected by benthic activity and bioturbation [*Canfield*, 1994; *Hartnett et al.*, 1998], host sediment composition [*Keil and Hedges*, 1993; *Keil et al.*, 1994], and sedimentation rates [*Müller and Suess*, 1979]. Excess barium, primarily in the form of barite [*Dymond et al.*, 1992; *Hernandez-Sanchez et al.*, 2011], is sensitive to sedimentary redox conditions [*van Os et al.*, 1991; *Dymond et al.*, 1992; *McManus et al.*, 1994, 1998;

Torres et al., 1996; *Eagle et al.*, 2003; *Paytan and Griffith*, 2007; *Hernandez-Sanchez et al.*, 2011], such that under substantial sulfate reduction, barite dissolves and releases barium back to the pore waters, reducing or even eliminating any productivity record in that sedimentary proxy [*Dymond et al.*, 1992; *Dickens*, 2001; *Schenau et al.*, 2001]. Dissolution of opal is omnipresent on the seafloor, since seawater is always undersaturated in dissolved silica, and thermodynamically, opal will dissolve until the porewater concentrations of silica reach equilibrium [*Archer et al.*, 1993; *Ragueneau et al.*, 2000]. Kinetically, the rate of opal dissolution will depend on the abundance of structural flaws [*Van Cappellen and Qiu*, 1997], organic and inorganic coatings [*Ragueneau et al.*, 2000], water saturation [*Archer et al.*, 1993; *Ragueneau et al.*, 2000], trace metal defects [*Archer et al.*, 1993; *Nelson et al.*, 1995; *Treguer and de la Rocha*, 2013], and resilience of the diatom assemblage [*Grigorov et al.*, 2014]. The influence of preservation biases on opal flux at the JdFR is suggested by the nearly exponential decay in opal flux with age (Figure 4.4B), which would be consistent with increasing opal dissolution over time.

The extent of opal diagenesis may be quite extreme, as evidenced by a comparison of opal flux with Si_{xs} flux (Figure 4.4). In practice, opal is operationally defined by the silica that can be leached from the sediment in an alkaline solution [e.g., *Mortlock and Froelich*, 1989]. Any biogenic silica that metamorphizes into an unleachable mineral phase, for example through reaction with Al, Fe, and Mg in the surrounding sedimentary matrix [*Cole*, 1985; *Archer et al.*, 1993; *Nelson et al.*, 1995; *Dixit et al.*, 2001; *Treguer and de la Rocha*, 2013], may not be recoverable as opal. In such a case, the reconstructed opal fluxes would underestimate the original opal signal at the time of burial [*Rahman et al.*, 2016]. The loss of opal by diagenetic transformation may be quantified by measuring Si_{xs} fluxes, which are insensitive to the mineralogy of the silica in the sediment. At the JdFR, opal and Si_{xs} fluxes indicate similar productivity trends for the last 50kyr (Figure 4.4), but they

diverge in the older part of the record, when Si_{xs} fluxes suggest much higher levels of productivity during the last interglacial period (MIS5) than opal. In fact, Si_{xs} fluxes suggest that opal productivity during MIS5 (13.4 mg/cm^{2}kyr) was similar to that of the Holocene (15.2 mg/cm^{2}kyr), in contrast to the nearly 65% lower productivity suggested by opal in MIS5 (10.0 mg/cm^{2}kyr) versus the Holocene (28.3 mg/cm^{2}kyr). If this loss of opal could be attributed to transformation into non-opalline phases, it may indicate that the reverse weathering reaction [*Sillen*, 1961; *Mackenzie and Kump*, 1995; *Michalopoulos et al.*, 2000] can occur at a relatively rapid rate if conditions are appropriate [*Rahman et al.*, 2016]. Future work on opal diagenesis might focus on the mineralogy of the sedimentary matrix and the resulting non-opalline silica-rich phases in order to provide greater understanding of the environments that may reduce the utility of opal as a productivity proxy.

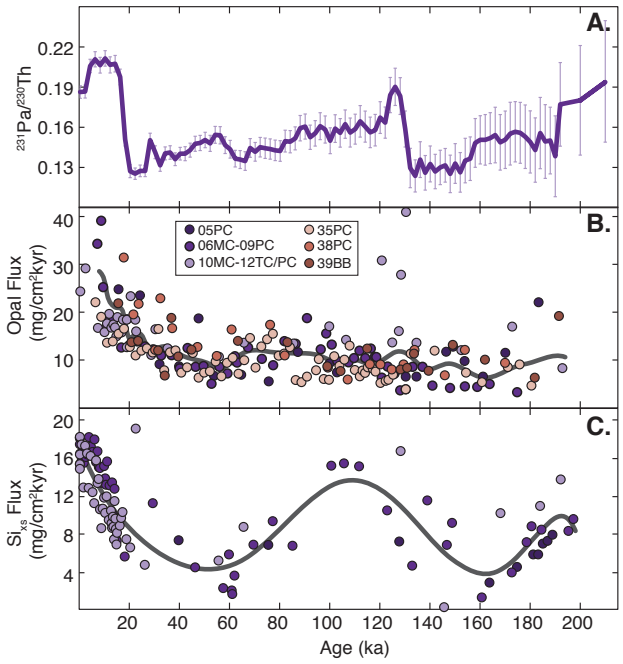

Figure 4.4. Preservation effects on opal. A) ^{231}Pa/^{230}Th stack, as in Figure 4.3. B) Opal fluxes, calculated with ^{230}Th-normalized fluxes [*Costa et al.*, 2018]. C) Excess silica (Si_{xs}) fluxes, calculated with ^{230}Th-normalized fluxes. Gray lines show general trends based on 10-pt smoothing (B) and best polynomial fit (C). Legend in (B) also applies to (C). Both opal and Si_{xs} fluxes show increasing trends for the last 50kyrs, but they differ in the older part of the record (>50ka). Si_{xs} fluxes show similar levels of productivity during MIS5 and the Holocene, while opal fluxes suggest productivity was 2/3 lower in MIS5 compared to the Holocene.

One of the main advantages of $^{231}Pa/^{230}Th$ over opal, as well as other productivity proxies, is its relative insensitivity to changes in preservation and diagenesis [*Chase et al.*, 2003; *Pichat et al.*, 2004]. The limited solubility of both ^{231}Pa and ^{230}Th increases the likelihood that even if their original host particle dissolved, these nuclides would most likely adsorb onto an adjacent particle in the sedimentary pile rather than diffuse through the porewater and out of the sediment as dissolved ions [*Henderson and Anderson*, 2003; *Francois et al.*, 2004]. Thus $^{231}Pa/^{230}Th$ is likely to be the most robust and reliable productivity indicator currently available.

4.4.2. Glacial-interglacial variability in productivity in the Subarctic Pacific

Low productivity during cold periods is a pervasive feature of the Subarctic Pacific, on both million-year [*Sigman et al.*, 2004; *Haug et al.*, 2005] and orbital timescales [*Kienast et al.*, 2004; *Jaccard et al.*, 2005; *Okazaki et al.*, 2005b, 2005a; *Galbraith et al.*, 2007]. Long productivity records from across the region (Figure 4.5) show generally coherent glacial-interglacial variability in the open ocean (West and East Subarctic) and in the marginal seas (Bering and Okhotsk Sea). In all but one core from the Okhotsk Sea, productivity peaks in MIS5 and the Holocene and reaches minima in MIS2 and MIS4. Regional differences are more apparent on sub-glacial timescales. In the West and East Subarctic, productivity varies with mean global climate, as represented by the LR04 benthic $\delta^{18}O$ stack [*Lisiecki and Raymo*, 2005], such that there is an early interglacial maximum (MIS5e), followed by relatively high interglacial productivity (MIS5a-d), a step decrease in productivity that coincides with glacial onset (MIS4), a return to higher productivity during the warm MIS3, a minimum at the last glacial maximum (MIS2), and a rapid increase in productivity during the last deglaciation. This sub-glacial variability is somewhat evident in the Okhotsk Sea but notably absent in the Bering Sea, where productivity hovers at low

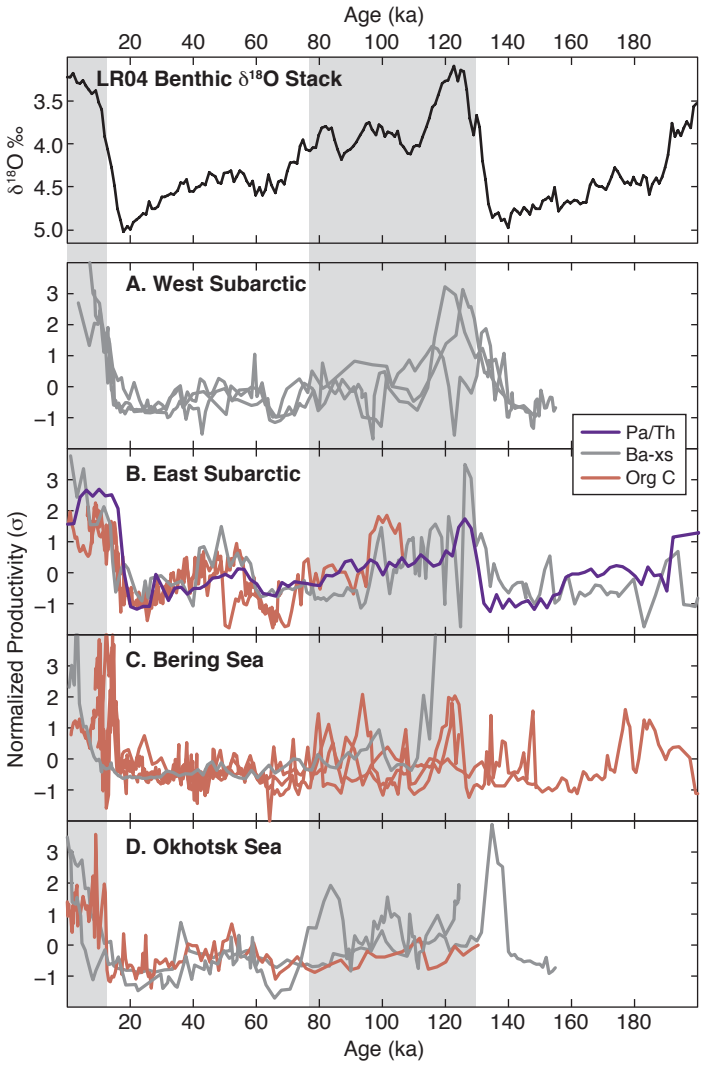

Figure 4.5. Other long productivity records from the Subarctic Pacific. Records are color coded based on the proxy used, and grouped based on region. Organic carbon (Org C) and excess barium (Ba-xs) were corrected for changes in dilution based on calcium carbonate content and opal content, since ^{230}Th-based flux calculations were not feasible. All records have been normalized (z-scored) by subtracting the mean and dividing by the standard deviation in order to facilitate plotting on the same scale. A) West Subarctic: ODP882 [*Jaccard et al.*, 2009], RNDP-PC13 [*Brunelle et al.*, 2010], and MR98-05-3PC [*Shigemitsu et al.*, 2007]. B) East Subarctic: JdFR [*this study*], W8709-8 and W8709-13 [*Kienast*, 2003], and ODP887 [*McDonald et al.*, 1999]. C) Bering Sea: SO201-2-85 and SO201-2-77 [*Riethdorf et al.*, 2013a], U1342 [*Knudson and Ravelo*, 2015a], and JPC17 [*Brunelle et al.*, 2007]. D) Okhotsk Sea: PC936 [*Gorbarenko et al.*, 2004], GGC27 [*Brunelle et al.*, 2010], and X98-01PC [*Sato et al.*, 2002]. Top panel shows the LR04 benthic δ^{18}O stack for climatic context [*Lisiecki and Raymo*, 2005], and gray bars highlight interglacial periods.

background values except for the few peaks that occur in interglacial periods. Thus, high productivity occurs only but not always during warm climate periods in marginal seas, while it always responds to climate in the open ocean.

The apparent climate dependency of productivity is primarily attributed to changes in stratification in the Subarctic Pacific, akin to those of the Antarctic Zone of the Southern Ocean [*Mortlock et al.*, 1991; *Francois et al.*, 1997; *Robinson et al.*, 2004; *Sigman et al.*, 2004; *Basak et al.*, 2018]. Stratification and density-driven mixing control nutrient delivery to the surface in the modern Subarctic Pacific, because high precipitation relative to evaporation (P-E) creates a low salinity surface cap that is so fresh that even near-freezing winter temperatures are insufficient for densification and deep water formation [*Warren*, 1983; *Emile-Geay et al.*, 2003]. Average mixed-layer depths in the East Subarctic are only 50m in the summer, too shallow to reach nutrient-rich deep waters, but can extend up to 100m in the winter, so that annual average nutrient concentrations in surface waters are almost entirely dependent on deep winter mixing [*Tabata*, 1975; *Glover et al.*, 1994; *Whitney and Freeland*, 1999; *Whitney*, 2011]. Seasonality is even stronger in the West Subarctic, where mixing reaches less than 50m in the summer but 150m or more in the winter [*Glover et al.*, 1994; *Honda et al.*, 2002], leading to higher nutrient concentrations in surface waters of the west [*Harrison et al.*, 1999]. Across the Subarctic region, the main growing season (May-September) begins [*Harrison et al.*, 1999] in the spring when the nutrient-rich winter mixed layer stratifies and light limitation is relieved. Without continued replenishment the nutrient supply progressively declines through the summer [*Whitney and Freeland*, 1999; *Wong et al.*, 2002; *Kawakami et al.*, 2007; *Whitney*, 2011] until further production is limited by iron availability [*Martin and Fitzwater*, 1988; *Boyd and Harrison*, 1999; *Tsuda et al.*, 2005]. Integrated over tens to hundreds of years, the

average nutrient concentrations in surface waters are set by the rates of winter mixing versus summer drawdown, that is, net nutrient utilization, as well as iron supply.

High dust fluxes during glacial periods [e.g., *Winckler et al.*, 2008; *McGee et al.*, 2010; *Serno et al.*, 2015, 2017] would have likely increased surface iron concentrations, a boon to iron-limited waters that would have promoted high productivity, rather than the low productivity that is actually observed. The combination of low glacial productivity (Figure 4.5), high iron availability, and high nutrient utilization [*Ren et al.*, 2015] indicates reduced nutrient supply to the euphotic zone during glacial periods [*Jaccard et al.*, 2010], which may have evolved as result of several possible mechanisms. A fresher surface layer, saltier deep layer, or both would create a stronger pycnocline that would impede mixing to significant depths [*Zahn et al.*, 1991], while a thicker volume of low density surface water would depress nutrient-rich deep waters out of reach of the mixed layer depth. A decrease in wind strength would shoal mixing depths, potentially enhancing the stratifying effects of coincident changes to the pycnocline. Also, a reduction of nutrient concentrations in the subsurface water would limit the resupply of nutrients to the surface during mixing, in addition to any changes to the physical mixing regime. These processes are not mutually exclusive, and all would contribute to the umbrella mechanism of increased glacial stratification. In the next sections, we consider the current evidence for or against each of these mechanistic components for reducing nutrient delivery to the glacial surface ocean.

4.4.2.1 Strengthening the pycnocline

The primary element that contributes to stratification is the vertical density profile of the upper ocean (0-200m). The depth and intensity of the pycnocline acts as a resistor against the downward mixing forces applied at the surface (such as wind strength, see next section). A steep pycnocline (large change in density over a short depth interval) creates a

diapycnal barrier against which the available energy for mixing is rapidly consumed, and a near-surface pycnocline places this barrier high in the water column, further limiting the mixed layer depth. The polar stratification hypothesis suggests that simply cooling the entire water column (as during a glacial period) can be sufficient to strengthen the pycnocline due to the non-linear temperature dependence of the equation of state [*Sigman et al.*, 2004]. In the Antarctic Ocean, the steepness of the pycnocline doubles when the entire water column is cooled by 2˚C [*Sigman et al.*, 2004]. Conversely, negative temperature excursions have the opposite effect on density profiles in the Subarctic Pacific (Figure 4.6), based on reproducing the Sigman et al. (2004) calculations on a representative temperature and salinity profile from Station PAPA. Cooling the water column by 2˚C actually weakens the density gradient in the upper ocean ($\sigma_{200m} - \sigma_{0m}$) from 1.047g/m^3 to 1.017 kg/m^3. Continuing to cool the water column all the way to the freezing point (-1.9˚C) only further weakens the density gradient, to 0.8958 kg/m^3. Only by also decreasing the surface salinity (by 0.5 in the upper 100m, in this example) relative to the rest of the water column does the pycnocline steepen, with an increased density gradient of 1.39 kg/m^3. The dissimilar response of Subarctic Pacific and Antarctic density profiles is likely driven by the order of magnitude steeper halocline in the Subarctic Pacific (change in salinity of 1.1) compared to the Antarctic (change in salinity of 0.2, in Sigman et al., 2004), giving salinity much more influence over the density profiles in the Subarctic Pacific than in the Antarctic. A consequence of the dominance of salinity in the Subarctic Pacific is that glacial cooling cannot, on its own, generate enhanced stratification, as it can in the Antarctic. Additional processes reducing the salinity of surface waters during glacial periods must also be invoked in order to create the steep density profiles that characterize stratification.

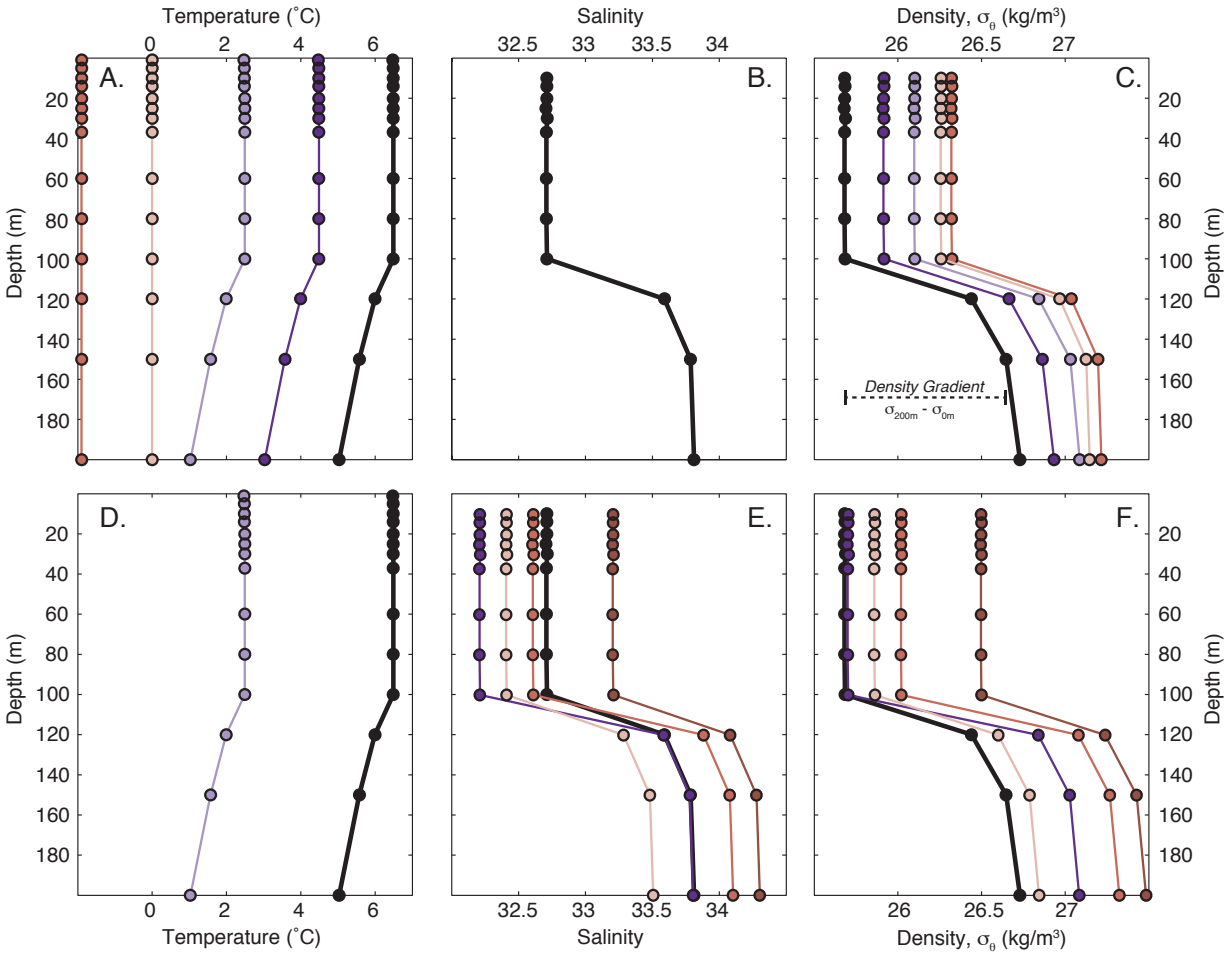

Figure 4.6. Simulated response of upper ocean (0-200m) density profiles to changes in temperature and salinity. Representative wintertime profile (January 21, 2017) from Station PAPA (bold black lines) from National Oceanic and Atmospheric Administration Pacific Marine Environmental Laboratory (NOAA-PMEL). Analyses follow those presented in Sigman et al. (2004) for the Antarctic Ocean. Potential temperature profiles (A) are modified by cooling the entire water column by 2˚C, cooling the entire water column by 4˚C, cooling the entire water column to 0˚C, and cooling the entire water column to -1.9˚C, the freezing point of seawater. Density profiles (C) calculated using the modified temperatures and unchanged salinity (B) demonstrate weaker density gradients than that of the unmodified density profile (bold black line), indicating reduced stratification. Only when the water column is cooled (D) and the upper 100m salinity is reduced (E) does the density gradient steepen, indicating increased stratification. Dashed bar (C) represents the density gradient as calculated by subtracting the density at 0m from the density at 200m. Results are not dependent on the initial profile selected for the analysis (see Supplemental Figure S4.2).

One mechanism of freshening surface waters may have been the glacial closure of the Bering Strait, which reduced freshwater export out of the Pacific. In the modern ocean, approximately 1 Sv of relatively fresh water flows through the shallow (50m) strait from the Pacific to the Atlantic via the Arctic [*Talley*, 2008]. Lower sea level during the glacial period would have cut off this pathway and retained that freshwater flux in the North Pacific [*Keigwin and Cook*, 2007], and the opening and closure of the Bering Strait may be a toggle between Atlantic Meridional Overturning Circulation (MOC) and Pacific MOC on glacial-interglacial timescales [*Shaffer and Bendtsen*, 1994; *De Boer and Nof*, 2004; *Hu et al.*, 2010, 2012b, 2012a, 2015]. Only one study has modeled the consequent influence of Bering strait closure on sea surface salinity in the Subarctic Pacific, generating a spatially heterogeneous decrease in sea surface salinity of up to 1 [*Hu et al.*, 2010]. The relatively coherent productivity records (Figure 4.5) are inconsistent with simulated regionally specific changes in surface salinity and stratification, but it is unclear if these patterns would be robust with integration over longer time periods. Future efforts on modeling the spatial patterns of sea surface salinity during glacial periods will help corroborate the distribution of freshwater and the potential role for closure of the Bering Strait on stratification in the glacial Subarctic Pacific.

An additional mechanism to redistribute salinity, add freshwater to the surface, and generate stratification in the Subarctic Pacific may be the formation, transport, and melting of sea ice [*Sancetta*, 1983; *Keigwin et al.*, 1992; *Gorbarenko*, 1996; *Seki et al.*, 2004]. Sea ice forms in the wintertime in the Okhotsk and Bering Seas, and localized brine rejection in thin coastal margin regions removes buoyancy from near-surface waters enough to create North Pacific Intermediate Water (NPIW) [*Shcherbina et al.*, 2003]. Because winds blow the sea ice away from their originating polynyas [*Pease*, 1980; *Sakamoto et al.*, 2005], brine rejection occurs repeatedly in the same spatially limited location, in a

densification process that is distinct and independent from deep vertical mixing (and nutrient supply). Sequestering the relatively saline water into the NPIW at subsurface depths (>50m) allows for a net freshening of surface waters (0-50m) [*Hillaire-Marcel and de Vernal*, 2008], which retain the sea ice and meltwater. Enhanced formation and export of NPIW due to an amplified sea ice cycle during glacial periods [*Katsuki and Takahashi*, 2005; *Sakamoto et al.*, 2005; *Caissie et al.*, 2010; *Artemova et al.*, 2017] may sufficiently freshen surface waters to instigate stratification and thus diminish productivity. Indeed, reconstructions of $d^{13}C$ from benthic foraminifera have identified a high $\delta^{13}C$, high eNd water mass above 2000m during the last glacial maximum that is attributed to a more vigorous NPIW [*Keigwin*, 1987, 1998; *Matsumoto et al.*, 2002; *Horikawa et al.*, 2010; *Knudson and Ravelo*, 2015b; *Cook et al.*, 2016; *Jang et al.*, 2017; *Max et al.*, 2017].

Connecting NPIW formation with the sea ice cycle rather than focusing on a seesaw with Atlantic Meridional Overturning Circulation (AMOC) [e.g., *Mikolajewicz et al.*, 1997; *Okazaki et al.*, 2010; *Hu et al.*, 2012b; *Freeman et al.*, 2015; *Menviel et al.*, 2017] allows for enhanced NPIW formation even when AMOC is relatively strong [*Lynch-Stieglitz et al.*, 2007; *Böhm et al.*, 2015; *Jonkers et al.*, 2015; *Henry et al.*, 2016] and releases NPIW formation from the transience of millennial scale events that characterize AMOC variability [*Ng et al.*, n.d.; *Boyle and Keigwin*, 1987; *McManus et al.*, 2004; *Praetorius et al.*, 2008; *Henry et al.*, 2016]. Because sea ice formation increases when temperature cools, NPIW formation would follow global climate [e.g., *Lisiecki and Raymo*, 2005] creating the glacial-interglacial cycles in stratification inferred from the productivity records. Furthermore, in contrast to previous studies that have anticipated spatial variability from sea ice effects [*Brunelle et al.*, 2007, 2010], rapid advection across the Subarctic Pacific (1-2 years, [*Smith et al.*, 2015]) would distribute freshwater fluxes on timescales consistent with

the spatially homogeneous productivity records. Thus the sea ice-NPIW mechanism for generating stratification can account for both the spatially homogeneous productivity response as well as the link between stratification and global climate.

The sea ice-NPIW hypothesis could be tested by reconstructing the seawater $\delta^{18}O$ ($\delta^{18}O_{sw}$) profile of the upper ocean (0-200m) over time. When sea ice forms, it fractionates $\delta^{18}O$ such that the ice is isotopically enriched and the residual brine is isotopically depleted [*O'Neil*, 1968], making sea ice formation the only process by which a negative correlation between $\delta^{18}O$ and salinity develops [*Hillaire-Marcel and de Vernal*, 2008]. Thus sea ice melt can be identified in surface waters (<50m) by the presence of cold (fresh) and high $\delta^{18}O_{sw}$ water overlying saltier but lower $\delta^{18}O_{sw}$ water (subducted brines) [*Hillaire-Marcel and de Vernal*, 2008; *Brennan et al.*, 2013; *Riethdorf et al.*, 2013b]. Such a profile may be constructed by analyzing paired $\delta^{18}O$ and temperature (e.g., Mg/Ca) in planktonic foraminifera that inhabit different depths in the surface ocean (Figure 4.7). Although foraminiferal depth habitats appear to be highly variable across the Subarctic Pacific [*Kuroyanagi et al.*, 2008; *Iwasaki et al.*, 2017; *Taylor et al.*, 2018], at any one station a depth distribution in foraminifera species is often observed. For example, plankton tows from Station PAPA suggest that *G. bulloides, G. quinqueloba,* and *N. incompta* are most abundant in the upper 50m, while *N. pachyderma* and *O. universa* are most abundant in the 200-300m depth [*Iwasaki et al.*, 2017]. Under normal conditions the surface (<50m) to deep (200-300m) $\delta^{18}O_{sw}$ gradient ($\Delta\delta^{18}O_{sw}$ $^{200\text{-}0m}$) would be slightly positive (Figure 4.7A), according to the standard positive relationship between $\delta^{18}O_{sw}$ and density. During either winter sea ice formation (Figure 4.7B) or spring sea ice melt (Figure 4.7C), the $\delta^{18}O_{sw}$ gradient would invert, with higher $\delta^{18}O_{sw}$ observed in the surface (<50m) species and a negative gradient with depth. This approach would, of course, have to contend with

complicating factors such as the sensitivity of upper ocean $\delta^{18}O_{sw}$ to perturbations in the sea ice, the seasonality of each planktonic species [e.g., *Reynolds and Thunell*, 1985; *Fraile et al.*, 2009],

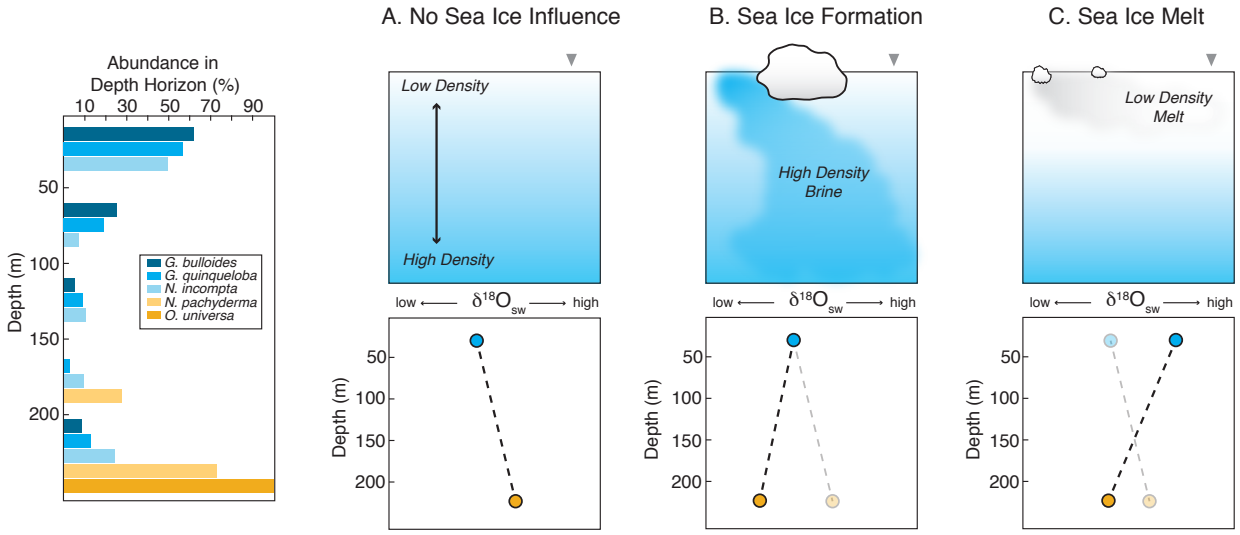

Figure 4.7. Hypothetical effects of sea ice formation on upper ocean $\delta^{18}O_{sw}$ profiles. (*Left)* Planktonic foraminiferal distribution in a plankton tow at Station PAPA [*Iwasaki et al.*, 2017]. At least 50% of all *G. bulloides, G. quinqueloba, and N. incompta* were recovered within the 0-50m depth, making these species the best candidates for recording shallow conditions. More than 70% of all *N. pachyderma* and *O. universa* were recovered from the 200-300m depth, making these species the best candidates for recording subsurface conditions. (*Right*) Hypothetical changes to upper ocean $\delta^{18}O_{sw}$ profiles recorded by shallow (blue) and subsurface (orange) foraminiferal species in response to different sea ice events. Gray triangles indicate the relative location for the water column profiles shown in the bottom panels. (A) When no sea ice is present, the $\delta^{18}O_{sw}$ gradient is positive. (B) During sea ice formation, high density low $\delta^{18}O_{sw}$ brines invert the $\delta^{18}O_{sw}$ gradient. Faint line and circle show the initial profile as in scenario A. (C) During sea ice melt, low density high $\delta^{18}O_{sw}$ meltwater also enhances the negative $\delta^{18}O_{sw}$ gradient. Faint line and circles show the starting profile from A.

the local depth habitats of different planktonic species [e.g., *Iwasaki et al.*, 2017; *Taylor et al.*, 2018], secondary influences on both $\delta^{18}O_{sw}$ and Mg/Ca (e.g., Hönisch et al., 2013), and calibration uncertainties on Mg/Ca for each planktonic species (e.g., Anand et al., 2003). Yet, unlike other sea ice proxies like diatom assemblages or IP_{25}, the $\Delta\delta^{18}O_{sw}$ $^{200\text{-}0m}$ has the advantage of recording the distal extent of sea ice melt far from the sea ice margin as well as the in situ consequences of sea ice melt on stratification of the upper ocean (0-200m). Future work to develop this proxy may contribute towards understanding the density structure of the upper ocean and its effects on stratification, nutrient delivery to the surface, and thus productivity under glacial-interglacial climate conditions.

4.4.2.2. Weaker winds

Changes in wind strength may compound changes in the pycnocline to influence stratification (Figure 4.8). Wind forcing at the sea surface provides the energy to propel downward mixing. The depth of the mixed layer is thus a function of both the energy (wind strength) applied to and the resistance (density structure) within the surface ocean. For example, weak winds combined with a strong pycnocline would severely depress the winter mixing depth and nutrient delivery to the surface [e.g., *Beaufort et al.*, 1997]. On the other hand, if strong winds countered a strong pycnocline, the increased mixing energy might overcome the increased resistance to mixing, such that there may be no net change in the winter mixing depth. The influence of winds on mixing depth and nutrient delivery to the surface was directly observed during the strong El Niño of 1997-1998, when weakening of winds during winter 1997 [*Sasaoka et al.*, 2002] resulted in lower than average surface nutrient concentrations the subsequent summer at station KNOT in the West Subarctic [*Honda et al.*, 2002]. In general, a positive correlation between the strength of winter winds

and primary productivity in the following summer has been observed in the Subarctic gyre in the twentieth century [*Brodeur and Ware*, 1992]. Thus considering how wind strength may have varied under glacial climate conditions is imperative to understanding the mechanisms behind enhanced stratification and surface nutrient delivery.

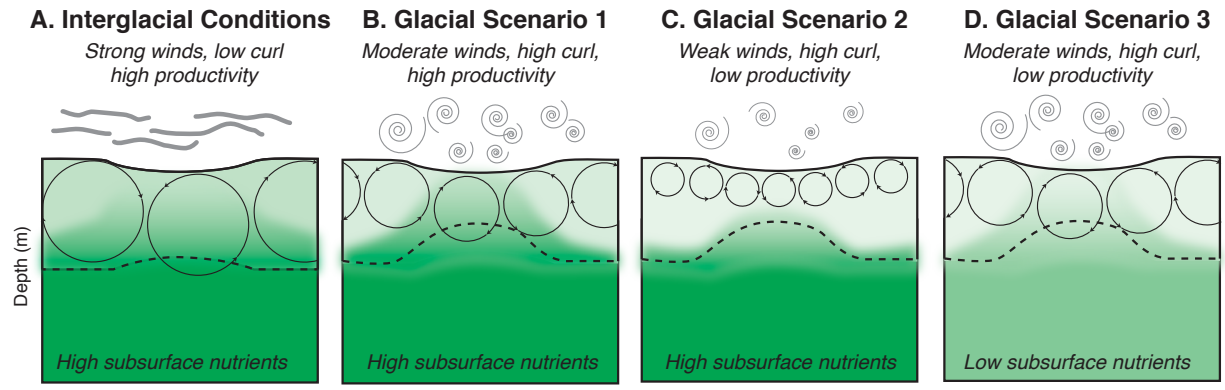

Figure 4.8. Hypothetical effects of changing winds on nutrient concentrations in the upper ocean. Schematic shows wind strength (gray lines), wind curl (spirality of gray lines), surface mixing (arrowed circles), nutricline (dashed line), and nutrient concentrations (green shading). (A) During interglacial periods, strong winds create deep mixing that can penetrate the high subsurface nutrients, despite a deep nutricline. Relatively high surface nutrient concentrations leads to high productivity. (B) During glacial periods, enhanced wind stress curl shoals the nutricline and moderate winds reduce the mixing depths. If the mixing depth intersects the nutricline, then surface nutrient concentrations would still remain high. This scenario is inconsistent with low glacial productivity in the Subarctic Pacific (Figure 4.5). (C) Weak winds (or strong pycnocline, not shown) may reduce mixing depths so that they are unable to reach the nutrient rich subsurface waters. Nutrient concentrations in the surface ocean remain low, consistent with low glacial productivity. (D) Surface mixing and nutricline as in (B), but with low subsurface nutrient concentrations. Upward mixing only supplies low nutrient concentrations to surface waters, consistent with low glacial productivity. A fourth scenario could combine the weak winds of (C) and the low subsurface nutrients of (D) to also generate low glacial productivity.

Globally, steeper meridional temperature gradients during the last glacial period predict stronger winds [*McGee et al.*, 2010], particularly in the mid-latitudes [*Rind*, 1998]. Strong mid-latitude jets are associated with an increase in eddy kinetic energy (storminess) [*Penny et al.*, 2013], which should increase mixing depths and nutrient delivery to surface waters [*O'Gorman*, 2010]. However, the presence of the Laurentide Ice Sheet likely deflected (or possibly bifurcated) the westerly storm track [*COHMAP*, 1988; *Bromwich et al.*, 2004; *Oba et al.*, 2006; *Kirby et al.*, 2013; *Oster et al.*, 2015], shifting it as much as 10˚ latitude to the south in the middle of the North Pacific [*Lora et al.*, 2017] (Figure 4.1). The more southerly storm track likely pushed this zone of storminess into the subtropical gyre, and models corroborate a net decrease in eddy kinetic energy over much of the Subarctic Pacific [*Li and Battisti*, 2008; *Lora et al.*, 2017]. This finding is consistent with modeled reductions of storminess over similar latitudes in the North Atlantic during the last glacial period [*Li and Battisti*, 2008; *Dohonoe and Battisti*, 2009; *Riviere et al.*, 2018]. Therefore, it seems likely that winds were weaker in the Subarctic Pacific during glacial compared to interglacial periods, and these weak winds potentially contributed to reduced mixing depths, increased stratification, decreased nutrient delivery, and reduced productivity under glacial conditions.

In addition to powering winter mixing of surface waters, wind strength and wind stress curl can also affect nutrient delivery to the surface by upwelling and Ekman divergence. Seasonal upwelling along the continental margin delivers nutrient-rich subsurface waters (~100m) to the surface [*Wheeler et al.*, 2003], extending about 100km off the coast [*Whitney et al.*, 2005]. These nutrients can be transported laterally by tidal mixing, eddy diffusion, and local turbulence [*Whitney et al.*, 2005], so that coastal upwelling may be able to influence surface nutrient concentrations into the open ocean. Weak winds during glacial periods likely reduced coastal upwelling and repressed the potential nutrient

leak from the coast to the open ocean. As all of the sites investigated here show similar patterns in productivity (Figure 4.5) regardless of distance from the coast, they do not appear to be sensitive to changes in the rates of coastal upwelling and nutrient leakage. Instead, they are more likely to respond to changes in the major source of nutrients in the subarctic gyre, Ekman divergence [*Reid*, 1962; *Gargett*, 1991].

Ekman divergence occurs within the subpolar gyre as a result of positive wind stress curl [*Reid*, 1962], and the rates of associated upwelling are more or less equivalent in the East and the West Subarctic [*Gargett*, 1991; *Harrison et al.*, 1999]. This upwelling leads to shoaling of the nutricline that may be sufficient to allow deep winter mixing to tap into those nutrient rich waters [*Reid*, 1962; *Brodeur and Ware*, 1992]. During glacial periods, the wind stress curl would have increased in the Subarctic as the westerlies, the zero point of wind stress curl [*Thomson*, 1981], shifted southward and away from the Subarctic (Figure 4.8). Indeed, models suggest that wind stress curl may have been as much as 60% higher in this region during the last glacial period [*Gray et al.*, 2018], increasing Ekman divergence and shoaling sub-surface waters. Yet glacial productivity was still lower than interglacial productivity. This contradiction between high rates of upwelling and low productivity can be reconciled either by particularly weak surface mixing or by low subsurface nutrient concentrations. If the decrease in mixing depth outpaced the shoaling of the nutricline, it is possible that the mixing depths were insufficient to breach the nutrient rich sub-surface waters (Figure 4.8C), due to either very weak winds or a strong pycnocline (Section 4.4.2.1). Alternatively, surface mixing may have intersected the sub-surface waters, but nutrient concentrations of those waters may have been lower during glacial periods than during interglacial periods (Figure 4.8D). In either case, changes to wind stress do not appear to have been the primary driving force for changes in productivity on glacial-interglacial timescales.

4.4.2.3. Reduced subsurface nutrient concentrations

Changes in ocean ventilation suggest that reduced subsurface nutrient concentrations may have been characteristic of the glacial Subarctic [*Jaccard et al.*, 2010; *Lam et al.*, 2013]. This mechanism is based on the chemical properties of water masses, and it is distinct from physical stratification, although the two are sometimes considered homologous. Today, deep winter mixing reaches depths of ~150m and intersects with high subsurface nutrient concentrations (Figure 4.8A), propagating those high nutrients into surface waters. Nutrient concentrations within subsurface waters (>150m) are a balance between mixing of young, nutrient-poor NPIW formed in the Okhotsk Sea [*Talley*, 1993; *You*, 2003] and old, nutrient-rich North Pacific Deep Water (NPDW), and modern NPIW is characterized by a steep vertical seawater $\delta^{13}C$ gradient from high $\delta^{13}C$ at the surface to low $\delta^{13}C$ at depth [*Kroopnick*, 1985]. Enhanced NPIW formation during glacial periods (see Section 4.4.2.1) expanded the high $d^{13}C$ (low nutrient) water mass to 2000m [*Keigwin*, 1998; *Matsumoto et al.*, 2002], pushing the nutrient-rich NPDW to greater depths [*Boyle*, 1988] and reducing the nutrient concentrations of subsurface waters potentially attainable by winter mixing [*Gray et al.*, 2018]. Thus lower subsurface nutrient concentrations likely combined with weaker winds and enhanced surface freshening to reduce productivity during glacial periods.

4.5. Conclusions

Productivity across the Subarctic Pacific varies coherently with glacial-interglacial cycles, with low productivity characterizing glacial periods in the open ocean and the marginal seas in both the east and the west. Stratification of surface waters has been

suggested as the main driver of variability in productivity, and here we investigated the potential mechanisms for generating stratification during glacial periods. Cooling of the water column alone is insufficient to increase the density gradient of the upper ocean (0-200m), but increased freshwater inputs to the surface may have contributed to a steeper pycnocline. Possible freshwater sources include sea ice melt and closure of the Bering Strait. Weaker winds, due to a southward shift of the westerlies, may have reduced the surface mixing depths, limiting nutrient supply to the surface, but increased wind stress curl would have increased upwelling and shoaled the nutricline, making subsurface waters more accessible to even shallow mixing. A near-surface nutricline may be reconcilable with low glacial productivity if the subsurface nutrient concentrations were also low, perhaps due to enhanced NPIW formation of flushing of subsurface waters during glacial periods. In summary, low glacial productivity was caused by stratification and low surface nutrient concentrations induced by reduced surface mixing (weak winds and strong pycnocline) combined with upwelling of nutrient poor subsurface waters.

4.6. Data Archiving

All data are archived at the National Oceanic and Atmospheric Administration National Centers for Environmental Information (NCEI) database.

4.7. Supplementary Material

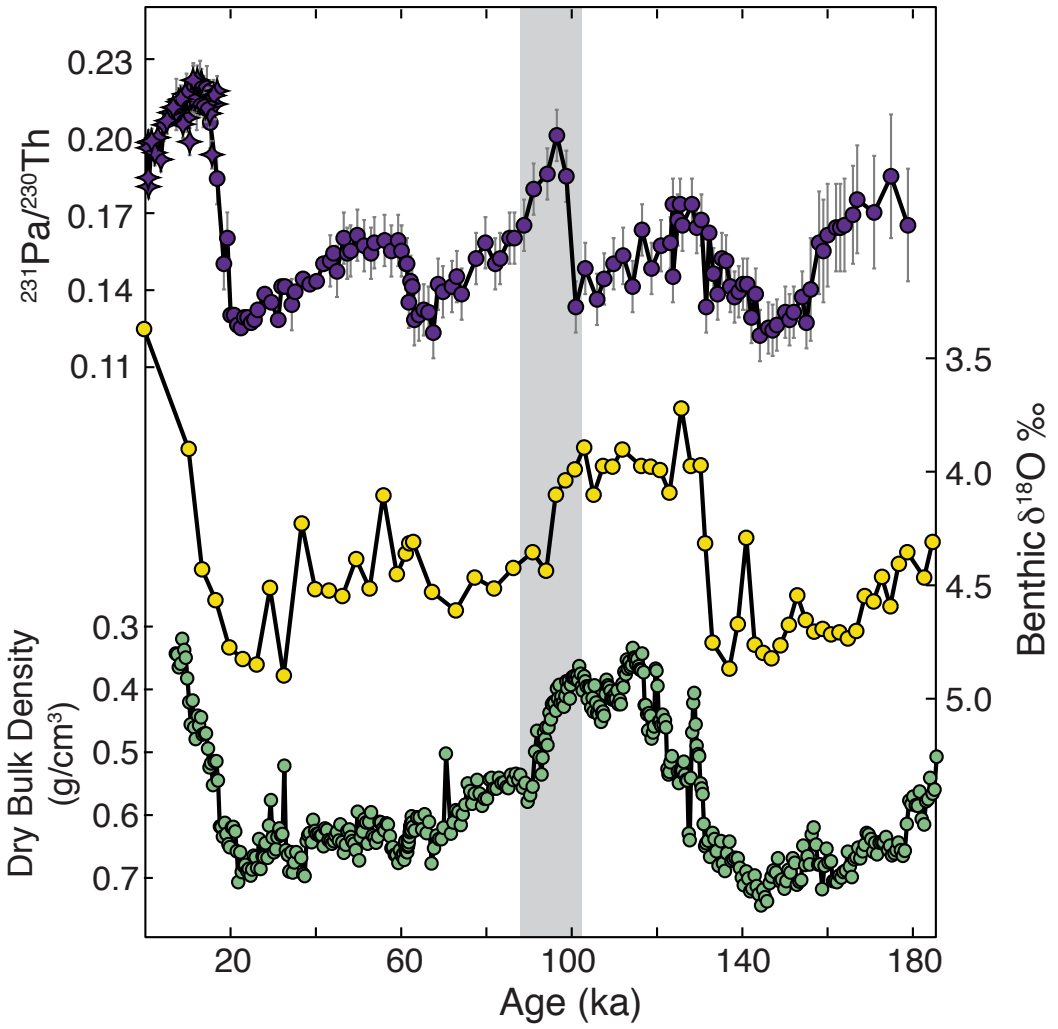

Figure S4.1. ^{231}Pa/^{230}Th record compared with chronostratigraphic indicators for site 06MC-09PC. (*Top*) ^{231}Pa/^{230}Th as in Figure 4.2, with error bars indicating the 2 σ range. (*Center*) Benthic oxygen isotopes from core 09PC (Costa et al., 2016). (*Bottom*) Dry bulk density from core 09PC (Costa et al., 2016), which demonstrates glacial-interglacial variability in this region due to changes in carbonate preservation (e.g., Farrell and Prell, 1989). Note inverted y-axis, with low-density sediment characterizing interglacial periods, and high-density sediment characterizing glacial periods. The transition from MIS6 into MIS5 is well constrained by both an abrupt decrease in δ^{18}O and a decrease in dry bulk density. The peak in ^{231}Pa/^{230}Th around 96.5ka (highlighted by the gray bar) clearly occurs after the MIS6/5 transition. It appears to coincide with an increase in δ^{18}O and increase in dry bulk density that would indicate the end of MIS5. Thus this ^{231}Pa/^{230}Th peak is distinct from the MIS5e peaks observed in other cores.

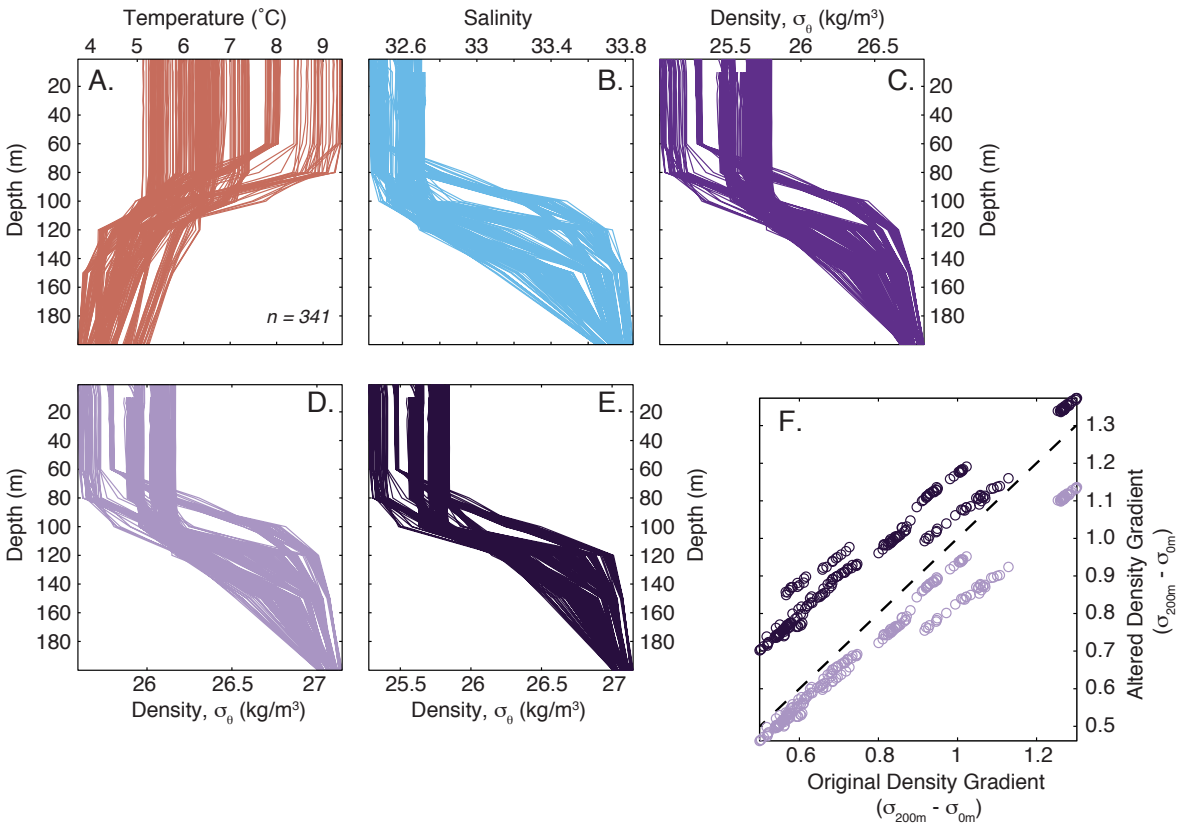

Figure S4.2. Simulated response of upper ocean (0-200m) density profiles to changes in temperature and salinity. As in Figure 4.7, but for all available water column profiles in January from 2007-2018 (*n* = 341). All temperature (A), salinity (B), and density (C) data from Station PAPA from National Oceanic and Atmospheric Administration Pacific Marine Environmental Laboratory (NOAA-PMEL). D) Density profiles recalculated after applying a 2˚C cooling to the temperature profiles (A) with no change to the salinity. E) Density profiles recalculated after applying a 2˚C cooling to the temperature profiles (A) and a 0.4psu freshening to the top 100m of the salinity profiles (B). F) Change in the surface (0m) to subsurface (200m) density gradient due to the applied temperature and salinity changes. The original density gradient is calculated from the unaltered density profiles in (C). The altered density gradient is calculated from the profiles in D (light purple) and E (dark purple). Dashed line is the 1:1 line. When only a temperature effect is applied, the density gradient becomes less steep. To steepen the density gradient, a change in surface salinity (<100m) is also required.

Chapter 5

Dust deposition in the East Subarctic Pacific on glacial-interglacial timescales

Abstract:

Across the North Pacific, the predominant dust source is presumed to be the Asian continent, with dust fluxes generally decreasing with increasing distance. While it is well established that dust fluxes vary on glacial-interglacial timescales, the evolution of dust distribution from Asian source to Pacific sediment is poorly constrained, largely due to a lack of long-term dust flux records from this region. Here we reconstruct dust flux variability in the East Subarctic Pacific over the past 500kyr using ^{232}Th as a lithogenic tracer and ^{230}Th normalization to calculate fluxes. Dust fluxes generally vary by a factor of two between glacial, high-dust flux, and interglacial, low-dust flux periods, consistent with global patterns. We compare these new records from the East Subarctic with dust flux records from the West Subarctic and the Equatorial Pacific to better constrain how dust deposition varied spatially during the last glacial maximum. Glacial dust fluxes appear asymmetric, with more dust concentrated in the West Subarctic than in the East Subarctic relative to the depositional patterns of interglacial periods. We investigate multiple mechanisms that can reorganize the spatial deposition of dust across the North Pacific, including changes in precipitation, the trajectory and speed of the westerlies, and non-Asian lithogenic sources. Deconvolving lithogenic provenance using trace element ratios identifies a substantial North American lithogenic component to the East Subarctic, with nearly 45% of lithogenic material derived from much North. Asian ^{232}Th fluxes are

generally higher than North American ^{232}Th fluxes, but North American ^{232}Th fluxes demonstrate clearer glacial-interglacial cycles. We suggest that the southward shift of the westerlies may deflect Asian dust away from the East Subarctic during glacial periods.

5.1. Introduction

Dust is an important component of the climate system, with both direct (e.g., radiative) and indirect (e.g., biogeochemical) consequences for the atmosphere and ocean (Anderson et al., 2014; Jickells et al., 2005; Martinez-Garcia et al., 2014). On glacial-interglacial timescales, global dust fluxes vary consistently, with greater marine dust deposition during glacial compared to interglacial periods (e.g., Winckler et al., 2008). Numerous mechanisms for this variability have been proposed, including, for example, increased gustiness (McGee et al., 2010), aridification (Prospero et al., 2002), increased overall wind strength (Lunt and Valdes, 2002; Mahowald et al., 2006; Werner et al., 2002), enhanced glaciogenic production (Kaiser and Lamy, 2010; Mahowald et al., 2006; Sugden et al., 2009), and expanded source areas (Delmonte et al., 2017; Mahowald et al., 2011). Dust emissions from Asia, the presumed dust source across the North Pacific (Mahowald et al., 2011; Prospero et al., 2002), have specifically been linked to changes in seasonality such that dustier periods correspond to a lengthened dust-producing season (Serno et al., 2017). Because of the prevailing westerlies, Asian dust can be transported thousands of kilometers across the North Pacific to the North American coast (Creamean et al., 2014; McKendry et al., 2001; Uno et al., 2011; Zdanowicz et al., 2006), while transport from the more proximal North American dust source is typically directed away from the Subarctic Pacific. Indeed, models of dust provenance suggest that North America contributes less than 10% of the eolian material that reaches the East Subarctic today (Tanaka and Chiba, 2006). This controlling influence of the westerlies on dust sources to the East Subarctic may have been

weaker during glacial periods, when the westerlies were shifted substantially to the south (e.g., COHMAP, 1988). In this study, we reconstruct lithogenic fluxes in the East Subarctic over the last 500,000 years and compare them with well-established Asian dust flux records to constrain how dust delivery and provenance may have varied in this region over time.

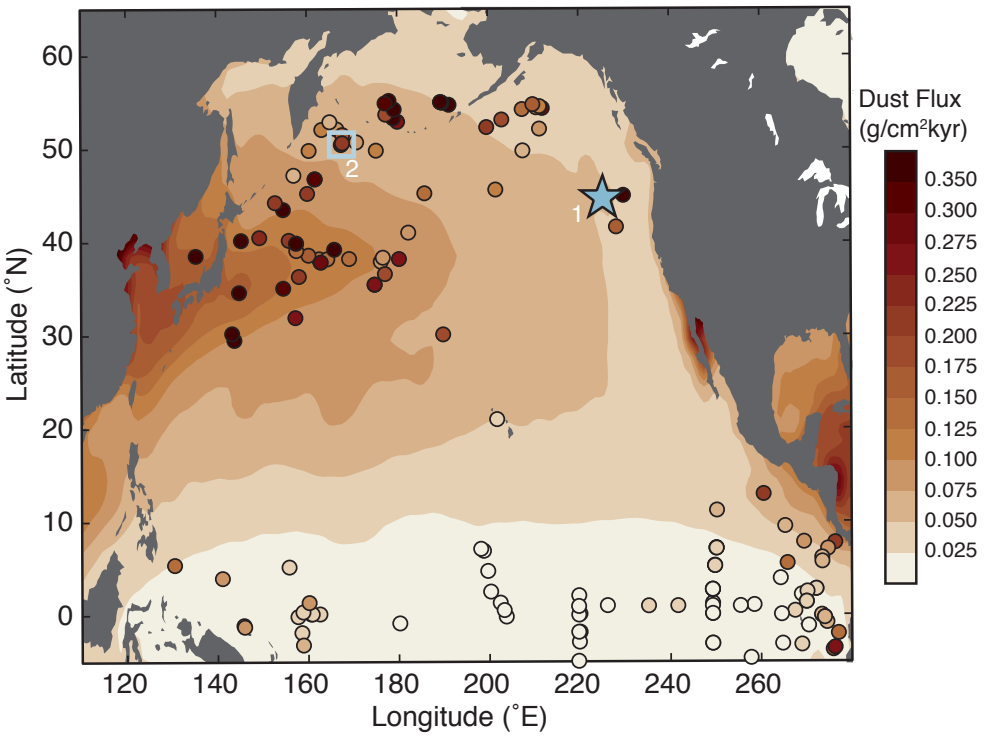

Figure 5.1. Dust deposition in the North Pacific. Background shading shows simulated modern dust deposition (Mahowald et al., 2011), while colored circles reflect Holocene dust fluxes measured in sediment samples using ^{230}Th-normalized ^{232}Th fluxes, compiled in ThoroMap (Kienast et al., 2016). The Juan de Fuca Ridge (JdFR) is shown by the teal star (1). The long dust flux record from the West Subarctic (ODP882, Serno et al., 2017) is identified with a teal square (2). Both the dust model and sediment samples capture a primary dust source emanating from Asia. Fine scale spatial variability in the sediment samples may suggest additional (atmospheric) processes affecting the spatial distribution of dust over the North Pacific.

5.2. Methods

Sediment cores were collected from the Juan de Fuca Ridge (JdFR, Figure 5.1) at approximately 45˚N, 230˚E (Table 5.1) on the SeaVOICE cruise (AT26-19) of the R/V Atlantis in September 2014. The cores are closely clustered (within 50km) and from similar depth range (2655-2794m), such that they can be combined as if representing multiple realizations of the same paleo-record (Costa and McManus, 2017). Age models for the piston cores (05PC, 09PC, 12TC/PC, 35PC, 38PC, and 39BB) are well-constrained based on radiocarbon dates, benthic $\delta^{18}O$, and stratigraphically tuned density cycles (Costa et al., 2016). Two multicores (06MC, 10MC) corresponding to piston cores (09PC, 12TC/PC respectively) are added to provide high-resolution data for the last 30,000 years. Age models for these multicores are primarily based on benthic $\delta^{18}O$ due to bioturbative effects on coretop radiocarbon dates (Costa et al., 2017a).

Samples (n=1170) were analyzed for thorium (^{230}Th, ^{232}Th) and uranium (^{238}U, ^{235}U, ^{234}U) by isotope dilution inductively coupled plasma mass spectrometry (ICP-MS). ^{230}Th data (Costa and McManus, 2017) and authigenic U data (Costa et al., 2018) have been previously published. Briefly, samples (100mg) were randomized and spiked with ^{229}Th and ^{236}U and processed with complete acid digestion and column chromatography (Fleisher and Anderson, 2003). Isotopes were measured on an Element 2 ICP-MS at Lamont-Doherty Earth Observatory (LDEO) of Columbia University. Discrete sediment aliquots (n=106) of an internal sediment standard (VOICE Internal MegaStandard, VIMS) were processed and analyzed for quality control, and these total replicates of VIMS indicate that the analytical procedure and measurement are externally reproducible within 3.7% (1σ) on ^{232}Th. Lithogenic fluxes are determined by ^{230}Th-normalization (Francois et al., 2004) of ^{232}Th concentrations. The ^{232}Th approach to reconstructing lithogenic fluxes has been successfully

applied on a global scale (e.g., Adkins et al., 2006; Bradtmiller et al., 2007; Jacobel et al., 2017; Lamy et al., 2014; Serno et al., 2017; Winckler et al., 2008), and substantial review of its utility is provided elsewhere (Anderson et al., 2006; McGee et al., 2016).

Table 5.1. Core locations on the Juan de Fuca Ridge.

Core	Lat ˚N	Long ˚E	Water Depth (m)
AT26-19-05PC	44.97283	229.1215	2711
AT26-19-09PC/06MC	44.88717	229.36317	2678
AT26-19-12PC-TC/10MC	44.8975	229.49567	2689
AT26-19-35PC	44.99118	229.54263	2731
AT26-19-38PC	44.97053	229.39347	2655
AT26-19-39BB	45.04507	229.16682	2794

5.3. Results

Lithogenic fluxes on the Juan de Fuca Ridge ranged over a factor of three (1.5-6.4 μg/cm^{2}kyr) during the last 500kyr (Figure 5.2). Generally, high lithogenic fluxes occurred during glacial periods, and low lithogenic fluxes occurred during interglacial periods. Average lithogenic fluxes were low during interglacial MIS13 (478-500ka, 2.03±0.51 μg/cm^{2}kyr), and they were followed by some of the highest lithogenic fluxes in the major glacial stage MIS12 (424-478ka, 4.32±0.96 μg/cm^{2}kyr). The next glacial cycle nearly repeated the same pattern, with low lithogenic fluxes (2.69±0.71 μg/cm^{2}kyr) in interglacial MIS11 (374-424ka) and high lithogenic fluxes (4.11±0.58 μg/cm^{2}kyr) in glacial MIS10 (337-374ka). Then, lithogenic fluxes moderately decreased into MIS9 (300-337ka, 3.02±0.27 μg/cm^{2}kyr), a prominent interglacial stage that was nevertheless nearly 50% dustier than

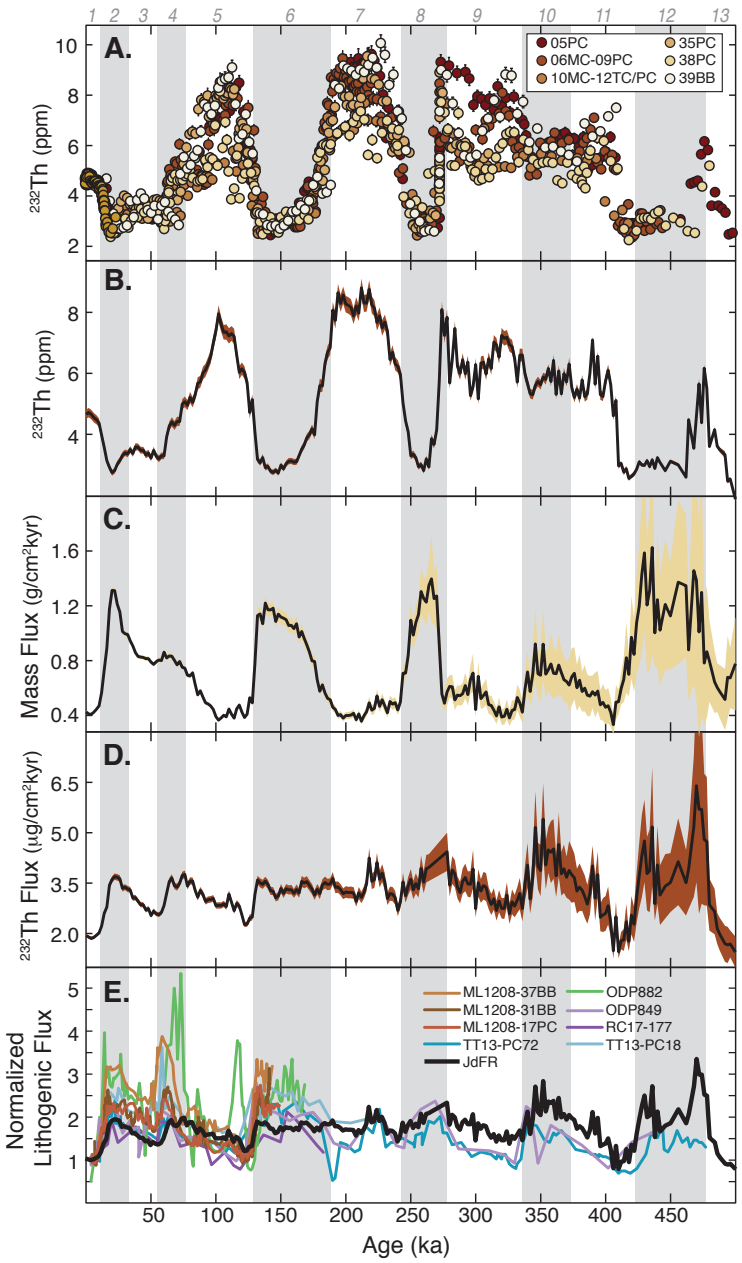

Figure 5.2. Dust flux data for the Juan de Fuca Ridge, East Subarctic Ocean. A) Individual ^{232}Th concentration measurements (n=1170). Error bars show 2σ. B) Stacked ^{232}Th concentration record for the Juan de Fuca Ridge. Data in (A) are averaged (mean) in 2kyr bins. Shaded region shows 2σ. C) ^{230}Th normalized mass flux stack, from Costa and McManus (2017), averaged (mean) in 2kyr bins. Shaded region shows 2σ. D) ^{232}Th flux stack for the Juan de Fuca Ridge, calculated by multiplying the ^{232}Th stack in (B) by the mass flux stack in (C). Shaded region shows 2 standard error. E) Relative lithogenic fluxes, each normalized to its Holocene dust flux average (0-10ka). TT13-PC72 (Anderson et al., 2006; Winckler et al., 2008); TT13-PC18 (Anderson et al., 2006); RC17-177, ODP849 (Winckler et al., 2008); ML1208-31BB, ML1208-37BB, ML1208-17PC (Jacobel et al., 2017); ODP882 (Serno et al., 2017). All records are normalized to ^{230}Th-derived mass fluxes. The West Subarctic (ODP882) shows the greatest glacial-interglacial variability, as much as a factor of 5. Other records from the Equatorial Pacific suggest glacial-interglacial variability closer to a factor of 2. Errors on normalized dust fluxes range from less than 4% (relative standard deviation) in the youngest sediment (<200ka) to ~20% in the oldest sediment (>400ka). Gray bars highlight glacial periods, identified by even Marine Isotope Stages (gray numbers at top).

the previous interglacial period MIS11 (statistically different at 95% confidence interval, $p<0.001$). Lithogenic fluxes were fairly constant for the next two glacial cycles, with only small shifts between adjacent glacial and interglacial periods, from MIS8 (244-300ka, 4.09±1.49 μg/cm^{2}kyr) to MIS7 (190-244ka, 3.36±0.34 μg/cm^{2}kyr), followed by MIS6 (130-190ka, 3.36±0.15 μg/cm^{2}kyr), MIS5 (74-130ka, 3.00±0.40 μg/cm^{2}kyr), and MIS2-3-4 (12-74ka, 3.13±0.40 μg/cm^{2}kyr). Only during the Holocene (MIS1, 0-12ka) did lithogenic fluxes return to the low interglacial values (1.98±0.14 μg/cm^{2}kyr) observed nearly 500kyr earlier.

5.4. Discussion

5.4.1 Spatial patterns

Lithogenic fluxes from the JdFR are consistent with long dust flux records from across the North Pacific (Figure 5.2E) (Anderson et al., 2006; Jacobel et al., 2017; Serno et al., 2017; Winckler et al., 2008). All show glacial-interglacial variability with higher lithogenic fluxes during glacial periods by at least a factor of 2 (relative to the Holocene), and the greatest dust flux variability (factor of 5) seems to occur in the record closest to the Asian dust source (ODP882, Serno et al., 2017). A spatial time slice of relative dust fluxes at the Last Glacial Maximum (Figure 5.3) generally corroborates the patterns suggested by the long records in Figure 5.2, with the Last Glacial Maximum (LGM, 18-28ka) and Holocene (H, 0-10ka) broadly defined to allow for age model uncertainties and to maximize the number of sites included. Within global databases like ThoroMap (Kienast et al., 2016) and DirtMap (Kohfeld and Harrison, 2001), marine records generally have LGM/H values greater than 1, with an average LGM/H around 2, in contrast to terrestrial records and ice cores that have even higher LGM/H values (e.g., as much 45 in Greenland, Ruth et al., 2007).

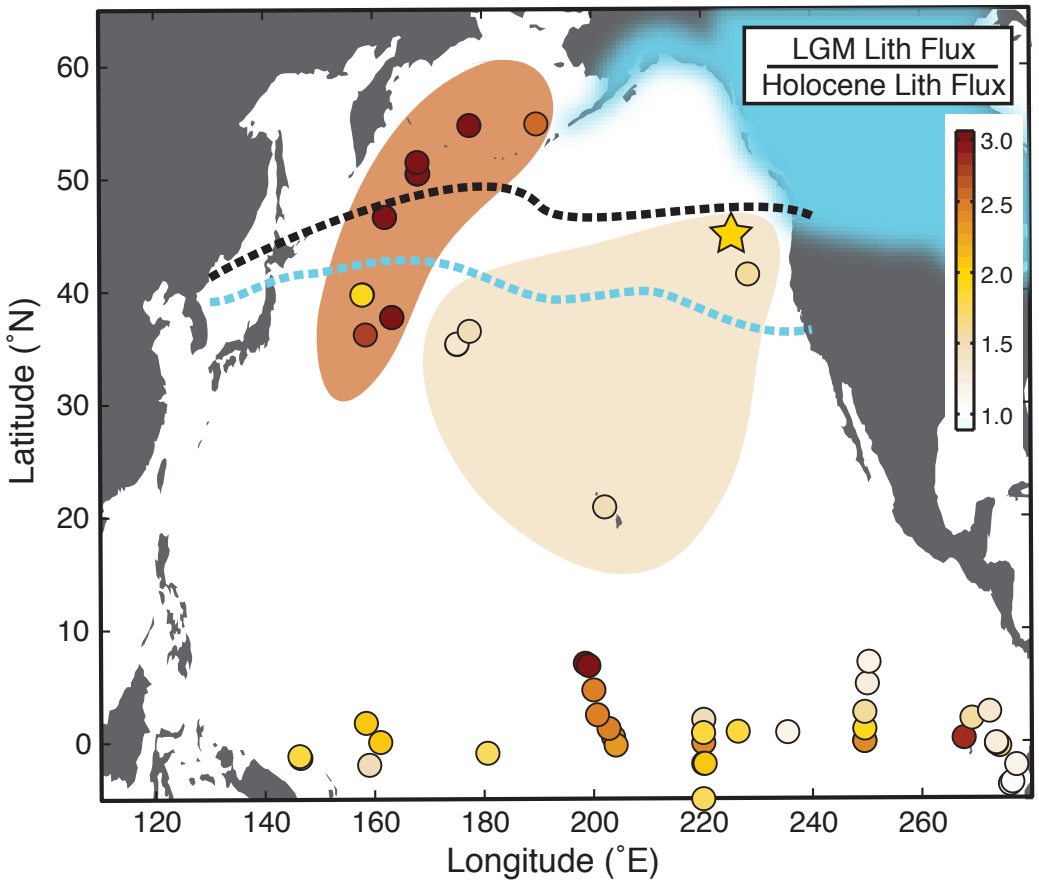

Figure 5.3. Spatial map of LGM/H lithogenic flux ratios. Relative change in lithogenic deposition in the last glacial period, with new JdFR record (star) and other ^{230}Th-normalized ^{232}Th or ^{4}He based lithogenic flux records (circles). Ice sheet extent at ~21ka on North America is shown in blue. The mean position of the westerlies is shown as a dashed line for the Holocene (black) and LGM (blue, after COHMAP, 1988); the full expanse of the westerlies (over 10˚ latitude) is not show to maintain clarity. Two broad regions of similar lithogenic deposition are identified by the shaded areas: high LGM/H lithogenic fluxes (>2) in the West Subarctic and the Bering Sea, and lower LGM/H lithogenic fluxes (≤2) in the East Subarctic and Subtropical Gyre.

Lithogenic fluxes about twice as high during the LGM compared to the Holocene characterize much of the North Pacific, from the North American coast as far west as 180˚E (V32-126, V32-128) and as far south as 20˚N (V21-59, Hawaii), and maybe even into the Eastern Equatorial Pacific (0-10˚N, 220-280˚E). The high LGM/H values and meridional gradient in LGM/H in the Central Equatorial Pacific (Jacobel et al., 2017) are likely related to the effects of migration of the Inter-Tropical Convergence Zone (ITCZ) and changing dust sources (Jacobel et al., 2016; McGee et al., 2007; Reimi and Marcantonio, 2016; Xie and Marcantonio, 2012). In the West Subarctic from east of Japan northward into the Bering Sea, there is a region of higher than average LGM/H (>2, and most >3) relative to other marine records from the North Pacific. For example, at about the same latitude, LGM/H is 4.5 in the West Subarctic (V20-122, 46.6˚N, 162˚E) but only 2 in the East Subarctic (JdFR, 45˚N, 230˚E). Consequently, the apparent zonal dust flux gradient across the Subarctic Pacific is more than twice as steep during the LGM relative to the Holocene.

If all the lithogenic material deposited in the North Pacific is Asian dust, then the zonal dust flux gradient would be primarily controlled by atmospheric processes, such as the transport trajectory and length of a dust-laden air mass, as well as the frequency and amount of precipitation. The high LGM/H in the West Subarctic relative to the rest of the North Pacific could therefore be partly due to increased glacial wet deposition in the West Subarctic. Dust deposition over the open ocean usually occurs by wet deposition (Bergametti and Foret, 2014; Mahowald et al., 2011; Tanaka and Chiba, 2006), including both in-cloud (rainout) and below-cloud (washout) scavenging of atmospheric dust particles (Bergametti and Foret, 2014). Across the modern Subarctic Pacific, wet deposition accounts for 75-85% of total dust deposition (Uematsu et al., 1985; Zhao et al., 2003), and models corroborate that wet deposition dominated in this region during the LGM as well (Mahowald et al., 2011). In the Subarctic Pacific, models have suggested that precipitation

was generally lower during the LGM, and particularly in the West Subarctic (Lora et al., 2017; Mahowald et al., 2011). With less rain in the west, the efficiency of wet deposition may have been reduced, retaining a higher dust load in the atmosphere and enhancing the zonal transport efficiency across the Subarctic Pacific. The modeled reduction in precipitation, therefore, would predict a glacial decrease in the zonal dust flux gradient in this region, the exact opposite of what is observed (Figure 5.3). The coincident reduced precipitation and increased zonal dust flux gradient during the LGM may be reconciled if wet deposition were more sensitive to the frequency, rather than the total amount, of precipitation, although models also suggest little change in the number of rainout events between the LGM and Holocene (Mahowald et al., 2011). The inconsistency between the observed dust flux gradient and the modeled precipitation change does not support this mechanism as the dominant forcing on the spatial distribution of dust fluxes on glacial-interglacial timescales.

Rather than precipitation history, the variations in the zonal dust flux gradient may be a consequence of changes in the position and strength of the westerlies. Over the Asian continent, the westerlies shift north and south seasonally, with the jump over the Tibetan Plateau in spring corresponding to enhanced dust storm activity (Roe, 2009). During glacial periods, enhanced seasonality shifts the mean position of the westerlies southward, generating greater dust export from East Asia (Chiang et al., 2015; Kong et al., 2017; Nagashima et al., 2011; Pullen et al., 2011), and creating an inverse relationship between summer insolation and dust deposition in the Subarctic Pacific (Serno et al., 2017). The net glacial displacement of the westerly jet is about 5˚ southward upon leaving the Asian continent, as inferred from forest ecosystems in Japan (Ono and Irino, 2004), snowlines and permafrost range in East Asia (Ono, 1991), dust provenance in the Japan Sea (Nagashima et al., 2011), sea surface temperatures in the Kuroshio current (Yamamoto et al., 2005),

microfossil assemblages in the Kuroshio current (Seo et al., 2018; Thompson, 1981), and pollen assemblages in the subtropical gyre (Kawahata and Ohshima, 2002).

Additionally, the orographic effects of the Tibetan plateau also determine the speed of the westerlies. When the westerlies are south of the Tibetan plateau, they are meridionally diffuse over the continent (at 40-50m/s) but consolidate into a narrow and high speed jet (65-75m/s) as they enter the North Pacific Ocean (Chiang et al., 2015; Molnar et al., 2010), an acceleration that does not characterize the westerlies when they are north of the plateau (Molnar et al., 2010). Thus a southward shift of the westerlies would coincide with an increase in wind strength during the glacial periods. Strong glacial westerlies are supported by generally coarser eolian grain sizes in marine sediment in the West Subarctic (Hovan et al., 1991; Nagashima et al., 2011; Rea, 1994), and they contribute to increasing dust emissions from Asia during glacial periods (McGee et al., 2010).

At sea, the westerly jet is steered by the Aleutian Low and the North Pacific High (Chiang and Fang, 2010; Wallace and Gutzler, 1981) on a more or less zonal pathway along 45˚N (today), directly above the JdFR. The Aleutian Low intensifies during periods of low insolation (Ueshima et al., 2006), and it pushes the westerlies southward as they travel east, deflecting as much as 15˚ to the south between 140 and 160˚W during the LGM (Lora et al., 2017). The speed of the westerlies may also evolve over the ocean, where a high meridional sea surface temperature gradient (as during glacial periods) can increase atmospheric baroclinicity, destabilize the westerlies, and increase average wind speeds by 10-20% (Lee and Poulsen, 2005; Timmermann et al., 2014). Strong glacial westerlies made landfall on the North American coast at ~35˚N (COHMAP, 1988; Kutzbach and Wright, 1985), nearly 15˚ south of modern landfall (50˚N), and delivered abundant moisture to the American Southwest (Kim et al., 2008; Lora et al., 2017; Oster et al., 2015), as reconstructed in hydroclimate records from lakes (e.g., Allen and Anderson, 2000; Kirby et

al., 2013; Menking et al., 2004) and speleothems (e.g., Asmerom et al., 2010; Brook et al., 2006; Wagner et al., 2010). The deflection of the jet stream to the south comprises one branch of a bifurcated westerly system induced by the topographic barrier of the Laurentide ice sheet (Bromwich et al., 2004; COHMAP, 1988; Kutzbach and Wright, 1985; Manabe and Broccoli, 1985), with the other branch taking a more northerly route over Alaska and towards Greenland (Fischer et al., 2007; Ruth et al., 2007).

Since the westerlies are the main conduit through which Asian dust is transported across the Subarctic Pacific (Sun et al., 2001), a southward shift of the westerlies would steer the Asian dust plume away from the East Subarctic and towards the California Margin. Sites in the West Subarctic may be less affected by the westerly position because the southward deflection is not as strong in the west (~5˚) compared to the east (~15˚), and proximity to the Asian continent may make dust transport less dependent on the westerlies themselves. Thus, while the West Subarctic might have received the same fraction of Asian dust (relative to emissions) in glacial and interglacial periods, the East Subarctic might have receive a smaller relative fraction of Asian dust during glacial periods, thus creating the steep zonal dust flux gradient across the Subarctic Pacific in the LGM. In other words, the zonal dust flux gradient would arise because the dust fluxes in the East Subarctic were too low, not because the dust fluxes in the West Subarctic were anomalously high. Two testable corollaries arise from this hypothesis. First, high LGM/H, similar to those in the West Subarctic, should exist under the southward shifted trajectory of the westerlies, e.g. off the coast of California. We currently have no reliable dust flux records from this region, but future work may yet find evidence for high dust deposition. Second, the southward migration of the westerlies would have caused a shift in lithogenic provenance, to less Asian dust, in the East Subarctic during glacial periods. We focus on the latter in the next section.

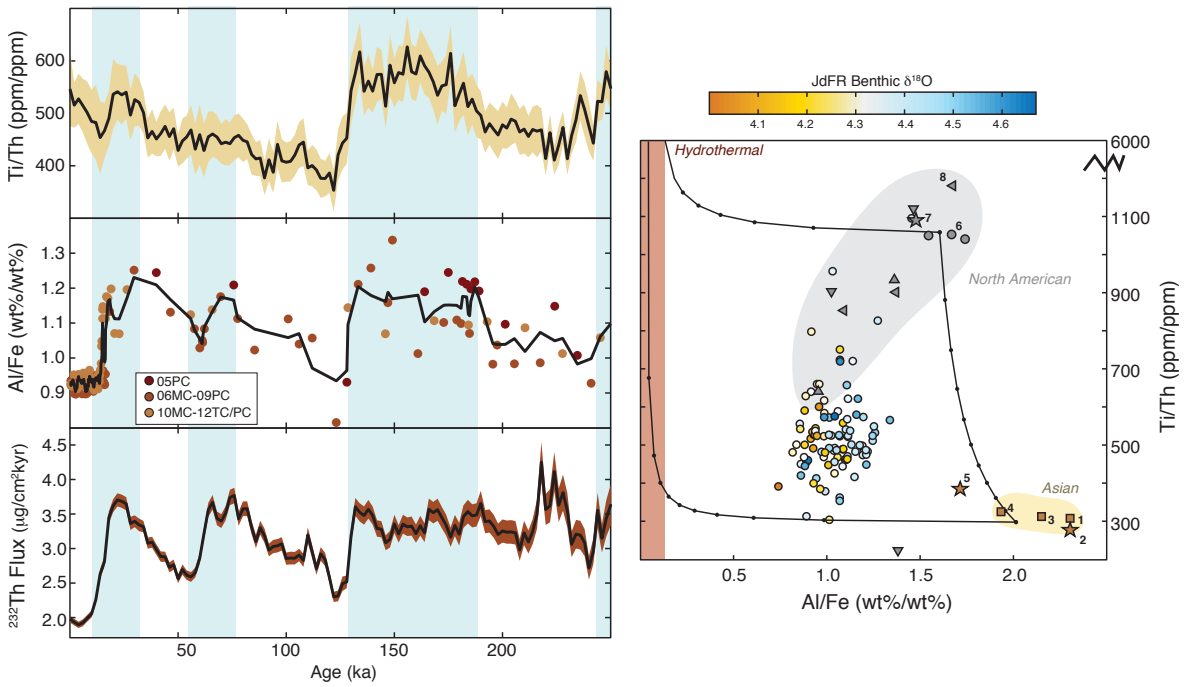

Figure 5.4. Changes in provenance in the East Subarctic Pacific. (*Left)* Ti/Th and Al/Fe variability on the JdFR, with ^{232}Th fluxes (as in Figure 5.2) for reference. Al, Fe, and Ti data have all been previously published (Costa et al., 2017b). *(Right*) Cross-plot of Ti/Th and Al/Fe for the JdFR, colorcoded by benthic δ^{18}O to identify glacial-interglacial cycles. Black lines show mixing lines between the three lithogenic endmembers, as summarized in Table 2. Numbered symbols show individual datapoints, while colored fields generally outline the variability within each endmember. Asian Loess, 1 (Ferrat et al., 2011). Upper continental crust, 2 (Taylor and McLennan, 1995). Asian Loess, 3 (Ding et al., 2001). Asian Loess, 4 (Taylor et al., 1983). Eolian continental endmember, 5, modeled after typical post-archean shale (Kyte et al., 1993). Turbidite, n=3, 6 (this study). Eolian andesitic endmember, 7, modeled after medium-K calc-alkaline andesite (Kyte et al., 1993). Eolian source materials from the Pacific Northwest, n=9, 8 (Aarons et al., 2017). Source 8 is further subdivided into 2-10 µm (upright triangle), 10-30 µm (inverse triangle), and 30-63 µm (left triangle).

5.4.2 Lithogenic Provenance

Unlike the monogenetic dust provenance of the West Subarctic, provenance in the East Subarctic is complicated by its proximity to a second lithogenic source: North America. While North American dust is most often equated with loess on the Great Plains [e.g., *Bettis et al.*, 2003], minor lithogenic sources adjacent to the East Subarctic may include river dust storms (Crusius et al., 2011; Nickling, 1978), river sediment loads (Cameron and Hattori, 1997), Alaskan and alpine loess (Biscaye et al., 1997; Muhs et al., 2003), volcanic ash from the Aleutians and Cascades (Weber et al., 1996), and material sloughed off of continental margins (Horn et al., 1971). During the last glacial period, the massive Cordilleran and Laurentide ice sheets may have suppressed alpine loess emissions, and possibly volcanic sources (Praetorius et al., 2016), but they may have simultaneously stimulated glaciogenic dust formation (Müller et al., 2018).

Lithogenic sediment near continental margins may be sourced from both hemipelagic and eolian deposition (Boven and Rea, 1998; Rea, 1994). Because the East Subarctic Pacific is quite distal from the Asian dust source yet quite proximal to the hemipelagic sediment source (North America), it would not be difficult to imagine how hemipelagic fluxes might overwhelm a small eolian contribution, and inconstant deposition of hemipelagic sediment could be the dominant source of lithogenic variability in the past. Grain size distributions have some utility in distinguishing eolian (<16μm, and generally <2 μm) and hemipelagic (often >16 μm) sediments (Rea and Hovan, 1995), and variability in grain size may be able to reconstruct the relative lithogenic provenance (eolian vs. hemipelagic) over time. One grain size study in the Equatorial Pacific at about 300km offshore (Boven and Rea, 1998) demonstrated that hemipelagic sedimentation may have

varied substantially (i.e., 20-96% hemipelagic) over the past 30kyr, proposing caution in interpreting near-shore lithogenic records as dust.

At about 500km off the coast of North America, the core sites at the Juan de Fuca Ridge may be expected to have similar, if slightly lower, hemipelagic contributions. However, one major difference at these core sites is the topographic barrier against hemipelagic deposition presented by the bathymetric high of the ridge itself. While sedimentation on the North American continental margin is characterized by frequent turbidity currents (e.g., Goldfinger et al., 2012; Horn et al., 1971), only one turbidite layer ~272ka is identified in sediments from the western flanks of the Juan de Fuca Ridge based on an anomalous peak in magnetic susceptibility (Costa et al., 2016). The core sites are instead dominated by a more pelagic sedimentation environment in which the primary variability is driven by carbonate dissolution cycles (Costa et al., 2016; Costa and McManus, 2017). Furthermore, the narrow continental shelf along the North American margin means that continental sediments are instead concentrated on the continental slope and in submarine canyons, and lower sea levels during glacial periods (e.g., Grant et al., 2014) are unlikely to substantially increase the hemipelagic flux from those regions to the open ocean. Consequently, it would not be unreasonable to assume a relatively constant hemipelagic flux of sediment to the JdFR, which would mute the amplitude of apparent dust flux variability. The damped glacial-interglacial amplitude in the East Subarctic could be entirely attributed to a background hemipelagic flux of 0.08 g/cm^{2}kyr, or about 60% of total lithogenic material in the Holocene and 30% in the LGM.

Such a high proportion of North American lithogenic material should be evident in provenance indicators, and radiogenic isotopes (εNd, $^{87}Sr/^{86}Sr$) from a nearby coretop (TT175-83P, 46.3˚N, 228.3˚E) on the west side of the JdFR have been interpreted as

reflecting a dominantly North American lithogenic source (Nakai et al., 1993). Here we attempt to use major and trace element lithogenic tracers (Al, Fe, Ti, Th) from our cores on the JdFR to reconstruct changes in provenance over time. Fe and Ti in the JdFR sediment cores are measured by calibrated x-ray fluorescence (Costa et al., 2017b), and Al is measured by flux fusion (Costa et al., 2017b). Both Th and Ti are almost entirely derived from the lithogenic fraction (McGee et al., 2016; Murray et al., 1993; Taylor and McLennan, 1995), and they are relatively inert to chemical fractionation in the water column and sediment, allowing the sedimentary Ti/Th to preserve the source Ti/Th signature. Al and Fe, while also primarily sourced from lithogenic material, are more susceptible to deviation from their lithogenic source values due to the influences of hydrothermal, volcanic (Resing et al., 2015; Shimmield and Price, 1988; Von Damm et al., 1985) and biological activity (Murray et al., 1993). These lithogenic tracers (Al/Fe and Ti/Th) suggest that provenance in the East Subarctic has varied systematically over time (Figure 5.4), with high Ti/Th (~600) and high Al/Fe (~1.2) characterizing glacial periods and low Ti/Th (~400) and low Al/Fe (~0.9) characterizing interglacial periods.

Table 5.2. Lithogenic endmember compositions.

End-member	**Al wt%**	**±**	**Fe wt%**	**±**	**Th ppm**	**±**	**Ti wt%**	**±**	**Al/Fe**	**±**	**Ti/Th**	**±**
Asian	7.57	1.23	3.76	0.92	12.69	2.79	0.38	0.08	2.01	0.59	296	89
North American	8.63	2.08	5.38	1.05	4.63	0.07	0.49	0.10	1.60	0.50	1049	215
Hydro-thermal	0.80	0.20	36.2	2.00	0.10	0.10	0.06	0.06	0.02	0.01	6000	8485

The JdFR provenance data can be modeled with a simple three-endmember lithogenic system: hydrothermal, North American, and Asian (Figure 5.4, Table 5.2). Of the three, the Asian dust endmember is the best constrained (Ding et al., 2001; Ferrat et al., 2011; Taylor et al., 1983), with a composition relatively close to that of upper continental crust (Taylor and McLennan, 1995). The North American lithogenic endmember is approximated using the chemistry of the turbidite layer in the Juan de Fuca Ridge sediment cores, identified by its high magnetic susceptibility (Costa et al., 2016) and $^{230}Th_{xs}$ concentrations below detection limits (Costa and McManus, 2017). The ^{232}Th concentrations are notably low (4.64ppm) compared with other global lithogenic sources that average closer to 14ppm (McGee et al., 2016). The subsequently high Ti/Th for North American lithogenic sediments suggests this endmember may be geochemically influenced by basalt components from the Columbia River Flood basalts (Cabato et al., 2015), Cascades (Bacon et al., 1997), and/or the Juan de Fuca Ridge itself (Dixon et al., 1986; Gale et al., 2013).

The JdFR provenance data can be modeled with a simple three-endmember lithogenic system: hydrothermal, North American, and Asian (Figure 5.4, Table 5.2). Of the three, the Asian dust endmember is the best constrained (Ding et al., 2001; Ferrat et al., 2011; Taylor et al., 1983), with a composition relatively close to that of upper continental crust (Taylor and McLennan, 1995). The North Pacific continental eolian source modeled by Kyte et al. (1993) approximates the Asian dust source quite well.

Hydrothermal particulates on the Cleft Segment of the JdFR have diagnostically low Al/Fe (0.03±0.02 ppm/ppm) (Feely et al., 1994), but unfortunately no Ti or Th measurements were made on these particles, likely because these elemental concentrations are expected to be low in hydrothermal Fe-Mn oxy-hydroxides. Instead, we utilize the modeled hydrothermal endmember of Kyte et al. (1993), which is primarily based on the hydrothermal chemistry of the East Pacific Rise (EPR). Although the EPR and the JdFR

may be expected to have unique hydrothermal chemistries, the Al/Fe ratio of the Kyte endmember is nearly identical to that of the JdFR, supporting the use of this endmember in our provenance model. We incorporate generous error estimates on the Ti and Th concentrations to account for the uncertainty in these elements.

For the North American lithogenic endmember, we use the chemistry of the turbidite layer, which can be identified by its high magnetic susceptibility (Costa et al., 2016) and $^{230}Th_{xs}$ concentrations below detection limits (Costa and McManus, 2017). The ^{232}Th concentrations are notably low (4.64ppm) compared with other global lithogenic sources that average closer to 14ppm (McGee et al., 2016). The subsequently high Ti/Th for North American lithogenic sediments suggests this endmember may be geochemically influenced by basalt components from the Columbia River Flood basalts (Cabato et al., 2015), Cascades (Bacon et al., 1997), and/or the Juan de Fuca Ridge itself (Dixon et al., 1986; Gale et al., 2013). Eolian source material from the Pacific Northwest comprises a wide range of compositions (Aarons et al., 2017), from 0.9-9.0wt% Al, 0.8-16wt% Fe, 0-16ppm ^{232}Th, and 0.07-3.0wt% Ti. The best analog for the turbidite composition is the 30-63mm sample from the sand dunes in Christmas Lake Valley, Oregon (Aarons et al., 2017), which has an almost identical geochemical signature. Interestingly the source material data appear to plot along an Al/Fe to Ti/Th trend that intersects with the JdFR data itself, with the turbidite endmember at the other end. This trend may suggest that using the turbidite as the North American endmember may underestimate North American contributions to lithogenic material on the JdFR. On the other hand, the North Pacific andesitic eolian source modeled by Kyte et al. (1993) approximates the North American dust source quite well, lending some plausibility towards using the turbidite as the North American endmember in the following analyses.

Due to the relative uncertainties in the lithogenic endmember compositions, we took a statistical approach to reconstructing the provenance over time. First, Ti, Th, and Fe concentrations in the JdFR sediments were normalized to a carbonate free basis to isolate the lithogenic component chemistry. Aluminum data were not included due to their much lower resolution (discrete flux fusion vs. continuous XRF). For each run, the concentrations of Fe, Ti, and Th for each source endmember were calculated as a randomly generated number from a normally distributed population with the means and standard deviations shown in Table 2. The fraction of each endmember was then solved using least-squares non-negative matrix inversion. This analysis was repeated 1000 times (Figure 5.5), in order to establish robust trends in provenance over time within the uncertainties of the given endmembers.

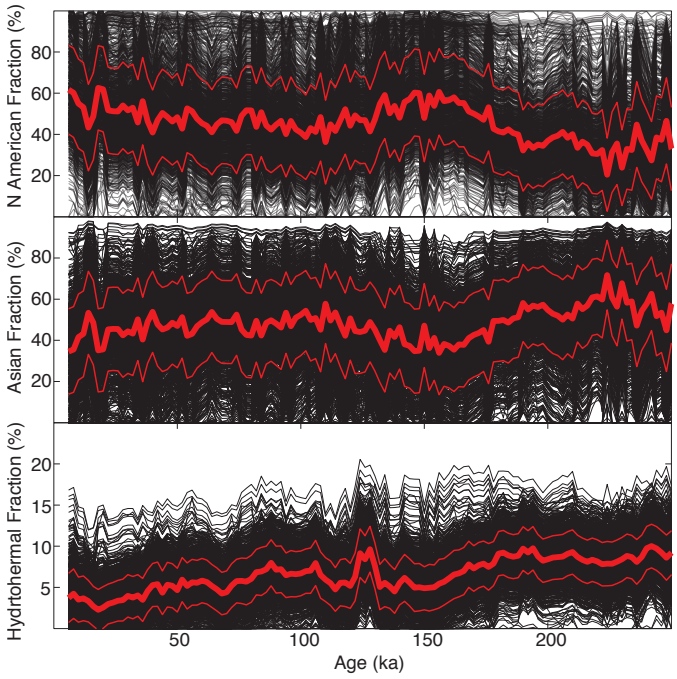

Figure 5.5. Simulations (n=1000) of lithogenic source distributions over the past 250ka. Source chemistry was varied by randomly selecting concentrations of Ti, Fe, and ^{232}Th from a population with the same mean and standard deviation as shown in Table 5.2. Black lines are the individual source deconvolution for each run. Thick red lines show the average, and thin red lines show 1σ.

In general, the mixing model suggests nearly equal contributions of North American (45%) and Asian (48%) lithogenic material over the past 250kyr, with relatively small amounts of hydrothermal deposition (6.5%) (Figure 5.5, Figure 5.6). Hydrothermal contributions are some what higher during interglacial periods and may include a deglacial peak at Termination II (~128ka), as previously observed based on iron records in these cores (Costa et al., 2017b). The fraction of Asian lithogenic material appears to decrease during glacial periods (notably, MIS6) while the total dust flux is compensated by higher fractions of North American lithogenic material at those times. This shift in provenance is consistent with southward-shifted glacial westerlies deflecting Asian dust away from the East Subarctic.

The total lithogenic provenance can be converted into sources of ^{232}Th (Figure 5.6B) by scaling each sources contribution by its average ^{232}Th concentration (Table 5.2); the low ^{232}Th concentrations in hydrothermal activity makes this source negligible. The ^{232}Th source fraction (Figure 5.6B) can then be applied to the total ^{232}Th flux (Figure 5.6C) to calculate the ^{232}Th fluxes of each source component (Figure 5.6D-E). There are clear glacial-interglacial cycles in the North American ^{232}Th flux, with nearly twice as much material deposited during glacial periods than during interglacial periods. Asian ^{232}Th fluxes are more stable, with higher overall fluxes and less apparent glacial-interglacial patterns; while fluxes are high in the last glacial maximum (18-23ka) and MIS4 (60-70ka) relative to the Holocene and MIS3, the penultimate glacial (MIS6) and interglacial (MIS5) periods have similar fluxes, excepting MIS5e. Given the large errors in these analyses, it is difficult to confidently interpret glacial-interglacial patterns in the absolute Asian ^{232}Th fluxes. Future work using provenance indicators like ^{4}He/^{232}Th (McGee et al., 2016; Serno et al., 2017) and Pb isotopes, as well as better defined endmembers, will hopefully provide more robust decomposition of lithogenic provenance in the East Subarctic.

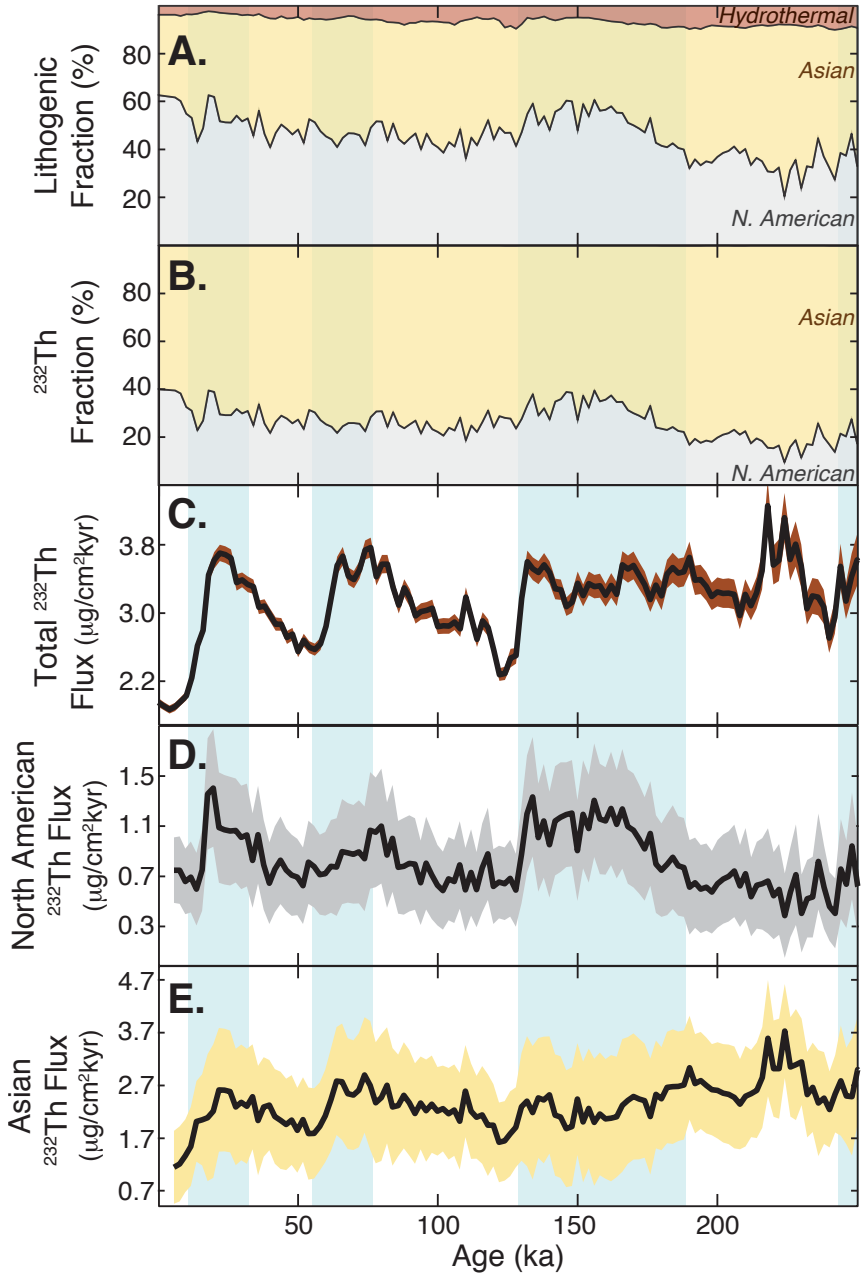

Figure 5.6. **Deconvolution of total lithogenic flux into different source components.** (A) Relative provenance distribution for total lithogenic material over the last 250ka (as in Figure 5.5). (B) Relative provenance distribution for ^{232}Th over the last 250ka. (C) Total ^{232}Th fluxes (as in Figure 5.2). Shaded area shows 2σ standard deviation. (D) Absolute flux of North American lithogenic material. Shaded area shows 1σ standard deviation. (E) Absolute flux of Asian lithogenic material. Shaded area shows 1σ standard deviation. Light blue bars identify glacial periods.

5.5. Conclusions

Lithogenic fluxes in the East Subarctic are generally higher in glacial periods relative to interglacial periods, similar to other long dust flux records from the North Pacific. Whereas dust in the West Subarctic can vary by as much as a factor of 4-5 between glacial and interglacial periods (Serno et al., 2017), lithogenic fluxes in the East Subarctic, and much of the North Pacific, only vary by a factor of 2. We investigated several different mechanisms to deposit relatively more dust in the West Subarctic than in the East Subarctic. Deflection of the glacial westerlies to the south may have contributed reduced the relative transport efficiency of dust from the Asian continent to the East Subarctic, and new provenance data from the East Subarctic support weakened zonal transport of Asian lithogenic material during glacial periods. We find that during glacial periods, there is shift towards more North American-sourced lithogenic material. There is a clear glacial-interglacial pattern in the North American ^{232}Th fluxes, while the fluxes from Asia are more ambiguous. Future work on modern and paleo dust provenance should serve to elucidate the role of the westerlies and North American lithogenic material in the spatial distribution of dust in this region. Our findings may suggest that the assumption of a monogenetic Asian dust source across the North Pacific may be underestimating the contributions of North America to this region.

References

Aarons, S. M., M. A. Blakowski, S. M. Aciego, E. I. Stevenson, K. W. W. Sims, S. R. Scott, C. Aarons (2017), Geochemical characterization of critical dust source regions in the American West. *Geochim. Cosmochim. Acta*, **215**, 141–161.

Addison, J. A., B. P. Finney, W. E. Dean, M. H. Davies, A. C. Mix, J. S. Stoner, J. M. Jaeger (2012), Productivity and sedimentary d15N variability for the last 17,000 years along the northern Gulf of Alaska continental slope, *Paleoceanography,* **27**, 1–17.

Adkins, J., P. deMenocal, G. Eshel (2006), The "African humid period" and the record of marine upwelling from excess 230 Th in Ocean Drilling Program Hole 658C, *Paleoceanography*, **21**(4), PA4203.

Albani, S., N. M. Mahowald, A. T. Perry, R. A. Scanza, C. S. Zender, N. G. Heavens, V. Maggi, J. F. Kok, B. L. Otto-Bliesner (2014), Improved dust representation in the Community Atmosphere Model, *J. Adv. Model. Earth Syst.*, **6**, 541–570.

Allen, B. D., R. Y. Anderson (2000), A continuous, high-resolution record of late Pleistocene climate variability from the Estancia basin, New Mexico, *Geol. Soc. Am. Bull.*, **112**(9), 1444–1458.

Anand, P., H. Elderfield, M. H. Conte (2003), Calibration of Mg/Ca thermometry in planktonic foraminifera from a sediment trap time series, *Paleoceanography* **18**(2).

Anderson R. F., M. P. Bacon, P. G. Brewer (1983) Removal of 230Th and 231Pa at ocean margins. *Earth Planet. Sci. Lett.,* **66**, 73–90.

Anderson R. F., M. Q. Fleisher, Y. Lao, G. Winckler (2008) Modern CaCO3 preservation in equatorial Pacific sediments in the context of late-Pleistocene glacial cycles. *Mar. Chem.,* **111**, 30–46.

Anderson, R. F. (1982), Concentration, vertical flux, and remineralization of particulate uranium in seawater. *Geochim. Cosmochim. Acta,* **46**, 1293–1299.

Anderson, R. F., A. P. LeHuray, M. Q. Fleisher, J. W. Murray (1989), Uranium deposition in Saanich Inlet sediments, Vancouver Island. *Geochim. Cosmochim. Acta,* **53**, 2205–2213.

Anderson, R. F., G. Winckler (2005), Problems with paleoproductivity proxies, *Paleoceanography,* **20**(3), 1–7.

Anderson, R. F., M. Q. Fleisher, A. P. LeHuray (1989), Concentration, oxidation state, and particulate flux of uranium in the Black Sea. *Geochim. Cosmochim. Acta* **53**, 2215–2224.

Anderson, R. F., S. Ali, L. Bradtmiller, S. H. H. Nielson, M. Q. Fleisher, B. E. Anderson, L. H. Burckle (2009), Wind-driven upwelling in the Southern Ocean and the deglacial rise in atmospheric CO2. *Science,* **323**, 1443–1448.

Anderson, R. F., S. Barker, M. Q. Fleisher, R. Gersonde, S. L. Goldstein, G. Kuhn, P. G. Mortyn, K. Pahnke, J. P. Sachs (2014), Biological response to millennial variability of dust and nutrient supply in the Subantarctic South Atlantic Ocean. *Philos. Trans. R. Soc. London*, **372**, 20130054.

Anderson, R. F., Y. Lao, W. S. Broecker, S. E. Trumbore, H. J. Hofmann, W. Wolfli (1990), Boundary scavenging in the Pacific Ocean: a comparison of 10Be and 231Pa, *Earth Planet. Sci. Lett.*, **96**, 287–304.

Anderson, R., M. Fleisher, Y. Lao (2006), Glacial–interglacial variability in the delivery of dust to the central equatorial Pacific Ocean, *Earth Planet. Sci. Lett.*, **242**(3–4), 406-414.

Anderson, R. F., S. Barker, M. Fleisher, R. Gersonde, S. L. Goldstein, G. Kuhn, P.G. Mortyn, K. Pahnke, J. P. Sachs (2014), Biological response to millennial variability of dust and nutrient supply in the Subantarctic South Atlantic Ocean. *Philos. Trans. R. Soc. London*, **372**, 20130054.

Archer, D., M. Lyle, K. Rodgers, P. Froelich (1993), What controls opal preservation in tropical deep-sea sediments, *Paleoceanography*, **8**(1), 7–21.

Arndt, S., B. B. Jørgensen, D. E. LaRowe, J. J. Middelburg, R. D. Pancost, P. Regnier (2013), Quantifying the degradation of organic matter in marine sediments: A review and synthesis, *Earth-Science Rev.*, **123**, 53–86.

Artemova, A., S. Gorbarenko, Y. Vasilenko, X. Shi, Y. Liu, M. Chen (2017), Palaeoceanography changes in the Okhotsk Sea during Late Pleistocene and Holocene according to diatoms, *Quat. Int.*, **459**, 175–186.

Asmerom, Y., V. J. Polyak, S. J. Burns (2010), Variable winter moisture in the southwestern United States linked to rapid glacial climate shifts, *Nat. Geosci.*, **3**(2), 114–117.

Bacon, C. R., P. E. Bruggman, R. L. Christiansen, M. A. Clynne, J. M. Donnelly-Nolan, W. Hildreth (1997), Primitive magmas at five Cascade volcanic fields: Melts from hot, heterogeneous sub-arc mantle. *Can. Mineral.* **35**, 397–423.

Bacon, M. P. (1984) Glacial to interglacial changes in carbonate and clay sedimentation in the Atlantic Ocean estimated from 230Th measurements. *Isot. Geosci.,* **2**, 97–111.

Bacon, M. P. (1988), Tracers of chemical scavenging in the ocean: boundary effects and large-scale chemical fractionation, *Philos. Trans. R. Soc. London*, **325**, 147–160.

Baker, E. T., J. W. Lavelle, R. A. Feely, G. J. Massoth, S. L. Walker, J. E. Lupton (1989), Episodic Venting of Hydrothermal Fluids From the Juan de Fuca Ridge. *J. Geophys. Res.*, **94**, 9237–9250.

Balzer, W. (1982). On the distribution of iron and manganese at the sediment/water interface: thermodynamics versus kinetic control. *Geochim. Cosmochim. Acta,* **46**, 1153–1161.

Barnes, C. E., J. K. Cochran (1990). Uranium removal in oceanic sediments and the oceanic U balance. *Earth Planet. Sci. Lett.*, **97**, 94–101.

Basak, C., H. Fröllje, F. Lamy, R. Gersonde, V. Benz, R. F. Anderson, M. Molina-Kescher, K. Pahnke (2018), Breakup of last glacial deep stratification in the South Pacific, *Science*, **904**, 900–904.

Beaufort, L., Y. Lancelot, P. Camberlin, O. Cayre, E. Vincent, F. Bassinot, L. Labeyrie (1997), Insolation cycles as a mojor control of equatorial Indian Ocean primary production, *Science*, **278**, 1451–1454.

Beaulieu, S. E. (2002), Accumulation and fate of phytodetritus on the sea floor. *Oceanogr. Mar. Biol. Annu. Rev.*, **40**, 171–232.

Bergametti, G., G. Foret (2014), Dust Deposition, in *Mineral Dust: A Key Player in the Earth System*, edited by P. Knippertz and J. B. W. Stuut, pp. 179–200, Springer, Dordrecht.

Berger, W. H. (1979), Preservation of foraminifera, in: Lipps, J.H. (Ed.), Foraminiferal Ecology and Paleoecology. Tulsa, OK, pp. 105–155.

Bettis, E. A., D. R. Muhs, H. M. Roberts, A. G. Wintle (2003), Last Glacial loess in the conterminous USA, *Quat. Sci. Rev.*, **22**(18–19), 1907–1946.

Biscaye, P. E., F. E. Grousset, M. Revel, G. A. Zielinski, A. Vaars, G. Kukla (1997), Asian provenance of glacial dust (stage 2) in the Greenland Ice Sheet Project 2 Ice Core, Summit, Greenland, *J. Geophys. Res.*, **102**(C12), 26765–26781.

Bloemendal, J., P. B. deMenocal (1989), Evidence for a change in the periodicity of tropical

climate cycles at 2.4Myr from whole-core magnetic susceptibility measurements. *Nature*, **342**, 897–900.

Böhm, E., J. Lippold, M. Gutjahr, M. Frank, P. Blaser, B. Antz, J. Fohlmeister, N. Frank, M. B. Andersen, M. Deininger (2015), Strong and deep Atlantic meridional overturning circulation during the last glacial cycle, *Nature*, **517**, 73–76.

Boven, K. L., D. K. Rea (1998), Partitioning of eolian and hemipelagic sediment in eastern equatorial Pacific core TR 163-31B and the late Quaternary paleoclimate of the Northern Andes, *J. Sediment. Res.*, **68**(5), 850–855.

Boyd, P. W., P. J. Harrison (1999), Phytoplankton dynamics in the NE subarctic Pacific, *Deep Sea Res. II,*, **46**(11–12), 2405–2432.

Boyle, E. A. (1983), Manganese carbonate overgrowths on foraminifera tests. *Geochim. Cosmochim. Acta*, **47**, 1815–1819.

Boyle, E. A. (1988), Vertical oceanic nutrient fractionation and glacial/interglacial CO2 cycles, *Nature*, **331**(6151), 55–56.

Boyle, E. A., L. D. Keigwin (1987), North Atlantic thermohaline circulation during the past 20,000 years linked to high latitude surface temperature, *Nature*, **350**, 35–40.

Bradtmiller, L. I., R. F. Anderson, J. P. Sachs, M. Q. Fleisher (2010), A deeper respired carbon pool in the glacial equatorial Pacific Ocean. *Earth Planet. Sci. Lett.*, **299**, 417–425.

Bradtmiller, L. I., R. F. Anderson, M. Q. Fleisher, L. H. Burckle (2007), Opal burial in the equatorial Atlantic Ocean over the last 30 ka: Implications for glacial-interglacial changes in the ocean silicon cycle, *Paleoceanography*, **22**(4).

Bradtmiller, L. I., R. F. Anderson, M. Q. Fleisher, L. H. Burckle (2006), Diatom productivity in the equatorial Pacific Ocean from the last glacial period to the present: A test of the silicic acid leakage hypothesis, *Paleoceanography*, **21**(4), PA4201.

Bray, N. A. (1988), Thermohaline circulation in the Gulf of California. *J. Geophys. Res.*, **93**, 4993–5020.

Breitzke, M., 2006. Physical Properties of Marine Sediments, in: Schulz, H.D., Zabel, M. (Eds.), Marine Geochemistry. Springer, Berlin Heidelberg, pp. 27–71.

Brennan, C. E., K. J. Meissner, M. Eby, C. Hillaire-Marcel, A. J. Weaver (2013), Impact of sea ice variability on the oxygen isotope content of seawater under glacial and interglacial conditions, *Paleoceanography*, **28**(3), 388–400.

Brodeur, R. D., D. M. Ware (1992), Long-term variability in zooplankton biomass in the subarctic *Pacific Ocean, Fish. Oceanogr.*, I(I), 32–38.

Broecker, W. S. (1971) Calcite accumulation rates and glacial to interglacial changes in oceanic mixing. In *The Late Cenozoic Glacial Ages* (ed. K. K. Turekian). Yale University Press, New Haven, CT. pp. 239–265.

Broecker, W. S. (1982), Glacial to interglacial changes in ocean chemistry. *Prog. Oceanogr.* **11**, 151–197.

Broecker, W. S. (2008) Excess sediment 230Th: Transport along the sea floor or enhanced water column scavenging? *Global Biogeochem. Cycles* **22**.

Bromwich, D. H., E. R. Toracinta, H. Wej, R. J. Oglesby, J. L. Fastook, T. J. Hughes (2004), Polar MM5 simulations of the winter climate of the Laurentide Ice Sheet at the LGM, *J. Clim.,* **17**, 3415–3433.

Brook, G. A., B. B. Ellwood, L. B. Railsback, J. B. Cowart (2006), A 164 ka record of environmental change in the American Southwest from a Carlsbad Cavern speleothem, *Palaeogeogr. Palaeoclimatol. Palaeoecol.*, **237**, 483–507.

Brunelle, B. G., D. M. Sigman, M. S. Cook, L. D. Keigwin, G. H. Haug, B. Plessen, G. Schettler, S. L. Jaccard (2007), Evidence from diatom-bound nitrogen isotopes for

subarctic Pacific stratification during the last ice age and a link to North Pacific denitrification changes, *Paleoceanography*, **22**(1).

Brunelle, B. G., D. M. Sigman, S. L. Jaccard, L. D. Keigwin, B. Plessen, G. Schettler, M. S. Cook, G. H. Haug (2010), Glacial/interglacial changes in nutrient supply and stratification in the western subarctic North Pacific since the penultimate glacial maximum, *Quat. Sci. Rev.*, **29**(19–20), 2579–2590.

Burdige, D. J., J. M. Gieskes (1983), A pore water/solid phase diagenetic model for manganese in marine sediments. *Am. J. Sci.* **283**, 29–47.

Burke, A., L. F. Robinson (2012), The Southern Ocean's Role in Carbon Exchange During the Last Deglaciation. *Science,* **335**, 557–561.

Butterfield, D. A., I. R. Jonasson, G. J. Massoth, R. A. Feely, K. K. Roe, R. E. Embley, J. F. Holden, R. E. McDuff, M. D. Lilley, J. R. Delaney (1997), Seafloor eruptions and evolution of hydrothermal fluid chemistry. *Philos. Trans. R. Soc. London,* **355**, 369–386.

Cabato, J. A., C. J. Stefano, S. B. Mukasa (2015), Volatile concentrations in olivine-hosted melt inclusions from the Columbia River flood basalts and associated lavas of the Oregon Plateau: Implications for magma genesis, *Chem. Geol.*, *392*, 59–73.

Caissie, B. E., J. Brigham-Grette, K. T. Lawrence, T. D. Herbert, M. S. Cook (2010), Last Glacial Maximum to Holocene sea surface conditions at Umnak Plateau, Bering Sea, as inferred from diatom, alkenone, and stable isotope records, *Paleoceanography*, **25**(1).

Calvert, S. E., T. F. Pedersen (1993), Geochemistry of recent oxic and anoxic sediments: Implications for the geological record. *Mar. Geol.* **113**, 67–88.

Cameron, E. M., K. Hattori (1997), Strontium and neodymium isotope ratios in the Fraser River, British Columbia: A riverine transect across the Cordilleran orogen, *Chem. Geol.*, **137**, 243–253.

Canfield, D. E. (1994), Factors Influencing Organic-Carbon Preservation in Marine-Sediments, *Chem. Geol.*, **114**(3–4), 315–329,

Carbotte, S. M., M. R. Nedimović, J. P. Canales, G. M. Kent, A. J. Harding, M. Marjanović (2008), Variable crustal structure along the Juan de Fuca Ridge: Influence of on-axis hot spots and absolute plate motions. *Geochemistry, Geophys. Geosystems* **9**.

Carbotte, S. M., R. S. Detrick, A. Harding, J. P. Canales, J. Babcock, G. Kent, E. Van Ark, M. Nedimovic, J. Diebold (2006), Rift topography linked to magmatism at the intermediate spreading Juan de Fuca Ridge. *Geology* **34**, 209–212.

Carmichael, R. S. (1982), Magnetic properties of minerals and rocks, in: Carmichael, R.S. (Ed.), Handbook of Physical Properties of Rocks. CRC Press, Boca Raton, Florida, pp. 229–287.

Chappell, J., N. J. Shackleton (1986), Oxygen isotopes and sea level. *Nature* **324**, 137–140.

Chase, Z., R. F. Anderson, M. Q. Fleisher, P. W. Kubik (2002), The influence of particle composition and particle flux on scavenging of Th, Pa and Be in the ocean, *Earth Planet. Sci. Lett.*, **204**, 215–229.

Chase, Z., R. F. Anderson, M. Q. Fleisher, P. W. Kubik (2003), Scavenging of 230Th, 231Pa and 10Be in the Southern Ocean (SW Pacific sector): The importance of particle flux and advection, *Deep Sea Res. Part II Top. Stud. Oceanogr.*, **50**, 739–768.

Chen, J., G. Li, J. Yang, W. Rao, H. Lu, W. Balsam, Y. Sun, J. Ji (2007), Nd and Sr isotopic characteristics of Chinese deserts: Implications for the provenances of Asian dust, *Geochim. Cosmochim. Acta*, **71**, 3904–3914.

Cheng H., R. L. Edwards, C. C. Shen, V. J. Polyak, Y. Asmerom, J. Woodhead, J. Hellstrom, Y. Wang, X. Kong, C. Spötl, X. Wang, E. C. Alexander (2013) Improvements in

230Th dating, 230Th and 234U half-life values, and U-Th isotopic measurements by multi-collector inductively coupled plasma mass spectrometry. *Earth Planet. Sci. Lett.,* **371-372**, 82–91.

Chiang, J. C. H., I. Y. Fung, C. H. Wu, Y. Cai, J. P. Edman, Y. Liu, J. A. Day, T. Bhattacharya, Y. Mondal, C. A. Labrousse (2015), Role of seasonal transitions and westerly jets in East Asian paleoclimate, *Quat. Sci. Rev.*, **108**, 111–129.

Chiang, J. C. H., Y. Fang (2010), Was the north Pacific wintertime climate less stormy during the mid-Holocene? *J. Clim.*, **23**, 4025–4037.

Clague D. A., J. B. Paduan, A. S. Davis (2009) Widespread strombolian eruptions of mid-ocean ridge basalt. *J. Volcanol. Geotherm. Res.,* **180**, 171–188.

Cochran, J. K., A. E. Carey, E. R. Sholkovitz, L. D. Surprenant (1986), The geochemistry of uranium and thorium in coastal marine sediments and sediment pore waters. *Geochim. Cosmochim. Acta,* **50**, 663–680.

COHMAP (1988), Climatic Changes of the Last 18,000 Years: Observations and Model Simulations, *Science*, **241**(4869), 1043–1052.

Cole, T. G. (1985), Composition, oxygen isotope geochemistry and origin of smectite in the metalliferous sediments of the Bauer Deep, southeast Pacific, *Geochim. Cosmochim. Acta*, **49**(1), 221–235.

Cook, M. S., A. C. Ravelo, A. Mix, I. M. Nesbitt, N. V. Miller (2016), Tracing subarctic Pacific water masses with benthic foraminiferal stable isotopes during the LGM and late Pleistocene, *Deep. Res. Part II Top. Stud. Oceanogr.*, **125–126**, 84–95.

Cook, M. S., L. D. Keigwin, C. A. Sancetta (2005), The deglacial history of surface and intermediate water of the Bering Sea, *Deep Sea Res. II*, **52**, 2163–2173.

Costa, K. M., A. W. Jacobel, J. F. McManus, R. F. Anderson, G. Winckler, N. Thiagarajan (2017), Productivity patterns in the Equatorial Pacific over the last 30,000 years, *Global Biogeochem. Cycles*, **31**.

Costa, K. M., J. F. McManus (2017), Efficacy of 230Th normalization in sediments from the Juan de Fuca Ridge, northeast Pacific Ocean, *Geochim. Cosmochim. Acta*, **197**, 215–225.

Costa, K. M., J. F. McManus, B. Boulahanis, S. M. Carbotte, G. Winckler, P. Huybers, C. H. Langmuir (2016), Sedimentation, stratigraphy and physical properties of sediment on the Juan de Fuca Ridge. *Mar. Geol.* **380**, 163–173.

Costa, K. M., J. F. McManus, J. L. Middleton, C. H. Langmuir, P. J. Huybers, G. Winckler, S. Mukhopadhyay (2017), Hydrothermal deposition on the Juan de Fuca Ridge over multiple glacial-interglacial cycles. *Earth Planet. Sci. Lett.*, **479**, 120–132.

Costa, K. M., J. F. McManus, R. F. Anderson (2017), Radiocarbon and Stable Isotope Evidence for Changes in Sediment Mixing in the North Pacific Over the Past 30 kyr, *Radiocarbon*, doi:10.1017/RDC.2017.91.

Costa, K. M., J. F. McManus, R. F. Anderson, H. Ren, D. M. Sigman, G. Winckler, M. Q. Fleisher, F. Marcantonio, A. C. Ravelo (2016), No iron fertilization in the equatorial Pacific Ocean during the last ice age, *Nature*, **529**(7587), 519–522.

Costa, K. M., R. F. Anderson, J. F. McManus, G. Winckler, J. L. Middleton, C. H. Langmuir (2018), Trace element (Mn, Zn, Ni, V) and authigenic uranium (aU) geochemistry reveal sedimentary redox history on the Juan de Fuca Ridge, North Pacific Ocean, *Geochim. Cosmochim. Acta*, in press, doi:10.1016/j.gca.2018.02.016.

Cowen, J. P., G. J. Massoth, E. T. Baker (1986), Bacterial scavenging of Mn and Fe in a mid- to far-field hydrothermal particle plume. *Nature,* **322**, 169–171.

Creamean, J. M., R. Spackman, J, S. M. Davis, A. B. White (2014), Climatology of long-range transported Asian dust along the West Coast of the United States, *J. Geophys.*

Res. Atmos., **119**, 12171–12185.
Creamean, J. M., J. R. Spackman, S. M. Davis, A. B. White (2014), Climatology of long-range transported Asian dust along the West Coast of the United States. *J. Geophys. Res. Atmos.*, **119**, 12171–12185.
Crusius, J., A. W. Schroth, S. Gassó, C. M. Moy, R. C. Levy, M. Gatica (2011), Glacial flour dust storms in the Gulf of Alaska: Hydrologic and meteorological controls and their importance as a source of bioavailable iron, *Geophys. Res. Lett.*, **38**(6), 1–5.
Crusius, J., S. Calve, T. Pedersen, D. Sage (1996), Rhenium and molybdenum enrichments in sediments as indicators of oxic, suboxic and sulfidic conditions of deposition. *Earth Planet. Sci. Lett.*, **145**, 65–78.
Crusius, J., T. F. Pedersen, S. Kienast, L. Keigwin, L. Labeyrie (2004), Influence of northwest Pacific productivity on North Pacific Intermediate Water oxygen concentrations during the Bolling-Allerod interval (14.7-12.9 ka). *Geology*, **32**, 633–636.
Davies, M. H., A. C. Mix, J. S. Stoner, J. A. Addison, J. Jaeger, B. Finney, J. Wiest (2011), The deglacial transition on the southeastern Alaska Margin: Meltwater input, sea level rise, marine productivity, and sedimentary anoxia, *Paleoceanography*, **26**(2), 1–18.
Davis, E. E., J. L. Karsten (1986), On the cause of the asymmetric distribution of seamounts about the Juan de Fuca ridge: ridge-crest migration over a heterogeneous asthenosphere. *Earth Planet. Sci. Lett.*, **79**, 385–396.
De Boer, A. M., D. Nof (2004), The Bering Strait's grip on the northern hemisphere climate, *Deep. Res. Part I Oceanogr. Res. Pap.*, **51**(10), 1347–1366.
Delmonte, B., C. Paleari, S. I. Andò, E. Garzanti, P. S. Andersson, J. R. Petit, X. Crosta, B. Narcisi, C. Baroni, M. C. Salvatore, G. Baccolo, V. Maggi (2017), Causes of dust size variability in central East Antarctica (Dome B): Atmospheric transport from expanded South American sources during Marine Isotope Stage 2, *Quat. Sci. Rev.*, **168**, 55–68.
deMenocal, P.B., J. Bloemendal, J. King (1991), A rock magnetic record of monsoonal dust deposition to the Arabian Sea: evidence for a shift in the mode of deposition at 2.4 Ma. *Proc. ODP Sci. Res.* **117**, 389–407.
Dick, G. J., B. G. Clement, S. M. Webb, F. J. Fodrie, J. R. Bargar, B. M. Tebo (2009), Enzymatic microbial Mn(II) oxidation and Mn biooxide production in the Guyamas Basin deep-sea hydrothermal plume. *Geochim. Cosmochim. Acta,* **73**, 6517–6530.
Dickens, G. R. (2001), Sulphate profiles and barium fronts in sediments on the Blake Ridge: present and past methane fluxes through a large gas hydrate resevoir, *Geochim. Cosmochim. Acta*, **65**(4), 529–543.
Ding, Z. L., J. M. Sun, S. L. Yang, T. S. Liu (2001), Geochemistry of the pliocene red clay formation in the chinese loess plateau and implication for its origin, source provenance and paleochlimate change, *Geochim. Cosmochim. Acta*, **65**(6), 901–913.
Dixit, S., P. Van Cappellen, A. J. Van Bennekom (2001), Processes controlling solubility of biogenic silica and pore water build-up of silicic acid in marine sediments, *Mar. Chem.*, **73**(3–4), 333–352.
Dixon, J. E., D. A. Clague, J.-P. Eissen (1986), Gabbroic zenoliths and host ferrobasalt from the Southern Juan de Fuca Ridge. *J. Geophys. Res.*, **91**, 3795–3820.
Dohonoe, A., D. S. Battisti (2009), Causes of reduced North Atlantic storm activity in a CAM3 simulation of the last glacial maximum, *J. Clim.,* **22**(18), 4793–4808.
Dubois, N., M. Kienast, S. Kienast, S. E. Calvert, R. Francois, R. F. Anderson (2010), Sedimentary opal records in the eastern equatorial Pacific: It is not all about leakage, *Global Biogeochem. Cycles*, **24**(4), 1–15.

Dubois, N., N. C. Mitchell (2012), Large-scale sediment redistribution on the equatorial Pacific seafloor. *Deep. Res. Part I Oceanogr. Res. Pap.*, **69**, 51–61.
Dunk, R.M., R. A. Mills (2006), The impact of oxic alteration on plume-derived transition metals in ridge flank sediments from the East Pacific Rise. *Mar. Geol.*, **229**, 133–157.
Duplessy, J. C., N. J. Shackleton, R. G. Fairbanks, L. Labeyrie D. W. Oppo, N. Kallel (1988), Deepwater source variations during the last climatic cycle and their impact on the global deepwater circulation. *Paleoceanography*, **3**, 343–360.
Dymond, J. (1981), Geochemistry of Nazca plate surface sediments: an evaluation of hydrothermal, biogenic, detrital, and hydrogenous sources. *Geol. Soc. Am. Bull.*, **154**, 133–172.
Dymond, J., E. Suess, M. W. Lyle (1992), Barium in deep-sea sediment: A geochemical proxy for paleoproductivity, *Paleoceanography*, **7**(2), 163–181.
Dyrssen, D., K. Kremling (1990), Increasing hydrogen sulfide concentration and trace metal behavior in the anoxic Baltic waters. *Mar. Chem.*, **30**, 193–204.
Eagle, M., A. Paytan, R. W. Murray (2003), A comparison between excess barium and barite as indicators of carbon export, *Paleoceanography*, **18**(1), 1–13.
Edmonds, H. N., C. R. German (2004), Particle geochemistry in the Rainbow hydrothermal plume, Mid-Atlantic Ridge. *Geochim. Cosmochim. Acta,* **68**, 759–772.
Egbert, G. D., R. D. Ray, B. G. Bills (2004), Numerical modeling of the global semidiurnal tide in the present day and in the last glacial maximum. *J. Geophys. Res.*, **109**, C03003.
Elderfield, H. (1981), Metal-organic associations in interstitial waters of Narragansett bay sediments. *Am. J. Sci.*, **281**, 1184–1196.
Elderfield, H. (1985), Element cycling in bottom sediments. *Philos. Trans. R. Soc. London* **23**, 19–23.
Elderfield, H., M. J. Greaves, M. D. Rudnicki, D. J. Hydes (1993), Aluminum reactivity in hydrothermal plumes at the Mid-Atlantic Ridge. *J. Geophys. Res.*, **98**, 9667–9670.
Emile-Geay, J., M. A. Cane, N. Naik, R. Seager, A. C. Clement, A.C., A. van Geen (2003), Warren revisited: Atmospheric freshwater fluxes and "'Why is no deep water formed in the North Pacific'" *J. Geophys. Res.,* **108**.
Ewing, M., J. I. Ewing, M. Talwani (1964), Sediment distribution in the oceans: The Mid-Atlantic Ridge. *Geol. Soc. Am. Bull.*, **75**, 17–36.
Farrell, J. W., W. L. Prell (1989), Climatic change and CaCO3 Preservation: An 800,000 year bathymetric reconstruction from the Central Equatorial Pacific Ocean. *Paleoceanography* **4**, 447–466.
Feely, R. A., G. J. Massoth, J. H. Trefry, E. T. Baker, A. J. Paulson, G. T. Lebon (1994), Composition and sedimentation of hydrothermal plume particles from north Cleft segment, Juan de Fuca Ridge. *J. Geophys. Res.*, **99**, 4985–5006.
Feely, R. A., M. Lewison, G. J. Massoth, G. Robert-Baldo, J. W. Lavelle, R. H. Byrne, K. L. Von Damm, H. C. Curl, Jr. (1987), Composition and Dissolution of Black Smoker Particulates From Active Vents on the Juan de Fuca Ridge. *J. Geophys. Res.* **92**, 11347–11363.
Ferrat, M., D. J. Weiss, S. Strekopytov, S. Dong, H. Chen, J. Najorka, Y. Sun, S. Gupta, R. Tada, R. Sinha (2011), Improved provenance tracing of Asian dust sources using rare earth elements and selected trace elements for palaeomonsoon studies on the eastern Tibetan Plateau, *Geochim. Cosmochim. Acta*, **75**(21), 6374–6399.

Findlay, A. J., A. Gartman, T. J. Shaw, G. W. Luther (2015), Trace metal concentration and partitioning in the first 1.5m of hydrothermal vent plumes along the Mid-Atlantic Ridge: TAG, Snakepit, and Rainbow. *Chem. Geol.*, **412**, 117–131.

Fischer, H., M. L. Siggaard-Andersen, U. Ruth, R. Röthlisberger, E. W. Wolff (2007), Glacial/Interglacial Changes in Mineral Dust and Sea-Salt Records in Polar Ice Cores: Sources, Transport, and Deposition, *Rev. Geophys.*, **45**, 1–26.

Fitzsimmons, J. N., S. G. John, C. M. Marsay, C. L. Hoffman, S. L. Nicholas, B. M. Toner, C. R. German, R. M. Sherrell (2017), Iron persistence in a distal hydrothermal plume supported by dissolved-particulate exchange. *Nat. Geosci.*, **10**, 195–201.

Fleisher, M. Q., R. F. Anderson (2003), Assessing the collection efficiency of Ross Sea sediment traps using 230Th and 231Pa. *Deep Sea Res. Part II Top. Stud. Oceanogr.* **50**, 693–712.

Ford, R. G., K. M. Kemner, P. M. Bertsch (1999), Influence of sorbate-sorbent interactions on the crystallization kinetics of nickel- and lead-ferrihydrite coprecipitates. *Geochim. Cosmochim. Acta*, **63**, 39–48.

Fraile, I., M. Schulz, S. Mulitza, U. Merkel, M. Prange, A. Paul (2009), Modeling the seasonal distribution of planktonic foraminifera during the last glacial maximum, *Paleoceanography*, **24**(2), 1–15.

Francis, A. J., C. J. Dodge, F. Lu, G. P. Halada, C. R. Clayton (1994), XPS and XANES studies of uranium reduction by Clostridium sp. *Environ. Sci. Technol.*, **28**, 636–639.

Francois R., M. Frank, M. Rutgers van der Loeff, M. P. Bacon (2004), 230Th normalization: An essential tool for interpreting sedimentary fluxes during the late Quaternary. *Paleoceanography* **19**, PA1018.

Francois R., M. Frank, M. Rutgers van der Loeff, M. P. Bacon, W. Geibert, S. Kienast, R. F. Anderson, L. Bradtmiller, Z. Chase, G. Henderson, F. Marcantonio, S. E. Allen (2007), Comment on "Do geochemical estimates of sediment focusing pass the sediment test in the equatorial Pacific?" by M. Lyle et al. *Paleoceanography* **22**, PA1216.

Francois R., M. P. Bacon, D. O. Suman (1990), Thorium230 profiling in deep-sea sediments: High resolution records of flux and dissolution of carbonate in the Equatorial Atlantic during the last 24,000 years. *Paleoceanography,* **5**, 761–787.

Francois, R., M. A. Altabet, E. Yu, D. M. Sigman, M. P. Bacon, M. Frank, G. Bohrmann, G. Bareille, L. D. Labeyrie (1997), Contribution of Southern Ocean surface-water stratification to low atmospheric CO2 concentrations during the last glacial period. *Nature*, **389**, 929–936.

Freeman, E., L. C. Skinner, A. Tisserand, T. Dokken, A. Timmermann, L. Menviel, T. Friedrich (2015), An Atlantic-Pacific ventilation seesaw across the last deglaciation, *Earth Planet. Sci. Lett.*, **424**, 237–244.

Froelich, P. N., G. P. Klinkhammer, M. L. Bender, N. A. Luedtke, G. R. Heath, D. Cullen, P. Dauphin, D. Hammond, B. Hartman, V. Maynard (1979), Early oxidation of organic matter in pelagic sediments of the eastern equatorial Atlantic: suboxic diagenesis, *Geochim. Cosmochim. Acta,* **43**, 1075–1090.

Galbraith, E. D., M. Kienast, S. L. Jaccard, T. F. Pedersen, B. D. Brunelle, D. M. Sigman, T. Kiefer (2008), Consistent relationship between global climate and surface nitrate utilization in the western subarctic Pacific throughout the last 500 ka, *Paleoceanography*, **23**(2).

Galbraith, E. D., S. L. Jaccard (2015), Deglacial weakening of the oceanic soft tissue pump: Global constraints from sedimentary nitrogen isotopes and oxygenation proxies, *Quat. Sci. Rev.*, **109**, 38–48.

Galbraith, E. D., S. L. Jaccard, T. F. Pedersen, D. M. Sigman, G. H. Haug, M. Cook, J. R. Southon, R. Francois (2007), Carbon dioxide release from the North Pacific abyss during the last deglaciation, *Nature*, **449**(7164), 890–893.

Gale, A., C. A. Dalton, C. H. Langmuir, Y. Su, J. G. Schilling (2013), The mean composition of ocean ridge basalts. *Geochemistry, Geophys. Geosystems* **14**, 489–518.

Ganesh, R., K. G. Robinson, G. D. Reed (1997), Reduction of Hexavalent Uranium from Organic Complexes by Sulfate- and Iron-Reducing Bacteria, *Applied and Environmental Microbiology*, **63**, 4385–4391.

Ganeshram, R. S., S. E. Calvert, T. F. Pedersen, G. L. Cowie (1999), Factors controlling the burial of organic carbon in laminated and bioturbated sediments off NW Mexico: Implications for hydrocarbon preservation, *Geochim. Cosmochim. Acta*, **63**(11–12), 1723–1734.

Garcia, H. E., R. A. Locarnini, T. P. Boyer, J. I. Antonov, O. K. Baranova, M. M. Zweng, J. R. Reagan, D. R. Johnson (2014), World Ocean Atlas 2013, Volume 3: Dissolved Oxygen, Apparent Oxygen Utilization, and Oxygen Saturation, in: Levitus, S., Mishonov, A. (Eds.), NOAA Atlas NESDIS 75. p. 25.

Gargett, A. E. (1991), Physical processes and the maintenance of nutrient-rich euphotic zones*, Limnol. Oceanogr.*, **36**(8), 1527–1545.

Gebhardt, H., M. Sarnthein, P. M. Grootes, T. Kiefer, H. Kuehn, F. Schmieder, U. Röhl (2008), Paleonutrient and productivity records from the subarctic North Pacific for Pleistocene glacial terminations I to V, *Paleoceanography*, **23**(4), 1–21.

Geibert, W., R. Usbeck (2004), Adsorption of thorium and protactinium onto different particle types: Experimental findings, *Geochim. Cosmochim. Acta*, **68**(7), 1489–1501.

German, C. R., A. P. Fleer, M. P. Bacon, J. M. Edmond (1991), Hydrothermal scavenging at the Mid-Atlantic Ridge : radionuclide distributions, *Earth Planet. Sci. Lett.*, **105**, 170–181.

German, C. R., S. Colley, M. R. Palmer, A. Khripounoff, G. P. Klinkhammer (2002), Hydrothermal plume-particle fluxes at 13 degrees N on the East Pacific Rise, *Deep. Res. Part I-Oceanographic Res. Pap.*, **49**, 1921–1940.

Gherardi, J.-M., L. Labeyrie, S. Nave, R. Francois, J. F. McManus, E. Cortijo (2009), Glacial-interglacial circulation changes inferred from 231 Pa/ 230 Th sedimentary record in the North Atlantic region, *Paleoceanography*, **24**.

Glover, D. M., J. S. Wroblewski, C. R. McClain (1994), Dynamics of the transition zone in coastal zone color scanner-sensed ocean color in the North Pacific during oceanographic spring, *J. Geophys. Res.*, **99**(C4), 7501.

Goldfinger, C., C. H. Nelson, A. E. Morey, J. E. Johnson, J. R. Patton, E. Karabanov, J. Gutierrez-Pastor, A. T. Eriksson, E. Gracia, G. Dunhill, R. J. Enkin, A. Dallimore, T. Vallier (2012), Turbidite Event History — Methods and Implications for Holocene Paleoseismicity of the Cascadia Subduction Zone. *U.S. Geol. Surv. Prof. Pap*. 1661-F 170 p.

oGorbarenko, S. A. (1996), Stable Isotope and Lithologic Evidence of Late-Glacial and Holocene Oceanography of the Northwestern Pacific and Its Marginal Seas, *Quat. Res.*, **250**, 230–250.

Gorbarenko, S. A., J. R. Southon, L. D. Keigwin, M. V. Cherepanova, I. G. Gvozdeva (2004), Late Pleistocene-Holocene oceanographic variability in the Okhotsk Sea: Geochemical, lithological and paleontological evidence, *Palaeogeogr. Palaeoclimatol. Palaeoecol.*, **209**(1–4), 281–301.

Grant, K. M. E. J. Rohling, C. B. Ramsey, H. Cheng, R. L. Edwards, F. Florindo, D. Heslop,

F. Marra, A. P. Roberts, M. E. Tamisiea, F. Williams (2014), Sea-level variability over five glacial cycles., *Nat. Commun.*, **5**:5076.

Gray, W. R., J. W. B. Rae, R. C. J. Wills, A. E. Shevenell, B. Taylor, A. Burke, G. L. Foster, C. H. Lear (2018), Deglacial upwelling, productivity and CO2 outgassing in the North Pacific Ocean, *Nat. Geosci.*, 1, doi:10.1038/s41561-018-0108-6.

Grigorov, I., A. S. Rigual-Hernandez, S. Honjo, A. E. S. Kemp, L. K. Armand (2014), Settling fluxes of diatoms to the interior of the Antarctic circumpolar current along 170°W, *Deep. Res. Part I Oceanogr. Res. Pap.*, **93**, 1–13.

Gunn, D. E., A. I. Best (1998), A new automated nondestructive system for high resolution multi-sensor core logging of open sediment cores, *Geo-Marine Lett.,* **18**, 70–77.

Harrison, P. J., P. W. Boyd, D. E. Varela, S. Takeda, A. Shiomoto, T. Odate (1999), Comparison of factors controlling phytoplankton productivity in the NE and NW subarctic Pacific gyres, *Prog. Oceanogr.*, **43**(2–4), 205–234.

Hartnett, H. E., R. G. Keil, J. I. Hedges, A. H. Devol (1998), Influence of oxygen exposure time on organic carbon preservation in continental margin sediments, *Nature*, **391**, 572–575.

Haug, G. H., A. Ganopolski, D. M. Sigman, A. Rosell-Mele, G. E. A. Swann, R. Tiedemann, S. L. Jaccard, M. A. Maslin, M. J. Leng, G. Eglinton (2005), North Pacific seasonality and the glaciation of North America 2.7 million years ago, *Nature*, **433**, 821–825.

Haug, G. H., D. M. Sigman, R. Tiedemann, T. F. Pedersen, M. Sarntheim (1999), Onset of permanent stratifcation in the subarctic Pacific Ocean, *Nature*, **401**, 779–782.

Hauschild J., I. Grevemeyer, N. Kaul, H. Villinger (2003), Asymmetric sedimentation on young ocean floor at the East Pacific Rise, 15°S, *Mar. Geol.* **193**, 49–59.

Hayes, C. T., R. F. Anderson, M. Q. Fleisher, S. Serno, G. Winckler, R. Gersonde (2014), Biogeography in 231Pa/230Th ratios and a balanced 231Pa budget for the Pacific Ocean, *Earth Planet. Sci. Lett.*, **391**, 307–318.

Hayes, C. T., R. F. Anderson, S. L. Jaccard, R. François, M. Q. Fleisher, M. Soon, R. Gersonde (2013), A new perspective on boundary scavenging in the North Pacific Ocean, *Earth Planet. Sci. Lett.*, **369–370**, 86–97.

Hedges, J. I., F. S. Hu, A. H. Devol, H. E. Hartnett, E. Tsamakis, R. G. Keil (1999), Sedimentary organic matter preservation: A test for selective degradation under oxic conditions, *Am. J. Sci.*, **299**(7–9), 529–555.

Heezen, B. C., M. Rawson (1977), Visual observations of contemporary current erosion and tectonic deformation on the Cocos Ridge Crest, *Mar. Geol.*, **23**, 173–196.

Hegner, E., M. Tatsumoto (1987), Pb, Sr, and Nd isotopes in basalts and sulfides from the Juan de Fuca Ridge, *J. Geophys. Res.*, **92**(B11), 11380.

Henderson G. M., C. Heinze, R. F. Anderson, A. M. E. Winguth (1999), Global distribution of the 230Th flux to ocean sediments constrained by GCM modelling. *Deep Sea Res. I* **46**, 1861–1893.

Henderson, G. M., R. F. Anderson (2003), The U-series Toolbox for Paleoceanography, *Rev. Mineral. Geochemistry* **52**, 493–531.

Hendy, I. L., T. Cosma (2008), Vulnerability of the Cordilleran Ice Sheet to iceberg calving during late quaternary rapid climate change events, *Paleoceanography*, **23**(2), 1–8.

Henry, L. G., J. F. McManus, W. B. Curry, N. L. Roberts, A. M. Piotrowski, L. D. Keigwin (2016), North Atlantic ocean circulation and abrupt climate change during the last glaciation, *Science*, **353**(6298), 470–474.

Herguera, J. C., T. Herbert, M. Kashgarian, C. Charles (2010), Intermediate and deep water mass distribution in the Pacific during the Last Glacial Maximum inferred from oxygen and carbon stable isotopes, *Quat. Sci. Rev.,* **29**, 1228–1245.

Hernandez-Sanchez, M. T., R. A. Mills, H. Planquette, R. D. Pancost, L. Hepburn, I. Salter, T. Fitzgeorge-Balfour (2011), Quantifying export production in the Southern Ocean: Implications for the Ba xs proxy, *Paleoceanography*, **26**, PA4222.

Hickey, B. M., (1979), The California current system—hypotheses and facts, *Prog. Oceanogr*. **8**, 191–279.

Hillaire-Marcel, C., A. de Vernal (2008), Stable isotope clue to episodic sea ice formation in the glacial North Atlantic, *Earth Planet. Sci. Lett*., **268**(1–2), 143–150.

Honda, M. C., K. Imai, Y. Nojiri, F. Hoshi, T. Sugawara, M. Kusakabe (2002), The biological pump in the northwestern North Pacific based on fluxes and major components of particulate matter obtained by sediment-trap experiments (1997-2000), *Deep. Res. II*, **49**, 5595–5625.

Hönisch, B., K. A. Allen, D. W. Lea, H. J. Spero, S. M. Eggins, J. Arbuszewski, P. deMenocal, Y. Rosenthal, A. D. Russell, H. Elderfield (2013), The influence of salinity on Mg/Ca in planktic foraminifers - Evidence from cultures, core-top sediments and complementary δ18O, *Geochim. Cosmochim. Acta*, **121**, 196–213.

Horikawa, K., Y. Asahara, K. Yamamoto, Y. Okazaki (2010), Intermediate water formation in the Bering Sea during glacial periods: Evidence from neodymium isotope ratios, *Geology*, **38**(5), 435–438.

Horn, D. R., M. Ewing, M. N. Delach, B. M. Horn (1971), Turbidites of the Northeast Pacific. *Sedimentology*, **16**, 55–69.

Hovan, S. A., D. K. Rea, N. G. Pisias (1991), Late Pleistocene continental climate and oceanic variability recorded in Northwest Pacific sediments, *Paleoceanography*, **6**(3), 349–370.

Hovan, S. A., D. K. Rea, N. G. Pisias, N. J. Shackleton (1989), A direct link between the China loess and marine d18O records: Aeolian flux to the north Pacific, *Nature*, **340**, 296–298.

Hu, A., G. A. Meehl, B. L. Otto-Bliesner, C. Waelbroeck, W. Han, M. F. Loutre, K. Lambeck, J. X. Mitrovica, N. Rosenbloom (2010), Influence of Bering Strait flow and North Atlantic circulation on glacial sea-level changes, *Nat. Geosci*., **3**(2), 118–121.

Hu, A., G. A. Meehl, W. Han, A. Abe-Ouchi, C. Morrill, Y. Okazaki, M. O. Chikamoto (2012), The Pacific-Atlantic seesaw and the Bering Strait, *Geophys. Res. Lett.,* **39**(3), 1–6.

Hu, A., G. A. Meehl, W. Han, A. Timmermann, B. Otto-Bliesner, Z. Liu, W. M. Washington, W. Large, A. Abe-Ouchi, M. Kimoto, K. Lambeck, B. Wu (2012), Role of the Bering Strait on the hysteresis of the ocean conveyor belt circulation and glacial climate stability, *Proc. Natl. Acad. Sci*., **109**(17), 6417–6422.

Hu, A., G. A. Meehl, W. Han, B. Otto-Bliestner, A. Abe-Ouchi, N. Rosenbloom (2015), Effects of the Bering Strait closure on AMOC and global climate under different background climates, *Prog. Oceanogr*., **132**, 174–196.

Huerta-Diaz, M. A., J. W. Morse (1992), Pyritisation of trace metals in anoxic marine sediments. *Geochim. Cosmochim. Acta,* **56**, 2681–2702.

Iwasaki, S., K. Kimoto, A. Kuroyanagi, H. Kawahata (2017), Horizontal and vertical distributions of planktic foraminifera in the subarctic Pacific, *Mar. Micropaleontol*., **130**, 1–14.

Jaccard, S. L., E. D. Galbraith (2012), Large climate-driven changes of oceanic oxygen concentrations during the last deglaciation, *Nat. Geosci.,* **5**, 151–156.

Jaccard, S. L., E. D. Galbraith, A. Martínez-Garcia, R. F. Anderson (2016), Covariation of abyssal Southern Ocean oxygenation and pCO2 throughout the last ice age, *Nature* **530**, 207–210.

Jaccard, S. L., E. D. Galbraith, D. M. Sigman, G. H. Haug (2010), A pervasive link between Antarctic ice core and subarctic Pacific sediment records over the past 800 kyrs, *Quat. Sci. Rev.*, **29**(1–2), 206–212.

Jaccard, S. L., E. D. Galbraith, D. M. Sigman, G. H. Haug, R. Francois, T. F. Pedersen, P. Dulski, H. R. Thierstein (2009), Subarctic Pacific evidence for a glacial deepening of the oceanic respired carbon pool, *Earth Planet. Sci. Lett.*, **277**(1–2), 156–165.

Jaccard, S. L., G. H. Haug, D. M. Sigman, T. F. Pedersen, H. R. Thierstein, U. Rohl (2005), Glacial/Interglacial Changes in Subarctic North Pacific Stratification, *Science*, **308**(5724), 1003–1006.

Jacobel, A. W., J. F. McManus, R. F. Anderson, G. Winckler (2016), Large deglacial shifts of the Pacific Intertropical Convergence Zone, *Nat. Commun.*, **7.**

Jacobel, A. W., J. F. McManus, R. F. Anderson, G. Winckler (2017), Climate-related response of dust flux to the central equatorial Pacific over the past 150 kyr, *Earth Planet. Sci. Lett.*, **457**, 160–172.

Jacobel, A. W., J. F. McManus, R. F. Anderson, G. Winckler (2017), Repeated storage of respired carbon in the equatorial Pacific Ocean over the last three glacial cycles, *Nat. Commun.* **8**.

Jahn, B., S. Gallet, J. Han (2001), Geochemistry of the Xining, Xifeng and Jixian sections, Loess Plateau of China: eolian dust provenance and paleosol evolution during the last 140 ka, *Chem. Geol.*, **178**, 71–94.

Jang, K., Y. Huh, Y. Han (2017), Authigenic Nd isotope record of North Pacific Intermediate Water formation and boundary exchange on the Bering Slope, *Quat. Sci. Rev.*, **156**, 150–163.

Jickells, T. D., Z. S. An, K. K. Andersen, A. R. Baker, G. Bergametti, N. Brooks, J. J. Cao, P. W. Boyd, R. A. Duce, K. A. Hunter, H. Kawahata, N. Kubilay, J. LaRoche, P. S. Liss, N. Mahowald, J. M. Prospero, A. J. Ridgwell, I. Tegen, R. Torres (2005), Global iron connections between desert dust, ocean biogeochemistry, and climate., *Science*, **308**(5718), 67–71.

Johnson, D. A., T. C. Johnson (1970), Sediment redistribution by bottom currents in the central Pacific. *Deep Sea Res.* **17**, 157–169.

Jones, C. E., A. N. Halliday, D. K. Rea, R. M. Owen (2000), Eolian inputs of lead to the North Pacific, *Geochim. Cosmochim. Acta*, **64**(8), 1405–1416.

Jonkers, L., R. Zahn, A. Thomas, G. Henderson, W. Abouchami, R. François, P. Masque, I. R. Hall, T. Bickert (2015), Deep circulation changes in the central South Atlantic during the past 145 kyrs reflected in a combined 231Pa/230Th, Neodymium isotope and benthic d13C record, *Earth Planet. Sci. Lett.,* **419**, 14–21.

Jung, M., J. Ilmberger, A. Mangini, K. C. Emeis (1997), Why some Mediterranean sapropels survived burn-down (and others did not), *Mar. Geol.*, **141**, 51–60.

Kaiser, J., F. Lamy (2010), Links between Patagonian Ice Sheet fluctuations and Antarctic dust variability during the last glacial period (MIS 4-2), *Quat. Sci. Rev.*, **29**(11–12), 1464–1471.

Karlin, R., M. W. Lyle, R. Zahn (1992), Carbonate variations in the northeast Pacific during the late Quaternary. *Paleoceanography* **7**, 43–61.

Karsten, J. L., J. R. Delaney (1989), Hot spot-ridge crest convergence in the northeast Pacific. *J. Geophys. Res.* **94**, 700–712.

Katsuki, K., K. Takahashi (2005), Diatoms as paleoenvironmental proxies for seasonal productivity, sea-ice and surface circulation in the Bering Sea during the late Quaternary, *Deep. Res. Part II Top. Stud. Oceanogr.*, **52**(16–18), 2110–2130.

Kawahata, H., H. Ohshima (2002), Small latitudinal shift in the Kuroshio Extension

(Central Pacific) during glacial times: Evidence from pollen transport, *Quat. Sci. Rev.*, **21**(14–15), 1705–1717.
Kawakami, H., M. C. Honda, M. Wakita, S. Watanabe (2007), Time-series observation of dissolved inorganic carbon and nutrients in the northwestern North Pacific, *J. Oceanogr.*, **63**(6), 967–982.
Keigwin, L. D. (1987), North Pacific deep water formation during the latest glaciation, *Nature*, **330**, 362–364.
Keigwin, L. D. (1998), Glacial-age hydrography of the far northwest Pacific Ocean, *Paleoceanography*, **13**(4), 323–339.
Keigwin, L. D., G. A. Jones (1990), Deglacial climatic oscillations in the Gulf of California. *Paleoceanography*, **5**, 1009–1023.
Keigwin, L. D., G. A. Jones, P. N. Froelich (1992), A 15,000 year paleoenvironmental record from Meiji Seamount, far northwestern Pacific, *Earth Planet. Sci. Lett.*, **111**, 425–440.
Keigwin, L. D., M. A. Schlegel (2002), Ocean ventilation and sedimentation since the glacial maximum at 3 km in the western North Atlantic, *Geochemistry Geophys. Geosystems* **3**.
Keigwin, L. D., M. S. Cook (2007), A role for North Pacific salinity in stabilizing North Atlantic climate, *Paleoceanography*, **22**(3).
Keil, R. G., D. B. Montlucon, F. G. Prahl, J. I. Hedges (1994), Sorptive preservation of labile organic matter in marine sediments, *Nature*, **370**, 549–552.
Keil, R. G., J. I. Hedges (1993), Sorption of organic matter to mineral surfaces and the preservation of organic matter in coastal marine sediments, *Chem. Geol.*, **107**(3–4), 385–388.
Kennett, J. P., B. L. Ingram (1995), A 20,000 year record of ocean circulation and climate change from the Santa Barbara basin, *Nature*, **377**, 510–514.
Key, R. M., P. D. Quay, P. Schlosser, A. McNichol, K. von Reden, R. J. Schneider, K. L. Elder, M. Stuiver, H. G. Östlund (2002), WOCE radiocarbon IV: Pacific ocean results; P10, P13N, P14C, P18, P19 & S4P, *Radiocarbon*, **44**, 239–392.
Kienast S. S., M. Kienast, A. C. Mix, S. E. Calvert, R. François (2007), Thorium-230 normalized particle flux and sediment focusing in the Panama Basin region during the last 30,000 years, *Paleoceanography* **22**.
Kienast, S. S. (2003), Palaeoceanography of the mid-latitude North East Pacific during the late Pleistocene, Ph.D. Dissertation, The University of British Columbia.
Kienast, S. S., G. Winckler, J. Lippold, S. Albani, N. M. Mahowald (2016), Tracing dust input to the global ocean using thorium isotopes in marine sediments: ThoroMap, *Global Biogeochem. Cycles*, **30**(10), 1526–1541.
Kienast, S. S., I. L. Hendy, J. Crusius, T. F. Pedersen, S. E. Calvert (2004), Export production in the subarctic North Pacific over the last 800 kyrs: No evidence for iron fertilization?, *J. Oceanogr.*, **60**(3), 189–203.
Kienast, S. S., M. Kienast, A. C. Mix, S. E. Calvert, R. François (2007), Thorium-230 normalized particle flux and sediment focusing in the Panama Basin region during the last 30,000 years, *Paleoceanography*, **22**(2).
Kim, S. J., T. J. Crowley, D. J. Erickson, B. Govindasamy, P. B. Duffy, B. Y. Lee (2008), High-resolution climate simulation of the last glacial maximum. *Clim. Dyn.* **31**, 1–16.
Kirby, M. E., S. J. Feakins, N. Bonuso, J. M. Fantozzi, C. A. Hiner (2013), Latest Pleistocene to Holocene hydroclimates from Lake Elsinore, California, *Quat. Sci. Rev.*, **76**, 1–15.

Klinkhammer, G. P., M. R. Palmer (1991), Uranium in the oceans: Where it goes and why. *Geochim. Cosmochim. Acta*, **55**, 1799–1806.

Knudson, K. P., A. C. Ravelo (2015a), Enhanced subarctic Pacific Stratification and nutrient utilization during glacials over the last 1.2 Myr, *Geophys. Res. Lett.*, **42**, 9870–9879.

Knudson, K. P., A. C. Ravelo (2015b), North Pacific Intermediate Water circulation enhanced by the closure of the Bering Strait, *Paleoceanography*, **30**, 1–18.

Kochenov, A. V., K. G. Korloev, V. T. Dubinchuk, Y. L. Medvedev (1977), Experimental data on the conditions of precipitation of uranium from aqueous solutions. *Geochemistry Int.*, **14**, 82–87.

Kohfeld, K. E., S. P. Harrison (2001), DIRTMAP: the geological record of dust, *Earth-Science Rev.*, **54**(1–3), 81–114.

Kohfeld, K. E., Z. Chase (2011), Controls on deglacial changes in biogenic fluxes in the North Pacific Ocean, *Quat. Sci. Rev.*, **30**(23–24), 3350–3363.

Kong, W., L. M. Swensona, J. C. H. Chiang (2017), Seasonal transitions and the westerly jet in the Holocene East Asian summer monsoon, *J. Clim.*, **30**(9), 3343–3365.

Korff, L., T. von Dobeneck, T. Frederichs, S. Kasten, G. Kuhn, R. Gersonde, B. Diekmann (2016), Cyclic magnetite dissolution in Pleistocene sediments of the abyssal northwest Pacific Ocean: Evidence for glacial oxygen depletion and carbon trapping, *Paleoceanography* **31**, 600–624.

Koski, R. A., I. R. Jonasson, D. C. Kadko, V. K. Smith, F. L. Wong (1994), Compositions, growth mechanisms, and temporal relations of hydrothermal sulfide-sulfate-silica chimneys at the northern Cleft segment, Juan de Fuca Ridge. *J. Geophys. Res. Solid Earth*, **99**, 4813–4832.

Kretschmer, S., W. Geibert, M. M. Rutgers van der Loeff, C. Schnabel, S. Xu, and G. Mollenhauer (2011), Fractionation of 230Th, 231Pa, and 10Be induced by particle size and composition within an opal-rich sediment of the Atlantic Southern Ocean, *Geochim. Cosmochim. Acta*, **75**(22), 6971–6987.

Kretschmer, S., W. Geibert, M. M. Rutgers van der Loeff, G. Mollenhauer (2010), Grain size effects on 230Thxs inventories in opal-rich and carbonate-rich marine sediments. *Earth Planet. Sci. Lett.* **294**, 131–142.

Kroopnick, P. M. (1985), The distribution of 13C of CO2 in the world oceans, *Deep Sea Res.*, **32**, 57–84.

Kuhn, T., H. Burger, D. Castradori, P. Halbach (2000), Volcanic and hydrothermal history of ridge segments near the Rodrigues Triple Junction (Central Indian Ocean) deduced from sediment geochemistry. *Mar. Geol.,* **169**, 391–409.

Kuroyanagi, A., H. Kawahata, H. Nishi, M. C. Honda (2008), Seasonal to interannual changes in planktonic foraminiferal assemblages in the northwestern North Pacific: Sediment trap results encompassing a warm period related to El Niño, *Palaeogeogr. Palaeoclimatol. Palaeoecol.*, **262**(1–2), 107–127.

Kutzbach, J. E., H. E. Wright (1985), Simulation of the climate of 18,000 years BP: Results for the North American/North Atlantic/European sector and comparison with the geologic record of North America, *Quat. Sci. Rev.*, **4**(3), 147–187.

Kyte, F. T., M. Leinen, G. Ross Heath, L. Zhou (1993), Cenozoic sedimentation history of the central North Pacific: Inferences from the elemental geochemistry of core LL44-GPC3, *Geochim. Cosmochim. Acta*, **57**(8), 1719–1740.

Labeyrie, L. D., J.-C. Duplessy, P. L. Blanc (1987), Variations in mode of formation and temperature of oceanic deep waters over the past 125,000 years, *Nature,* **327**, 477-482.

Lam, P. J., L. F. Robinson, J. Blusztajn, C. Li, M. S. Cook, J. F. McManus, L. D. Keigwin (2013), Transient stratification as the cause of the North Pacific productivity spike during deglaciation, *Nat. Geosci.*, **6**(8), 622–626.

Lamy, F., R. Gersonde, G. Winckler, O. Esper, a Jaeschke, G. Kuhn, J. Ullermann, a Martinez-Garcia, F. Lambert, R. Kilian (2014), Increased dust deposition in the Pacific Southern Ocean during glacial periods., *Science*, **343**(6169), 403–7.

Langmuir, D. (1978), Uranium solution-mineral equilibria at low temperatures with applications to sedimentary ore deposits. *Geochim. Cosmochim. Acta,* **42**, 547–569.

Larrasoaña, J. C., A. P. Roberts, E. J. Rohling (2008), Magnetic susceptibility of eastern Mediterranean marine sediments as a proxy for Saharan dust supply? *Mar. Geol.*, **254**, 224–229.

Lavelle, J. W. (2012), On the dynamics of current jets trapped to the flanks of mid-ocean ridges, *J. Geophys. Res. Ocean.*, **117**, 1–12.

Lavelle, J. W., G. A. Cannon (2001), On subinertial oscillations trapped by the Juan de Fuca Ridge, northeast Pacific, *J. Geophys. Res.* **106**, 31099.

Lee, S. Y., C. J. Poulsen (2005), Tropical Pacific climate response to obliquity forcing in the Pleistocene, *Paleoceanography*, **20**(4), 1–10.

Li, C., D. S. Battisti (2008), Reduced Atlantic storminess during last glacial maximum: Evidence from a coupled climate model, *J. Clim.*, **21**(14), 3561–3579.

Liger, E., L. Charlet, P. Van Cappellen (1999), Surface catalysis of uranium (VI) reduction by iron (II), *Geochim. Cosmochim. Acta,* **63**, 2939–2955.

Lindberg, R. D., D. D. Runnells (1984), Ground Water Redox Reactions: An Analysis of Equilibrium State Applied to Eh Measurements and Geochemical Modeling, *Science*, **225**, 925–927.

Lisiecki, L. E., M. E. Raymo (2005), A Pliocene-Pleistocene stack of 57 globally distributed benthic d18O records, *Paleoceanography*, **20**, PA1003.

Lister, C. R. B. (1976), Control of pelagic sediment distribution by internal waves of tidal period: Possible interpretation of data from the southern East Pacific Rise, *Mar. Geol.* **20**, 297–313.

Little, S. H., D. Vance, T. W. Lyons, J. McManus (2015), Controls on trace metal authigenic enrichment in reducing sediments: Insights from modern oxygen-deficient settings, *Am. J. Sci.*, **315**, 77–119.

Lonsdale, P., W. R. Normark, W. A. Newman (1972), Sedimentation and Erosion on Horizon Guyot, *Geol. Soc. Am. Bull.* **83**, 289–316.

Lora, J. M., J. L. Mitchell, C. Risi, A. E. Tripati (2017), North Pacific atmospheric rivers and their influence on western North America at the Last Glacial Maximum, *Geophys. Res. Lett.*, **44**(2), 1051–1059.

Loubere, P., F. Mekik, R. Francois, S. Pichat (2004), Export fluxes of calcite in the eastern equatorial Pacific from the Last Glacial Maximum to present, *Paleoceanography* **19**, PA2018.

Loveley, M. R., F. Marcantonio, M. M. Wisler, J. E. Hertzberg, M. W. Schmidt, M. Lyle (2017), Millennial-scale iron fertilization of the eastern equatorial Pacific over the past 100,000 years, *Nat. Geosci.*, **10**.

Lovley, D. R., E. J. P. Phillips, Y. A. Gorby, E. R. Landa (1991), Microbial reduction of Uranium, *Nature,* **350**, 413–416.

Lund, D. C., P. D. Asimow, K. A. Farley, T. O. Rooney, E. Seeley, E. W. Jackson, Z. M. Durham (2016), Enhanced East Pacific Rise hydrothermal activity during the last two glacial terminations, *Science,* **351**, 478–482.

Lunel, T., M. D. Rudnicki, H. Elderfield, D. J. Hydes (1990), Aluminium as a depth-sensitive tracer of entrainment in submarine hydrothermal plumes, *Nature*, **344**, 137–139.

Lunt, D. J., P. J. Valdes (2002), Dust deposition and provenance at the Last Glacial Maximum and present day, *Geophys. Res. Lett.*, **29**(22), 42-1-42–4.

Lyle, M., F. Marcantonio, W. S. Moore, R. W. Murray, C. Huh, B. P. Finney, D. W. Murray, A. C. Mix (2014), Sediment size fractionation and focusing in the equatorial Pacific: Effect on 230Th normalization and paleo flux measurements, *Paleoceanography* **29**, 747–763.

Lyle, M., N. Mitchell, N. Pisias, A. Mix, J. I. Martinez, A. Paytan (2005), Do geochemical estimates of sediment focusing pass the sediment test in the equatorial Pacific? *Paleoceanography* **20**.

Lyle, M., N. Pisias, A. Paytan, J. I. Martinez, A. Mix (2007), Reply to comment by R. Francois et al. on "Do geochemical estimates of sediment focusing pass the sediment test in the equatorial Pacific?": Further explorations of 230 Th normalization, *Paleoceanography* **22**.

Lynch-Stieglitz, J., J. F. Adkins, W. B. Curry, T. Dokken, I. R. Hall, J. C. Herguera, J. J. M. Hirschi, E. Ivanova, C. V. Kissel, O. Marchal, T. M. Marchitto, I. N. McCave, J. F. McManus, S. Mulitza, U. Ninnemann, F. Peeters, E.-F. Yu, R. Zahn (2007), Atlantic meridional overturning circulation during the Last Glacial Maximum, *Science*, **316**(5821), 66–69.

Lynn, D. C., E. Bonatti (1965), Mobility of manganese in diagenesis of deep-sea sediments, *Mar. Geol.*, **3**, 457–474.

Macdonald, A. M., S. Mecking, P. E. Robbins, J. M. Toole, G. C. Johnson, L. Talley, M. Cook, S. E. Wijffels (2009), The WOCE-era 3-D Pacific Ocean circulation and heat budget, *Prog. Oceanogr.* **82**, 281–325.

Mackenzie, F. T., L. R. Kump (1995), Reverse Weathering, Clay Mineral Formation, and Oceanic Element Cycles, *Science*, **270**(5236), 586–586.

Mahowald, N. M., D. R. Muhs, S. Levis, P. J. Rasch, M. Yoshioka, C. S. Zender, C. Luo (2006), Change in atmospheric mineral aerosols in response to climate: Last glacial period, preindustrial, modern, and doubled carbon dioxide climates, *J. Geophys. Res.*, **111**(D10).

Mahowald, N., S. Albani, S. Engelstaedter, G. Winckler, M. Goman (2011), Model insight into glacial-interglacial paleodust records, *Quat. Sci. Rev.*, **30**(7–8), 832–854.

Manabe, S., A. J. Broccoli (1985), The influence of continental ice sheets on the climate of an ice age, *J. Geophys. Res.*, **90**(D1), 2167.

Mangini, A., A. Eisenhauer, P. Walter (1990), Response of manganese in the ocean to the climatic cycles in the Quaternary, *Paleoceanography*, **5**, 811–821.

Mangini, A., M. Jung, S. Laukenmann (2001) What do we learn from peaks of uranium and of manganese in deep sea sediments? *Mar. Geol.,* **177**, 63–78.

Marcantonio, F., M. Lyle, R. Ibrahim (2014) Particle sorting during sediment redistribution processes and the effect on 230Th-normalized mass accumulation rates, *Geophys. Res. Lett.* **41**, 5547–5554.

Marks, N. S. (1981), Sedimentation on new ocean crust: The Mid-Atlantic Ridge at 37˚N, *Mar. Geol.,* **43**, 65–82.

Martin, J. H., S. E. Fitzwater (1988), Iron deficiency limits phyto-plankton growth in the north-east Pacific subarctic, *Nature*, **331**, 341–343.

Martinez-Garcia, A., D. M. Sigman, H. Ren, R. F. Anderson, M. Straub, D. A. Hodell, S. L. Jaccard, T. I. Eglinton, G. H. Haug (2014), Iron Fertilization of the Subantarctic Ocean During the Last Ice Age, *Science*, **343**, 1347–1350.

Martinson, D. G., N. G. Pisias, J. D. Hays, J. Imbrie, T. C. Moore, N. J. Shackleton (1987), Age dating and the orbital theory of the ice ages: Development of a high-resolution 0 to 300,000 year chronostratigraphy, *Quat. Res.,* **27**, 1–29.

Massoth, G. J., E. T. Baker, J. E. Lupton, R. A. Feely, D. A. Butterfield, K. L. Von Damm, K. K. Roe, G. T. Lebon (1994), Temporal and spatial variability of hydrothermal manganese and iron at Cleft segment, Juan de Fuca Ridge. *J. Geophys. Res*., **99**, 4905–4923.

Matsumoto, K., T. Oba, J. Lynch-Stieglitz, H. Yamamoto (2002), Interior hydrography and circulation of the glacial Pacific Ocean, *Quat. Sci. Rev*., **21**, 1693–1704.

Matul, A. G. (2017), Probable limits of sea ice extent in the northwestern Subarctic Pacific during the last glacial maximum, *Oceanology*, **57**(5), 700–706.

Max, L., N. Rippert, L. Lembke-Jene, A. Mackensen, D. Nurnberg, R. Tiedemann (2017), Evidence for enhanced convection of North Pacific Intermediate Water to the low-latitude Pacific under glacial conditions, *Paleoceanography*, **32**, 41–55.

Mayer, L. A. (1979), Deep Sea Carbonates: Acoustic, Physical, and Stratigraphic Properties, *J. Sediment. Res.,* **49**, 819–836.

Mayer, L. A. (1991), Extraction of high-resolution carbonate data for palaeoclimate reconstruction, *Nature*, **352**, 148-150.

McCave, I. N., I. R. Hall (2006), Size sorting in marine muds: Processes, pitfalls, and prospects for paleoflow-speed proxies, *Geochemistry, Geophys. Geosystems* **7**.

McDonald, D., T. F. Pedersen, J. Crusius (1999), Multiple late Quaternary episodes of exceptional diatom production in the Gulf of Alaska, *Deep Sea Res. II*, **46**, 2993–3017.

McGee, D., F. Marcantonio, J. F. McManus, G. Winckler (2010), The response of excess 230Th and extraterrestrial 3He to sediment redistribution at the Blake Ridge, western North Atlantic. *Earth Planet. Sci. Lett.* **299**, 138–149.

McGee, D., F. Marcantonio, J. Lynch-Stieglitz (2007), Deglacial changes in dust flux in the eastern equatorial Pacific, *Earth Planet. Sci. Lett.*, **257**(1–2), 215–230.

McGee, D., G. Winckler, A. Borunda, S. Serno, R. F. Anderson, C. Recasens, A. Bory, D. Gaiero, S. L. Jaccard, M. Kaplan, J. F. McManus, M. Revel, Y. Sun (2016), Tracking eolian dust with helium and thorium: Impacts of grain size and provenance, *Geochim. Cosmochim. Acta*, **175**, 47–67.

McGee, D., W. S. Broecker, G. Winckler (2010), Gustiness: The driver of glacial dustiness?, *Quat. Sci. Rev*., **29**(17–18), 2340–2350.

McKendry, I. G., J. P. Hacker, R. Stull (2001), Long-range transport of Asian dust to the Lower Fraser Valley, British Columbia, Canada, *J. Geophys. Res.*, **106**(D16), 18361–18370.

McManus, J. F., R. F. Anderson, W. S. Broecker, M. Q. Fleisher, S. M. Higgins (1998), Radiometrically determined sedimentary fluxes in the sub-polar North Atlantic during the last 140,000 years, *Earth Planet. Sci. Lett.* **155**, 29–43.

McManus, J. F., R. Francois, J.-M. Gherardi, L. D. Keigwin, S. Brown-Leger (2004), Collapse and rapid resumption of Atlantic meridional circulation linked to deglacial climate changes., *Nature*, **428**(6985), 834-837.

McManus, J., W. Berelson, G. Klinkhammer, K. Johnson, K. Coale, R. Anderson, N. Kumar, D. Burdige, D. Hammond, H. Brumsack, D. McCorkle, A. Rushdi (1998),

Geochemistry of barium in marine sediments: implications for its use as a paleoproxy, *Geochim. Cosmochim. Acta,,* **62**(21–22), 3453–3473.
McManus, J., W. M. Berelson, G. P. Klinkhammer, D. E. Hammond, C. Holm (2005), Authigenic uranium: relationship to oxygen penetration depth and organic carbon rain, *Geochim. Cosmochim. Acta,* **69**, 95–108.
McManus, J., W. M. Berelson, G. P. Klinkhammer, T. E. Kilgore, D. E. Hammond (1994), Remobilization of barium in continental margin sediments, *Geochim. Cosmochim. Acta,*, **58**(22), 4899–4907.
Méheust, M., R. Stein, K. Fahl, R. Gersonde (2018), Sea-ice variability in the subarctic North Pacific and adjacent Bering Sea during the past 25 ka: new insights from IP25 and Uk′37 proxy records, *arktos*, **4**(8).
Menking, K. M., R. Y. Anderson, N. G. Shafike, K. H. Syed, B. D. Allen (2004), Wetter or colder during the Last Glacial Maximum ? Revisiting the pluvial lake question in southwestern North America, *Quat. Res.*, **62**, 280–288.
Menviel, L., J. Yu, F. Joos, A. Mouchet, K. J. Meissner, M. H. England (2017), Poorly ventilated deep ocean at the Last Glacial Maximum inferred from carbon isotopes: A data-model comparison study, *Paleoceanography*, **32**, 2–17.
Metz, S., J. H. Trefry, T. A. Nelsen (1988), History and geochemistry of a metalliferous sediment core from the Mid-Atlantic Ridge at 26°N, *Geochim. Cosmochim. Acta*, **52**, 2369–2378.
Michalopoulos, P., R. C. Aller, R. J. Reeder (2000), Conversion of diatoms to clays during early diagenesis in tropical, continental shell muds, *Geology*, **28**(12), 1095–1098.
Middelburg, J. J., G. J. de Lange, C. H. Van der Weijden (1987), Manganese solubility control in marine pore waters, *Geochim. Cosmochim. Acta,* **51**, 759–763.
Mikolajewicz, U., T. J. Crowley, A. Schiller, R. Voss (1997), Modelling teleconnections between the North Atlantic and North Pacific during the Younger Dryas, *Nature*, **387**, 384–387.
Mills, R. A., H. Elderfield, J. Thomson (1993), A Dual Origin for the Hydrothermal Component in a Metalliferous, *J. Geophys. Res.,* **98**, 9671–9681.
Mills, R. A., J. Thomson, H. Elderfield, R. W. Hinton, E. Hyslop (1994), Uranium enrichment in metalliferous sediments from the Mid-Atlantic Ridge, *Earth Planet. Sci. Lett.*, **124**, 35–47.
Mills, R. A., R. M. Dunk (2010), Tracing low-temperature fluid flow on ridge flanks with sedimentary uranium distribution, *Geochemistry Geophys. Geosystems* **11**.
Mills, R. A., S. L. Taylor, H. Pälike, J. Thomson (2010), Hydrothermal sediments record changes in deep water oxygen content in the SE Pacific, *Paleoceanography,* **25**, PA4226.
Mitchell, N. C. (1993), A model for attenuation of backscatter due to sediment accumulations and its application to determine sediment thicknesses with GLORIA sidescan sonar, *J. Geophys. Res.*, **98**, 22477–22493.
Mitchell, N. C. (1995), Diffusion transport model for pelagic sediments on the Mid-Atlantic Ridge, *J. Geophys. Res.*, 100, 19991–20009.
Mitchell, N. C. (1998), Sediment accumulation rates from Deep Tow profiler records and DSDP Leg 70 cores over the Galapagos spreading centre, in: Cramp, A., MacLeod, C.J., Lee, S. V, Jones, E.J.W. (Eds.), Geological Evolution of Ocean Basins: Results from the Ocean Drilling Program. Geological Society, London, pp. 199–209.
Mitchell, N. C., J. M. Huthnance (2013) Geomorphological and geochemical evidence (230Th anomalies) for cross-equatorial currents in the central Pacific, *Deep Sea Res. Part I Oceanogr. Res. Pap.* **78**, 24–41.

Mitchell, N. C., J. M. Huthnance (2013), Geomorphological and geochemical evidence (230Th anomalies) for cross-equatorial currents in the central Pacific, *Deep Sea Res. Part I Oceanogr. Res. Pap*. **78**, 24–41.
Mitchell, N. C., S. Allerton, J. Escartin (1998), Sedimentation on young ocean floor at the Mid-Atlantic Ridge, 29˚N, *Mar. Geol.,* **148**, 1–8.
Mitchener, H., H. Torfs (1996), Erosion of mud / sand mixtures, *Coast. Eng*. **29**, 1–25.
Molnar, P., W. R. Boos, D. S. Battisti (2010), Orographic Controls on Climate and Paleoclimate of Asia: Thermal and Mechanical Roles for the Tibetan Plateau, *Annu. Rev. Earth Planet. Sci.*, **38**(1), 77–102.
Morford, J. L., S. Emerson (1999), The geochemistry of redox sensitive trace metals in sediments, *Geochim. Cosmochim. Acta,* **63**, 1735–1750.
Morford, J. L., W. R. Martin, C. M. Carney (2009), Uranium diagenesis in sediments underlying bottom waters with high oxygen content, *Geochim. Cosmochim. Acta*, **73**, 2920–2937.
Mortlock, R. A., C. D. Charles, P. N. Froelich, M. A. Zibello, J. Saltzman, J. D. Hays, L. H. Burckle (1991), Evidence for lower productivity in the Antarctic Ocean during the last glaciation, *Nature*, **351**(6323), 220–223.
Mortlock, R. A., P. N. Froelich (1989), A simple method for the rapid determination of biogenic opal in pelagic marine sediments, *Deep Sea Res.*, **36**(9), 1415–1426.
Mortlock, R. A., P. N. Froelich (1989), A simple method for the rapid determination of biogenic opal in pelagic marine sediments, *Deep Sea Res.*, **36**, 1415–1426.
Muhs, D. R., T. A. Ager, E. A. Bettis, J. McGeehin, J. M. Been, J. E. Begét, M. J. Pavich, T. W. Stafford, D. A. S. P. Stevens (2003), Stratigraphy and palaeoclimatic significance of Late Quaternary loess-palaeosol sequences of the Last Interglacial-Glacial cycle in central Alaska, *Quat. Sci. Rev.*, **22**(18–19), 1947–1986.
Müller, J., O. Romero, E. A. Cowan, E. L. McClymont, M. Forwick, H. Asahi, C. März, C. M. Moy, I. Suto, A. Mix, J. Stoner (2018), Cordilleran ice-sheet growth fueled primary productivity in the Gulf of Alaska, northeast Pacific Ocean, *Geology*, **46**(4), 307–310.
Müller, P. J., E. Suess (1979), Productivity, sedimentation rate, and sedimentary organic matter in the oceans-I. Organic carbon preservation, *Deep Sea Res. Part A, Oceanogr. Res. Pap.,* **26**(12), 1347–1362.
Muñoz, P., L. Dezileau, L. Cardenas, J. Sellanes, C. B. Lange, J. Inostroza, J. Muratli, M. A. Salamanca (2012), Geochemistry of trace metals in shelf sediments affected by seasonal and permanent low oxygen conditions off central Chile, SE Pacific (~36°S), *Cont. Shelf Res*. **33**, 51–68.
Murray, R. W., D. J. Miller, K. A. Kryc (2000), Analysis of Major and Trace Elements in Rocks, Sediments, and Interstitial Waters by Inductively Coupled Plasma-Atomic Emission Spectrometry (ICP-AES), *ODP Tech. Note*.
Murray, R. W., M. Leinen, A. R. Isern (1993), Biogenic Flux of Al to Sediment in the Central Equatorial Pacific Ocean: Evidence for Increased Productivity during Glacial Periods, *Paleoceanography,* **8**, 651–670.
Murray, R. W., M. Leinen, C. W. Knowlton (2012), Links between iron input and opal deposition in the Pleistocene equatorial Pacific Ocean, *Nat. Geosci*., **5**(4), 270–274.
Nagashima, K., R. Tada, A. Tani, Y. Sun, Y. Isozaki, S. Toyoda (2011), Millennial-scale oscillations of the westerly jet path during the last glacial period, *J. Asian Earth Sci.*, **40**(6), 1214–1220.
Nakai, S., A. N. Halliday, D. K. Rea (1993), Provenance of dust in the Pacific Ocean, *Earth Planet. Sci. Lett.*, **119**, 143–157.

Nakashima, S., J.-R. Disnar, A. Perruchot, J. Trichet (1984), Experimental study of mechanisms of fixation and reduction of uranium by sedimentary organic matter under diagenetic or hydrothermal conditions, *Geochim. Cosmochim. Acta*, **48**, 2321–2329.

Nameroff, T. J., S. E. Calvert, J. W. Murray (2004), Glacial-interglacial variability in the eastern tropical North Pacific oxygen minimum zone recorded by redox-sensitive trace metals, *Paleoceanography*, **19**, PA1010.

Narita, H., M. Sato, S. Tsunogai, M. Murayama, N. Harada (2002), Biogenic opal indicating less productive northwestern North Pacific during the glacial ages, *Geophys. Res. Letters*, **29**(15), 2–5.

Nelson, D. M., P. Treguer, M. A. Brzezinski, A. Leynaert, B. Queguiner (1995), Production and dissolution of biogenic silica in the ocean: Revised global estimates, comparison with regional data and relationship to biogenic sedimentation, *Global Biogeochem. Cycles*, **9**(3), 359–372.

Ng, H.-C., L. F. Robinson, J. F. McManus, K. J. Mohamed, A. W. Jacobel, R. F. Ivanovic, L. Gregoire, T. Chen (*in revision*), Coherent deglacial changes in deep Atlantic Ocean circulation, *Nat. Commun.*

Nickling, W. G. (1978), Eolian Sediment Transport During Dust Storms - Slims River Valley, Yukon Territory, *Can. J. Earth Sci.*, **15,** 1069–1084.

Normark, W. R., J. L. Morton, R. A. Koski, D. A, Clague, J. R. Delaney (1983), Active hydrothermal vents and sulfide deposits on the southern Juan de Fuca Ridge, *Geology,* **11**, 158.

Nozaki, Y., Y. Horibe, H. Tsubota (1981), The water column distributions of thorium isotopes in the western North Pacific, *Earth Planet. Sci. Lett.* **54**, 203–216.

O'Gorman, P. A. (2010), Understanding the varied response of the extratropical storm tracks to climate change, *Proc. Natl. Acad. Sci.*, **107**(45), 19176–19180.

O'Neil, J. R. (1968), Hydrogen and oxygen isotope fractionation between ice and water, *J. Phys. Chem.*, **72**, 3683–3684.

Oba, T., T. Irino, M. Yamamoto, M. Murayama, A. Takamura, K. Aoki (2006), Paleoceanographic change off central Japan since the last 144,000 years based on high-resolution oxygen and carbon isotope records, *Glob. Planet. Change,* **53**(1–2), 5–20.

Okazaki, Y., A. Timmermann, L. Menviel, N. Harada, A. Abe-Ouchi, M. O. Chikamoto, A. Mouchet, H. Asahi (2010), Deepwater Formation in the North Pacific during the Last Glacial Termination, *Science*, **329**(5988), 200–204.

Okazaki, Y., K. Takahashi, H. Asahi, K. Katsuki, J. Hori, H. Yasuda, Y. Sagawa, H. Tokuyama (2005), Productivity changes in the Bering Sea during the late Quaternary, *Deep. Res. Part II Top. Stud. Oceanogr.*, **52**(16–18), 2150–2162.

Okazaki, Y., K. Takahashi, K. Katsuki, A. Ono, J. Hori, T. Sakamoto, M. Uchida, Y. Shibata, M. Ikehara, K. Aoki (2005), Late Quaternary paleoceanographic changes in the southwestern Okhotsk Sea: Evidence from geochemical, radiolarian, and diatom records, *Deep. Res. Part II Top. Stud. Oceanogr.*, **52**(16–18), 2332–2350.

Olson, L., K. A. Quinn, M. G. Siebecker, G. W. Luther, D. Hastings, J. L. Morford (2017), Trace metal diagenesis in sulfidic sediments: Insights from Chesapeake Bay, *Chem. Geol.,* **452**, 47–59.

Ono, Y. (1991), Glacial and Periglacial Paleoenvironments in the Japanese Islands, *Quat. Res.*, **30**(3), 203–211.

Ono, Y., T. Irino (2004), Southern migration of westerlies in the Northern Hemisphere PEP II transect during the Last Glacial Maximum, *Quat. Int.*, **118–119**, 13–22.

Oster, J. L., D. E. Ibarra, M. J. Winnick, K. Maher (2015), Steering of westerly storms over western North America at the Last Glacial Maximum, *Nat. Geosci.,* **8**(3), 201–205.

Owens, S. A., K. O. Buesseler, K. W. W. Sims (2011), Re-evaluating the 238U-salinity relationship in seawater: Implications for the 238U–234Th disequilibrium method, *Mar. Chem*. **127**, 31–39.

Paytan, A., E. M. Griffith (2007), Marine barite: Recorder of variations in ocean export productivity, *Deep. Res. Part II Top. Stud. Oceanogr*., **54**(5–7), 687–705.

Pease, C. H. (1980), Eastern Bering Sea Ice Processes, *Mon. Weather Rev*., **108**(12), 2015–2023.

Pedersen, T. F., N. B. Price (1982), The geochemistry of manganese carbonate in Panama Basin sediments, *Geochim. Cosmochim. Acta* **46**, 59–68.

Penny, S. M., D. S. Battisti, H. R. Gerard (2013), Examining mechanisms of variability within the pacific storm track: Upstream seeding and jet-core strength, *J. Clim*., **26**(14), 5242–5259.

Pettke, T., A. N. Halliday, C. M. Hall, D. K. Rea (2000), Dust production and deposition in Asia and the north Pacific Ocean over the past 12 Myr, *Earth Planet. Sci. Lett.*, **178**, 397–413.

Pichat, S., K. W. W. Sims, R. Francois, J. F. McManus, S. Brown-Leger, F. Albarede (2004), Lower export production during glacial periods in the equatorial Pacific derived from (231Pa/230Th)xs,0 measurements in deep-sea sediments, *Paleoceanography*, **19**(4), PA4023.

Plank, T. (2014), The Chemical Composition of Subducting Sediments, *Treatise Geochemistry (Second Ed.*, *4: The Crust)*, 607–629.

Poggemann, D., E. C. Hathorne, D. Nürnberg, M. Frank, I. Bruhn, S. Reißig, A. Bahr (2017), Rapid deglacial injection of nutrients into the tropical Atlantic via Antarctic Intermediate Water, *Earth Planet. Sci. Lett*., **463**, 118–126.

Polzin, K. L. (1997), Spatial Variability of Turbulent Mixing in the Abyssal Ocean, *Science*, **276**, 93–96.

Postma, D. (1993), The reactivity of iron oxides in sediments: A kinetic approach, *Geochim. Cosmochim. Acta,* **57**, 5027–5034.

Praetorius, S. K., A. C. Mix, M. H. Walczak, M. D. Wolhowe, J. A. Addison, F. G. Prahl (2015), North Pacific deglacial hypoxic events linked to abrupt ocean warming, *Nature*, **527**, 362–366.

Praetorius, S. K., J. F. McManus, D. W. Oppo, W. B. Curry (2008), Episodic reductions in bottom-water currents since the last ice age, *Nat. Geosci.,* **1**(7), 449–452.

Praetorius, S., A. Mix, B. Jensen, D. Froese, G. Milne, M. Wolhowe, J. Addison, F. Prahl (2016), Interaction between climate, volcanism, and isostatic rebound in Southeast Alaska during the last deglaciation, *Earth Planet. Sci. Lett.*, **452**, 79–89.

Prell, W. L., J. Imbrie, D. G. Martinson, J. J. Morley, N. G. Pisias, N. J. Shackleton, H. F. Streeter (1986), Graphic correlation of oxygen isotope stratigraphy application to the Late Quaternary, *Paleoceanography,* **1**, 137–162.

Prospero, J. M., P. Ginoux, O. Torres, S. E. Nicholson, and T. E. Gill (2002), Environmental characterization of global sources of atmospheric soil dust identified with the NIMBUS 7 Total Ozone Mapping Spectrometer (TOMS) absorbing aerosol product, *Rev. Geophys.*, **40**(1), 1–31.

Pullen, A., P. Kapp, A. T. McCallister, H. Chang, G. E. Gehrels, C. N. Garzione, R. V. Heermance, L. Ding (2011), Qaidam Basin and northern Tibetan Plateau as dust sources for the Chinese Loess Plateau and paleoclimatic implications, *Geology*, **39**(11), 1031–1034.

Rae, J. W. B., M. Sarnthein, G. L. Foster, A. Ridgewell, P. M. Grootes, T. Elliott (2014), Deep water formation in the North Pacific and deglacial CO2 rise, *Paleoceanography* **29**, 1–23.

Ragueneau, O., P. Treguer, A. Leynaert, R. F. Anderson, M. A. Brzezinski, D. J. DeMaster, R. C. Dugdale, J. Dymond, G. Fischer, R. Francois, C. Heinze, E. Maier-Reimer, V. Martin-Jezequel, D. M. Nelson, B. Queguiner (2000), A review of the Si cycle in the modern ocean: Recent progress and missing gaps in the application of biogenic opal as a paleoproductivity proxy, *Glob. Planet. Change*, **26**(4), 317–365.

Rahman, S., R. C. Aller, J. K. Cochran (2016), Cosmogenic 32Si as a tracer of biogenic silica burial and diagenesis: Major deltaic sinks in the silica cycle, *Geophys. Res. Lett.*, **43**(13), 7124–7132.

Rea, D. K. (1994), The paleoclimatic deposition record provided of wind by eolian in the deep sea: The geolgic history of wind, *Rev. Geophys.*, **32**(2), 159–195.

Rea, D. K., S. A. Hovan (1995), Grain-size distribution and depositional processes of the mineral component of abyssal sediments—lessons from the North Pacific, *Paleoceanography*, **10**(2), 251–258.

Reid, J. L. (1962), On circulation, phosphate-phosphorus content, and zooplankton volumes in the upper part of the Pacific Ocean, *Limnol. Oceanogr.,* **7**, 287–306.

Reimer, P. J., E. Bard, A. Bayliss, J. W. Beck, P. G. Blackwell, C. B. Ramsey, C. E. Buck, H. Cheng, R. L. Edwards, M. Friedrich, P. M. Grootes, T. P. Guilderson, H. Haflidason, I. Hajdas, C. Hatte, T. J. Heaton, D. L. Hoffman, A. G. Hogg, K. A. Hughen, K. F. Kaiser, B. Kromer, S. W. Manning, M. Niu, R. W. Reimer, D. A. Richards, E. M. Scott, J. R. Southon, R. A. Staff, C. S. M. Turney, J. van der Plicht (2013), Intcal13 and Marine13 radiocarbon age calibration curves 0-50,000 years calBP, *Radiocarbon,* **55**, 1869–1887.

Reimi, M. A., F. Marcantonio (2016), Constraints on the magnitude of the deglacial migration of the ITCZ in the Central Equatorial Pacific Ocean, *Earth Planet. Sci. Lett.*, **453**, 1–8.

Ren, H., A. S. Studer, S. Serno, D. M. Sigman, G. Winckler, R. F. Anderson, S. Oleynik, R. Gersonde, G. H. Haug (2015), Glacial-to-interglacial changes in nitrate supply and consumption in the subarctic North Pacific from microfossil-bound N isotopes at two trophic levels, *Paleoceanography*, **30**(9), 1217–1232.

Resing, J. A., P. N. Sedwick, C. R. German, W. J. Jenkins, J. W. Moffett, B. M. Sohst, A. Tagliabue (2015), Basin-scale transport of hydrothermal dissolved metals across the South Pacific Ocean, *Nature,* **523**, 200–203.

Reynolds, L., R. C. Thunell (1985), Seasonal succession of planktonic foraminifera in the subpolar North Pacific, *J. Foraminifer. Res.*, **15**(4), 282–301.

Riethdorf, J. R., L. Max, D. Nürnberg, L. Lembke-Jene, R. Tiedemann (2013), Deglacial development of (sub) sea surface temperature and salinity in the subarctic northwest Pacific: Implications for upper-ocean stratification, *Paleoceanography*, **28**(1), 91–104.

Riethdorf, J.-R., D. Nurnberg, L. Max, R. Tiedemann, S. A. Gorbarenko, M. I. Malakhov (2013), Millennial-scale variability of marine productivity and terrigenous matter supply in the western Bering Sea over the past 180kyr, *Clim. Past*, **2**, 1345–1373.

Rind, D. H. (1998), Latitudinal temperature gradients and climate change, *J. Geophys. Res.*, **103**(D6), 5943.

Riviere, G., S. Berthou, G. Lapeyre, M. Kageyama (2018), On the Reduced North Atlantic Storminess during the Last Glacial Period: The Role of Topography in Shaping Synoptic Eddies, *J. Clim.*, **31**(4), 1637–1652.

Robinson, R. S., B. G. Brunelle, D. M. Sigman (2004), Revisiting nutrient utilization in the glacial Antarctic: Evidence from a new method for diatom-bound N isotopic analysis, *Paleoceanography*, **19**(3), 1–13.

Roe, G. (2009), On the interpretation of Chinese loess as a paleoclimate indicator, *Quat. Res.*, **71**(2), 150–161.

Roshan, S., J. Wu, W. J. Jenkins (2016), Long-range transport of hydrothermal dissolved Zn in the tropical South Pacific, *Mar. Chem.,* **183**, 25–32.

Ruddiman, W. F. (1972), Sediment Redistribution on the Reykjanes Ridge: Seismic Evidence, *Geol. Soc. Am. Bull.* **83**, 2039–2062.

Rudnicki, M. D., H. Elderfield (1993), A chemical model of the buoyant and neutrally buoyant plume above the TAG vent field, 26 degrees N, Mid-Atlantic Ridge, *Geochim. Cosmochim. Acta,* **57**, 2939–2957.

Ruhlemann, C., M. Frank, W. Hale, A. Mangini, S. Mulitza, P. J. Muller, G. Wefer (1996), Late Quaternary productivity changes in the western equatorial Atlantic: Evidence from Th-230-normalized carbonate and organic carbon accumulation rates. *Mar. Geol.* **135**, 127–152.

Ruth, U., M. Bigler, R. Rothlisberger, M.-L. Siggaard-Anderson, S. Kipfstuhl, K. Goto-Azuma, M. E. Hansson, S. J. Johnsen, H. Lu, J. P. Steffensen (2007), Ice core evidence for a very tight link between North Atlantic and east Asian glacial climate, *Geophys. Res. Lett.*, **34**, L03706.

Sakamoto, T., M. Ikehara, K. Aoki, K. Iijima, N. Kimura, T. Nakatsuka, M. Wakatsuchi (2005), Ice-rafted debris (IRD)-based sea-ice expansion events during the past 100 kyrs in the Okhotsk Sea, *Deep. Res. Part II Top. Stud. Oceanogr.*, **52**(16–18), 2275–2301.

Sancetta, C. (1983), Effect of Pleistocene glaciation upon oceanographic characteristics of the North Pacific Ocean and Bering Sea, *Deep Sea Res. Part A, Oceanogr. Res. Pap.*, **30**(8), 851–869.

Sani, R. K., B. M. Peyton, J. E. Amonette, G. G. Geesey (2004), Reduction of uranium (VI) under sulfate-reducing conditions in the presence of Fe (III)-(hydr)oxides, *Geochim. Cosmochim. Acta,* **68**, 2639–2648.

Santos-Echeandia, J., R. Prego, A. Cobelo-García, G. E. Millward (2009), Porewater geochemistry in a Galician Ria (NW Iberian Peninsula): Implications for benthic fluxes of dissolved trace elements (Co, Cu, Ni, Pb, V, Zn), *Mar. Chem.*, **117**, 77–87.

Sasaoka, K., S. Saitoh, I. Asanuma, K. Imai, M. C. Honda, Y. Nojiri, T. Saino (2002), Temporal and spatial variability of chlorophyll a in the subarctic northwestern Pacific determined from satellite and ship observations during 1997–1999, *Deep Sea Res. Part II Top. Stud. Oceanogr.*, **49**(24–25), 5557–5576.

Sato, M., H. Narita, S. Tsunogai (2002), Barium increasing prior to opal during the last termination of glacial ages in the Okhotsk Sea sediments, *J. Oceanogr.*, **58**, 461–467.

Schaller, T., J. L. Morford, S. Emerson, R. A. Feely (2000), Oxyanions in metalliferous sediments: tracers for paleoseawater metal concentrations? *Geochim. Cosmochim. Acta,* **64**, 2243–2254.

Schenau, S. J., M. A. Prins, G. J. De Lange, C. Monnin (2001), Barium accumulation in the Arabian Sea: Controls on barite preservation in marine sediments, *Geochim. Cosmochim. Acta*, **65**(10), 1545–1556.

Schmitz, Jr., W. J. (1995), On the interbasin-scale thermohaline circulation*, Rev. Geophys.* **33**, 151–173.

Scholz, F., J. McManus, S. Sommer (2013), The manganese and iron shuttle in a modern euxinic basin and implications for molybdenum cycling at euxinic ocean margins, *Chem. Geol.,* **355**, 56–68.

Schrag, D. P., G. Hampt, D. W. Murray (1996), Pore fluid constraints on the temperature and oxygen isotopic composition of the glacial ocean, *Science*, **272**, 1930–1932.

Scott, S. D. (1983), Chemical behaviour of sphalerite and arsenopyrite in hydrothermal and metamorphic environments, *Mineral. Mag.* **47**, 427–435.

Seewald, J. S., Seyfried, W. E. (1990), The effect of temperature on metal mobility in subseafloor hydrothermal systems: Constrains from basalt alteration experiments, *Earth Planet. Sci. Lett.*, **101**, 388–403.

Seki, O., M. Ikehara, K. Kawamura, T. Nakatsuka, K. Ohnishi, M. Wakatsuchi, H. Narita, T. Sakamoto (2004), Reconstruction of paleoproductivity in the Sea of Okhotsk over the last 30 kyr, *Paleoceanography*, **19**(1).

Seo, I., Y. Lee, C. M. Yoo, K. Hyeong (2018), Migration of the Kuroshio Extension in the Northwest Pacific since the Last Glacial Maximum, *Palaeogeogr. Palaeoclimatol. Palaeoecol.*, doi.org/10.1016/j.palaeo.2018.01.048.

Serno, S., G. Winckler, R. F. Anderson, C. T. Hayes, H. Ren, R. Gersonde, G. H. Haug (2014), Using the natural spatial pattern of marine productivity in the Subarctic North Pacific to evaluate paleoproductivity proxies, *Paleoceanography*, **29**, 438–453.

Serno, S., G. Winckler, R. F. Anderson, E. Maier, H. Ren, R. Gersonde, G. H. Haug (2015), Comparing dust flux records from the Subarctic North Pacific and Greenland: Implications for atmospheric transport to Greenland and for the application of dust as a chronostratigraphic tool, *Paleoceanography*, **30**(6), 583–600.

Serno, S., G. Winckler, R. F. Anderson, S. L. Jaccard, S. S. Kienast, G. H. Haug (2017), Change in dust seasonality as the primary driver for orbital-scale dust storm variability in East Asia, *Geophys. Res. Lett.*, **44**(8), 3796–3805.

Seyfried, W. E., J. S. Seewald, M. E. Berndt, K. Ding, D. I. Foustoukos (2003), Chemistry of hydrothermal vent fluids from the Main Endeavour Field, northern Juan de Fuca Ridge: Geochemical controls in the aftermath of June 1999 seismic events*, J. Geophys. Res.* **108,** 2429.

Shaffer, G., J. Bendtsen (1994), Role of the Bering Strait in controlling North Atlantic ocean circulation and climate, *Nature*, **367**(6461), 354–357.

Shaw, T. J., J. M. Gieskes, R. A. Jahnke (1990), Early diagenesis in differing depositional environments : The response of transition metals in pore water, *Geochim. Cosmochim. Acta* **54**, 1233–1246.

Shcherbina, A. Y., L. D. Talley, D. L. Rudnick (2003), Direct Observations of North Pacific Ventilation: Brine Rejection in the Okhotsk Sea, *Science*, **302**(5652), 1952–1955.

Shigemitsu, M., H. Narita, Y. W. Watanabe, N. Harada, S. Tsunogai (2007), Ba, Si, U, Al, Sc, La, Th, C and13C/12C in a sediment core in the western subarctic Pacific as proxies of past biological production, *Mar. Chem.*, **106**(3–4), 442–455.

Shimmield, G. B., N. B. Price (1986), The behaviour of molybdenum and manganese during early sediment diagenesis -- offshore Baja California, Mexico, *Mar. Chem.*, **19**, 261–280.

Shimmield, G. B., N. B. Price (1988), The scavenging of U, 230Th, and 231Pa during pulsed hydrothermal activity at 20˚S, East Pacific Rise, *Geochim. Cosmochim. Acta,* **52**, 669–677.

Sigman, D. M., E. A. Boyle (2000), Glacial/interglacial variationsin atmospheric carbon dioxide, *Nature*, **407**, 859–869.

Sigman, D. M., S. L. Jaccard, G. H. Haug (2004), Polar ocean stratification in a cold climate, *Nature*, **428**, 59–63.
Sillen, L. G. (1961), The physical chemistry of seawater, in Oceanography, pp. 549–581, *American Association for the Advancement of Science*, Washington, D.C.
Singh, A. K., F. Marcantonio, M. Lyle (2013), Water column 230Th systematics in the eastern equatorial Pacific Ocean and implications for sediment focusing, *Earth Planet. Sci. Lett.* **362**, 294–304.
Smith, J. N., R. M. Brown, W. J. Williams, M. Robert, R. Nelson, S. B. Moran (2015), Arrival of the Fukushima radioactivity plume in North American continental waters, *Proc. Natl. Acad. Sci.,* **112**(5), 1310–1315.
Stott, L. D., M. Neumann, D. Hammond (2000), Intermediate water ventilation on the northeastern Pacific margin during the late Pleistocene inferred from benthic foraminiferal δ13C, *Paleoceanography* **15**, 161–169.
Stuiver, M., P. J. Reimer (1993), Extended 14C database and revised Calib 3.0 14C age calibration program, *Radiocarbon* **35**, 215–230.
Sugden, D. E., R. D. McCulloch, A. J.-M. Bory, A. S. Hein (2009), Influence of Patagonian glaciers on Antarctic dust deposition during the last glacial period, *Nat. Geosci.*, **2**(4), 281–285.
Suman, D. O., M. P. Bacon (1989), Variations in Holocene sedimentation in the North American Basin determined from 230Th measurements, *Deep Sea Res.* **36**, 869–878.
Sun, J., M. Zhang, T. Liu (2001), Spatial and temporal characteristics of dust storms in China and its surrounding regions, 1960-1999: Relations to source area and climate, *J. Geophys. Res.*, **106,** 10325–10333.
Tabata, S. (1975), The general circulation of the Pacific Ocean and a brief account of the oceanographic structure of the North Pacific ocean: Part I — Circulation and Volume Transports, *Atmosphere*, **13**(4), 133–168.
Taguchi, K., Narita, H. (1995), 230Th and 231Pa distributions in surface sediments off Enshunada, Ja, in: Sakai, H., Nozaki, Y. (Eds.), Biogeochemical Processes and Ocean Flux in the Western Pacific. *Terra Scientific Publishing Company*, Tokyo, pp. 375–382.
Talley, L. D. (1993), Distribution and formation of North Pacific Intermediate Water, *Am. Meteorol. Soc.*, **23**, 517–537.
Talley, L. D. (2008), Freshwater transport estimates and the global overturning circulation: Shallow, deep and throughflow components, Prog. Oceanogr., 78(4), 257–303.
Talley, L.D. (1993), Distribution and formation of North Pacific Intermediate Water, *Am. Meteorol. Soc.*, **23**, 517–537.
Tanaka, T. Y., M. Chiba (2006), A numerical study of the contributions of dust source regions to the global dust budget, *Glob. Planet. Change*, **52**, 88–104.
Taylor, B. J., J. W. B. Rae, W. R. Gray, K. F. Darling, A. Burke, R. Gersonde, A. Abelmann, E. Maier, O. Esper, P. Ziveri (2018), Distribution and ecology of planktic foraminifera in the North Pacific: Implications for paleo-reconstructions, *Quat. Sci. Rev.*, **191**, 256–274.
Taylor, S. R., S. M. McLennan (1995), The geochemical evolution of the continental crust, *Rev. Geophys.,* **33**(95), 241–265.
Taylor, S. R., S. M. McLennan, M. T. McCulloch (1983), Geochemistry of loess, continental crustal composition and crustal model ages, *Geochim. Cosmochim. Acta*, **47**(11), 1897–1905.

Tebo, B. M., J. R. Bargar, B. G. Clement, G. J. Dick, K. J. Murray, D. Parker, R. Verity, S. M. Webb (2004), Biogenic Manganese Oxides: Properties and Mechanisms of Formation, *Annu. Rev. Earth Planet. Sci.,* **32**, 287–328.

Thompson, P. R. (1981), Planktonic foraminifera in the Western North Pacific during the past 150,000 years: Comparison of modern and fossil assemblages, *Palaeogeogr. Palaeoclimatol. Palaeoecol.*, **35**(C), 241–279.

Thomson, J., S. Colley, R. F. Anderson, G. T. Cook, A. B. MacKenzie, D. D. Harkness (1993), Holocene sediment fluxes in the Northeast Atlantic from 230Thexcess and radiocarbon measurements, *Paleoceanography* **8**, 631–650.

Thomson, R. E. (1981), Oceanography of the British Columbia Coast, Canadian Special Publication of Fisheries and Aquatic Sciences, National Research Council, Ottawa.

Thomson, R. E., S. F. Mihaly, A. B. Rabinovich, R. E. McDuff, S. R. Veirs, F. R. Stahr (2003), Constrained circulation at Endeavour ridge facilitates colonization by vent larvae, *Nature* **424**, 545–549.

Thomson, R. E., S. F. Mihaly, A. B. Rabinovich, R. E. McDuff, S. R. Veirs, F. R. Stahr (2003), Constrained circulation at Endeavour ridge facilitates colonization by vent larvae, *Nature*, **424**, 545–549.

Thurnherr, A.M., K. G. Speer (2003), Boundary Mixing and Topographic Blocking on the Mid-Atlantic Ridge in the South Atlantic, *J. Phys. Oceanogr.* **33**, 848–862.

Thurnherr, A.M., L. C. St. Laurent, K. G. Speer, J. M. Toole, J. R. Ledwell (2005), Mixing Associated with Sills in a Canyon on the Midocean Ridge Flank, *J. Phys. Oceanogr.* **35**, 1370–1381.

Timmermann, A., T. Friedrich, O. E. Timm, M. O. Chikamoto, A. Abe-Ouchi, A. Ganopolski (2014), Modeling obliquity and CO2effects on southern hemisphere climate during the past 408 ka, *J. Clim.*, **27**(5), 1863–1875.

Torres, M. E., H. J. Brumsack, G. Bohrmann, K.-C. Emeis (1996), Barite fronts in continental margin sediments: a new look at barium remobilization in the zone of sulfate reduction and formation of heavy barites in diagenetic fronts, *Chem. Geol.*, **127**(1–3), 125–139.

Trefry, J. H., D. B. Butterfield, S. Metz, G. J. Massoth, R. P. Trocine, R. A. Feely (1994), Trace metals in hydrothermal solution from Cleft segment on the southern Juan de Fuca Ridge, *J. Geophys. Res.* **99**, 4925–4935.

Treguer, P. J., C. L. de la Rocha (2013), The World Ocean Silica Cycle, *Ann. Rev. Mar. Sci.*, **5**, 477–501.

Tribovillard, N., T. J. Algeo, T. Lyons, A. Riboulleau (2006), Trace metals as paleoredox and paleoproductivity proxies: An update, *Chem. Geol.*, **232**, 12–32.

Trocine, R. P., Trefry, J. H. (1988), Distribution and chemistry of suspended particles from an active hydrothermal vent site on the Mid-Atlantic Ridge at 26˚N, *Earth Planet. Sci. Lett.* **88**, 1–15.

Tsuda, A., H. Kiyosawa, A. Kuwata, M. Mochizuki, N. Shiga, H. Saito, S. Chiba, K. Imai, J. Nishioka, T. Ono (2005), Responses of diatoms to iron-enrichment (SEEDS) in the western subarctic Pacific, temporal and spatial comparisons, *Prog. Oceanogr.*, **64**(2–4), 189–205.

Turnewitsch, R., J. Reyss, J. Nycander, J. J. Waniek, R. S. Lampitt (2008), Internal tides and sediment dynamics in the deep sea — Evidence from radioactive 234 Th / 238 U disequilibria, *Deep Sea Res. I,* **55**, 1727–1747.

Turnewitsch, R., J.-L. Reyss, D. C. Chapman, J. Thomson, R. S. Lampitt (2004), Evidence for a sedimentary fingerprint of an asymmetric flow field surrounding a short seamount, *Earth Planet. Sci. Lett.,* **222**, 1023–1036.

Turnewitsch, R., S. Falahat, J. Nycander, A. Dale, R. B. Scott, D. Furnival (2013), Deep-sea fluid and sediment dynamics-Influence of hill- to seamount-scale seafloor topography, *Earth-Science Rev.* **127**, 203–241.

Uematsu, M., R. A. Duce, J. M. Prospero (1985), Deposition of atmospheric mineral particles in the North Pacific Ocean, *J. Atmos. Chem.*, **3**(1), 123–138.

Ueshima, T., M. Yamamoto, T. Irino, T. Oba, M. Minagawa, H. Narita, and M. Murayama (2006), Long term Aleutian Low dynamics and obliquity-controlled oceanic primary production in the mid-latitude western North Pacific (Core MD01-2421) during the last 145,000 years, *Glob. Planet. Change*, **53**(1–2), 21–28.

Uno, I., K. Eguchi, K. Yumimoto, Z. Liu, Y. Hara, N. Sugimoto, A. Shimizu, T. Takemura (2011), Large Asian dust layers continuously reached North America in April 2010, *Atmos. Chem. Phys.*, **11**, 7333–7341.

van Andel, T., P. D. Komar (1969), Ponded sediments of the Mid-Atlantic Ridge between 22˚ and 23 north latitude, *Geol. Soc. Am. Bull.* 1163–1190.

Van Cappellen, P., L. Qiu (1997), Biogenic silica dissolution in sediments of the Southern Ocean. II. Kinetics, *Deep. Res. Part II Top. Stud. Oceanogr.*, **44**(5), 1129–1149.

van Os, B. J., J. J. Middelburg, G. J. de Lange (1991), Possible diagenetic mobilization of barium in sapropelic sediment from the eastern Mediterranean, *Mar. Geol.*, **100**(1–4), 125–136.

Von Damm, K. L., A. M. Bray, L. G. Buttermore, S. E. Oosting (1998), The geochemical controls on vent fluids from the Lucky Strike vent field, Mid-Atlantic Ridge, *Earth Planet. Sci. Lett.* **160**, 521–536.

Von Damm, K. L., J. L. Bischoff (1987), Chemistry of hydrothermal solutions from the southern Juan de Fuca Ridge, *J. Geophys. Res.*, **92**, 11334.

Von Damm, K.L., J. M. Edmond, B. Grant, C. I. Measures, B. Walden, R. F. Weiss (1985), Chemistry of submarine hydrothermal solutions at 21˚N , East Pacific Rise, *Geochim. Cosmochim. Acta* **49**, 2197–2220.

von Drach, V., B. D. Marsh, G. J. Wasserburg (1986), Nd and Sr isotopes in the Aleutians: multicomponent parenthood of island-arc magmas, *Contrib. to Mineral. Petrol.*, **92**, 13–34.

von Stackelberg, U., U. von Rad, B. Zobel (1979), Asymmetric sedimentation around Great Meteor Seamount (North Atlantic), *Mar. Geol.* **33**, 117–132.

Wagner, J. D. M., J. E. Cole, J. W. Beck, P. J. Patchett, G. M. Henderson, H. R. Barnett (2010), Moisture variability in the southwestern United States linked to abrupt glacial climate change, *Nat. Geosci.*, **3**(2), 110–113.

Wallace, J. M., D. S. Gutzler (1981), Teleconnections in the Geopotential Height Field during the Northern Hemisphere Winter. *Mon. Weather Rev.*

Warren, B. A. (1983), Why is no deep water formed in the North Pacific?, *J. Mar. Res.*, **41**(2), 327–347.

Webb, H. F., T. H. Jordan (2001), Pelagic sedimentation on rough topography 1. Forward Model, *J. Geophys. Res.*, **106**, 30433–30449.

Weber, E. T., R. M. Owen, G. R. Dickens, A. N. Halliday, C. E. Jones, D. K. Rea (1996), Quantitative resolution of eolian continental crustal material and volcanic detritus in North Pacific surface sediment, *Paleoceanography*, **11**(1), 115–127.

Werner, M., I. Tegen, S. P. Harrison, K. E. Kohfeld, I. C. Prentice, Y. Balkanski, H. Rodhe, C. Roelandt, (2002), Seasonal and interannual variability of the mineral dust cycle under present and glacial climate conditions. *J. Geophys. Res. Atmos.*, **107**, 1–19.

Wersin, P., M. F. Hochella, Jr., P. Persson, G. Redden, J. Leckie, D. W. Harris (1994), Interaction between aqueous uranium (VI) and sulfide minerals: Spectroscopic evidence for sorption and reduction, *Geochim. Cosmochim. Acta* **58**, 2829–2843.

Westerlund, S. F. G., L. G. Anderson, P. O. J. Hall, A. Iverfeldt, M. M. Rutgers van der Loeff, B. Sundby (1986), Benthic fluxes of cadmium, copper, nickel, zinc, and lead in the coastal environment, *Geochim. Cosmochim. Acta* **50**, 1289–1296.

Wheeler, P. A., A. Huyer, J. Fleischbein (2003), Cold halocline, increased nutrients and higher chlorophyll off Oregon in 2002, *Geophys. Res. Lett.*, **30**(15), 30–33.

Whitney, F. A. (2011), Nutrient variability in the mixed layer of the subarctic Pacific Ocean, 1987-2010, *J. Oceanogr.*, **67**(4), 481–492.

Whitney, F. A., H. J. Freeland (1999), Variability in upper-ocean water properties in the NE Pacific Ocean, *Deep Sea Res. Part II Top. Stud. Oceanogr.*, **46**, 2351–2370.

Whitney, F. A., W. R. Crawford, P. J. Harrison (2005), Physical processes that enhance nutrient transport and primary productivity in the coastal and open ocean of the subarctic NE Pacific, *Deep. Res. Part II Top. Stud. Oceanogr.,* **52**(5–6), 681–706.

Wilson, D. S. (1993), Confidence intervals for motion and deformation of the Juan de Fuca plate, *J. Geophys. Res.* 98.

Winckler, G., R. F. Anderson, M. Q. Fleisher, D. McGee, N. Mahowald (2008), Covariant glacial-interglacial dust fluxes in the equatorial Pacific and Antarctica, *Science*, **320**(5872), 93–96.

Winckler, G., R. F. Anderson, S. L. Jaccard, F. Marcantonio (2016), Ocean dynamics, not dust, have controlled equatorial Pacific productivity over the past 500,000 years, *Proc. Natl. Acad. Sci.*, **113**(22), 6119–6124.

Wong, C. S., N. A. D. Waser, Y. Nojiri, F. A. Whitney, J. S. Page, J. Zeng (2002), Seasonal cycles of nutrients and dissolved inorganic carbon at high and mid latitudes in the North Pacific Ocean during the Skaugran cruises: Determination of new production and nutrient uptake ratios, *Deep. Res. Part II Top. Stud. Oceanogr.*, **49**(24–25), 5317–5338.

Xie, R. C., F. Marcantonio (2012), Deglacial dust provenance changes in the Eastern Equatorial Pacific and implications for ITCZ movement, *Earth Planet. Sci. Lett.*, **317–318**, 386–395.

Yamamoto, M., R. Suemune, T. Oba (2005), Equatorward shift of the subarctic boundary in the northwestern Pacific during the last deglaciation, *Geophys. Res. Lett.*, **32**, 10–13.

Yarincik, K. M., R. W. Murray, T. W. Lyons, L. C. Peterson, G. H. Haug (2000), Oxygenation history of bottom waters in the Cariaco Basin, Venezuela, over the past 578,000 years: Results from redox-sensitive metals (Mo, V, Mn, and Fe), *Paleoceanography* **15**, 593–604.

Yokoo, Y., T. Nakano, M. Nishikawa, H. Quan (2004), Mineralogical variation of Sr-Nd isotopic and elemental compositions in loess and desert sand from the central Loess Plateau in China as a provenance tracer of wet and dry deposition in the northwestern Pacific, *Chem. Geol.*, **204**(1–2), 45–62.

You, Y. (2003), Implications of cabbeling on the formation and transformation mechanism of North Pacific Intermediate Water, *J. Geophys. Res.*, **108**, 1–24.

Zahn, R., T. F. Pedersen, B. D. Bornhold, A. C. Mix (1991), Water Mass Conversion in the Glacial Subarctic Pacific (54°N, 148°W): Physical Constraints and the Benthic-Planktonic Stable Isotope Record, *Paleoceanography*, **6**(5), 543–560.

Zdanowicz, C., G. Hall, J. Vaive, Y. Amelin, J. Percival, I. Girard, P. Biscaye, A. Bory (2006), Asian dustfall in the St. Elias Mountains, Yukon, Canada, *Geochim.*

Cosmochim. Acta, **70**, 3493–3507.
Zhao, T. L., S. L. Gong, X. Y. Zhang, I. G. McKendry (2003), Modeled size-segregated wet and dry deposition budgets of soil dust aerosol during ACE-Asia 2001: Implications for trans-Pacific transport, *J. Geophys. Res.*, **108**(D23), 8665.
Zheng, L., T. Minami, S. Takano, H. Minami (2017), Distribution and stoichiometry of Al , Mn , Fe , Co , Ni , Cu , Zn , Cd , and Pb in seawater around the Juan de Fuca Ridge, *J. Oceanogr.*, **73**, 669–685.
Zheng, Y., R. F. Anderson, A. Van Geen, M. Q. Fleisher (2002a), Preservation of particulate non-lithogenic uranium in marine sediments, *Geochim. Cosmochim. Acta,* **66**, 3085–3092.
Zheng, Y., R. F. Anderson, A. Van Geen, M. Q. Fleisher (2002b), Remobilization of authigenic uranium in marine sediments by bioturbation, *Geochim. Cosmochim. Acta,* **66**, 1759–1772.

Appendix

Complete List of Publications

I. Subarctic Pacific

Costa, K. M., R. F. Anderson, J. F. McManus, G. Winckler, J. L. Middleton, C. H. Langmuir, (2018), Trace element (Mn, Zn, Ni, V) and authigenic uranium (aU) geochemistry reveal sedimentary redox history on the Juan de Fuca Ridge, North Pacific Ocean. *Geochim. Cosmochim. Acta*

Costa K. M., J. F. McManus, R. F. Anderson (2017), Radiocarbon and stable isotope evidence for changes in sediment mixing in the North Pacific over the past 30kyr, *Radiocarbon* **60**(1).

Costa, K. M., J. F. McManus (2017), Efficacy of ^{230}Th normalization in sediments from the Juan de Fuca Ridge, northeast Pacific Ocean, *Geochim. Cosmochim. Acta* 197, 215-225.

Costa, K. M., J. F. McManus, J. L. Middleton, C. H. Langmuir, P. J. Huybers, G. Winckler, S. Mukhopadhyay (2017), Hydrothermal deposition on the Juan de Fuca Ridge over multiple glacial-interglacial cycles, *Earth and Planetary Science Letters,* **479**, 120-132.

Costa, K. M., J. F. McManus, B. Boulahanis, S. M. Carbotte, G. Winckler, P. J. Huybers, C. H. Langmuir (2016), Sedimentation, stratigraphy and physical properties of sediment on the Juan de Fuca Ridge, *Mar. Geol.*, **380**, 163–173.

II. Equatorial Pacific

Costa K. M., A. W. Jacobel, J. F. McManus, R. F. Anderson, G. Winckler, N. Thiagarajan (2017), Productivity patterns in the Equatorial Pacific over the last 30,000 years, *Global Biogeochem. Cycles* **31**.

Costa, K. M., J. F. McManus, R. F. Anderson, H. Ren, D. M. Sigman, G. Winckler, M. Q. Fleisher, F. Marcantonio, A. C. Ravelo (2016), No iron fertilization in the equatorial Pacific Ocean during the last ice age, *Nature,* **529**, 519–522.